42
0-2-91 95 (2)

UCLA-PPG-1200

THE TITAN REVERSED-FIELD-PINCH FUSION REACTOR STUDY

Final Report 1990

Volume IV: TITAN-II Fusion Power Core

University of California, Los Angeles
Department of Mechanical, Aerospace,
and Nuclear Engineering and
Institute of Plasma and Fusion Research,
Los Angeles, CA

Los Alamos National Laboratory
Los Alamos, NM

General Atomics
San Diego, CA

Rensselaer Polytechnic Institute
Department of Nuclear Engineering
Troy, NY

UCLA/PPG--1200-Vol.4

DE92 000138

THE TITAN REVERSED-FIELD-PINCH FUSION REACTOR STUDY

FINAL REPORT
1990

Volume IV: TITAN-II Fusion Power Core

University of California, Los Angeles
Department of Mechanical, Aerospace,
and Nuclear Engineering and
Institute of Plasma and Fusion Research
Los Angeles, CA

Los Alamos National Laboratory
Los Alamos, NM

General Atomics
San Diego, Ca

Rensselaer Polytechnic Institute
Department of Nuclear Engineering
Troy, NY

CONTRIBUTING AUTHORS

UNIVERSITY OF CALIFORNIA, LOS ANGELES

Farrokh Najmabadi, Robert W. Conn, Nasr Ghoniem

James P. Blanchard, Yuh-Yi Chu, Patrick I. H. Cooke[1]
Steven P. Grotz, Mohammad Z. Hasan, Charles E. Kessel
Rodger C. Martin, Anil K. Prinja[2], George E. Orient
Shahram Sharafat, Erik L. Vold

GENERAL ATOMICS

Kenneth R. Schultz

Edward T. Cheng, Richard L. Creedon, Charles G. Hoot
Clement P. C. Wong

LOS ALAMOS NATIONAL LABORATORY

Robert A. Krakowski

John R. Bartlit[3], Charles G. Bathke, Ronald L. Miller
Ken A. Werley

RENSSELAER POLYTECHNIC INSTITUTE

Don Steiner

William P. Duggan, William P. Kelleher

ARGONNE NATIONAL LABORATORY

Dai-Kai Sze

CANADIAN FUSION FUELS TECHNOLOGY PROJECT

Paul J. Gierszewski, Otto K. Kevton

(1) Permanent address: Culham Laboratory, Abington, Oxfordshire, United Kingdom.
(2) Present address: University of New Mexico, Albuquerque, New Mexico.
(3) TSTA Program.

Contents

Volume I: EXECUTIVE SUMMARY

Volume II: TITAN PLASMA ENGINEERING

Volume III: TITAN-I FUSION POWER CORE

Volume IV: TITAN-II FUSION POWER CORE

ACKNOWLEDGEMENTS

The TITAN design team wishes to acknowledge the consultations and advice given by the TITAN Physics Advisory Committee on reversed-field-pinch physics issues and by the TITAN Engineering Review Committee on engineering design and analysis. Useful discussions with Frank Clinard of Los Alamos National Laboratory on properties of ceramic insulators, with John Davis of McDonnel Douglas on refractory metals, with John Haines of McDonnel Douglas on vacuum pumping issues, with Steve Piet of Idaho National Engineering Laboratory on safety aspects of the design, with Mark Tillack of University of California, Los Angeles on liquid-metal MHD issues, and with scientists of Fusion Engineering Design Center at Oak Ridge National Laboratory on design maintenance and integration are also acknowledged. The authors also wish to express their appreciation to Ms. Joan George for her effort in preparing this report.

The TITAN research program is supported by the U. S. Department of Energy, Office of Fusion Energy, at University of California, Los Angeles under grant DE-FG03-86ER52126, at General Atomics under contract DE-AC03-84ER53158, at Rensselaer Polytechnic Institute under grant DE-FG02-85ER52118, and at Los Alamos National Laboratory which is operated by the University of California for the U. S. DOE under contract W-7405-ENG-36.

TITAN PHYSICS ADVISORY COMMITTEE

Richard A. Nebel	Los Alamos National Laboratory
Allan Newton	Culham Laboratory
Stewart C. Prager	University of Wisconsin, Madison
Michael J. Schaffer	General Atomics
Kurt F. Schoenberg	Los Alamos National Laboratory
Teruo Tamano	General Atomics
Starnes Walker	*Phillips Petroleum Company*

TITAN ENGINEERING REVIEW COMMITTEE

Mohamed A. Abdou	University Of California, Los Angeles
Charles C. Baker	Argonne National Laboratory
Daniel Cohn	Massachusetts Institute Of Technology
James D. Gordon	TRW
Carl D. Henning	Lawrence Livermore National Laboratory
Michael J. Schaffer	General Atomics

ABSTRACT

The TITAN Reversed-Field-Pinch (RFP) fusion-reactor study is a multi-institutional research effort to determine the technical feasibility and key developmental issues for an RFP fusion reactor operating at high power density, and to determine the potential economic (cost of electricity), operational (maintenance and availability), safety and environmental features of high mass-power-density fusion systems. Mass power density (MPD) is defined as the ratio of net electric output to the mass of the fusion power core (FPC). The fusion power core includes the plasma chamber, first wall, blanket, shield, magnets, and related structure.

Two different detailed designs, TITAN-I and TITAN-II, have been produced to demonstrate the possibility of multiple engineering-design approaches to high-MPD reactors. TITAN-I is a self-cooled lithium design with a vanadium-alloy structure. TITAN-II is a self-cooled aqueous loop-in-pool design with 9C ferritic steel as the structural material. Both designs would use RFP plasmas operating with essentially the same parameters. Both conceptual reactors are based on the DT fuel cycle, have a net electric output of about 1000 MWe, are compact, and have a high MPD of 800 kWe per tonne of FPC. The inherent physical characteristics of the RFP confinement concept make possible compact fusion reactors with such a high mass power density. The TITAN designs would meet the U. S. criteria for the near-surface disposal of radioactive waste (Class C, 10CFR61) and would achieve a high Level of Safety Assurance with respect to FPC damage by decay afterheat and radioactivity release caused by accidents. Very importantly, a "single-piece" FPC maintenance procedure has been worked out and appears feasible for both designs.

Parametric system studies have been used to find cost-optimized designs, to determine the parametric design window associated with each approach, and to assess the sensitivity of the designs to a wide range of physics and engineering requirements and assumptions. The design window for such compact RFP reactors would include machines with neutron wall loadings in the range of $10 - 20\ MW/m^2$ with a shallow minimum-COE at about $18\ MW/m^2$. Even though operation at the lower end of the this range of wall loading ($10 - 12\ MW/m^2$) is possible, and may be preferable, the TITAN study adopted the design point at the upper end ($18\ MW/m^2$) in order to quantify and assess the technical feasibility and physics limits for such high-MPD reactors. From this work, key physics and engineering issues central to achieving reactors with the features of TITAN-I and TITAN-II have emerged.

15. OVERVIEW OF TITAN-II DESIGN

Farrokh Najmabadi Steven P. Grotz Clement P. C. Wong

Contents

15. OVERVIEW OF TITAN-II DESIGN

15.1. INTRODUCTION

The TITAN research program is a multi-institutional [1] effort to determine the potential of the reversed-field-pinch (RFP) magnetic fusion concept as a compact, high-power-density, and "attractive" fusion energy system from economics (cost of electricity, COE), safety, environmental, and operational viewpoints.

In recent reactor studies, the compact reactor option [2-5] has been identified as one approach toward a more affordable and competitive fusion reactor. The main feature of a compact reactor is a fusion power core (FPC) with a mass power density in excess of 100 to 200 kWe/tonne. Mass power density (MPD) is defined [2] as the ratio of the net electric power to the mass of the FPC, which includes the plasma chamber, first wall, blanket, shield, magnets, and related structure. The increase in MPD is achieved by increasing the plasma power density and neutron wall loading, by reducing the size and mass of the FPC through decreasing the blanket and shield thicknesses and using resistive magnet coils, as well as by increasing the blanket energy multiplication. A compact reactor, therefore, strives toward a system with an FPC comparable in mass and volume to the heat sources of alternative fission power plants, with MPDs ranging from 500 to 1000 kWe/tonne and competitive cost of energy.

Other potential benefits for compact systems can be envisaged in addition to improved economics. The FPC cost in a compact reactor is a small portion of the plant cost and, therefore, the economics of the reactor will be less sensitive to changes in the unit cost of FPC components or the plasma performance. Moreover, since a high-MPD FPC is smaller and cheaper, a rapid development program at lower cost should be possible, changes in the FPC design will not introduce large cost penalties, and the economics of learning curves can be readily exploited throughout the plant life.

The RFP has inherent characteristics which allow it to operate at very high mass power densities. This potential is available because the main confining field in an RFP is the poloidal field, which is generated by the large toroidal current flowing in the plasma. This feature results in a low field at the external magnet coils, a high plasma beta, and a very high engineering beta (defined as the ratio of the plasma pressure to the square of the magnetic field strength at the coils) as compared to other confinement schemes.

Furthermore, sufficiently low magnetic fields at the external coils permit the use of normal coils while joule losses remain a small fraction of the plant output. This option allows a thinner blanket and shield. In addition, the high current density in the plasma allows ohmic heating to ignition, eliminating the need for auxiliary heating equipment. Also, the RFP concept promises the possibility of efficient current-drive systems based on low-frequency oscillations of poloidal and toroidal fluxes and the theory of RFP relaxed states. The RFP confinement concept allows arbitrary aspect ratios, and the circular cross section of plasma eliminates the need for plasma shaping coils. Lastly, the higher plasma densities particularly at the edge, together with operation with a highly radiative RFP plasma, significantly reduce the divertor heat flux and erosion problems.

These inherent characteristics of the RFP [6] allow it to meet, and actually far exceed, the economic threshold MPD value of 100 kWe/tonne. As a result, the TITAN study also seeks to find potentially significant benefits and to illuminate main drawbacks of operating well above the MPD threshold of 100 kWe/tonne. The program, therefore, has chosen a minimum cost, high neutron wall loading of 18 MW/m^2 as the reference case in order to quantify the issue of engineering practicality of operating at high MPDs. The TITAN study has also put strong emphasis on safety and environmental features in order to determine if high-power-density reactors can be designed with a high level of safety assurance and with low-activation material to qualify for Class-C waste disposal.

An important potential benefit of operating at a very high MPD is that the small physical size and mass of a compact reactor permits the design to be made of only a few pieces and a single-piece maintenance approach will be feasible [7,8]. Single-piece maintenance refers to a procedure in which all of components that must be changed during the scheduled maintenance are replaced as a single unit, although the actual maintenance procedure may involve the movement, storage, and reinstallation of some other reactor components. In TITAN designs, the entire reactor torus is replaced as a single unit during the annual scheduled maintenance. The single-piece maintenance procedure is expected to result in the shortest period of downtime during the scheduled maintenance period because: (1) the number of connects and disconnects needed to replace components will be minimized; and (2) the installation time is much shorter because the replaced components are pretested and aligned as a single unit before committment to service. Furthermore, recovery from unscheduled events will be more standard and rapid because complete components will be replaced and the reactor brought back on line. The repair work will then be performed outside the reactor vault.

To achieve the design objectives of the TITAN study, the program was divided into two phases, each roughly one year in length: the Scoping Phase and the Design Phase.

The objectives of the Scoping Phase were to define the parameter space for a high-MPD RFP reactor and to explore a variety of approaches to major subsystems. The Design Phase focused on the conceptual engineering design of basic ideas developed during the Scoping Phase with direct input from the parametric systems analysis and with strong emphasis on safety, environmental, and opertional (maintenance) issues.

Scoping Phase activities of the TITAN program were reported separately [1]. Four candidate TITAN FPCs were identified during the Scoping Phase:

1. A self-cooled, lithium-loop design with a vanadium-alloy structure;
2. An aqueous, self-cooled "loop-in-pool" design in which the entire FPC is submerged in a pool of water to achieve a high level of passive safety;
3. A self-cooled FLiBe pool design using a vanadium-alloy structure; and
4. A helium-cooled ceramic design with a solid breeder and silicon carbide structure.

Two of the above FPC designs were selected for detail evaluation during the Design Phase because of inadequate resources to pursue all four designs. The choice of which two concepts to pursue was difficult; all four concepts have attractive features. The lithium-loop design promises excellent thermal performance and is one of the main concepts being developed by the blanket technology program. The water-cooled design promises excellent safety features and uses more developed technologies. The helium-cooled ceramic design offers true inherent safety and excellent thermal performance. The molten-salt pool design is the only low-pressure blanket and promises a high degree of passive safety. The lithium-loop (TITAN-I) and the aqueous "loop-in-pool" (TITAN-II) concepts were chosen for detailed conceptual design and evaluation in the Design Phase. The choice was based primarily on the capability to operate at high neutron wall load and high surface heat flux. The choice not to pursue the helium-ceramic and molten-salt designs should in no way denigrate these concepts. Both concepts offer high performance and attractive features when used at lower wall loads; these concepts should be pursued in future design studies.

The operating space of a compact RFP reactor has been examined using a comprehensive parametric systems model which includes the evolving state of knowledge of the physics of RFP confinement and embodies the TITAN-I and TITAN-II engineering approaches (Section 3). Two key figures of merit, the cost of electricity (COE) and mass power density (MPD), are monitored by the parametric systems model and are displayed

in Figure 15.1-1 as functions of the neutron wall loading. Figure 15.1-1 shows that the COE is relatively insensitive to wall loadings in the range of 10 to 20 MW/m^2, with a shallow minimum at about 19 MW/m^2. The MPD is found to increase monotonically with the wall load. For designs with a neutron wall load larger than about 10 MW/m^2, the FPC is physically small enough such that single-piece FPC maintenance is feasible. These considerations point to a design window for compact RFP reactors with neutron wall loading in the range of 10 to 20 MW/m^2. The TITAN-class RFP reactors in this design window have an MPD in excess of 500 kWe/tonne, and an FPC engineering power density in the range of 5 to 15 MWt/m^3; these values represent improvements by factors of 10 to 30 compared with earlier fusion reactor designs. The FPC cost is a smaller portion of the total plant cost (typically about 12%) compared with 25% to 30% for earlier RFP designs [4,5]. Therefore, the unit direct cost (UDC) is less sensitive to related physics and technology uncertainties.

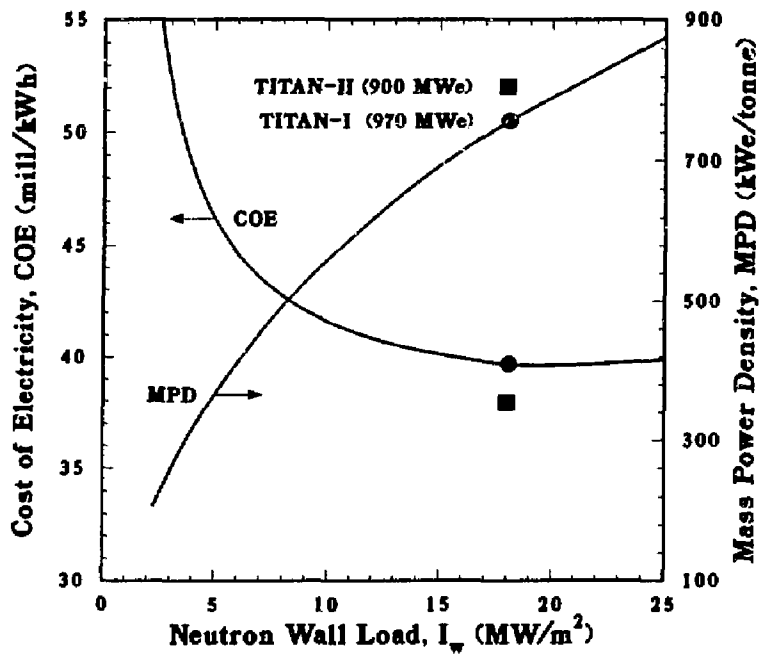

Figure 15.1-1. The COE and MPD as functions of neutron wall loading for the TITAN-class RFP reactors. TITAN-I (filled circle) and TITAN-II (filled squares) reference design points are also shown.

Near-minimum-COE TITAN-I and TITAN-II design points, incorporating distinct blanket thermal-hydraulic options, materials choices, and neutronics performances have been identified in Figure 15.1-1. The major parameters of the TITAN reactors are summarized in Table 15.1-I. In order to permit a comparison, the TITAN reference design points have similar plasma parameters and wall loadings allowing for certain plasma engineering analyses to be common between the two designs.

The TITAN RFP plasma operates at steady state using oscillating-field current-drive (OFCD) to maintain the 18 MA of plasma current. This scheme [9,10] utilizes the strong coupling, through the plasma relaxation process which maintains the RFP profiles [11], between the toroidal and poloidal fields and fluxes in the RFP. Detailed plasma/circuit simulations have been performed which include the effects of eddy currents induced in the FPC (Section 7). The calculated efficiency of the TITAN OFCD system is 0.3 A/W delivered to the power supply (0.8 A/W delivered to the plasma).

The impurity-control and particle-exhaust system consists of three high-recycling, toroidal-field divertors (Sections 5, 11, and 17). The TITAN designs take advantage of the beta-limited confinement observed in RFP experiments [12,13] to operate with a highly radiative core plasma, deliberately doped with a trace amount of high-Z Xe impurities (Section 5). The highly radiative plasma distributes the surface heat load uniformly on the first wall (4.6 MW/m^2). Simultaneously, the heat load on the divertor target plates is reduced to less than about 9 MW/m^2. The ratio of impurity density to electron density in the plasma is about 10^{-4}, Z_{eff} is about 1.7, and 70% of the core plasma energy is radiated (an additional 25% of the plasma energy is radiated in the edge plasma).

The "open" magnetic geometry of the divertors (Section 4.4), together with the intensive radiative cooling, leads to a high-recycling divertor with high density and low temperature near the divertor target ($n_e \simeq 10^{21}\,m^{-3}$, $T_e \simeq 5\,eV$) relative to the upstream separatrix density and temperature ($n_e \simeq 2 \times 10^{20}\,m^{-3}$, $T_e \simeq 200\,eV$). The radial temperature profile is calculated to decay sharply to 2 eV near the first wall (Section 5). Negligible neutral-particle leakage from the divertor chamber to the core plasma and adequate particle exhaust are predicted. The first-wall and divertor-plate erosion rate is negligibly small because of the low plasma temperature and high density at that location.

Table 15.1-I.

OPERATING PARAMETERS OF TITAN FUSION POWER CORES

	TITAN-I	TITAN-II
Major radius (m)	3.9	3.9
Minor plasma radius (m)	0.60	0.60
First wall radius (m)	0.66	0.66
Plasma current (MA)	17.8	17.8
Toroidal field on plasma surface (T)	0.36	0.36
Poloidal beta	0.23	0.23
Neutron wall load (MW/m^2)	18	18
Radiation heat flux on first wall (MW/m^2)	4.6	4.6
Primary coolant	Liquid lithium	Aqueous solution
Structural material	V-3Ti-1Si	Ferritic steel 9-C
Breeder material	Liquid lithium	$LiNO_3$
Neutron multiplier	none	Be
Coolant inlet temperature (°C)	320	298
First-wall-coolant exit temperature (°C)	440	330
Blanket-coolant exit temperature (°C)	700	330
Coolant pumping power (MW)	48	49
Fusion power (MW)	2301	2290
Total thermal power (MW)	2935	3027
Net electric power (MW)	970	900
Gross efficiency	44%	35%
Net efficiency	33%	30%
Mass power density, MPD (kWe/tonne)	757	806
Cost of electricity, COE (mill/kWh)	39.7	38.0

15.2. CONFIGURATION

Detailed subsystem designs for the TITAN-II FPC are given in Sections 16 through 20. The parameters of the TITAN-II reference design point, based on detailed subsystem designs, are included in Appendix B and follow the DOE/OFE standard reporting format. Appendix B also includes detailed cost tables and parametric systems code predictions of subsystem parameters for comparison with DOE/OFE tables. The elevation view of the FPC is shown in Figure 15.2-1. Figures 15.2-2 and 15.2-3 show the general arrangement of the TITAN-II reactor.

The major feature of the TITAN-II reactor is that the entire primary loop is located at the bottom of a low-temperature, atmospheric-pressure pool of pure water (Figure 15.2-1). Detailed safety analyses have been performed (Section 19) which show that the TITAN-II pool can contain the afterheat energy of the FPC and will remain at a low enough temperature such that tritium or other radioactive material in the primary-coolant system will not be released.

The TITAN plasma is ohmically heated to ignition by using a set of normal-conducting ohmic-heating (OH) coils and a bipolar flux swing. The TITAN start-up requires minimum on-site energy storage, with the start-up power directly obtained from the power grid (maximum start-up power is 500 MW). The TITAN-II OH coils are cooled by pure water. A pair of relatively low-field superconducting equilibrium-field (EF) coils produce the necessary vertical field and a pair of small, copper EF trim coils provide the exact equilibrium during the start-up and OFCD cycles. The poloidal-field-coil arrangement allows access to the complete reactor torus by removing only the upper OH-coil set. The toroidal-field (TF) and divertor coils of TITAN-II are also composed of copper alloy.

The first wall and blanket of the TITAN-II design are integrated in the form of blanket lobes (Figure 15.2-4). The construction procedure for each blanket lobe is shown in Figure 15.2-5. Each blanket lobe is made of two plates, called "J-plates" because one edge of each plate is rolled to the appropriate radius to form a J-section. Both J-plates are made of the low-activation, high-strength ferritic steel, 9-C [15]. The first-wall plate is thicker than the other plate, since it is subject to erosion. Two plates are then brazed or welded together to form a complete blanket lobe. A channel manifold ring completes the lobe and allows the coolant and breeder mixture to flow. This configuration will require a multistage pressing operation, perhaps even hot-pressing to achieve this shape.

An alternate design, also shown in Figure 15.2-5, is the U-plate design. The advantages of this design are that the thin material can be used for both sides, and the edge U

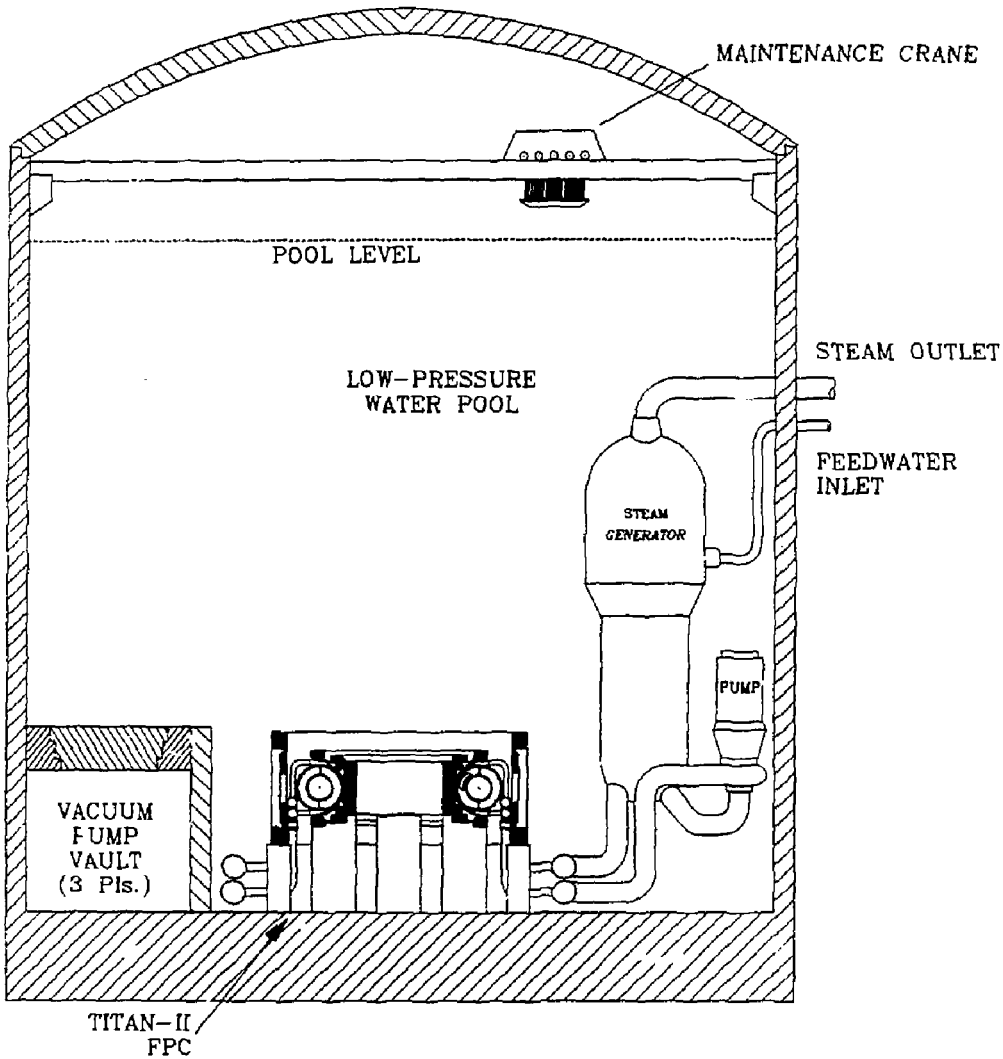

Figure 15.2-1. Elevation view of the TITAN-II reactor building through the reactor centerline showing the water pool and the maintenance crane.

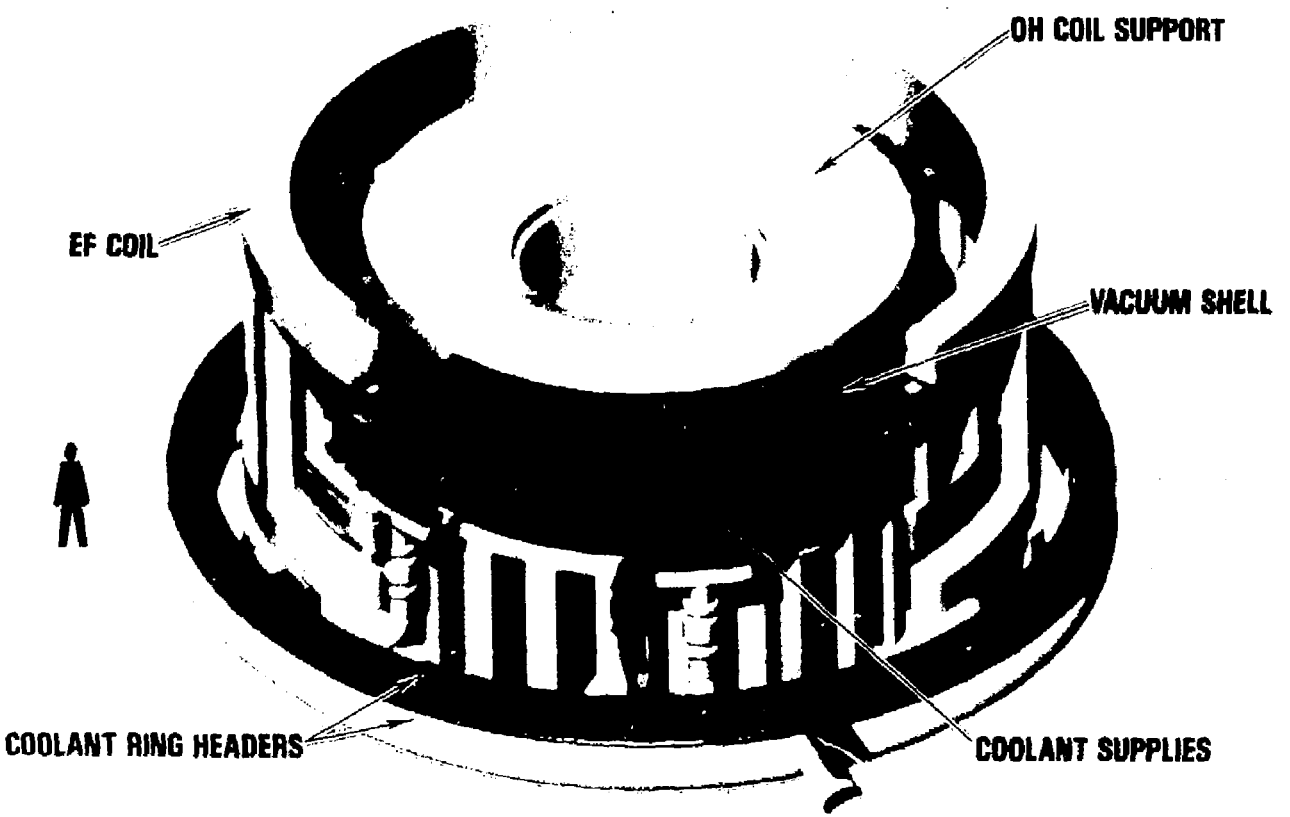

J-947(1)
3-1-91

Figure 15.2-2. The TITAN-II fusion power core. The coolant inlet headers are in white and the outlet headers are in red.

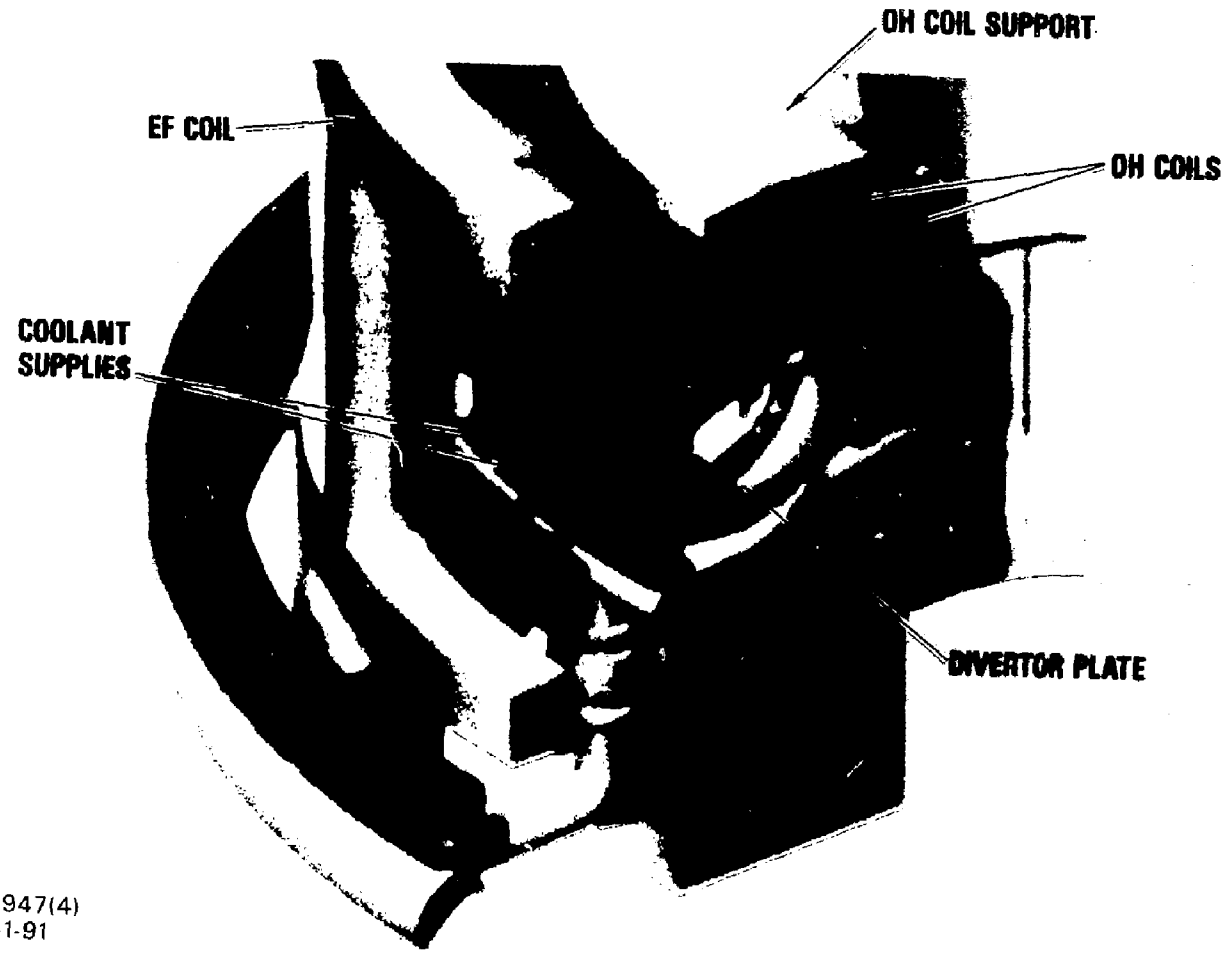

Figure 15.2-3. Cut-away view of the TITAN-II fusion power core. The coolant inlet headers are in white and the outlet headers are in red.

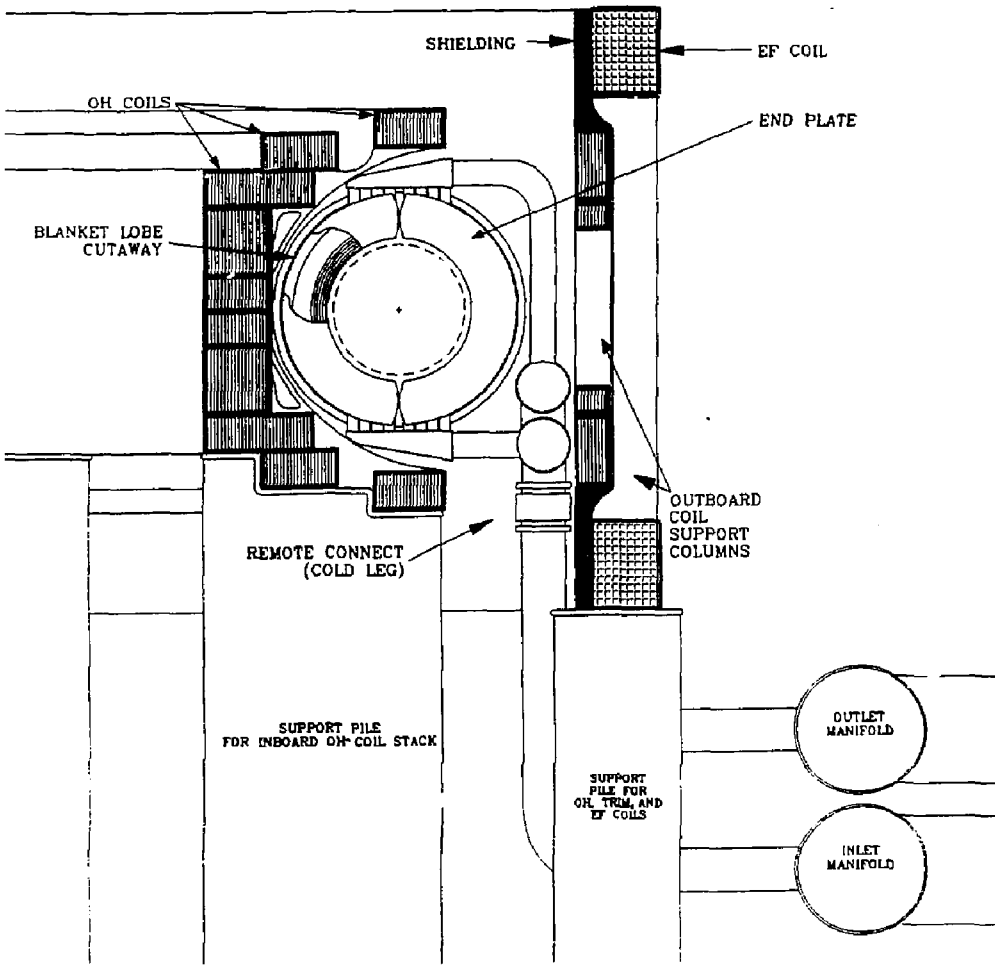

Figure 15.2-4. Poloidal cross section of the TITAN-II fusion power core.

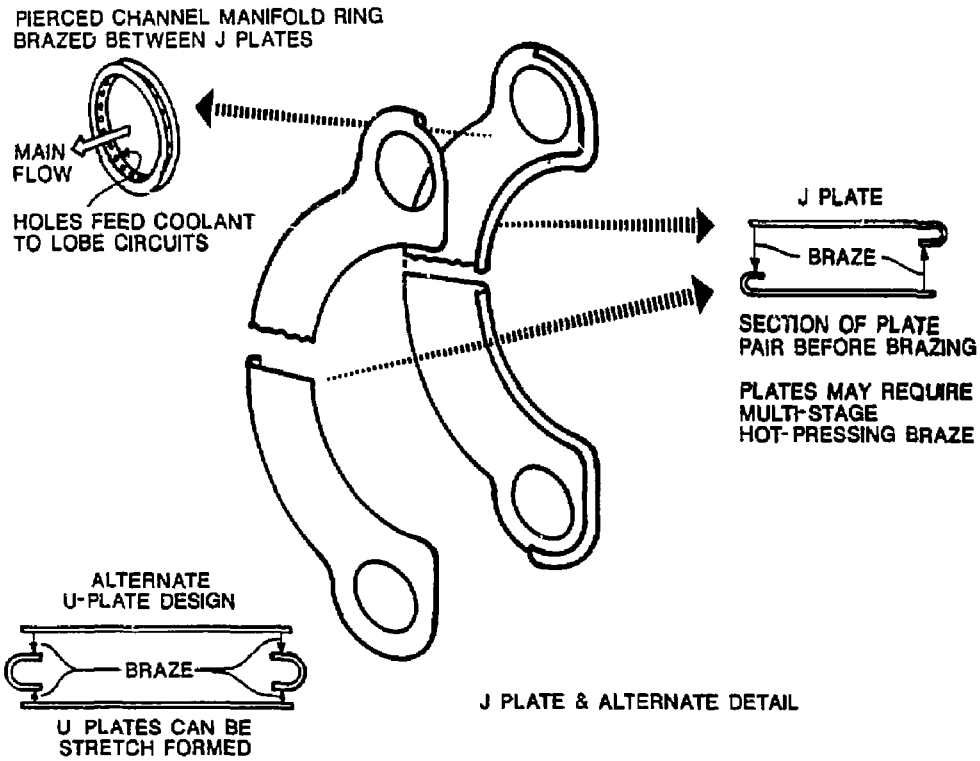

Figure 15.2-5. The TITAN-II blanket lobe, J-plate design.

members are easier to make than the J-plates. However, acceptance of either configuration will depend on detailed investigation of the thick braze or weld area to ensure that there is no focusing of thermal radiation or other heat-transfer problems.

The outer dimensions of the blanket lobes are 3 cm toroidally and 30 cm radially. The lobe wall thickness is 1.4 mm. The cross section of the first wall is a semicircular channel with the convex side facing the plasma. The outer diameter is 3 cm, and the wall thickness of 1.5 mm includes a 0.25-mm allowance for erosion (the first-wall erosion is estimated to be negligible). A neutron multiplier zone is located behind the first wall and contains 7 rows of beryllium rods clad in 9-Cr alloy, with a diameter of 2.6 cm. The thickness of the clad is 0.25 mm. The multiplier zone is 20-cm long in the radial direction and contains 12% structure, 59% beryllium, and 29% coolant (all by volume). Nuclear heating rate in the blanket decreases away from the first wall, therefore, to ensure proper coolant velocity, poloidal flow separators are placed behind the 2nd, 4th, and 7th rows of beryllium rods to form channels which have individual orifices. The remaining 10 cm of the blanket lobe (the breeder/reflector zone) does not contain beryllium and consists of 9% structure and 91% coolant (by volume).

Seventy blanket lobes are then stacked side-by-side to form a blanket module. The structural details of a blanket module are shown in Figure 15.2-6. This arrangement is structurally a membrane pressure vessel with balancing forces, derived from identical neighboring lobes, maintaining its flat sides. This configuration requires an external constraining structure to keep it pressed into oval form, which is readily derived from the shield as discussed below. The advantage of this design is that the structural fraction in the important near-first-wall radial zone is nearly as low as ideally possible, giving good tritium-breeding performance. This configuration also has a much lower void fraction when compared to a tubular design, giving a minimum-thickness blanket. The assembly technique for each blanket module is expected to be multistage brazing with intermediate leak checking. Since the lobes only require constraint in the blanket toroidal direction and because they are structurally soft in this direction, high precision is not necessary.

The TITAN-II FPC consists of three sectors, separated by the divertor modules. Four blanket modules are assembled together to form a sector. The shield is made of cast half-ring sectors, welded together at the inside edge (Figure 15.2-6) to form a blanket container. The shield is 10-cm thick in the radial direction and contains two rows of circular coolant channels. The volume percentages of structure and coolant in the shield are 90% and 10%, respectively.

The split at the top and bottom of the torus divides the blanket and the shield into inner and outer half shells which are structurally independent. The coolant channels are

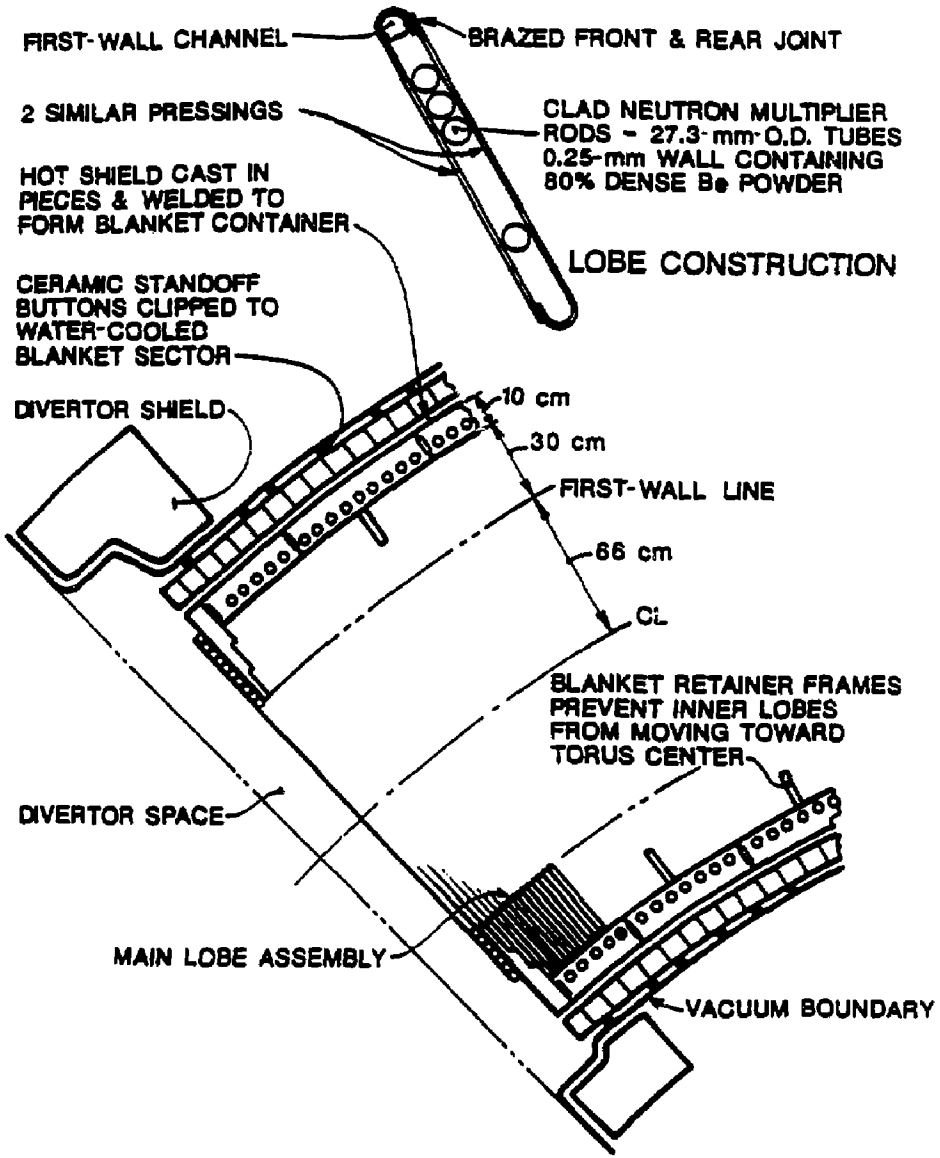

Figure 15.2-6. Equatorial-plane cross section of a TITAN-II blanket module.

in the poloidal direction. The coolant enters at the bottom and exits at the top of the torus. One set of coolant channels runs along the out-board side of the torus and the other along the in-board side. The tendency of the flat sides of a sector to blow out has to be resisted by what are, in effect, the divertor walls (Figure 15.2-6). These walls are 12-cm-thick cantilever beam members which also derive some of their strength from their torsional stiffness and will require internal cooling. These walls are anchored to the shield shell by welds at the inside and outside of the shield.

Immediately behind the shield there is a 5-cm-thick zone occupied by the toroidal field (TF) coil which is a multi-turn copper coil held in position by ceramic standoffs from the shield (Figure 15.2-6). The design of the TF-coil support elements is straightforward since the gravitational and magnetic forces on the TF coils are relatively small and are carried externally.

The vacuum boundary is a continuous, 5-mm-thick metal shell immediately outside the TF coil. Because of the large toroidal radius of 5.06 m, such a shell cannot withstand the atmospheric and water-pool pressures totaling about 3 atm without buckling. Accordingly, since the working stress is only about 7 MPa, nonconducting stabilizers similar to those used for the 5-cm-thick TF coil can be used. If necessary, the vacuum boundary can be electrically insulated in the toroidal direction by alternate layers of soft aluminum and hard, anodized 7075 aluminum-alloy sheets. The soft aluminum provides a deformable vacuum seal, and the anodized layer provides the electrical insulation. The two vacuum boundary skins can then be held together by 15-mm-thick stainless-steel, insulator-lined swagged clamps. Details of this method of vacuum-vessel insulation will still need to be demonstrated.

A number of electrically insulated penetrations of the vacuum shell also have to be made for the TF-coil leads. It is envisaged that the technology of automotive spark plugs can be developed to do this job. This consists of the embedment of a precision ceramic insulator in soft metal (usually copper) gaskets. This technique is presently available for diameters an order of magnitude larger than spark plugs, and its extension to sizes relevant to our task appears feasible. This also needs to be developed.

A skirt, welded to the lower header system and extended to the pool bottom, will support the entire removable first wall, blanket, and shield assembly. This skirt will be of open-frame form to allow free circulation of the pool.

The lifetime of the TITAN-II reactor torus (including the first wall, blanket, shield, and divertor modules) is estimated to be in the range of 15 to 18 MWy/m^2, with the more conservative value of 15 MWy/m^2 requiring the change-out of the reactor torus on

a yearly basis for operation at 18 MW/m^2 of neutron wall loading at 76% availability. The TF coils are designed to last the entire plant life (30 full-power years). However, during the maintenance procedure, the TF coils are not separated from the reactor torus and are replaced each year. After the completion of the maintenance procedure, the used TF coils can be separated from the reactor torus and reused at a later time. The impact of discarding (not reusing) the TF-coil set annually is negligible on the COE.

15.3. MATERIALS

The TITAN-II FPC is cooled by an aqueous lithium-salt solution which also acts as the breeder material [14]. Issues of corrosion and radiolysis, therefore, greatly impact the choice of the dissolved lithium salt and the structural material.

Two candidate lithium salts, lithium hydroxide (LiOH) and lithium nitrate ($LiNO_3$), are considered because they are highly soluble in water. The $LiNO_3$ salt is selected as the reference salt material for two main reasons. First, LiOH is more corrosive than $LiNO_3$ (Section 16.2.1). Recently, electrochemical corrosion tests were performed for LiOH and $LiNO_3$ aqueous solutions in contact with AISI 316 L stainless steels [16]. It was found that stainless steels, particularly low-carbon steels, exhibit better corrosion resistance in an $LiNO_3$ solution than in LiOH. From the point of view of radiolysis, lithium-nitrate solutions are also preferable. Radiolytic decomposition of water results in the formation of free radicals that will ultimately form highly corrosive hydrogen peroxide and OH ions. Nitrate ions (NO_3^-) in a lithium-nitrate solution, act as scavengers to reduce the probability of survival of highly reactive radicals in the water during exposure to radiation (Section 16.2.2).

Among the candidate low-activation vanadium alloys, V-3Ti-1Si (the structural material for the TITAN-I design) had to be ruled out because of its poor water-corrosion resistance. Other vanadium alloys which contain chromium (*e.g.*, V-15Cr-5Ti) show excellent resistance to corrosion by water coolant but their properties are inferior to those of ferritic steels when helium-embrittlement effects are taken into account [17] (Section 10.2). Therefore, various steels were considered as TITAN-II structural material.

Reported results of the low-activation ferritic-steel (LAFS) development program indicate that a reduced-activation alloy can be developed without compromising mechanical properties, primarily by replacing Mo with W. For the TITAN-II reactor, the HEDL/UCLA 12Cr 0.3V-1W-6.5Mn alloy (alloy 9-C) has been chosen as the structural

material primarily because of its high strength and good elongation behavior after irradiation as compared with other LAFSs [15]. The high chromium content of this alloy ensures an excellent corrosion resistance. The low carbon content of this alloy results in good weldability, high sensitization resistance (Section 16.2.1), and reduces hydrogen-embrittlement susceptibility (Section 16.2.5). Furthermore, alloy 9-C has a low tungsten content ($< 0.9\%$) which reduces the waste-disposal concerns of the production of the radionuclide ^{186m}Re by fusion-neutron reaction with W [18]. The high concentration of manganese in alloy 9-C prevents the formation of delta-ferrite phases, which is responsible for high ductile-to-brittle transition temperature (DBTT) and low hardness. The composition (wt.%) of alloy 9-C was determined by the vendor as: 11.81Cr, 0.097C, 0.28V, 0.89W, 6.47Mn, 0.11Si, 0.003N, $<$ 0.005P, 0.005S with the balance in iron.

Radiolytic decomposition of aqueous solutions exposed to a radiation environment is always cause for concern. Radiolysis of pure water and of aqueous $LiNO_3$ salt solutions by light particles (e, γ, X ray) and heavy particles (n, p, T, α) was investigated. Gamma-ray radiolysis yields of $LiNO_3$ salt solutions are known as a function of salt concentration. At high concentrations, the H_2 yields are very small and the H_2O_2 yield decreases by a factor of about 3 relative to pure water. Oxygen yields of light-particle radiation are fairly independent of the salt concentration.

Energetic alpha particles ($\sim$ 2 MeV) are produced by nuclear reactions with lithium in the aqueous $LiNO_3$ salt solution. Reaction yields were estimated as a function of salt concentration based on the power law measurements of 3.4 MeV alpha particles. The oxygen production by heavy-particle radiation increases while the yields of H_2, H_2O_2, H, OH, and HO_2 all decrease with increasing salt concentration. The increase in oxygen production due to radiolysis may be balanced by the production of tritium atoms. It has been shown that oxygen added to non-boiling fission-reactor coolants at high power levels rapidly combines with any hydrogen present. The decrease in the yield of free radicals in concentrated $LiNO_3$ solutions makes this salt more favored than LiOH solutions.

The effect of elevated temperature on radiolysis was investigated. From experience gained in the fission industry with pure water, it can be ascertained that the stability of non-boiling water to radiolysis increases as temperature increases. The apparent stability is actually caused by an increase in recombination-reaction rates of radicals at elevated temperatures.

In summary, although many uncertainties remain and much research is required in the area of radiolysis, the use of a highly concentrated, aqueous $LiNO_3$ salt solutions should not lead to the formation of volatile or explosive gas mixtures. The effects of radiolytic

decomposition products on corrosion, however, remain uncertain and experimental data on the behavior of radiolytic decomposition products in a fusion environment are needed.

Stress-corrosion cracking (SCC) is a major concern in the nuclear industry. Most recent experiences with SCC in a nuclear environment clearly show that reducing the oxygen content through the addition of hydrogen to the coolant can reduce SCC in most ferritic and austenitic alloys. The production of tritium in an aqueous lithium-salt solution is seen as an SCC controlling mechanism. The proper choice of structural material can further reduce the probability of SCC. In particular, a high chromium content together with a low carbon content is shown to reduce SCC. The ferritic alloy, 9-C, fulfills this requirement.

Experience with various aqueous nitrate-salt solutions shows that the choice of the cation will affect the degree of corrosion attack. The aggressiveness of nitrates decreases with choice of cation in the following order: NH_4, Ca, Li, K, and Na. Thus, for the $LiNO_3$ salt, the aggressiveness of NO_3^- ions is in the medium range. The effect of the cation choice on SCC has been related to the acidity of the solution. Investigations into buffering the $LiNO_3$ salt solutions to an optimum pH value could lead to a marked reduction in the aggressiveness of the solution. Reduction of the oxidizing strength of the salt solution has been found to retard failure of test samples by SCC. On the other hand, an increase in the oxidizing power of the solution decreases radiolytic decomposition rates. An optimum oxidizing strength will have to be established experimentally since the number of factors involved are too large to make analytical predictions.

Recent experiments [19] on the corrosion rates of $LiNO_3$ salt solutions with 316 SS and a martensitic alloy at 95 and 250 °C show a lack of a marked transition between the primary and secondary passive regions. This data implies that a relatively stable passive layer is formed in this salt. Microscopic examination of the 316 SS showed that a smooth oxide film was formed on the metal surface in $LiNO_3$, with the roughness independent of solution concentration and temperature. Recently, electrochemical corrosion tests were performed for aqueous LiOH and $LiNO_3$ solutions in contact with AISI 316 L stainless steel [16]. It was found that stainless steels, particularly low-carbon steels, exhibit better corrosion resistance in $LiNO_3$ solution than in LiOH.

It should be noted that most of the above experimental findings regarding corrosion and SCC of steels in $LiNO_3$ salt solutions were obtained without any control of the oxygen content of the solution which plays a significant role in corrosion processes. In a fusion environment, the production of tritium will undoubtedly affect the oxygen content of the aqueous solution through recombination. Thus, breeding of tritium in the aqueous

solution can potentially reduce corrosion and SCC of the structural material used in the FPC.

The investigation of the corrosion of ferritic steels in an aqueous $LiNO_3$ salt solution does not show unexpectedly high corrosion rates or high susceptibility to SCC. In addition, the latest experimental findings do not indicate any unforeseen catastrophic corrosion attack. However, an extensive research effort needs to be undertaken to confirm these observations. Furthermore, the effects of high-energy neutron irradiation on corrosion mechanisms and rates should be examined.

Another form of attack on structural material in an aqueous environment is hydrogen embrittlement, caused primarily by the trapping of absorbed hydrogen in metals under applied stresses. The main factor influencing hydrogen embrittlement is the hydrogen content, which depends strongly on the temperature, microstructure, and strength of the alloy. Hydrogen content can be reduced by minimizing the source of nascent hydrogen (mostly due to corrosion) and by operating at high temperatures ($> 200\,°C$), provided that a low-carbon steel is used. High concentrations of chromium, nickel, or molybdenum ($> 10\,wt.\%$) increase the resistance of ferrous alloys to hydrogen damage. Microstructural features (*e.g.*, a fine-grained and annealed alloy with minimum cold work) further reduce susceptibility to hydrogen embrittlement. Because of the lower strength and higher ductility of ferritic steels, these alloys are generally less susceptible to hydrogen embrittlement than austenitic steels.

Atomic hydrogen is produced on metal surfaces during corrosion processes. Thus, minimizing corrosion also reduces hydrogen embrittlement of the structure. The addition of nitrate salts to the aqueous solution reduces the corrosion rate of ferrous alloys (Section 10.2.1), resulting in a reduction in the production of hydrogen atoms on the surfaces, and thus reducing the nascent hydrogen content. The production of tritium in the coolant does not necessarily result in an increased hydrogen attack because of rapid recombination to form molecular hydrogen or water molecules. The production of hydrogen by nuclear reactions and by plasma-driven permeation through the first wall of a fusion device increases the hydrogen content inside the alloy matrix which may lead to unacceptable hydrogen embrittlement of the structure for operation at or near room temperature (the highest susceptibility of high-strength alloys to hydrogen embrittlement is at or near room temperature [20]). But the TITAN-II structural material operates at high temperatures ($> 400\,°C$), minimizing the effective trapping of hydrogen inside the matrix. Experiments show that above $\sim 200\,°C$, hydrogen embrittlement of ferrous alloys is reduced markedly [21]. Furthermore, the Nelson curves [22], used by the petrochemical industry as guidelines, show that chromium steels can operate at $400\,°C$ with a hydrogen

partial pressure of 17 MPa without experiencing internal decarburization and hydrogen embrittlement [20].

Based on the above discussion, the ferritic alloy 9-C is expected to exhibit a high resistance to hydrogen embrittlement. The number of factors influencing hydrogen embrittlement are numerous and their interdependence is a complex function of the specific microstructure and operating conditions of an alloy. Therefore, experimental data are needed in order to perform a complete evaluation of hydrogen embrittlement of the 9-C alloy under TITAN-II operating conditions.

The physical properties of concentrated solutions of $LiNO_3$ at high temperatures differ from those of pure water. Therefore, the exact coolant conditions should be considered in designing the blanket. The thermal-hydraulic design of an aqueous-salt blanket can be very different from that of a water-cooled design, and advantage can be taken of the differences in properties by, for example, reducing the coolant pressure or increasing the temperature without incurring an increased risk of burnout.

A fairly detailed investigation of the physical properties of the aqueous solutions was made, including an extensive literature survey, to ensure that reliable data were used in analyzing the performance of the TITAN-II FPC. In many cases, experimental data for some physical properties of interest for $LiNO_3$ solutions are not available at high temperatures. Where this is the case, and reasonable extrapolations cannot be made, the corresponding data for NaCl solutions have been used. The NaCl-H_2O system has been much more widely studied than any other solution and many solutions of 1-1 electrolytes (*e.g.*, NaCl, KBr, and $LiNO_3$) have similar properties at the same concentrations. It is expected that such estimates should be accurate to about 20% [23], which is adequate for a worthwhile assessment of the thermal performance of the blanket to be made.

The physical properties of $LiNO_3$ solutions as a function of temperature and salt concentration are given in Section 10.2.3. The most drastic effect of adding $LiNO_3$ to the coolant water lies in the elevation of the boiling point of the solution. This implies that the thermal-hydraulic design of such an aqueous-salt blanket will be different from that of a pure-water-cooled design. Therefore, a lower coolant pressure or a higher operating temperature can be chosen. The estimated boiling temperature of the $LiNO_3$ solutions at various pressures are shown in Figure 15.3-1 for a range of lithium-atom concentration in the aqueous coolant.

Many of the estimates of the properties of $LiNO_3$ aqueous solution are extrapolations from experimental data or have been obtained from the results for other salt solutions. Although these predictions should give good indications of the expected trends for the

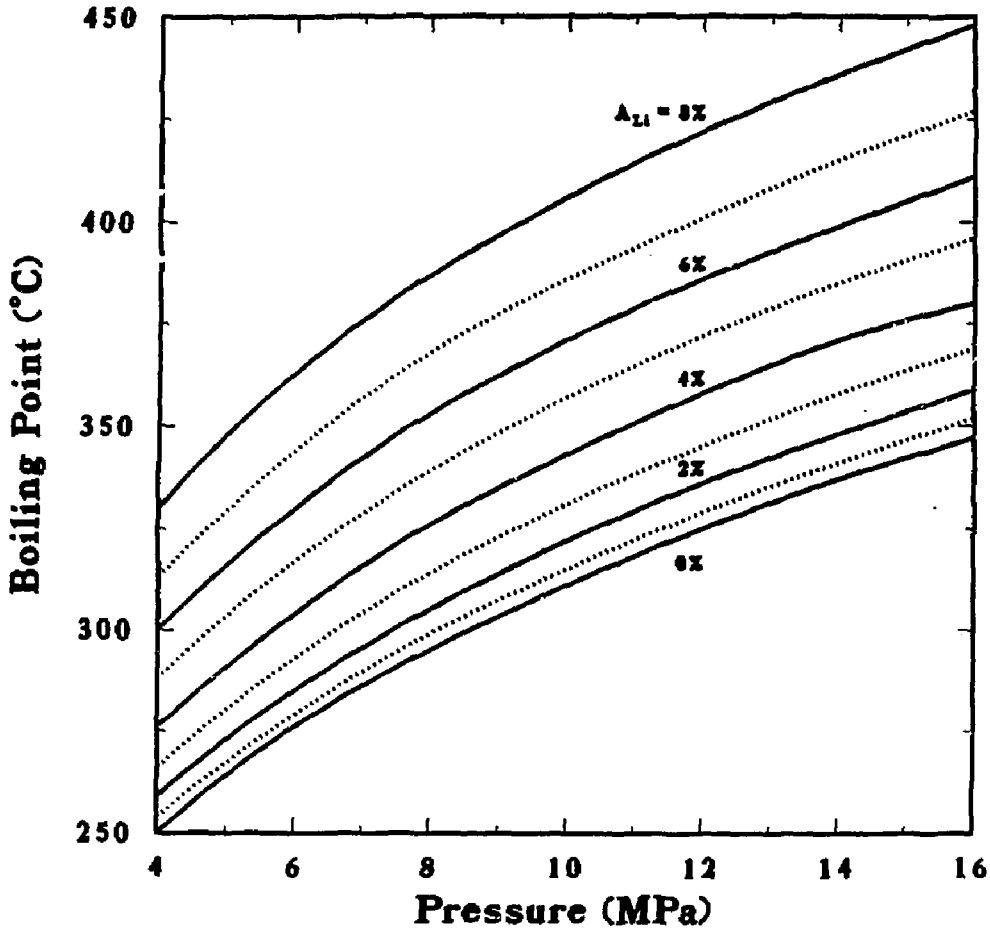

Figure 15.3-1. Boiling temperatures of $LiNO_3$ solutions at various pressures and for a range of lithium-atom percentages.

various properties, a much expanded experimental data base is required for the salts and conditions proposed before the thermal performance of an aqueous-salt blanket at high temperature can be confidently predicted.

The TITAN-II design requires a neutron multiplier to achieve an adequate tritium-breeding ratio. Beryllium is the primary neutron multiplier for the TITAN-II design. Corrosion of beryllium in aqueous solutions is a function of the cleanliness of the beryllium surface and of solution impurities. Beryllium surfaces should be free of carbonates and sulfates and the water should have minimum chlorate and sulfate impurities to assure minimum corrosion rates. Coatings to protect beryllium against attack have been developed and their effectiveness has been demonstrated in a neutron-free environment. Research is needed to develop coatings that can withstand harsh radiation environments. For the TITAN-II design, a cladding of 9-Cr surrounds the beryllium rods.

Swelling levels of above $\sim 10\%$ will most likely result in a network of interlinking helium bubbles, thus promoting helium release. This means that swelling will stop temporarily until large enough temperature gradients cause sintering of open channels. The sintering temperature for beryllium has been estimated to be around 660 °C. The ongoing process of closing and opening of porosity will ultimately lead to an equilibrium helium-venting rate with an associated maximum swelling value. Realistic prediction of this process is currently not feasible because of the lack of experimental data. A phenomenological swelling equation for beryllium is developed which predicts a maximum swelling value between 9% and 15% depending on the amount of retained helium atoms. A swelling value of 10% is taken as the basis for design calculations. Swelling may be accommodated, to a degree, by employing beryllium with low theoretical density ($\sim 70\%$). This density can easily be achieved by using sphere-packed beryllium. The maximum operating temperature must be kept below 660 °C to prevent sintering of the spheres.

Two methods for accommodating the high rate of swelling in beryllium are available: (1) using a very fine grain beryllium operating at temperatures above 750 °C to ensure interlinkage of bubbles to vent the helium gas into the plenum of the cladding tube and (2) using sphere-packed beryllium with a low theoretical density (about 70%) and accumulating the helium inside the porosity. The latter approach, however, results in a lower neutron multiplication and a reduction of thermal conductivity.

Irradiation data on the strength of beryllium are sparse. Irradiation hardening does occur at temperatures above 300 °C. McCarville *et al.* [24], predict that thermal creep may help extend the lifetime by relieving stresses caused by differential swelling, with irradiation-creep effects being negligible.

15.4. NEUTRONICS

Neutronics calculations for the TITAN-II design were performed with ANISN [25], a 1-D neutron and gamma-ray transport code, using a P_3S_8 approximation in cylindrical geometry. The nuclear data library ENDF/B-V-based MATXS5 was used. The energy group structures in this library are 30 groups for the neutron cross sections and 12 groups for the gamma-ray cross sections. The library was processed with the NJOY system at Los Alamos National Laboratory [26] for coupled neutron and gamma-ray transport calculations. Neutronics scoping studies are performed with the configurational parameters based on the coupled mechanical and thermal-hydraulic design evaluations of the TITAN-II FPC.

Scoping calculations were performed for several combinations of blanket and shield thicknesses and different levels of ^6Li enrichment in the $LiNO_3$ salt dissolved in the water coolant. The option of using heavy water (D_2O) as the coolant for TITAN-II design was also considered, since D_2O has a lower neutron absorption cross section compared to ordinary water (H_2O). It is of interest to determine if heavy water can be used alone without any beryllium for the TITAN-II design. The effects of the beryllium density factor on the neutronics performance of the TITAN-II design were also studied. It is found that:

1. The thickness of the Be zone or the level of ^6Li enrichment can be adjusted to obtain the desired tritium-breeding ratio (TBR). A 0.15-m-thick Be zone with 30% ^6Li enrichment level results in a TBR of 1.2.

2. The ordinary-water blanket has a higher TBR than the one cooled by heavy water, within the range of blanket parameters used. The reason is that hydrogen has a better neutron moderation capability then deuterium. As a result, the neutron leakage into the TF coils is also higher for heavy-water blanket.

3. Without beryllium, both H_2O and D_2O aqueous nitrate-salt blankets have insufficient TBR. Marginal TBR can be achieved for a heavy-water blanket if the structural content is reduced to 1% to 2%.

4. For blankets that were considered, the blanket-energy multiplication ranges from 1.25 to 1.4.

Based on the neutronics scoping studies, the reference design of the TITAN-II reactor was determined and is illustrated in Figure 15.4-1. The neutronics performance of the

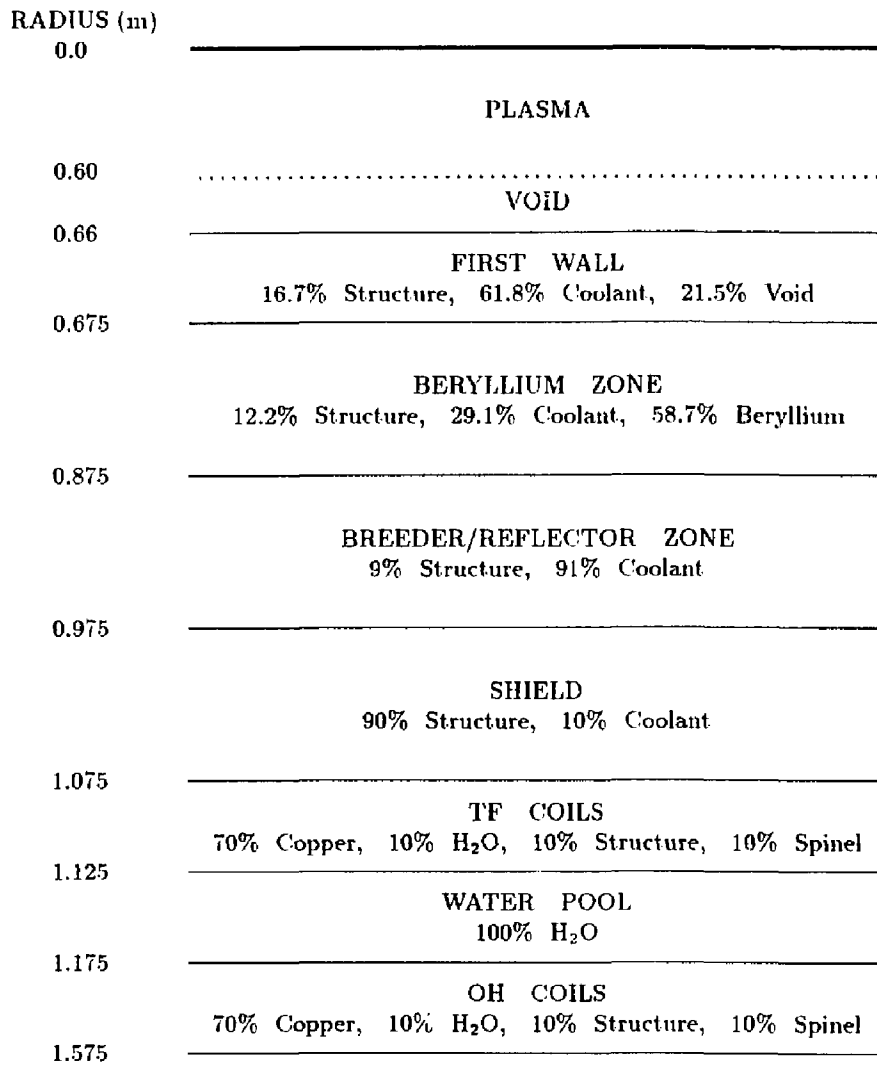

Figure 15.4-1. Schematic of the blanket and shield for the TITAN-II reference design. The coolant is an aqueous lithium-nitrate salt solution (6.4 at.% Li) and beryllium is 90% dense.

reference design is given in Table 15.4-I. The ^{6}Li enrichment level is 12%, beryllium density factor is 0.9, TBR is 1.2, and the blanket-energy multiplication is 1.36. The fast-neutron flux at the TF coils is about 3×10^{25} n/m^2 and the total fast-neutron fluence on the TF coils after 30 full-power years of operation is about 1×10^{27} n/m^2, about a factor of 2 to 3 below the lifetime estimate for the spinel insulator.

15.5. THERMAL AND STRUCTURAL DESIGN

The TITAN-II design uses an aqueous salt solution as the coolant. The coolant circulation is essentially loop-type, similar to that of TITAN-I, although the geometry of the blanket-coolant channels is very different. The salt is $LiNO_3$ and its lithium atom concentration is 6.4 at.% with a ^{6}Li enrichment of 12%. The aqueous salt solution has two advantages as coolant. First, the coolant can act as tritium breeder. Second, the salt content elevates the boiling point of the coolant which can be utilized to reduce primary-coolant pressure below the pressure in the steam generator, eliminating the need for intermediate heat exchangers. Pressure reduction in a pure-water system cannot be realized because of the lower saturation temperature and the resulting lower critical heat flux.

The design peak heat flux on the TITAN-II first wall is 4.6 MW/m^2, corresponding to a plasma radiation fraction of 0.95. The inlet and exit temperatures of the coolant are, respectively, 298 and 330 °C. The resulting exit subcooling is 17 °C and, at moderate coolant velocities, nucleate boiling will take place in the first-wall coolant channels because of the high heat flux. Therefore, the mode of heat transfer in the first-wall coolant channels will be subcooled flow boiling (SFB).

In any application of boiling heat transfer, it must be ensured that the maximum possible heat flux is less than the critical heat-flux (CHF) limit by a certain safety margin. A large amount of data for CHF of pure liquids, especially for water, is available and numerous empirical correlations for the CHF exist. Because of the scatter in the data, these correlations are generally accurate to ±20% over the applicable range of the data [27]. In the absence of any CHF correlations specifically for high-temperature aqueous solutions, a general correlation, derived for water, has been used. This correlation for CHF, q''_{CHF}, was developed by Jens and Lottes [28] and has the range of parameters for boiling heat transfer which is close to those of the first-wall coolant channel of TITAN-II. Conversion to more convenient units of MW/m^2 yields

$$q''_{CHF} = C \left(\frac{G}{1356} \right)^m (\Delta T_{sub})^{0.22}, \qquad (15.5\text{-}1)$$

Table 15.4-I.

NEUTRONICS PERFORMANCE OF THE TITAN-II REFERENCE DESIGN

Beryllium zone thickness (m)	0.2
Breeder/reflector zone thickness (m)	0.1
Shield thickness (m)	0.1
^{6}Li enrichment (%)	12.
Tritium-breeding ratio	1.22
Blanket-energy multiplication, M	1.36
Fraction (% of M) of nuclear energy in	
First wall	12.4
Beryllium zone	69.2
Breeder/reflector zone	12.7
Shield	5.7
Energy leakage (% of M) to	
TF coils	1.27
Water pool	0.31
OH coils	1.09
TOTAL:	2.67

where G is the mass velocity of the coolant ($= \rho v$) in kg/m^{2}s, the factor 1356 aries from the conversion of units, and ΔT_{sub} is the local subcooling in °C. Constants C and m depend on the pressure, p, through:

$$C = 3.00 - 0.102p\,, \tag{15.5-2}$$

$$m = \frac{p}{30} + 0.04\,. \tag{15.5-3}$$

Data used in deriving the above CHF correlation was limited to maximum values of critical heat flux of 38 MW/m^2, water velocity of 17 m/s, pressure of 13.6 MPa, and local subcooling of 90 °C.

Because of the scatter in the data for critical heat flux, the maximum heat flux on the TITAN-II first wall is kept within 60% of that predicted by the correlation of Jens and Lottes so that an adequate safety margin for CHF is available. References cited in [27] show that the CHF is increased by about 40% in an aqueous solution of ethanol compared with that of pure water. Since CHF correlation for pure water is used for TITAN-II design, any increase in the CHF because of the lithium salt content will add to the safety margin.

The important temperatures in the blanket and shield are those at the center of the beryllium rods, the clad, the channel wall, and the maximum temperature in the shield region which should not exceed the design limits. In the blanket and shield regions, the heat flux removed by the coolant is very low, and the coolant flow is turbulent. Forced-convective heat transfer is adequate to remove the heat without raising the wall temperature to the level which would initiate nucleate boiling. Therefore, the maximum structure temperatures in the blanket and shield are calculated under the condition of non-boiling, forced-convective heat transfer.

The thermal-hydraulic design for TITAN-II FPC is found based on certain constraints such as the maximum allowable structure temperature (550 °C), maximum allowable pressure and thermal stresses in the structure (respectively, 200 and 400 MPa), coolant velocities, and pumping power. The inlet and exit temperatures of the primary coolant are set, respectively, at 298 and 330 °C in order to use an existing fission pressurized-water-reactor-type (PWR) power cycle. Because the salt content elevates the boiling point of the coolant, the primary-coolant pressure is reduced to 7 MPa, below the pressure in the steam generator, thus eliminating the need for intermediate heat exchangers. The thermal-hydraulic reference design of TITAN-II first wall is given in Table 15.5-1.

The thermal-hydraulic design of TITAN-II is expected to have adequate safety margins. The maximum heat flux crossing the coolant film in the first-wall channel is

Table 15.5-I.

THERMAL-HYDRAULIC DESIGN OF TITAN-II FIRST WALL

Channel outer diameter, b	30.0	mm
Channel inner diameter, a	27.0	mm
Wall thickness, t	1.5	mm
Erosion allowance	0.25	mm
Structure volume fraction	0.17	
Coolant volume fraction	0.62	
Void volume fraction	0.21	
Volumetric heating (structure)	202	MW/m^3
Volumetric heating (coolant)	270	MW/m^3
Total thermal power	770.2	MW
Coolant inlet temperature, T_{in}	298	°C
Coolant exit temperature, T_{ex}	330	°C
Maximum wall temperature, $T_{w,max}$	503	°C
Coolant pressure, p	7	MPa
Maximum primary stress	98	MPa
Maximum secondary stress	363	MPa
Coolant flow velocity, U	22.6	m/s
Mass flow rate	1.15×10^4	kg/s
Volumetric flow rate	10	m^3/s
Pressure drop, Δp	0.5	MPa
Total pumping power	12.5	MW
Reynolds number, Re	1.49×10^6	
Nusselt number, Nu	2360	
Prandtl number, Pr	16.5	
Critical heat flux, q''_{CHF}	8.3	Mw/m^2
Subcooling at exit, $T_{ex,sub}$	17	°C

5.1 MW/m^2, 63% lower than the critical heat flux (8.34 MW/m^2). The maximum temperature at the mid-plane of the first wall is 503 °C which is less than the allowable limit of 550 °C. The structure temperatures in the blanket and shield coolant channels have even greater safety margins. The maximum pressure stress is less than 50% of the allowable, and the thermal stress is below its limit.

Among other effects of the salt content, the specific heat capacity is reduced by a factor of about two while the density increases only by 15% which results in a significant reduction in the heat capacity of the coolant. The temperature rise of the primary coolant is 32 °C. Therefore, although the coolant pressure drop is only 1 MPa, the large coolant-volume flow rate (39 m^3/s) results in a pumping power of 49 MW, which is very close to that for TITAN-I. For coolant circulation, pumps supplying a head of 1 MPa are used. Because the coolant flows in parallel through the first wall, multiplier, reflector, and shield zones, orifices are used to reduce the pressure as necessary for each channel. Separate coolant supplies for each of the flow channels (or zones) would alleviate the need for orifices and reduce the pumping power considerably. However, the added complexity of more coolant systems and hydraulic separation of the flow channels does not justify this change.

15.6. MAGNET ENGINEERING

Two types of magnets are used in the TITAN-II design (Figure 15.2-4). The ohmic-heating (OH), equilibrium-field (EF) trim, divertor coils, and toroidal-field (TF) coils are normal-conducting with copper alloy as the conductor, spinel as the insulator, and pure water as the coolant. The main EF coils are made of NbTi superconductor and steel structural material. The poloidal-field coils are designed to last the life of the plant. The TF coils are removed with the FPC during the scheduled maintenance but are reused on a new torus afterwards. Because of the simple geometry of the TITAN-II magnets, the robust support structure, and the relatively low field produced by these coils, little or no extrapolation of current technology should be required.

15.7. POWER CYCLE

The selection of the inlet and exit temperatures of the TITAN-II primary coolant (respectively, 298 and 330 °C) is motivated by the possibility of using an existing PWR-type power cycle. The lithium-salt content of the aqueous coolant (6.4 at.%) elevates the

boiling point of the coolant from 285 °C for pure water to 347 °C at a pressure of 7 MPa. Since the primary-coolant pressure is less than the steam pressure in the steam generator (7.2 MPa), any leakage in steam generator tubes will not result in the primary coolant leaking into the steam side. Therefore, the TITAN-II reference design uses a power cycle without an intermediate heat exchanger, which results in an increase in the power cycle efficiency. The parameters of TITAN-II reference power cycle are given in Table 15.7-I. The steam cycle conditions are similar to those of existing PWR-type power cycles [29]. The estimated gross thermal efficiency of the TITAN-II power cycle is 35%.

15.8. DIVERTOR ENGINEERING

The design of the impurity-control system poses some of the most severe problems of any component of a DT fusion reactor. The final TITAN-II divertor design represents the result of extensive iterations between edge-plasma analysis, magnetic design, thermal-hydraulic and structural analyses and neutronics.

The TITAN-II impurity-control system is based on the use of toroidal-field divertors to minimize the perturbation to the global magnetic configuration and to minimize the coil currents and stresses. The TITAN divertor uses an "open" configuration, in which the divertor target is located close to the null point, facing the plasma, rather than in a separate chamber. This positioning takes advantage of the increased separation between the magnetic-field lines (flux expansion) in this region, which tends to reduce the heat loading on the divertor plate because the plasma flowing to the target is "tied" to the field lines. The high plasma density in front of the divertor target ensures that the neutral particles emitted from the surface have a short mean free path; a negligible fraction of these neutral particles enter the core plasma (Section 5.5).

The TF-coil design for TITAN-II, which consists of copper coils as opposed to the integrated-blanket coils (IBC) of TITAN-I, prompted a new divertor magnetic design. The final magnetic design, similar to that of TITAN-I, includes three divertor modules which are located 120° apart in the toroidal direction. An equatorial-plane cross section of the one of the divertor modules is shown in Figure 15.8-1. The magnetic-field lines are diverted onto the divertor plate using one nulling and two flanking coils with the latter localizing the nulling effect (divertor-trim coils are not required as opposed to the the TITAN-I design). The TITAN-II divertor coils are made of copper and the joule losses in the TITAN-II divertor coils (9.8 MW) are much smaller than those of the TITAN-I IBC divertor coils (120 MW). Also shown on the outboard view in Figure 15.8-1 is the

Table 15.7-I.

TITAN-II REFERENCE POWER CYCLE

Primary Coolant (Water):		
Total thermal power	3027	MW
Inlet temperature	298	°C
Exit temperature	330	°C
Coolant pressure	7	MPa
Saturation temperature	347	°C
Exit subcooling	17	°C
Mass flow rate	4.5×10^4	kg/s
Total pumping power	49	MW
Throttle Steam Conditions:		
Temperature	308	°C
Pressure	7.2	MPa
Saturation temperature	289	°C
Degree of superheat	19	°C
Gross thermal efficiency	0.35	

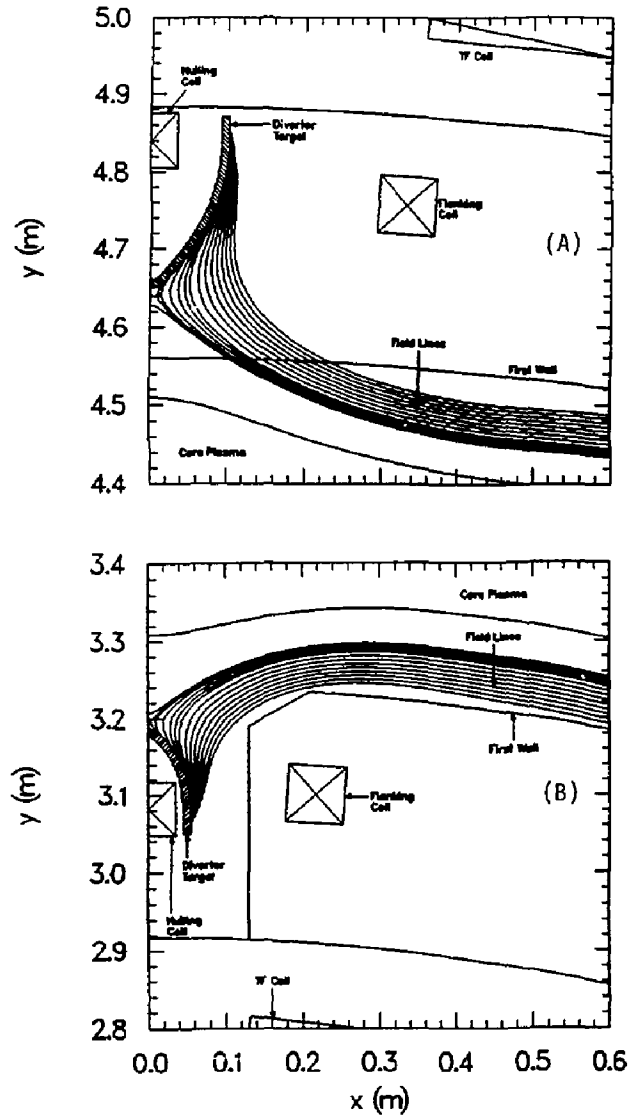

Figure 15.8-1. Outboard (A) and inboard (B) equatorial-plane views of the divertor region for TITAN-II.

Table 15.8-I.

SUMMARY OF TITAN-II EDGE-PLASMA CONDITIONS

Number of divertors	3	
Scrape-off layer thickness	6	cm
Peak edge density	1.7×10^{20}	m^{-3}
Peak edge ion temperature	380	eV
Peak edge electron temperature	220	eV
Plasma temperature at first wall	1.7	eV
Peak divertor density	6.0×10^{21}	m^{-3}
Peak divertor plasma temperature	4.5	eV
Divertor recycling coefficient	0.995	
Throughput of DT	6.7×10^{21}	s^{-1}
Throughput of He	8.2×10^{20}	s^{-1}
Vacuum tank pressure	20	mtorr

pumping aperture which leads to the vacuum tank surrounding the torus. This aperture is present for only the outboard 90° in poloidal angle; elsewhere shielding material protects the OH coils.

The results of the magnetics design of TITAN-II divertor (*e.g.*, field-line connection length) were not sufficiently different from those of the TITAN-I to warrant a separate edge-plasma analysis. A summary of the results of the edge-plasma modeling for TITAN-I, which is also used for the TITAN-II design, is given in Table 15.8-I and is described in detail in Section 5.4. The plasma power balance is controlled by the injection of a trace amount of a high atomic number impurity (xenon) into the plasma, causing strong radiation from the core plasma, the scrape-off layer (SOL) plasma, and the divertor plasma. About 95% of the steady-state heating power (alpha particle and ohmic heating by the current-drive system) is radiated to the first wall and divertor plate, with about 70% being radiated from the core plasma (*i.e.*, inside the separatrix). This

intense radiation reduces the power deposited on the divertor target by the plasma to an acceptably low level. Preliminary experimental results [12,13] suggest that beta-limited RFP plasmas can withstand a high fraction of power radiated without seriously affecting the operating point (Section 5.3). A further result of the radiative cooling is to reduce the electron temperature at the first wall and divertor target (also assisted by recycling) which reduces the sputtering-erosion problem.

To satisfy the requirement for a high-Z material for the plasma-facing surface of the divertor target, a tungsten-rhenium alloy (W-26Re) is used. The high rhenium content provides the high ductility and high strength necessary for the severe loading conditions. A single structural material is used for the divertor target to avoid the problem of bonding dissimilar materials and of stress concentrations which occur at the interface of the two materials. The coolant tubes, therefore, are also made from W-26Re alloy.

The coolant for the divertor system is an aqueous $LiNO_3$ solution, as used in the TITAN-II blanket. Advantage is taken of the predicted differences in the physical properties of this solution compared with those of pure water to obtain the high critical heat fluxes ($\sim 16\,MW/m^2$) necessary to provide an adequate safety margin against burnout. The divertor-plate coolant flows in the toroidal/radial direction to equalize the power deposited on each tube, although this causes gaps between adjacent tubes (if they are of constant cross section) because of the double curvature of the divertor plate. Fabrication of the divertor target is based on brazing of the tungsten-alloy plate (which is produced by powder-metallurgy techniques) to a bank of constant cross-section coolant tubes, although alternative methods which allow tubes of variable cross section to be constructed, have also been considered.

Despite the intense radiation arising from the impurities injected into the plasma, careful shaping of the divertor target, as shown in Figure 15.8-1, is also required to maintain the heat flux at acceptable levels at all points on the plate. Figure 15.8-2 shows the distribution of the various components of the surface heat flux along the divertor target for the inboard and outboard locations. The heat flux on the inboard and outboard targets are respectively, 7.5 and $5.8\,MW/m^2$ (compared with corresponding levels of 9.5 and $6.0\,MW/m^2$ for TITAN-I).

The temperature distribution of the divertor-plate coolant and structure is shown in Figure 15.8-3. Given the heat loadings on the divertor-plate cooling tubes, the coolant conditions are determined by the requirements of obtaining an adequate safety factor on critical heat flux, and allowing the heat deposited into the divertor-target cooling loop to be removed by a heat exchanger with the inlet coolant for the blanket. Additional constraints were that the coolant velocity should not exceed 20 m/s and that its composition

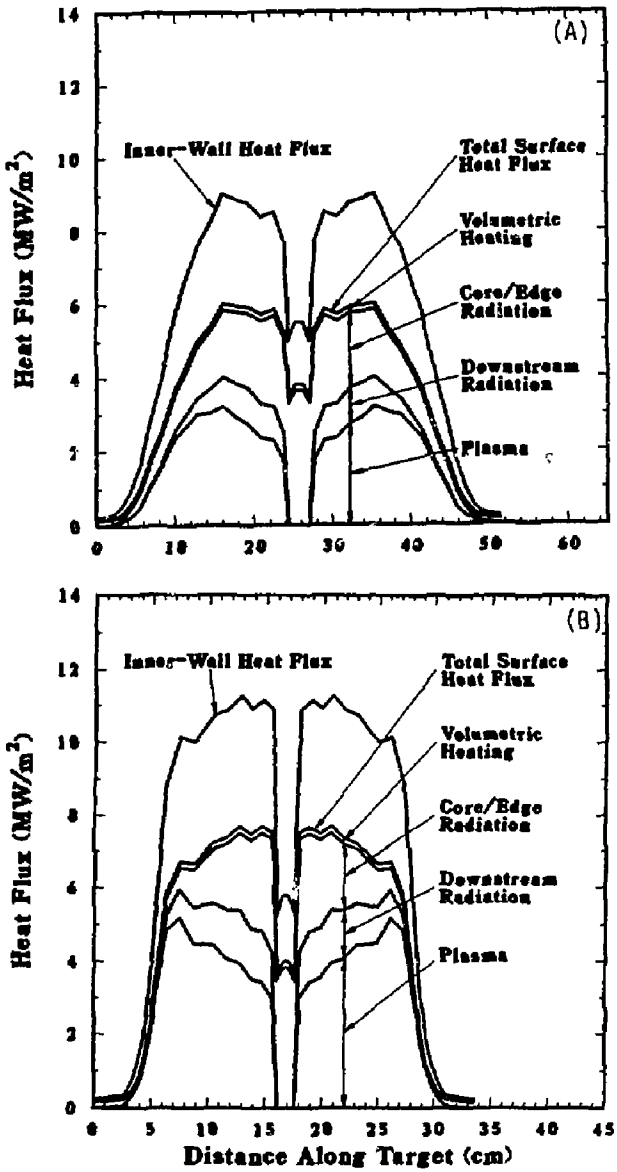

Figure 15.8-2. Heat flux distribution on outboard (A) and inboard (B) sections of divertor target. The critical heat flux for TITAN-II divertor coolant is estimated at 16.2 MW/m^2. Distance along target is measured in the direction of coolant flow.

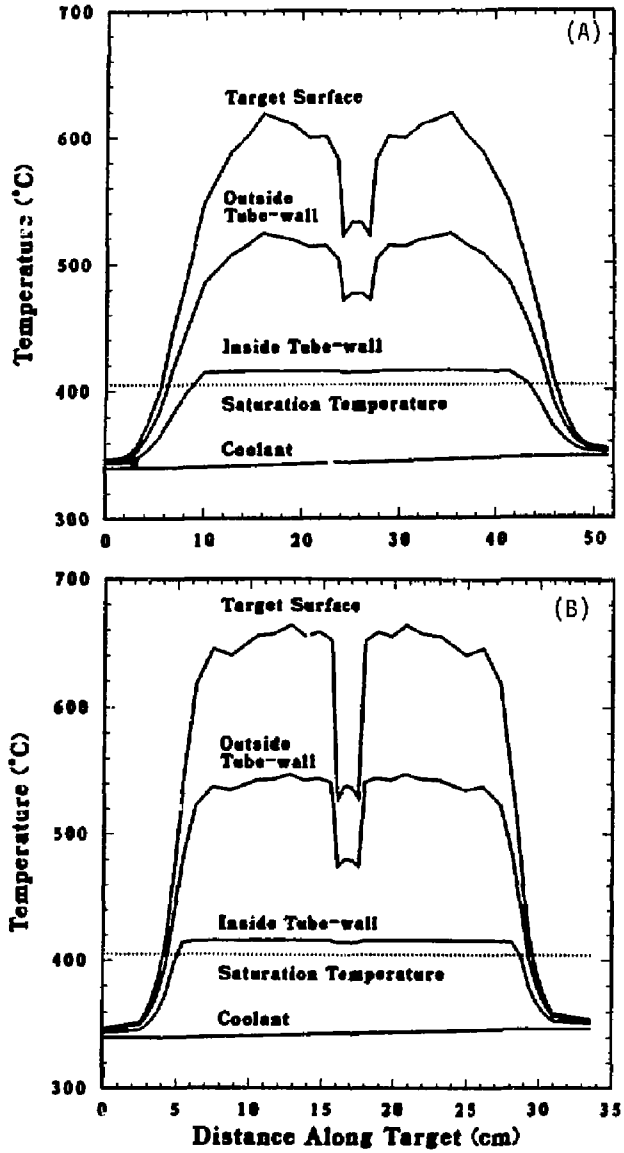

Figure 15.8-3. Coolant and structure temperature distribution on outboard (A) and inboard (B) sections of the divertor target. Distance along target is measured in the direction of coolant flow.

should be the same as for the blanket (*i.e.*, a lithium-atom percentage of 6.4%). These considerations led to the selection of the coolant-outlet conditions of 345 °C and 14 MPa. At this pressure, the boiling point of a 6.4% $LiNO_3$ solution is 405 °C (Section 16.2), yielding a subcooling at the outlet conditions of 60 °C, and a critical heat flux of 16.2 MW/m^2 as predicted by the Jens and Lottes correlation [28] (Equation 15.5-1). A safety factor in excess of 1.4 with respect to critical heat flux is achieved at all points on the target; on the outboard target, where the heat fluxes are lower, the minimum safety factor is about 1.8.

The heat removed from the divertor plate is deposited into the blanket cooling circuit through a heat exchanger. In order to maintain a minimum temperature difference of 20 °C in the heat exchanger between the inlet divertor coolant and the inlet blanket coolant (298 °C), the divertor-coolant inlet temperature must be not less than 318 °C. For a divertor-coolant exit temperature of 345 °C and temperature rise of about 7 °C per pass, the TITAN-II divertor coolant passes four times across the target.

A 2-D finite-element analysis of the steady-state temperatures and stresses in the divertor was made using the finite-element code ANSYS [30]. This analysis indicated that the maximum equivalent thermal stress is about 500 MPa, within the allowable level of 600 MPa for tungsten. The thermal analysis showed that geometric effects concentrate the heat flux from its value on the plate surface to a higher value at the tube-coolant interface, and that the effects of the gaps between adjacent tubes in elevating structural temperatures are acceptable.

The vacuum system is based on the use of a large vacuum tank encompassing the entire torus, and connected to the divertor region by a duct located at each of the three divertor locations. Lubricant-free magnetic-suspension-bearing turbo-molecular pumps are proposed for the high-vacuum pumps to avoid the possibility of tritium contamination of oil lubricants. Pumps of the required size need to be developed.

15.9. TRITIUM SYSTEMS

In TITAN-II design, the tritium is bred directly in the aqueous coolant of the primary heat-transport system. Tritium recovery and control of the tritium level in the primary coolant represent critical issues. In particular, tritium recovery from water is required on a scale larger than existing water-detritiation systems. However, considerable industrial experience with recovery of hydrogen and its isotopes from water is available, and some relevant process equipment is used on a larger scale in non-tritium applications.

The TITAN-II design has a higher tritium level (50 Ci/kg) in the primary-coolant water relative to previous design studies (*e.g.*, 1 Ci/kg in BCSS [31]) in order to minimize the cost of water-processing equipment required for tritium recovery. This tritium level is possible for TITAN-II design because of: (1) a lower pressure in the primary system which is the result of the elevation of the fluid boiling point caused by the addition of the Li salt, (2) possible use of double-walled steam generators, (3) presence of the water pool which captures a large part of the tritiated-water leakage, (4) routine use of welded joints, and (5) removal of tritiated water to safe storage during major maintenance operations. Component leakage rates and air-drier technology are based on CANDU systems performance [32]. The overall tritium-loss rate for the TITAN-II design is estimated at 50 Ci/d.

The tritium inventory in TITAN-II design is shown in Table 15.9-I. The total tritium inventory is four kilograms, roughly comparable to the inventory in some CANDU reactors at present. The largest inventory is in the primary circuit, which requires a larger blanket processing system.

The blanket tritium-recovery system reference design is summarized in Table 15.9-II. This system recovers 430 g/d of tritium, primarily through a five-stage vapor-phase catalytic-exchange (VPCE) system which transfers the tritium from the water to hydrogen gas, and then by cryogenic distillation for isotope separation. The TITAN-II FPC is submerged in the pool of water to achieve a high level of safety. The water pool contains tritium from primary-coolant system leakage, which is maintained at 0.37 Ci/kg by water distillation, with the enriched tritiated water from the distillation columns mixed with the primary-coolant water for final tritium recovery. The water-feed rate to the VPCE system is about 4000 kg/h at 50 Ci/kg. The estimated installed cost of the TITAN-II tritium recovery system is 130 M$ (1986), not including building, air cleanup, and indirect costs. Although the water-feed rate is about 10 times larger than the Darlington Tritium-Removal Facility, the cost is only 3 to 4 times larger because of the economy of scale, fewer VPCE stages, and the lower reflux ratio needed in the cryogenic columns by the light-water feed.

The other TITAN-II tritium-related systems and flow rates are also assessed. The fuel-processing systems are similar to those of TITAN-I, which are described in Section 12. Unique features include a redundant impurity-removal loop rather than relying on large tritium storage capacity, and a small feed to the isotope separation system because of the use of mixed DT fueling. Plasma-driven permeation is less important in TITAN-II than in TITAN-I because the first wall is at a lower temperature and is made of ferritic steel rather than vanadium. Back diffusion of protium is significant but acceptable. The

air-detritiation system has a larger drier (but not recombiner) capacity to recover most of the tritiated water leaking from primary-system components.

The overall cost of the TITAN-II tritium system is 170 M$ (1986, installed). The cost is dominated by the blanket tritium-recovery system. Since tritium recovery in TITAN-II involves isotope separation of tritium from low concentrations in water, it is expected to be more expensive than for other fusion-blanket concepts. The present design approach is based on proven chemical exchange and distillation concepts. Costs for other tritium systems are similar to those for TITAN-I (except for a larger air-drier capacity). Some costs are estimated from Reference [33].

Table 15.9-I.

TITAN-II TRITIUM INVENTORIES

System	T Inventory (g)	Form
Primary-heat transport	1420[a]	HTO
Beryllium	10	T in metal
Piping and structure	< 1	T in metal
Plasma chamber and vacuum	5	DT
Fuel processing	20	DT
Blanket tritium recovery	44	HTO
	550	HT
Shield	< 10	HTO
Tritium storage	1000	Metal tritide
Pool	940[b]	HTO
TOTAL	4000	

(*a*) Based on 274 m^3 at 50 Ci/kg.

(*b*) Based on 22,640 m^3 at 0.4 Ci/kg.

Table 15.9-II.

TITAN-II BLANKET TRITIUM-RECOVERY SYSTEM (BASED ON EXTRACTING 465 g/d of T AT 50 Ci/kg)

Maximum tritium concentration	50 Ci/kg in water
Tritium-extraction rate	465 g/d of T
Tritium inventory as water	44 g T
Tritium inventory as gas	550 g T
Blanket detritiation factor	93% per pass
Hydrogen-refrigeration power	5.7 MWe
Low-pressure steam to water distribution	5.7 MWth at 300 kPa
Low-pressure steam to VPCE	1.2 MWth at 600 kPa
High-pressure steam to VPCE	8.5 MWth at 2.5 MPa
Hydrogen-gas inventory	1500 kg
Building volume	36,000 m^3

A major reduction in the costs and tritium levels requires a new water-detritiation approach. At present, laser separation is under investigation, but probably requires improvements in the lasers and optical materials to be attractive. Radiolysis might be helpful if a high yield of HT is obtained (not clear from present experiments), and if the associated O_2 production is acceptable.

Relative to the TITAN-I tritium system (Section 12), the TITAN-II tritium system is more expensive, the total tritium inventory is larger, the overall tritium system is physically larger, and the chronic tritium releases are larger. However, the TITAN-II tritium inventory is much less at risk for major release because of the lack of reactive chemicals, the low temperatures and pressures of most of the tritiated water, and the pool surrounding the FPC hot primary-coolant loop.

15.10. SAFETY DESIGN

Strong emphasis has been given to safety engineering in the TITAN study. Instead of an add-on safety design and analysis task, the safety activity was incorporated into the process of design selection and integration at the beginning of the study. The safety-design objectives of the TITAN-II design are: (1) to satisfy all safety-design criteria as specified by the U. S. Nuclear Regulatory Commission on accidental releases, occupational doses, and routine effluents; and (2) to aim for the best possible level of passive safety assurance.

The elevation view of TITAN-II reactor is shown in Figures 15.2-1. The TITAN-II FPC is cooled by an aqueous lithium-salt solution and therefore the cooling circuit is a pressurized-water system. Furthermore, the primary coolant contains tritium at a high concentration of 50 Ci/kg. A passive safety system is thus required to handle different accident scenarios, to control the potential release of high-pressure primary coolant which contains tritium, and to prevent the release of induced radioactivities in the reactor structural materials even under the conditions of a loss-of-coolant-accident (LOCA).

The key safety feature of the TITAN-II design is the low-pressure, low-temperature water pool that surrounds the fusion power core and the entire primary-coolant system (Figures 15.2-1). In the case of a major coolant-pipe break, the pressurized coolant in the hot loop will mix with the pool of water since the complete primary loop is in the pool. With this mixing, the temperature of the pool would only rise moderately because of the much larger volume of the water pool. In fact, even if the heat transfer from the pool to the surrounding earth is ignored, it would take more than seven weeks for the temperature of the water pool to reach 100 °C. Therefore, the cold pool of water acts as a heat sink to dilute the reactor thermal and decay afterheat energy and also eliminates the possibility of releasing tritiated water vapor or other radioactive material to the environment.

Based on the "loop-in-pool" concept of the TITAN-II design, different scenarios for handling normal and off-normal situations were evaluated. The size and operating conditions of the TITAN-II water pool are determined by these analyses. In the TITAN-II design, the primary-cooling circuit is not completely insulated from the pool, so the pool can absorb the decay afterheat power in case of a loss-of-flow accident (LOFA) in either the primary circuit or the steam generators. This power is then removed by separate heat exchangers in the pool. The pool temperature should be kept as low as possible to maintain an adequate heat-sink capability in the pool in case of an accident. On the other hand, the pool temperature should be reasonably high so that the size of the

afterheat-removal heat exchangers in the pool, which are capable of removing the steady power of 34 MW, can be minimized. The exact pool temperature should be determined by detailed design. For the TITAN-II reactor, a pool temperature range of 60 to 70 °C is found to be reasonable based on detailed evaluation of the accident scenarios.

A potential accident for pressurized-water systems is a double-ended rupture of a main coolant line. The escaping jet of the primary coolant (as steam), which may contain radioactive material, will raise the pressure inside the primary containment building and may result in the release of radioactivity to the environment. Another advantage of the TITAN-II water pool surrounding the FPC is the potential to suppress the consequences of a double-ended rupture of the primary-coolant circuit by containing the escaping jet of the primary coolant inside the water pool. The analysis shows that for a double-ended rupture of a 0.5-m-diameter hot leg, at least 6 to 7 m of cold (60 °C), fully degassed water is needed above the break to prevent a direct discharge of steam into the containment building. This figure has been used to determine the minimum height of TITAN-II pool.

Two of the major accidents postulated for the FPC are the LOFA and LOCA. Thermal responses of the TITAN-II FPC to these accidents are modeled using a finite-element heat-conduction code, TACO2D [34]. Analysis of a LOCA without the pool showed that the peak temperature of the ferritic steel and beryllium would exceed the melting point of these materials. The necessity of the low-pressure pool is evident from these results.

Figure 15.10-1 shows the temperature of the TITAN-II FPC as a function of time after the initiation of a LOFA (with the pool). For this accident scenario, very little temperature excursion is observed, primarily because of the presence of natural convection within the pool and the primary loop. The first-wall peak temperature of 348 °C is reached after 355 seconds. The TITAN-II reactor appears to be capable of withstanding the loading conditions of this accident scenario.

The thermal response of the TITAN-II FPC to a LOCA with the low-pressure pool is also studied. The accident is assumed to be initiated with a guillotine break in the primary cold leg, below the level of the torus. At the onset of the accident, a very rapid ($\sim$ 1 s) de-pressurization of the primary loop occurs until the primary-loop pressure reaches the saturation pressure of the primary coolant. Following the initial de-pressurization to saturation conditions, a slower de-pressurization takes place until the primary loop and the pool are at equal pressure. Choked flow at the pipe break determines the rate of de-pressurization. As the pressure in the primary loop drops below the saturation pressure of the primary coolant, flashing of the primary coolant occurs, and the sudden volume change forces the coolant out of the pipe break (blow-down phase). The blow-down phase in typical design-basis accidents for PWRs lasts 10 to 20 seconds,

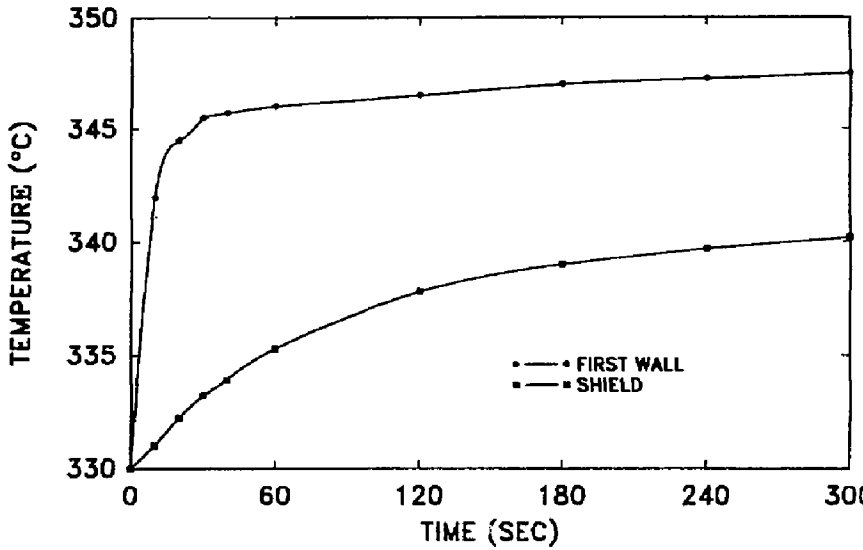

Figure 15.10-1. The thermal response of the TITAN-II FPC to a LOFA with the low-pressure pool as a function of time after the initiation of the accident.

provided that no emergency core-cooling system is engaged. If the pipe break occurs at the lowest point of the primary loop (*i.e.*, the worst case accident) any steam that forms inside the primary piping is trapped because of the buoyancy force. For accident analysis of the TITAN-II FPC, it is conservatively assumed that at the end of blow-down phase, the entire primary loop will be filled with 330 °C steam (operating conditions).

During the re-flood phase, heat is lost from the primary loop (steam) to the surrounding pool and the steam trapped in the primary loop begins to condense. The condensation rate depends on many variables; for this analysis, it is assumed that this phase would last 5 minutes. Virtually any condensation rate can be designed into the system simply by adding insulation to the piping (decreasing the rate of condensation), or by exposing more primary piping to the pool water (increasing the rate of condensation). The final phase of the accident is the onset of natural circulation.

Thermal response of the TITAN-II fusion power core to this accident scenario is shown in Figure 15.10-2. The peak temperature of the FPC is 732 °C which is 688 °C below the melting point of the ferritic steels. The peak beryllium temperature is 481 °C, which is 802 °C below its melting point.

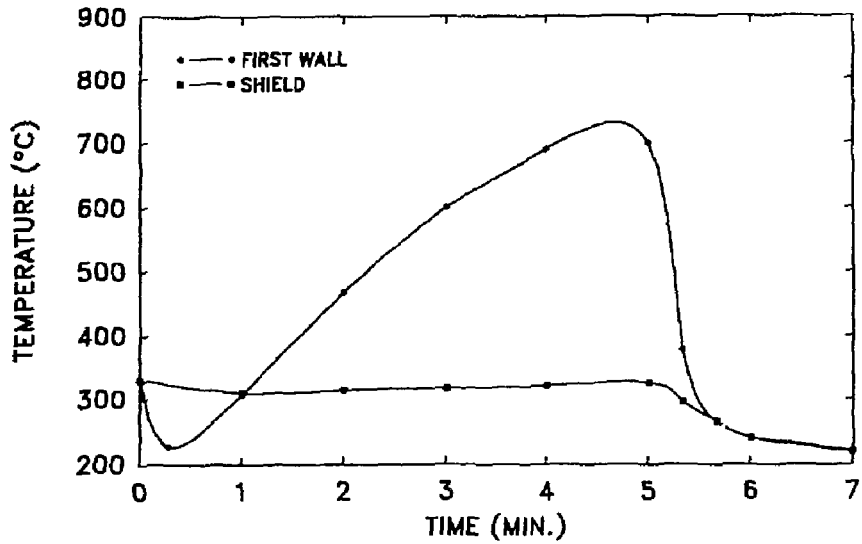

Figure 15.10-2. The thermal response of the TITAN-II FPC to a LOCA with the low-pressure pool as a function of time after the initiation of the accident (with a re-flood time of 300s).

The key safety feature of the TITAN-II design is the low-pressure, low-temperature water pool that surrounds the FPC. Detailed safety analyses have been performed which show that the TITAN-II pool can contain the thermal and afterheat energy of the FPC and will remain at a low enough temperature so that tritium or other radioactive material in the primary-coolant system will not be released. Therefore, the public safety is assured by maintaining the integrity of the water pool. Since the water-pool structure can be considered a large-scale geometry, the TITAN-II design can be rated as a level-2 of safety assurance design [35,36]. The potential safety concerns are the control of routine tritium releases and the handling of ^{14}C waste, which is generated from the nitrogen in the $LiNO_3$ salt.

Plasma-accident scenarios need to be further evaluated as the physics behavior of RFPs becomes better understood. Preliminary results indicate that passive safety features can be incorporated into the design so that the accidental release of plasma and magnetic energies can be distributed without leading to major releases of radioactivity. Activities in this area need to be continued, especially for high-power-density devices. It should be pointed out that for the TITAN-II design, plasma-related accidents are of con-

cern from the consideration of investment protection and would have minimum impact on public safety. This characteristic is again a result of the presence of the large pool of water that allows the passive protection of the public.

15.11. WASTE DISPOSAL

The neutron fluxes calculated for the reference TITAN-II reactor were used as the input to the activation calculation code, REAC [37]. These results were analyzed to obtain the allowable concentrations of alloying and impurity elements in the TITAN-II FPC components. Waste-disposal analysis has shown that the compact, high-power-density TITAN-II reactor can be designed to meet the criteria for Class-C waste disposal [38]. The key features for achieving Class-C waste in the TITAN-II reactor are attributed to: (1) materials selection and (2) control of impurity elements.

The first-wall, blanket, and shield components of the TITAN-II reactor are all integrated in a one-piece lobe design and are all replaced every year. Therefore, one may estimate the allowable concentration levels of the impurity elements by averaging over all components in the lobe. The maximum allowable impurity concentration in the "averaged" TITAN-II FPC are shown in Table 15.11-I. It appears that the concentration limits for all these impurity elements, except niobium and terbium, are readily achievable for the averaged TITAN-II FPC. Careful impurity control processes are necessary for Nb and Tb when the structural alloy is fabricated.

The reduced-activation ferritic steel (9-C) used as structural material for the TITAN-II reactor contains tungsten as one of the important alloying elements replacing molybdenum which is an undesirable element for Class-C waste disposal. However, the tungsten content should also be controlled because of the production of a second-step reaction daughter radionuclide, ^{186m}Re (with a half-life of 200,000 years). The "averaged" allowable concentration level of tungsten is 11.0%, more than two orders of magnitude larger than the present tungsten level in the reduced-activation ferritic steels (0.89%).

Assuming that the structural alloy meets all required levels of impurity and alloying elements as shown in the controlled case in Table 15.11-I, estimates are made for the TITAN-II reactor materials and related waste quantities for Class-C disposal. The divertor-shield coverage is taken as 13% in the TITAN-II design, identical to the TITAN-I design. The results are presented in Table 15.11-II. The annual replacement mass of TITAN-II FPC is estimated at about 71 tonne/FPY (9.1 m^3), assuming that the entire blanket lobe and the divertor shield are replaced every FPY. The data in Table 15.11-II

Table 15.11-I.

WASTE-DISPOSAL-RATINGS FOR
THE "AVERAGED" TITAN-II BLANKET[a]

	Present Case		Controlled Case	
Element	Nominal Level[b] (appm)	Class-C Rating	Controlled Level (appm)	Class-C Rating
Nb	0.1%[c]	8.33	1.0[d]	0.42
Mo	1.0%[c]	0.27	6.0[d]	0.30
Ag	1.	0.054	0.07	0.054
Tb	5.	1.06	0.1[d]	0.10
Ir	5.	0.0077	0.001	0.0077
W	0.9%[c,e]	0.081	0.9%[c]	0.081
TOTAL		9.78		0.96

(*a*) Based on operation at 18 MW/m^2 of neutron wall loading for 1 FPY. Note that a conservative lifetime fluence value of 15 MWy/m^2 is used for the TITAN-II reference design (0.8 FPY at 18 MW/m^2).

(*b*) From Reference [31].

(*c*) Concentrations in atomic percentage.

(*d*) Controlled levels lower than impurity levels in ferritic steel.

(*e*) Present tungsten content in the reduced-activation ferritic steel.

Table 15.11-II.

SUMMARY OF TITAN-II REACTOR MATERIALS AND RELATED WASTE QUANTITIES FOR CLASS-C WASTE DISPOSAL[a]

Component	Material	Lifetime (FPY)[a]	Volume (m^3)	Weight (tonne)	Annual Replacement Mass (tonne/FPY)
First wall	Ferritic steel (9-C)	1	0.26	2.0	2.0
Be zone	Ferritic steel (9-C)	1	2.5	19.7	19.7
Breeder zone	Ferritic steel (9-C)	1	2.0	15.3	15.3
Shield	Ferritic steel (9-C)	1	3.9	30.5	30.5
TF coils	Modified steel		0.54	4.8	0.08
	Copper		3.8	34.0	1.13
	Spinel		0.54	2.2	0.08
	TOTAL	30	4.9	41.0	1.39
OH coils	Modified steel		5.4	49.	1.63
	Copper		38.2	342.	11.4
	Spinel		5.4	23.	0.77
	TOTAL	30	49.0	414.	13.8
EF coils shield	Modified steel	30	5.6	50.	1.7
Divertor shield	Ferritic steel	1	0.48	3.78	3.78
TOTAL CLASS-C WASTE (lifetime)			334.	2643.	88.1

(*a*) Based on operation at 18 MW/m^2 of neutron wall loading for 1 FPY. Note that a conservative lifetime fluence value of 15 MWy/m^2 is used for the TITAN-II reference design (0.8 FPY at 18 MW/m^2).

is for a modified TITAN-II design with a 0.03-m shield and a 0.17-m blanket breeder zone, rather than the 0.1-m shield and 0.1-m blanket breeder zone of the reference design. The reduced shield thickness in this design will decrease the annual replacement mass by about 50 tonne/FPY and also satisfies the structural-design aspects of the blanket lobe. The penalty for this modified design is a 1.5% reduction in the blanket energy multiplication.

The TITAN-II divertor plates are fabricated with a tungsten armor because of its low sputtering properties. The waste-disposal rating of the divertor plates is estimated to be a factor of 10 higher than for Class-C disposal after one year of operation. The annual replacement mass of this non-Class-C waste is about 0.35 tonne/FPY, about 0.4% of the annual replacement mass.

Because of the nitrate salt dissolved in the aqueous-solution coolant, the TITAN-II reactor is also producing ^{14}C from ^{14}N (n,p) reactions. The annual production rate of ^{14}C is about 5.2×10^4 Ci. Using the present 10CFR61 regulations, where the allowable concentration of ^{14}C for Class-C disposal is 8 Ci/m^3 and if ^{14}C remains in the aqueous-solution coolant, the coolant should be replaced at a rate of 7×10^3 tonne/FPY (6.5×10^3 m^3). The replacement mass of the coolant can be reduced to about 80 tonne/FPY, if Fetter's evaluation [39] is used as the limiting value (700 Ci/m^3). Because of the large quantities of aqueous solution to be disposed of annually and uncertainties in the transport of the ^{14}C isotope in the primary loop, extraction of the ^{14}C activity from the coolant and disposal of the concentrated quantity as non-Class-C waste should be considered.

The safety and environmental conclusions derived from the TITAN reactor study are general, and provide strong indications that Class-C waste disposal can be achieved for other high-power-density approaches to fusion. These conclusions also depend on the acceptance of recent evaluations of limiting-specific activities carried out under 10CFR61 methodologies [39].

15.12. MAINTENANCE

The TITAN reactors are compact, high-power-density designs. The small physical size of these reactors permits each design to be made of only a few pieces, allowing a single-piece maintenance approach [7,8]. Single-piece maintenance refers to a procedure in which all of components that must be changed during the scheduled maintenance are replaced as a single unit, although the actual maintenance procedure may involve the movement, storage, and reinstallation of some other reactor components. The entire reactor torus

in both TITAN designs is replaced as a single unit during scheduled maintenance. Also, because of the small physical size and mass of the TITAN-II FPC, the maintenance procedures can be carried out by vertical lifts, allowing a much smaller reactor vault.

Potential advantages of single-piece maintenance procedures are identified:

1. Shortest period of downtime resulting from scheduled and unscheduled FPC repairs;
2. Improved reliability resulting from integrated FPC pretesting in an on-site, non-nuclear test facility where coolant leaks, coil alignment, thermal-expansion effects, *etc.*, would be corrected by using rapid and inexpensive hands-on repair procedures prior to committing the FPC to nuclear service;
3. No adverse effects resulting from the interaction of new materials operating in parallel with radiation-exposed materials;
4. Ability to modify continually the FPC as may be indicated or desired by reactor performance and technological developments; and
5. Recovery from unscheduled events would be more standard and rapid. The entire reactor torus is replaced and the reactor is brought back on line with the repair work being performed, afterwards, outside the reactor vault.

The lifetime of the TITAN-II reactor torus (including the first wall, blanket, and divertor modules) is estimated to be in the range of 15 to 18 MWy/m^2, and the more conservative value of 15 MWy/m^2 will require the change-out of the reactor torus on a yearly basis for operation a 18 MW/m^2 of neutron wall loading at 76% availability. The TF coils can last for the entire plant life. However, during the maintenance procedure, the TF coils are not separated from the reactor torus and are replaced each year. After the completion of the maintenance procedure, the TF coils can be separated from the reactor torus and reused at a later time. The impact of discarding (not reusing) the TF coils annually is negligible on the COE. The choice between reusing or discarding the TF coils requires a detailed consideration of: (1) activation intensity of the reused TF coils, (2) remote assembly of activated TF coils to a "clean" FPC, and (3) additional waste generated if TF coils are discarded annually.

Fourteen principal tasks must be accomplished for the annual, scheduled maintenance of the TITAN-II fusion power core. These steps are listed in Table 15.12-I. Tasks that will require a longer time to complete in a modular design are also identified in Table 15.12-I (assuming the same configuration for the modular design as that of TITAN-II). Vertical

Table 15.12-I.

PRINCIPAL TASKS
DURING THE TITAN-II MAINTENANCE PROCEDURE

1. Orderly shutdown of the plasma and discharge of the magnets;
2. Continue cooling the FPC at a reduced level until the decay heat is sufficiently low to allow natural convection cooling in the atmosphere;
3. During the cool-down period:
   a. Continue vacuum pumping until sufficient tritium is removed from the FPC,
   b. Valve-off all systems which will be disconnected during maintenance (*i.e.*, vacuum and electrical systems) and, depending on the maintenance method, drain the water pool above the FPC,
   c. Disconnect electrical and coolant supplies from the upper OH-coil set,
   d. Break vacuum;
4. Drain primary coolant from FPC;
5. Lift OH-coil set and store in the lay-down area;
6. Disconnect primary-coolant supplies at ring headers;[a]
7. Lift the reactor torus and move to the hot cell;[a]
8. Inspect FPC area;
9. Install the new, pretested torus assembly;[a]
10. Connect primary-coolant supplies, TF-coil electrical supplies, and re-weld all vacuum ducts;[a]
11. Replace the upper OH-coil set and connect electrical and coolant supplies;
12. Hot test the FPC;[b]
13. Pump-down the system;
14. Initiate plasma operations.

(*a*) The time required to complete these tasks is likely to be longer for a modular system than for a single-piece system, assuming similar configuration.

(*b*) The new torus assembly is pretested and aligned before committment to service. Only minimum hot testing would be required.

lifts have been chosen for the component movements during maintenance. Lift limits for conventional bridge cranes is around 500 tonnes, with special-order crane capacities in excess of 1000 tonnes. The most massive components lifted during TITAN-II maintenance are the reactor torus (180 tonnes) and the upper OH-coil set (OH coils 2 through 4) and its support structure (120 tonnes), which are easily manageable by the conventional cranes.

An important feature of the TITAN design is the pretest facility. This facility allows the new torus assemblies to be tested fully in a non-nuclear environment prior to committing it to full-power operation in the reactor vault. Any faults discovered during pretesting can be quickly repaired using inexpensive hands-on maintenance. Furthermore, additional testing can be used as a shakedown period to reduce the infant mortality rate of the new assemblies. A comprehensive pretest program could greatly increase the reliability of the FPC, hence increasing the overall plant availability. These benefits of pretesting (higher reliability, higher availability) must be balanced with the additional cost associated with the pretest facility. The more representative the pretests are of the actual operation, the more duplication of the primary-loop components is required.

15.13. SUMMARY AND KEY TECHNICAL ISSUES

The TITAN reversed-field-pinch (RFP) fusion reactor study [1] is a multi-institutional research effort to determine the technical feasibility and key developmental issues for an RFP fusion reactor operating at high power density and to determine the potential economic (cost of electricity, COE), operational (maintenance and availability), safety, and environmental features of high mass-power-density (MPD) fusion systems.

Two different detailed designs, TITAN-I and TITAN-II, have been produced to demonstrate the possibility of multiple engineering design approaches to high-MPD reactors. Both designs would use RFP plasmas operating with essentially the same parameters. The major features of the designs are listed in Table 15.1-I. Both conceptual reactors are based on the DT fuel cycle, have a net electric output of about 1000 MWe, are compact and have a high mass power density of about 800 kWe/tonne of fusion power core (FPC). The mass power density and the FPC power density of several fusion reactor designs and a fission pressurized-water reactor (PWR) are shown in Figure 15.13-1 and compared with those of the TITAN reactors. The TITAN study further shows that with proper choice of materials and FPC configuration, compact reactors can be made passively safe and that the potential attractive safety and environmental features of fusion need not be sacrificed in compact reactors. The TITAN designs would meet the U. S. criteria

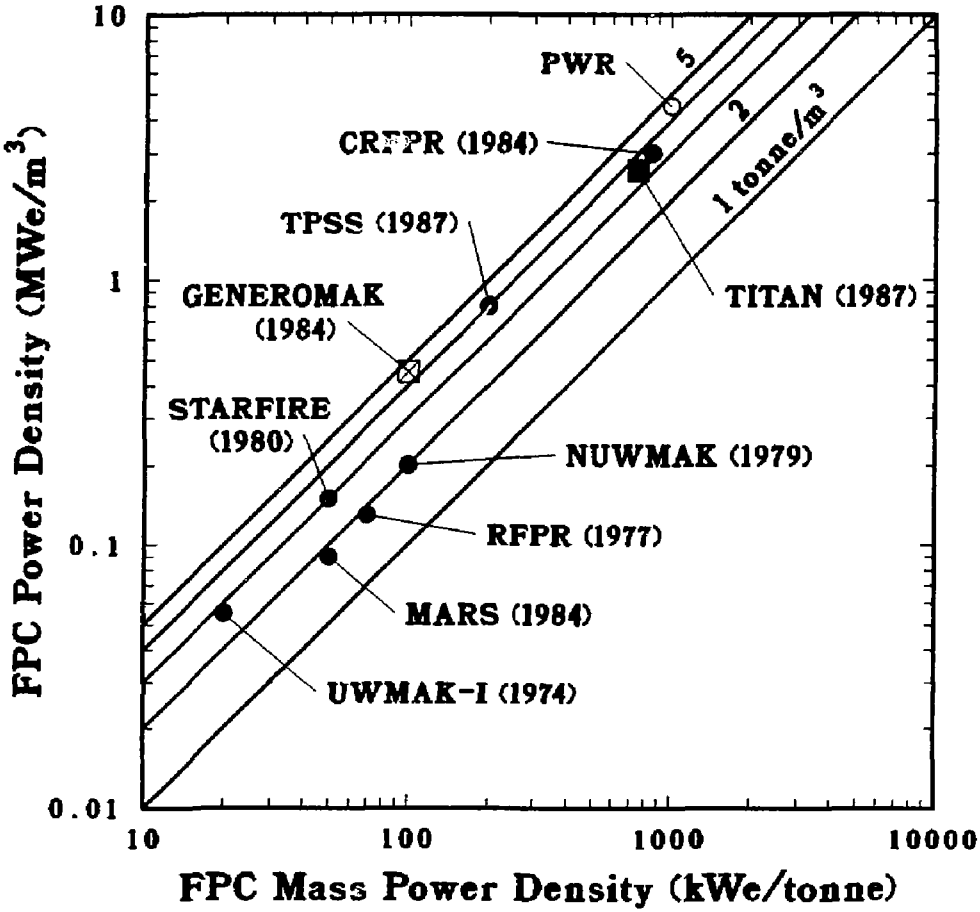

Figure 15.13-1. The mass power density and the FPC power density of several fusion reactor designs, including TITAN, and a fission PWR.

for the near-surface disposal of radioactive waste (Class-C, 10CFR61) [38] and achieve a high level of safety assurance [35,36] with respect to FPC damage by decay afterheat and radioactivity release caused by accidents. Very importantly, a "single-piece" FPC maintenance procedure, unique to high-MPD reactors, has been worked out and appears feasible for both designs.

Parametric system studies have been used to find cost-optimized designs, to determine the parametric design window associated with each approach, and to assess the sensitivity of the designs to a wide range of physics and engineering requirements and assumptions. The design window for such compact RFP reactors would include machines with neutron wall loadings in the range of 10 to 20 MW/m^2 with a shallow minimum for COE at about 19 MW/m^2. The high MPD values possible for the RFP appear to be a unique attribute of this confinement concept [6]. Reactors in this "design window" are physically small and a potential benefit of this "compactness" is improved economics. Also, the cost of the FPC for TITAN reactors is a small fraction of the overall estimated plant cost ($< 10\%$, similar to a PWR), making the economics of the reactor less sensitive to changes in the plasma performance or unit costs for FPC components. Moreover, since the FPC is smaller and cheaper, a development program should cost less. Even though operation at the lower end of the this range of wall loading (10 to 12 MW/m^2) is possible, and may be preferable, the TITAN study adopted the design point at the upper end (18 MW/m^2) in order to quantify and assess the technical feasibility and physics limits for such high-MPD reactors.

The TITAN-II FPC is a self-cooled aqueous "loop-in-pool" design with a dissolved Li salt ($LiNO_3$ with 6.4 at.% lithium) as the breeder. The structural material is ferritic-steel alloy, 9-C [15] (a reduced-activation high-strength alloy, 12Cr-0.3V-1W-6.5Mn-0.08C). The first-wall and blanket lobes are integrated and contain the pressurized coolant at 7 MPa. The structural load from the pressurized lobes is supported by a welded two-piece shield which forms a blanket container packing several lobes into a blanket sector. Three toroidal divertor chambers divide the reactor torus into three sectors. The coolant enters the lobes from the bottom, flows around the torus poloidally, and exits through the top plena. Subcooled-flow-boiling heat transfer is needed to cool the first wall. The blanket contains beryllium rods with ferritic-steel alloy 9-C cladding as the neutron multiplier.

Both lithium-hydroxide (LiOH) and lithium nitrate ($LiNO_3$) salts were considered because they are highly soluable in water. The $LiNO_3$ solution is selected as the reference breeding material because: (1) LiOH is more corrosive and (2) radiolytic decomposition of water which results in the formation of highly corrosive substances is minimized when nitrate salts are added to water. Account is taken of the thermophysical properties of

the salt solution, which are significantly different from those of the pure water. The TITAN-II tritium-control and extraction system would be, in principle, an extension of the technology developed by the Canadian CANDU fission reactor program [32].

A key feature of TITAN-II is that the FPC and the entire primary loop are submerged in a pool of low-temperature, low-pressure water. The basic sources of thermal energy after reactor shutdown are from the hot loop and the induced afterheat from the torus first wall and blanket structures. The first-wall and blanket coolant-channel configurations are designed to allow natural circulation to develop in the case of a loss-of-flow accident. In the case of a major break in the primary coolant pipes, the cold pool would absorb the thermal and afterheat energy from the hot loop. Calculations show that the pool remains at a sufficiently low temperature to prevent the release of tritium or other radioactivity in the blanket coolant system. As such, the TITAN-II design appears to achieve complete passive safety (level 2 of safety assurance [35,36]).

The general arrangement of the TITAN-II reactor is illustrated in Figures 15.2-1 through 15.2-6. The operational (maintenance and availability), safety, and environmental issues have been taken into account throughout the design. For example, the size of the expensive containment building is reduced because all maintenance procedures would be performed by vertical lift of the components (heaviest component weighs about 180 tonnes). The compactness of the TITAN designs would reduce the FPC to a few small and relatively low-mass components, making toroidal segmentation unnecessary. A "single-piece" FPC maintenance procedure, in which the first wall and blanket are removed and replaced as a single unit is, therefore, possible. This unique approach permits the complete FPC to be made of a few factory-fabricated pieces, assembled on site into a single torus, and tested to full operational conditions before installation in the reactor vault. The low cost of the FPC means a complete, "ready-for-operation" unit be can be kept on site for replacement in case of unscheduled events. All of these features are expected to improve the plant availability.

The results from the TITAN study support the technical feasibility, economic incentive, and operational attractiveness of compact, high mass-power-density RFP reactors. The road towards compact RFP reactors, however, contains major challenges and uncertainties, and many critical issues remain to be resolved. The TITAN study has identified the key physics and engineering issues which are central to achieving reactors with the features of TITAN-I and TITAN-II.

The experimental and theoretical bases for RFPs have grown rapidly during the last few years [6], but a large degree of extrapolation to TITAN-class reactors is still required. The degree of extrapolation is one to two orders of magnitude in plasma

current and temperature and two to three orders of magnitude in energy confinement time. However, the TITAN plasma density, poloidal beta, and plasma current density all are close to present-day experimental achievements. The next generation of RFP experiments [13,40] with hotter plasmas will extend the data base toward reactor-relevant regimes of operation. The TITAN study has brought out and illuminated a number of key physics issues, some of which require greater attention from the RFP physics community. These issues are discussed in detail in Section 8.

The physics of confinement scaling, plasma transport, and the role of the conducting shell are already major efforts in RFP research. However, the TITAN study points to three other major issues. First, operating high-power-density fusion reactors with intensely radiating plasmas is crucial. Confirming that the global energy confinement time remains relatively unaffected while core-plasma radiation increases (a possible unique feature of RFP) is extremely important. Second, the TITAN study has adopted the use of three "open-geometry" toroidal divertors as the impurity control and particle exhaust system. Even with an intensely radiative plasma, using an array of poloidal pump-limiters as the impurity-control system would suffer from the serious erosion of the limiter blades (and possibly the first wall). The physics of toroidal-field divertors in RFPs must be examined, and the impact of the magnetic separatrix on RFP confinement must be studied. If toroidal divertors are consistent with confinement and stability in RFPs, then high-recycling divertors and the predicted high-density, low-temperature scrape-off layer must be also confirmed. Third, early work in the TITAN study convinced the team that high mass-power-density, compact RFP reactors must operate at steady state. Current drive by magnetic-helicity injection utilizing the natural relaxation process in RFP plasma is predicted to be efficient [9,10] but experiments on oscillating-field current drive (OFCD) are inconclusive. Testing OFCD in higher temperature plasmas must await the next generation of RFP experiments, namely ZTH [13] and RFX [40].

The key engineering issues for TITAN-II FPC have been discussed. In the area of materials, more data on irradiation behavior (especially hydrogen embrittlement) of the ferritic-steel alloy, 9-Cr, are needed to confirm the materials prediction and accurately estimate the lifetime of TITAN-II first wall. The compatibility of ferritic steels with concentrated $LiNO_3$ solution is an important issue. Even though some experimental data do not show high corrosion rates or high susceptibility of stress-corrosion cracking, a research effort is needed to confirm these results in a fusion environment. The effects of radiolytic decomposition products and high-energy neutron irradiation on corrosion mechanisms and rates should be determined. Ceramic insulators offer the potential of minimum irradiation-induced conductivity, high melting and decomposition temperatures, reten-

tion of strength, and minium irradiation-induced swelling. Further experimental data on irradiation behavior of these insulators are needed.

The physical properties of the concentrated $LiNO_3$ salt solution are very different from those of pure water. The exact coolant conditions should be considered in designing the blanket. The thermal-hydraulic design of the FPC can take advantage of the differences in the properties of the concentrated solution, for example, by reducing the coolant pressure or increasing the temperature without incurring an increased risk of burnout. A much expanded experimental data base is required for the salts and conditions proposed before the thermal performance of an aqueous-salt blanket at high temperatures and heat fluxes can be confidently predicted.

The design of the impurity-control system poses some of the most severe problems of any component of a DT fusion reactor; for a compact or high-power-density design, these problems can be particularly challenging. Physics operation of high-recycling toroidal-field divertors in RFPs should be experimentally demonstrated and the impact of OFCD on the divertor performance studied. Cooling of the TITAN-II divertor plate requires experimental data on heat-transfer capabilities of concentrated-salt solutions, as outlined above. Fabrication of the tungsten divertor plate remains to be demonstrated and the degree of precision needed for target shaping and control of the position of the plasma separatrix are particularly difficult tasks.

A key concern for the aqueous blanket design is the area of tritium extraction and control. The overall cost of the TITAN-II tritium-recovery system is 170 M$. A major reduction in the costs and tritium levels requires a new water-detritiation approach. At present, laser isotope separation is under investigation but probably requires improvements in the laser and optical material to be attractive. Radiolysis might be helpful if a high yield of HT is obtained which is not clear from present experiments, and if the associated production of oxygen is acceptable.

In summary, the results from the TITAN study support the technical feasibility, economic incentive, and operational attractiveness of compact, high-mass-power-density RFP reactors. It must be emphasized, nevertheless, that in high-power-density designs such as TITAN, the in-vessel components (*e.g.*, first wall and divertor plates) are subject to high surface heat fluxes and that their design remains the most difficult engineering challenge. Also, the RFP plasma itself must operate in the manner outlined: with toroidal-field divertors, with a highly radiative core plasma, and at steady state. Future research will determine if, in fact, the physics and technology requirements of TITAN-like RFP reactors are achievable.

REFERENCES

[1] F. Najmabadi, N. M. Ghoniem, R. W. Conn, *et al.*, "The TITAN Reversed-Field Pinch Reactor Study, Scoping Phase Report," joint report of University of California Los Angeles, General Atomics, Los Alamos National Laboratory, and Rensselaer Polytechnic Institute, UCLA-PPG-1100 (1987).

[2] R. W. Conn (chairman and editor), "Magnetic Fusion Advisory Committee Panel X Report on High Power Density Fusion Systems" (May 8, 1985).

[3] J. Sheffield, R. A. Dory, S. M. Cohn, J. G. Delene, L. F. Parsley, *et al.*, "Cost Assessment of a Generic Magnetic Fusion Reactor," Oak Ridge National Laboratory report ORNL/TM-9311 (1986) 103.

[4] R. A. Krakowski, R. L. Miller, and R. L. Hagenson, "The Need and Prospect for Improved Fusion Reactors," *J. Fusion Energy* **5** (1986) 213.

[5] R. A. Krakowski, R. L. Hagenson, N. M. Schnurr, C. Copenhaver, C. G. Bathke, R. L. Miller, and M. J. Embrechts, "Compact Reversed-Field Pinch Reactors (CRFPR)," *Nucl. Eng. Design/Fusion* **4** (1986) 75.

[6] H. A. Bodin, R. A. Krakowski, and O. Ortolani, "The Reversed-Field Pinch: from Experiment to Reactor," *Fusion Technol.* **10** (1986) 307.

[7] R. L. Hagenson, R. A. Krakowski, C. G. Bathke, R. L. Miller, M. J. Embrechts, *et al.*, "Compact Reversed-Field Pinch Reactors (CRFPR): Preliminary Engineering Considerations," Los Alamos National Laboratory report LA-10200-MS (1984).

[8] C. Copenhaver, R. A. Krakowski, N. M. Schnurr, R. L. Miller, C. G. Bathke, *et al.*, "Compact Reversed-Field Pinch Reactors (CRFPR)," Los Alamos National Laboratory report LA-10500-MS (1985).

[9] M. K. Bevir and J. W. Gray, "Relaxation, Flux Consumption and Quasi Steady State Pinches," *Proc. of RFP Theory Workshop*, Los Alamos, NM, U. S. A. (1980), Los Alamos National Laboratory report LA-8944-C (1982) 176.

[10] K. F. Schoenberg, J. C. Ingraham, C. P. Munson, *et al.*, "Oscillating-Field Current-Drive Experiments in a Reversed-Field Pinch," *Phys. Fluids* **8** (1989) 2285; also R. A. Scardovelli, R. A. Nebel, and K. A. Werley, "Transport Simulation of the Oscillating Field Current Drive Experiment in the Z-40M," Los Alamos National Laboratory report LA-UR-2802 (1988).

[11] J. B. Taylor, "Relaxation and Magnetic Reconnection in Plasma," *Rev. Mod. Phys.* **58** (1986) 741; also "Relaxation of Toroidal Plasma and Generation of Reversed Magnetic Fields," *Phys. Rev. Lett.* **33** (1974) 1139; and "Relaxation of Toroidal Discharges," *Proc. 3rd Topical Conf. on Pulsed High-Beta Plasmas*, Abingdon (September 1975), Pergamon Press, London (1976) 59.

[12] M. M. Pickrell, J. A. Phillips, C. J. Buchenauer, T. Cayton, J. N. Downing, A. Haberstich, *et al.*, "Evidence for a Poloidal Beta Limit on ZT-40M," *Bull. Am. Phys. Soc.* **29** (1984) 1403.

[13] P. Thullen and K. Schoenberg (Eds.), "ZT-H Reversed-Field Pinch Experiment Technical Proposal," Los Alamos National Laboratory report LA-UR-84-2602 (1984) 26.

[14] D. Steiner *et al.*, "A Heavy Water Breeding Blanket," *Proc. 11th Symp. on Fusion Engineering*, Austin, TX (1985).

[15] D. S. Gelles, N. M. Ghoniem, and R. W. Powell, "Low Activation Ferritic Alloys Patent Description," University of California Los Angeles report UCLA/ENG-87-9 PPG-1049 (1987).

[16] W. F. Bogaerts, M. J. Embrechts, and R. Waeben, "Application of the Aqueous Self-Cooled Blanket Concept to a Tritium Producing Shielding Blanket for NET," University of Leuven (Belgium) report EUR-FU/XII-80/87/75 (1987).

[17] D. N. Braski, "The Effect of Neutron Irradiation on the Tensile Properties and Microstructure of Several Vanadium Alloys," *Proc. ASTM Conf. on Fusion Reactor Materials*, Seattle, WA (1986).

[18] E. T. Cheng and R. W. Conn, "Waste Disposal Ratings in the TITAN RFP Reactor," *Proc. IEEE 12th Symp. on Fusion Engineering*, Monterey, CA (October 1987) 913.

[19] R. Waeben, W. Bogaert, and M. Embrecht, "Initial Corrosion Evaluation of Candidate Materials for an ASCB Driver Blanket for NET," *Proc. IEEE 12th Symp. Fusion Engineering*, Monterey, CA (October 1987) 1332.

[20] R. S. Treseder, "Guarding Against Hydrogen Embrittlement," *Chem. Eng.* **29** (1981) 105.

[21] M. G. Fontana and N. D. Greene, *Corrosion Engineering*, McGraw-Hill International Book Company, Singapore (1978).

[22] "Steels for Hydrogen Service at Elevated Temperatures and Pressures in Petroleum Refineries and Petrochemical Plants," API Publication 941, 2nd edition (1971).

[23] R. H. Wood, University of Delaware, Newark, personal communication, August 1987.

[24] T. J. McCarville, D. H. Berwald, W. Wolfer, F. J. Fulton, J. D. Lee, *et al.*, "Technical Issues for Beryllium Use in Fusion Blanket Applications," Lawrence Livermore National Laboratory report UCID-20319 (1985).

[25] W. W. Engle, Jr., "A User's Manual for ANISN, A One-Dimensional Discrete Ordinates Transport Code with Anisotropic Scattering," Oak Ridge Gaseous Diffusion Plant report K-1693 (1967).

[26] R. MacFarlane, "Nuclear Data Libraries from Los Alamos for Fusion Neutronics Calculations," *Trans. Am. Nucl. Soc.* **36** (1984) 271.

[27] R. D. Boyd, C. P. C. Wong, and Y. S. Cha, "Technical Assessment of Thermal-Hydraulics for High Heat Flux Fusion Components," Sandia National Laboratory report SAND84-0159 (1985).

[28] W. H. Jens and P. A. Lottes, "Analysis of Heat Transfer, Burnout, Pressure Drop and Density Data for High Pressure Water," U. S. Atomic Energy Commission report ANL-4627 (1951).

[29] "Steam/Its Generation and Use," Babcock & Wilcox Co. (1978).

[30] G. J. DeSalvo and J. A. Swanson, "ANSYS User's Manual," Swanson Analysis Systems, Inc. (1979).

[31] D. L. Smith, G. D. Morgan, M. A. Abdou, C. C. Baker, J. D. Gordon, *et al.*, "Blanket Comparison and Selection Study – Final Report," Argonne National Laboratory report ANL/FPP-84-1 (1984).

[32] K. Y. Wong, T. A. Khan, F. Guglielmi, *et al.*, "Canadian Tritium Experience," Ontario Hydro report (1984).

[33] M. Abdou, C. Baker, J. Brooks, *et al.*, "A Demonstration Tokamak Power Plant Study (DEMO)," Argonne National Laboratory report ANL/FPP/82-1 (1982).

[34] P. J. Burns, "TACO2D - A Finite Element Heat Transfer Code," Lawrence Livermore National Laboratory report UCID-17980, Rev. 2 (1982).

[35] J. P. Holdren *et al.*, "Summary of the Report of the Senior Committee on Environmental, Safety and Economic Aspects of Magnetic Fusion Energy," Lawrence Livermore National Laboratory report UCRL-53766 (1987); also J. P. Holdren *et al.*, "Exploring the Competitive Potential of Magnetic Fusion Energy: The Interaction of Economics with Safety and Environmental Characteristics," *Fusion Technol.* **13** (1988) 7.

[36] S. J. Piet, "Approaches to Achieving Inherently Safe Fusion Power Plants," *Fusion Technol.* **10** (1986); also "Inherent/Passive Safety For Fusion," *Proc. 7th ANS Topical Meeting on Tech. of Fusion Energy*, Reno, NV (1986).

[37] F. M. Mann, "Transmutation of Alloys in MFE Facilities as Calculated by REAC (A Computer Code for Activation and Transmutation Calculations)," Hanford Engineering and Development Laboratory report HEDL-TME 81-37 (1982).

[38] "Standards for Protection Against Radiation," U. S. Nuclear Regulatory Commission, Code of Federal Regulations, Title 10, Part 0 to 199 (1986).

[39] S. Fetter, E. T. Cheng, and F. M. Mann, "Long-term Radioactivity in Fusion Reactors," *Fusion Eng./Des.* **6** (1988) 123.

[40] G. Malesani and G. Rostagni, "The RFX Experiment," *Proc. 14th Symp. Fusion Technology*, Avignon (1986) 173.

16. TITAN-II FUSION-POWER-CORE ENGINEERING

Clement P. C. Wong
James P. Blanchard
Edward T. Cheng
Patrick I. H. Cooke
Richard L. Creedon
Nasr M. Ghoniem
Paul J. Gierszewski
Steven P. Grotz
Mohammad Z. Hasan
Rodger C. Martin
Farrokh Najmabadi
Kenneth R. Schultz
Shahram Sharafat
Don Steiner
Dai-Kai Sze

Contents

16. TITAN-II FUSION-POWER-CORE ENGINEERING

16.1. INTRODUCTION

The TITAN-II reactor is a compact, high-neutron-wall-loading (18 MW/m^2) design. The TITAN-II fusion power core (FPC) is cooled by an aqueous lithium-salt solution which also acts as the breeder material [1]. An overview of the TITAN-II design is given in Section 15. Global parameters of the design are summarized in Table 16.1-I. A detailed list of the TITAN-II operating parameters can be found in Appendix B. The poloidal cross section of the TITAN-II FPC is shown in Figures 16.1-1.

The major feature of the TITAN-II reactor is that the entire primary loop is located at the bottom of a low-temperature, atmospheric-pressure, pure-water pool. Detailed safety analyses show that the TITAN-II pool can contain the afterheat energy of the FPC and will remain at a low enough temperature so that tritium or other radioactive material in the primary-coolant system will not be released (Section 19).

The first wall and blanket of the TITAN-II design consists of stamped side plates made of the low-activation, high-strength ferritic steel, 9-C [2]. These plates, called "J-plates" because of their cross section, are assembled into sub-modules (or blanket lobes) as shown in Figure 16.1-2. Inside each of the lobes are 9-C-clad beryllium rods. These rods occupy the first 20 cm behind the first wall. The blanket lobes are then stacked side-by-side to form a blanket module. The shield is used as a clamp to restrain the lobes from any movement. A cross section and an isometric view of a blanket module are shown, respectively, in Figures 16.1-3 and 16.1-4. Twelve blanket modules and three divertor sections are assembled into a single reactor torus. The vacuum boundary for the FPC, located outside the toroidal-field (TF) coils, acts as a boundary between the pool and the hot torus. The TF coils occupy the space between the back of the shield and the vacuum shell (Figure 16.1-3). Vacuum-duct penetrations through the vacuum shell are located in the region near the divertors.

In this section, the detailed engineering design and analysis of the TITAN-II FPC is presented. The FPC components considered here are the first wall, blanket, shield, and the coil sets. The use of an aqueous solution imposes special constraints on the selection of breeder and structural material because of the corrosion concerns, hydrogen embrittle-

ment, and radiolytic effects. These issues are discussed in Section 16.2. At the same time, the dissolved salt in the coolant changes the thermophysical properties of the coolant and the trade-offs between the lithium concentration in the coolant, neutronics performance (Section 16.3), thermal and structural design (Section 16.4), and power-cycle analysis (Section 16.5) are considered. Other engineering aspects of the TITAN-II design (*i.e.*, divertor and vacuum engineering, tritium systems, safety and waste disposal, and main-

Table 16.1-I.

TITAN-II OPERATING PARAMETERS

Major radius, R_T	3.90	m
Minor plasma radius, r_p	0.60	m
First wall radius, r_{FW}	0.66	m
Primary coolant	Aqueous solution	
Structural material	Ferritic steel 9-C	
Breeder material	$LiNO_3$	
Neutron multiplier	Be	
Coolant inlet temperature	298	°C
Coolant exit temperature	330	°C
Neutron wall load, I_w	18.0	MW/m^2
Radiation heat flux on first wall, q''_o	4.6	MW/m^2
Fusion power, P_f	2290	MW
Total thermal power, P_{th}	3027	MW
Net electric power, P_{net}	900	MWe
Gross efficiency, η_{gross}	35%	
Net efficiency, η_{net}	30%	
Mass power density, MPD	806	kWe/tonne

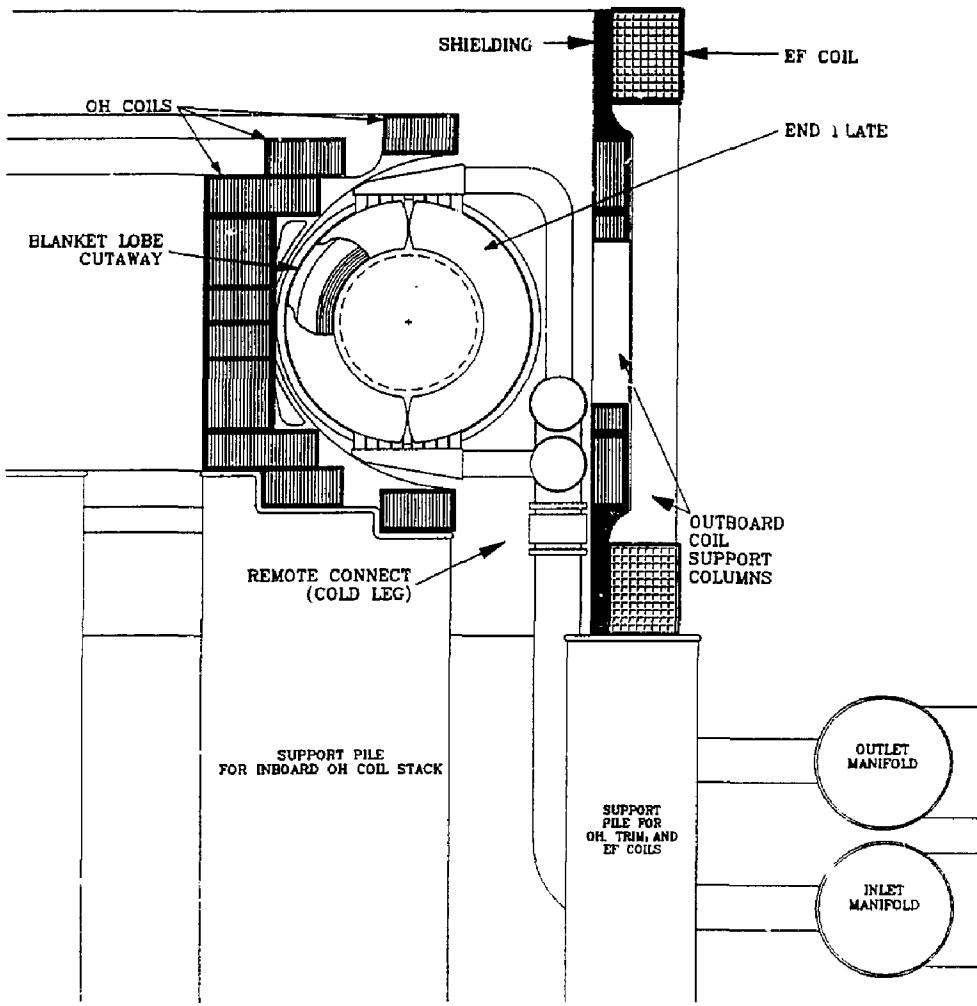

Figure 16.1-1. Poloidal cross section of the TITAN-II fusion power core.

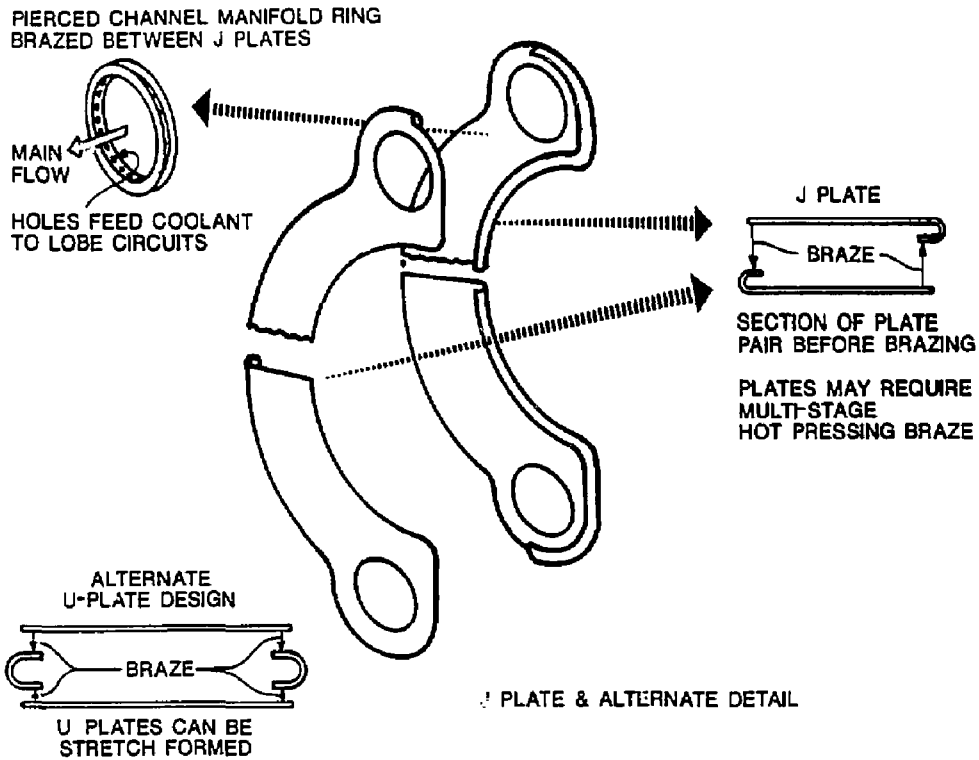

Figure 16.1-2. The TITAN-II blanket lobe, J-plate design.

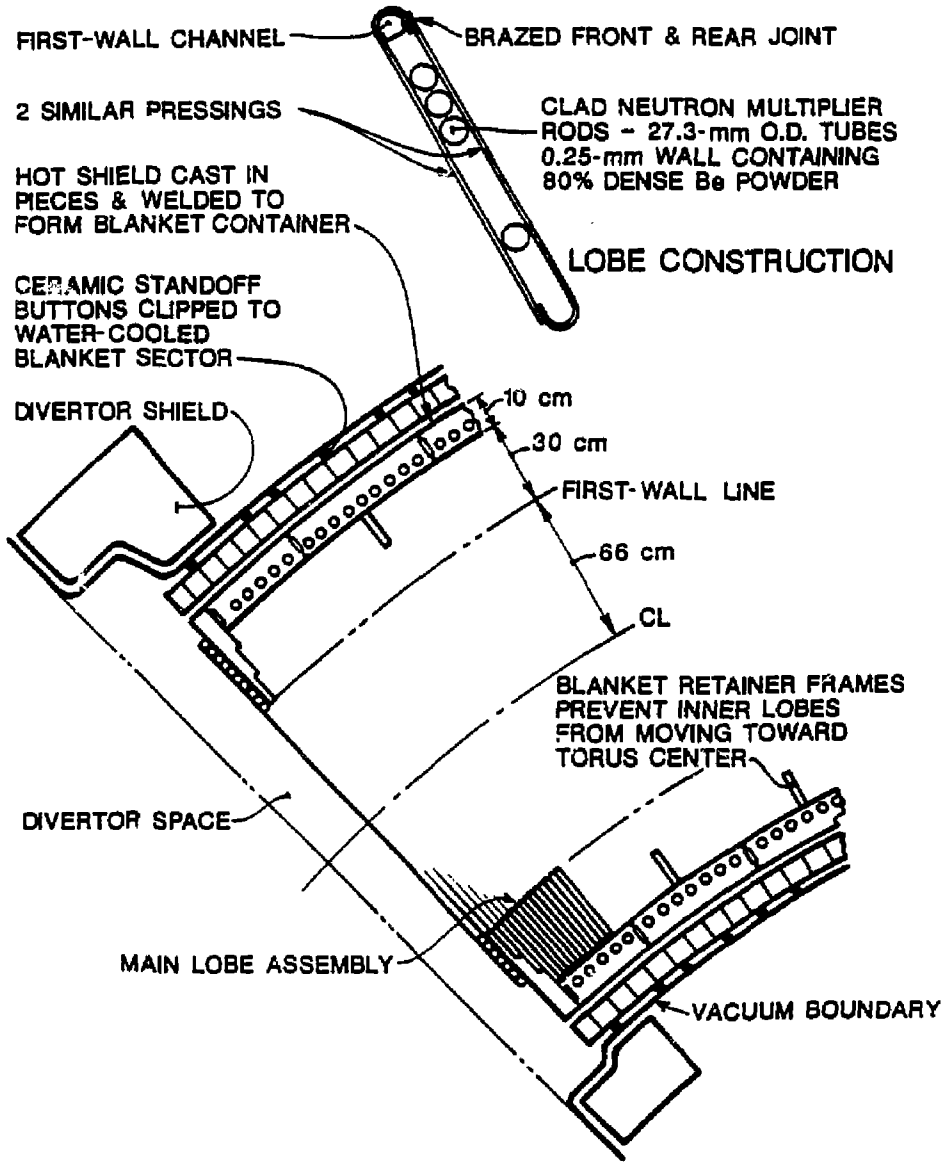

Figure 16.1-3. Equatorial-plane cross section of a TITAN-II blanket module.

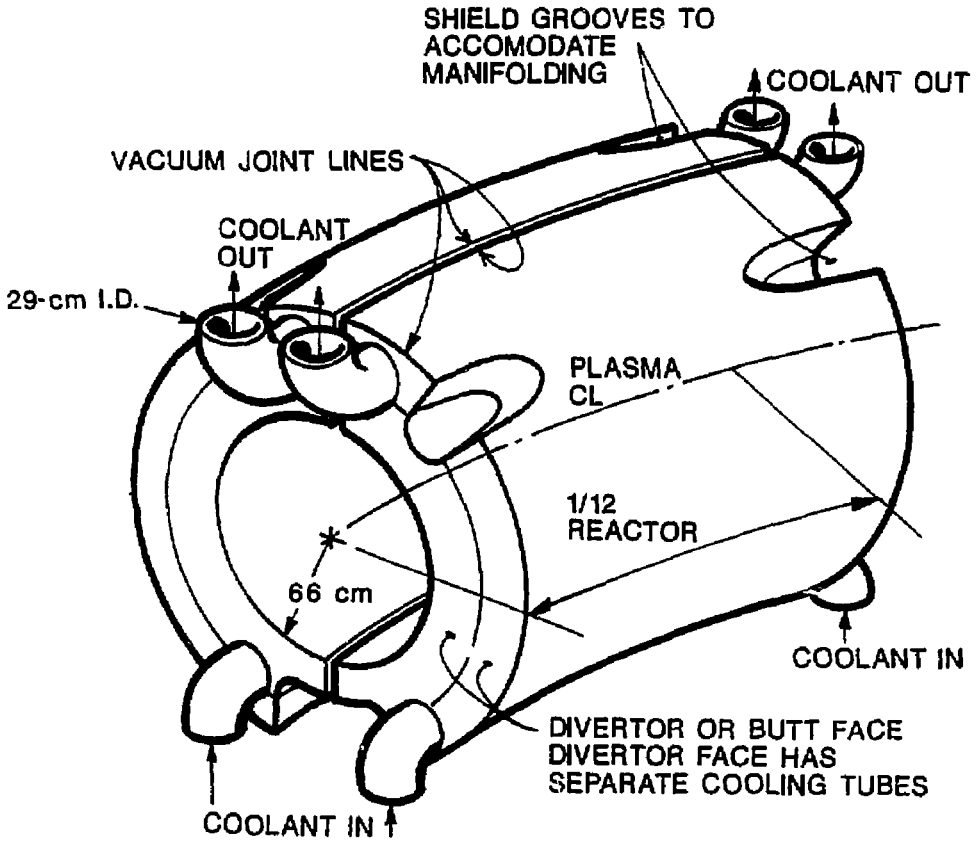

Figure 16.1-4. Isometric view of a TITAN-II blanket module.

tenance) are presented in subsequent sections. The engineering aspects of TITAN-II magnets are not covered because these magnets are based on present-day technology. Furthermore, TITAN-II magnets are, in principle, similar to those of the TITAN-I design except that water is used to cool the TITAN-II ohmic-heating (OH) coils instead of helium gas which cools the TITAN-I OH coils (Section 10.5).

The emphasis of the TITAN study has been on the investigation and demonstration of the feasibility of the compact, high-power-density reactors and also the identification of the critical issues for these devices. Therefore, some of the engineering issues that were not considered crucial to the design were for the most part not covered in detail in this study.

16.2. MATERIAL SELECTION

The attractiveness of commercial fusion-power devices depends, to a large extent, on material performance. Components of a fusion reactor are exposed to a unique set of stress, thermal, radiation, electromagnetic, and chemical loads and should function properly for the duration of the design lifetime. Material options are even more limited for a compact, high-power-density reactor such as TITAN because of high heat and radiation fluxes. The following sections will highlight various material selection issues for the TITAN-II FPC components.

The material issues in an aqueous-solution-cooled fusion reactor are quite different from those of a liquid-lithium-cooled FPC such as the TITAN-I design. The most significant differences between water-cooled and liquid-metal-cooled devices arise from the much higher coolant pressure in the water-cooled system, the electrochemical corrosion mechanisms of aqueous solutions, and the radiolysis of water by ionizing radiation.

In the TITAN-II design, tritium breeding is accomplished in a lithium salt which is dissolved in the primary coolant (water). Both lithium-hydroxide ($LiOH$) and lithium-nitrate ($LiNO_3$) salts were considered because they are highly soluble in water. The $LiNO_3$ salt was selected as the reference salt material because: (1) $LiOH$ is more corrosive than $LiNO_3$ (Section 16.2.1), and (2) radiolytic decomposition of water which results in the formation of highly corrosive substances is minimized when nitrate salts are added to water. The nitrates act as scavengers reducing the probability of survival of highly reactive radicals in the water during exposure to radiation. The radiolysis of aqueous solutions in a fusion device has been acknowledged as a potential problem. A description of fundamental radiolytic processes and a literature survey of the radiolysis effects are

given in Section 16.2.2. The thermophysical properties of the aqueous solutions can be very different from those of pure water and are reviewed in Section 16.2.3.

The choice of aqueous lithium-salt solution as the primary coolant requires a structural material capable of withstanding the combined corrosive and irradiation environment of the FPC. Furthermore, one of the goals of the TITAN study has been to satisfy Class-C waste disposal criteria and achieve a Level-2 of safety assurance (Section 19). The requirement of low activation further constrains structural material choices. The vanadium allow, V-3Ti-1Si, is chosen as the structural material for the liquid-lithium-cooled TITAN-I design. But this alloy does not possess adequate water-corrosion resistance because of the lack of chromium content. Water corrosion resistance of most alloys results from the formation of a highly water-insoluble chromium-oxide layer. Chromium-containing vanadium alloys such as V-15Cr-5Ti have very good water corrosion resistance, however, their radiation behavior indicates a much higher susceptibility to helium embrittlement than other vanadium alloys (Section 10.2.2).

Among the ferrous alloys, the low-activation ferritic steel, 9-C [2], was identified as the most suitable structural material candidate for the TITAN-II design (Section 16.2.4). First, ferritic steels possess superior swelling resistance when compared to austenitic steels. In addition, with a high enough chromium content, the corrosion resistance of ferritics is comparable to that of chromium-rich austenitic steels. The available data on the effects of the $LiNO_3$ salt solution on corrosion of ferrous alloys are reviewed in Section 16.2.1. Hydrogen embrittlement of ferrous alloys has always been a concern, and therefore, Section 16.2.5 is devoted to this topic.

The TITAN-II design requires a neutron multiplier to achieve an adequate tritium-breeding ratio Beryllium is the primary neutron multiplier for the TITAN-II design and the anticipated behavior of beryllium is presented in Section 16.2.6. The effects of radiation on the TITAN-II primary insulating material, spinel ($MgAl_2O_4$), have previously been discussed in Section 10.2. A detailed study of the lifetime of spinel for the TITAN-II radiation field was not performed, since small variations in the neutron spectrum would not markedly affect the radiation-damage response of spinel. Major findings are summarized in Section 16.2.7.

16.2.1. Corrosion in Aqueous Solutions

Corrosion has a far-reaching economic impact. It is estimated that the annual cost of corrosion and of corrosion protection is in the neighborhood of 8 billion dollars in the

United States [3]. Corrosion-related incidents appearing in piping and other components can impact plant availability, economics, reliability, and plant safety. Major corrosion-related problems encountered by the utility industry and nuclear-steam-system suppliers include the intergranular stress-corrosion cracking (IGSCC) of welded austenitic stainless-steel pipes in boiling-water reactors (BWRs) and the steam-generator corrosion in the pressurized-water reactors (PWRs) [4]. Despite the differences in operating conditions and coolant environments, the primary material problem for both BWRs and PWRs is stress-corrosion cracking (SCC).

Corrosion can be a uniform or localized (pitting) process. It is not uncommon for both forms of corrosion to occur at the same time, although one form usually predominates. Combined with other forms of attack such as erosion, fatigue, and SCC, corrosion can produce severe damage. Uniform attack may be rapid or slow and may leave the surface clean or coated with corrosion products. Uniform attack is easily evaluated and measurements are generally given in milligrams per square decimeter per day (mdd), in inches per year, or mils per year. Pitting corrosion, on the other hand, is difficult to evaluate and has to be measured by careful microscopic examination of a number of pits. Pits may start at an inclusion, a grain boundary, or at some other imperfection on the surface such as a dislocation.

The following subsections discuss the issues of corrosion by the aqueous salt coolant. A brief background on the electrochemical nature of corrosion is given first and some of the basic corrosion fundamentals are discussed (Section 16.2.1.1). Commonly used methods of mitigating corrosion are summarized in Section 16.2.1.2. Then, the data on SCC are reported and recent results of SCC mitigation efforts in the nuclear industry are summarized in Section 16.2.1.3. The corrosion issues of ferritic and austenitic steels in nitrate-salt solutions are discussed in Section 16.2.1.4. The effects of hydrogen and oxygen on corrosion and cracking are reviewed separately in Section 16.2.5.

16.2.1.1. Electrochemical nature of corrosion

Most metals exist in a combined state in nature and some energy has to be exerted to bring the metals into the metallic state. Thus, the metallic state represents a high-energy state of the metal and all metals tend to revert to a lower-energy state by combining with other substances, accompanied by release of energy. This decrease in free energy is the driving force of corrosion reactions. Grain boundaries, in particular, are high-energy areas, since the most stable configuration of the metal is its particular crystal structure. Grain boundaries constitute areas of lattice mismatch and are therefore slightly more

active chemically than the grain faces. The release of this stored mismatch energy leads to a higher corrosion attack along grain boundaries.

The change in the free energy by corrosion is mathematically related to the electromotive force (EMF) of the reaction. An electrochemical-corrosion reaction can be divided into anodic and cathodic parts, each with its own potential. Any reaction that can be divided into two or more partial reactions of oxidation and reduction is termed an electrochemical process. For example, in the anodic part, "oxidation" of a metal to form metal ions and free electrons takes place, while in the cathodic part, "reduction" of the metal ion to a metal occurs. The difference in these potentials is the EMF of the overall reaction which provides the driving force of corrosion.

The anodic reaction occurring during corrosion processes is the oxidation of a metal to its ion. However, the cathodic reactions can involve the reduction of hydrogen, oxygen, or metal. Examples of possible reduction equations in aqueous solutions are given in Table 16.2-I. More than one oxidation and more than one reduction reaction may occur simultaneously during corrosion. For example, in oxygenated acidic solutions, the evolution of hydrogen and the reduction of oxygen can occur simultaneously. Thus, aerated acidic solutions tend to accelerate corrosion because of an increase in reduction reactions (higher consumption of electrons).

Table 16.2-I.

POSSIBLE REDUCTION EQUATIONS IN AQUEOUS SOLUTIONS

Hydrogen evolution	$2H^+ + 2e \rightarrow H_2$
Oxygen reduction (acid solutions)	$O_2 + 4H^+ + 4e \rightarrow 2H_2O$
Oxygen reduction (neutral, basic solutions)	$O_2 + 2H_2O + 4e \rightarrow 4OH^-$
Metal-ion reduction (to ions)	$M^{+3} + e \rightarrow M^{+2}$
Metal-ion reduction (to neutrals)	$M^+ + e \rightarrow M.$

Galvanic coupling

Galvanic coupling can occur when two dissimilar metals are in contact with the same corrosive medium (*e.g.*, zinc and platinum in an acidic solution). Platinum is inert (noble) and will not undergo anodic reactions (no dissolution). However, the addition of platinum effectively increases the area for hydrogen evolution (*i.e.*, the cathodic reaction area). Also, hydrogen evolution occurs much more readily on platinum than on zinc, resulting in an increased cathodic reaction rate (higher hydrogen production). Since the anodic reaction rates are coupled to the cathodic reaction rates, an increase in one rate results in an increase of the other. Consequently, more zinc has to be dissolved to keep up with the increase in electron consumption because of hydrogen evolution on the platinum surface. Thus, platinum has effectively increased the oxidizing power of the solution (*i.e.*, consumption of electrons).

Most alloys are either solid-solution or heterogeneous. In solid-solution alloys (*e.g.*, stainless steels), the alloying elements are fully soluble in each other, while in heterogeneous alloys (*e.g.*, low-carbon steels) different phases can form because of the alloying elements. The presence of different phases in heterogeneous alloys can also lead to galvanic-coupling effects (*i.e.*, to an increase in corrosion rates). This is one of the reasons that solid-solution alloys are generally more corrosion resistant than heterogeneous alloys.

Because of phase formations in many alloys, the use of the standard EMF series to determine galvanic coupling between alloys can be misleading. Therefore, measurements have been made using common alloys to determine galvanic series, as shown in Table 16.2-II, which are based on potential measurements and galvanic corrosion tests in unpolluted seawater by The International Nickel Company at Harbor Island, N.C. [3]. It should be noted that galvanic coupling does not always lead to an increase in corrosion rates and in some cases it can lead to a decrease.

Polarization

Electrochemical reactions can be polarized or retarded by various physical or chemical environmental factors. Two types of polarization have been identified, activation and concentration, and both lead to decreased corrosion rates by reducing the rate of cathodic reactions. The polarization mechanism can be described by considering the hydrogen evolution in the water. Generally hydrogen ions diffuse through the fluid to the metal surfaces, are adsorbed to the surface, and pick up electrons to form atoms. In the

Table 16.2-II.

GALVANIC SERIES OF COMMERCIAL ALLOYS IN SEAWATER[a] [3]

↑ Noble or Cathodic	• Platinum
	• Gold
	• Graphite
	• Titanium
	• Silver
	• Chlorimet 3 (62 Ni, 18 Cr, 18 Mo) Hastelloy C (62 Ni, 17 Cr, 15 Mo)
	• 18-18 Mo stainless steel (passive) 18-8 stainless steel (passive) Chromium stainless steel 11%-30% Cr (passive)
	• Inconel (passive) (80 Ni, 13 Cr, 7 Fe) Nickel (passive)
	• Silver solder
	• Monel (70 Ni, 30 Cu) Cupronickels (60-90 Cu, 40-10 Ni) Bronzes (Cu-Sn) Copper Brasses (Cu-Zn)
	• Chlorimet 2 (66 Ni, 32 Cr, 1 Fe) Hastelloy B (60 Ni, 30 Mo, 6 Fe, 1 Mn)
	• Inconel (active) Nickel (active)
	• Tin
	• Lead
	• Lead-tin solders
	• 18-18 Mo stainless steel (active)
	• 18-8 stainless steel (active)
	• Chromium stainless steel, 13% Cr (active)
	• Cast iron Steel or iron
	• 2024 aluminum (4.5 Cu, 1.5 Mg, 0.6 Mn)
Active or Anodic ↓	• Cadmium
	• Commercially pure aluminum (1100)
	• Zinc
	• Magnesium and magnesium alloys

(a) Seawater is generally oxygenated and slightly acidic.

activation polarization process, the hydrogen atoms diffuse along the metal surface and two hydrogen atoms eventually combine to form a molecule which leaves the surface. Usually, the surface diffusion of hydrogen atoms is the rate-limiting process. In the concentration polarization process, the hydrogen atoms leave the surface to combine with another hydrogen atom inside the fluid and form a molecule (surface diffusion of hydrogen is not required). The factor that controls the hydrogen evolution rate is the diffusion of hydrogen ions through the fluid to the metal surface and, therefore, the hydrogen reduction rate is limited by hydrogen-ion concentrations. This type of polarization occurs mostly in dilute acids or in aerated, dilute salt solutions.

From the point of view of corrosion prevention, the distinction between activation and concentration polarizations is important. In the case of concentration polarization, environmental changes that lead to an enhancement of the diffusion of hydrogen ions to the metal surface (*e.g.*, velocity, agitation, and temperature) will reduce polarization and will cause an increase in the corrosion rate. Activation polarization, on the other hand, will not be affected by similar environmental changes.

Passivation

Under certain environmental conditions, some metals can become essentially inert and behave like noble metals. As the oxidizing power (consumption of electrons) of a solution increases, the anodic reactions (transforming metal atoms into their ions) also increase and result in a higher corrosion rate. In this "active" state, the corrosion rate increases exponentially. Increasing the oxidation power of the solution beyond a characteristic threshold value, however, will "passivate" the metal. Most common engineering metals are susceptible to passivation. Stainless steel and titanium, for example, are easily passivated metals.

In the passive state, the metal will show a sudden decrease in the corrosion rate. During the transition from the active to the passive region, a 10^3 to 10^6 reduction of the corrosion rate is usually observed. The precise processes responsible for this passivation and sudden decrease in corrosion are not known. It is, however, speculated that some form of activation polarization is producing a film on the metal surface which is stable over a considerable range of oxidation power of the solution [5]. Further increases in the oxidizing power of the solution to very high levels will eventually break down the protective film and corrosion again proceeds at about the same rate as during the active state. This latter state is termed "trans-passive." Active-passive characteristics are shown in Figure 16.2-1.

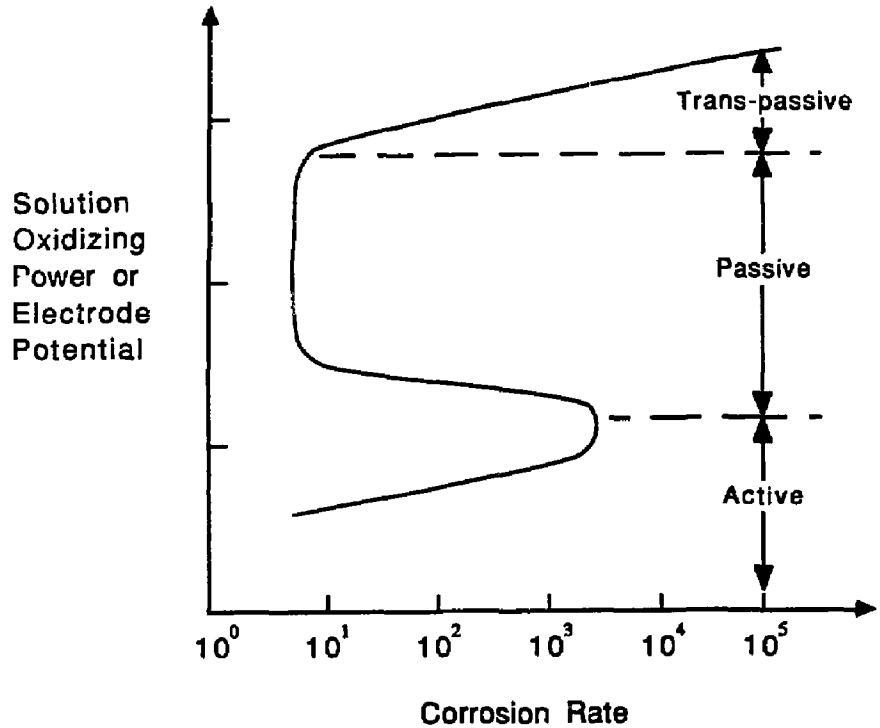

Figure 16.2-1. Corrosion characteristics of an active-passive metal as a function of the oxidizing strength of the solution [3].

Potentiodynamic polarization curves

Electrochemical studies called "potentiodynamic polarization" tests are routinely conducted to obtain mechanistic information on the corrosion rates. These tests measure the current density versus an applied potential. Results of these tests are usually shown as the potentiodynamic polarization curves (PPCs) similar to Figure 16.2-2. In a corrosion process, the rate constant can be replaced by an equivalent value of the polarizing current density [6].

Typically, the PPCs show three major zones where the current density increases, distinguishing two passive ranges. The first and second zones are called, respectively, the primary and the secondary passivation zones (Figure 16.2-2). In the passive zones, the current density remains fairly constant over a wide range of potentials. The corrosion

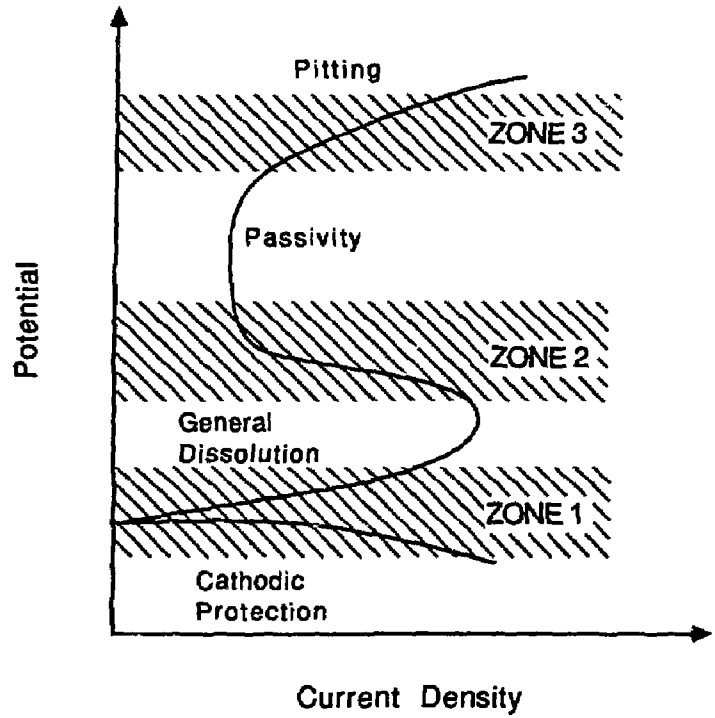

Figure 16.2-2. A typical potentiodynamic polarization curve (PPC).

rates in these passive zones are generally quite low. The transition zone between two passive zones is usually very susceptible to corrosion believed to be associated with the dissolution of one of the alloying elements. For example, chromium has been shown to play a significant role in corrosion processes in steels and chromium-enriched grain boundaries have been determined to be the major reason for the primary passivation zone on the PPCs [3].

At potentials much higher than those that cause the secondary passivation, the current density increases very sharply. This zone is associated with very rapid corrosion, such as pitting or the onset of gaseous oxygen formation by the electrolysis of water. It should be noted that the PPCs do not indicate the corrosiveness of material, only the spontaneity of corrosion processes.

Effects of temperature and oxygen concentration

It is found that corrosion processes and rates often depend strongly on the thermal history of the alloy. Chromium additions above ~ 10 wt.% to steel are responsible for most of the corrosion resistance of steels. At temperatures above $\sim 950\,^{\circ}C$, the chromium content along grain boundaries is effectively lowered through the formation of $Cr_{23}C_6$ molecules. These chromium carbides are virtually insoluble and precipitate out of solid solution, resulting in a depletion of solid-solution chromium and carbon. These steels are found to be susceptible to intergranular corrosion and are said to have become sensitized (the reduction in chromium sensitizes the grain boundaries to corrosive media).

Oxidation reactions play an important role in the corrosion process. A measure of the corrosiveness is the corrosion potential as a function of oxygen concentration that determines which corrosion reaction is favored thermodynamically. Stress-corrosion cracking (SCC) of sensitized stainless steel under boiling-water-reactor (BWR) conditions [7-9], rippling in boiler tubes [10,11], and erosion-corrosion on unalloyed steels [12] are some examples which are correlated to oxygen/corrosion potential.

The corrosion potential for stainless steels has been measured as a function of temperature and typical values of the oxygen content of the boiler water [14]. Figure 16.2-3 shows the values of the corrosion potential of AISI 304 SS as a function of oxygen concentration in high purity water [7]. Although the values of corrosion potentials are not fully identical for various experiments, in general, the potential increases from about -600 mV at zero oxygen content to about $+50$ to 100 mV at 10,000 ppb (parts per billion) of oxygen (Figure 16.2-3). The larger the potential value, the higher will be the anodic character of the metal (the electron sink strength is increased), causing a higher oxidation rate of the iron into Fe^{+2} ions. Highly negative corrosion potentials correspond to very low corrosion rates. While an increase in the oxygen content increases the corrosion potential, an increase in temperature decreases the potential for oxygen content in the range of 10 to 1,000 ppb in stainless steels (Figure 16.2-3).

16.2.1.2. *Corrosion prevention*

Mitigation of corrosion is possible by proper material selection, altering the environment, using corrosion inhibitors, and by using protective coatings. Some of these preventive measures are discussed below. The use of protective coatings, however, is not included because the stability of a particular coating in the TITAN-II nuclear environment should first be demonstrated.

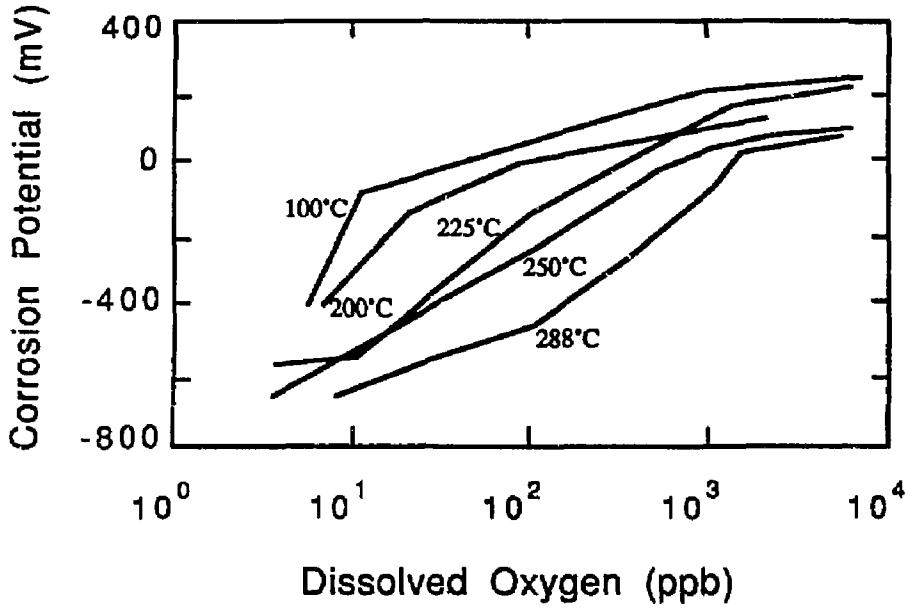

Figure 16.2-3. The corrosion potential of AISI 304 SS as a function of oxygen concentration at different temperatures in high-purity water [13].

Material Selection

The most important method of corrosion prevention is the selection of the proper material for a given environment. Stainless steels are frequently chosen as one of the primary structural materials. Under certain conditions (*e.g.*, chloride-containing mediums and stressed structures), however, stainless steels are less resistant than ordinary structural steel [15]. Also, stainless alloys are more susceptible to localized corrosion such as intergranular corrosion, stress-corrosion cracking, and pitting attack than ordinary structural steels [15]. On the other hand, stainless steels are found to have excellent resistance to nitric acid under a wide range of exposure conditions (the TITAN-II FPC is cooled by an aqueous $LiNO_3$ solution).

In general, for oxidizing conditions, chromium-containing alloys are used. For reducing environments (air-free acids and aqueous solutions), nickel, copper, and their alloys show good corrosion resistance. The most corrosion-resistant material is tantalum which resists most acids at all concentrations and temperatures.

To guide the material selection, corrosion engineers have lists of "natural" metal-corrosive combinations such as [3]:

- Nickel and nickel alloys – caustic,
- Monel – hydrofluoric acid,
- Hastelloys – hydrochloric acid,
- Lead – dilute sulfuric acid,
- Aluminum – nonstaining atmospheric exposure,
- Tin – distilled water,
- Titanium – hot strong oxidizing solutions,
- Tantalum – ultimate resistance,
- Stainless steels – nitric acid,
- Steel – concentrated sulfuric acid.

Altering the environment

Depending on the system, the corrosion rate can be drastically affected by physical changes in the environment (*e.g.*, temperature, velocity, and oxidizer concentration).

Temperature. Lowering the temperature usually results in a sharp decrease in the corrosion rates. In some cases, however, lowering the temperature may have the opposite effect. For example, increasing the temperature of pure or seawater from hot to boiling decreases the oxygen solubility in water and causes a decrease in the corrosion rate.

Velocity. The effects of velocity on corrosion are very complex and are highly dependent on the metal-environment combination. In corrosion processes that are controlled by activation polarization, velocity has little effect on the corrosion behavior (Section 16.2.1.1). On the other hand, when the corrosion rate is controlled by cathodic diffusion, then velocity or agitation will lead to an increase in the corrosion rate. If cathodic diffusion prevails and the metal is readily passivated, then an increase in velocity

can result in an active-to-passive transition (Section 16.2.1.1). Stainless steels and titanium, for this reason, are often more corrosion resistant when the velocity of the corrosive medium is high.

Some materials will form visible protective corrosion layers that retard any further corrosion. These films are unlike the passivation films and can be damaged and removed by high-velocity medium flow. This type of corrosion falls under the category of "erosion-corrosion" and can be highly velocity dependent. An increase in the velocity may have no effect or slightly increase the corrosion rate until a "critical" velocity is reached. Further increase in the velocity will result in a drastic increase in the erosion-corrosion rate. Table 16.2-III shows typical corrosion rates at three velocities for some common alloys.

Increased velocities may, in some cases, lead to a decrease in corrosion by preventing silt deposition. This is only true when silt or dirt buildup causes "crevice" corrosion. Crevice corrosion is a form of attack primarily associated with small volumes of stagnant solution caused by crevices under bolts and rivet heads, gaskets, surfaces, lap joints, surface deposits, and holes. The main cause of crevice corrosion is believed to be the depletion of oxygen in the trapped and stagnant fluid. Crevice corrosion is a serious problem and methods and procedures for minimizing it include the use of welded butt joints instead of riveted or bolted joints, closing of crevices in existing lap joints by continuous welding, and by frequent removal of deposits.

Oxidizers. Removing oxidizers is a very old corrosion-control technique. Techniques for removing oxygen include vacuum treatment, inert gas sparging, or the use of oxygen scavengers. Examples of oxygen scavengers include sodium sulfite and hydrazine which remove oxygen as indicated by the following reactions:

$$2Na_2SO_3 + O_2 \rightarrow 2Na_2SO_4\,, \tag{16.2-1}$$

$$N_2H_4 + O_2 \rightarrow N_2 + 2H_2O\,. \tag{16.2-2}$$

Monel and copper exhibit a distinct increase in the corrosion rate when oxidizers are added to acid solutions. Neither of these materials passivate. However, materials that require oxidizers to form and maintain a protective film would show an increase in the corrosion rate if deaeration was performed. For example, when oxidizers are added to the solution, active-passive alloys such as 18Cr-8Ni stainless steels experience an increase, followed by a rapid decrease, and finally arrive at an oxidizer-concentration-independent corrosion rate.

Table 16.2-III.

CORROSION RATES OF METALS EXPOSED TO SEAWATER[a]

Material	Seawater Flow Velocity					
	1 ft/s[b]		4 ft/s[c]		27 ft/s[d]	
Carbon steel	34	(0.16)	72	(0.33)	254	(1.18)
Cast iron	45	(0.23)	–		270	(1.37)
Silicon bronze	1		2		343	
Admiralty brass	2		20		170	
Hydraulic bronze	4		1		339	
G bronze	7		2		280	
Al bronze (10% Al)	5	(0.02)	–		236	(1.1)
Aluminum brass	2		–		105	
90-10 Cu Ni (0.8% Fe)	5	(0.02)	–		99	(0.40)
70-30 Cu Ni (0.05% Fe)	2	(0.008)	–		199	(0.81)
70-30 Cu Ni (0.5% Fe)	< 1	(0.004)	< 1		39	(0.16)
Monel	< 1	(0.004)	< 1		4	(0.017)
316 SS	1	(0.004)	0		< 1	
Hastelloy C	< 1	(0.009)	–		3	(0.028)
Titanium	0		–		0	

(*a*) Corrosion rates are given in mdd (mg/dm^2) and in mm/y (values in parenthesis).

(*b*) Immersed in tidal current.

(*c*) Immersed in seawater flume.

(*d*) Attached to immersed rotating disk.

The effects of oxygen on corrosion rates depend on both the medium and the metal used. Nesmeyanova *et al.* [16] showed that the addition of oxygen markedly increased the corrosion of low-alloy steels (having less than 12% total alloy content) and stainless steels in distilled water at 300 °C, while Maekawa *et al.* [17] and Ito *et al.* [18] found that the corrosion rate of austenitic stainless steel is generally greater in deaerated (oxygen free) water than in air-saturated water.

More recently, the role of dissolved oxygen on the corrosion behavior of mild and stainless steel in aqueous solutions at temperatures above 100 °C were studied by Fujii *et al.* [19]. They concluded that: (1) The passivity which appeared in deaerated solutions was caused by the formation of a protective magnetite film. On the other hand, the rather poorly protective oxide obtained under air-saturated conditions was identified as α-Fe_3O_3 together with small amounts of Fe_3O_4. (2) The corrosion potential of stainless steel was raised into the trans-passive state (higher corrosion rates) with increased temperature and amount of dissolved oxygen. (3) The pitting of stainless steel in high-temperature water containing chloride ions is attributable to the effect of dissolved oxygen. These results show that removal of oxygen at high operating temperatures is beneficial in minimizing corrosion of stainless steels.

Corrosion inhibitors

Another corrosion-control technique is the addition of "corrosion inhibitors" to the solution. The most commonly used are adsorption-type inhibitors which suppress metal dissolution by adsorbing to the surface and thereby reduce both anodic and cathodic processes. The majority of inhibitors are organic amines (*e.g.*, glycine, lysine, and tryosine). Hydrogen-evolution poisons (*e.g.*, antimony and arsenic ions) are very effective as corrosion inhibitors for acid solutions because they retard hydrogen evolution. In closed spaces such as the interior of machine rooms, vapor-phase inhibitors are sometimes applied. These inhibitors consist of high-vapor-pressure organic substances that are put in the vicinity of surfaces to be protected and act similar to adsorption-type inhibitors by building protective layers through sublimation on surfaces.

Inhibitors have to be chosen specifically for a certain metal, environment, concentration, and temperature range. Lists of appropriate inhibitors and their application ranges have been compiled and are available [20]. Table 16.2-IV lists some of the reference inhibitors. Only nitrite and nitrate inhibitors are listed to point out their corrosive inhibiting potentials for use in reactor designs.

The types and quantities of inhibitors to be used have to be determined empirically. Corrosion processes are very sensitive to the operating conditions. It is particularly important to determine the exact amounts of inhibitors to be used because too little can often lead to an increase in the localized attack (rather than prevent it). The general rule of corrosion engineers is to use inhibitors in abundance. In some cases, two or more inhibitors are added, resulting in a larger reduction in the corrosion rate than if these inhibitors were used individually. One such "synergistic" corrosion-inhibiting effect has been well documented for nitride and molybdate ions. Sodium nitride has long been used to inhibit ferrous-metal corrosion in closed cooling systems [21]. Sodium molybdate was

Table 16.2-IV.

REFERENCE LIST OF CORROSION INHIBITORS

Metal	Environment	Inhibitor
Aluminum	Alcohol antifreeze	Sodium nitrite or molybdate
Aluminum	Ethylene glycol	0.01% to 1.0% sodium nitrate
Aluminum	Hydrogen peroxide	Alkali metal nitrates
Aluminum	Methyl alcohol	Sodium nitrite or chromate
Copper & brass	Tetrahydrofurfuryl alcohol	1% sodium nitrate or 0.3% sodium chromate
Monel	Sodium chloride	0.1% sodium nitrite
Monel	Tap water	0.1% sodium nitrite
Steel	Tetrahydrofurfuryl alcohol	1% sodium nitrite or 0.3% sodium chromate
Steel	Water-saturated hydrocarbons	Sodium nitrite
Tin plate	Alkali cleaning agents	Diethylene diaminocobaltic nitrate
Tin plate	Alkaline soap	0.1% sodium nitrite
Tin plate	Sodium chloride	0.2% sodium nitrite

also shown to be an effective corrosion inhibitor of steel in aerated open or fully closed cooling-water systems [22]. Table 16.2-V indicates the individual corrosion-inhibiting effects of NO_2^- and MoO_4^{-2} ions of a fairly corrosive media. The test water contained 250 mg/l chloride, 520 mg/l sulfate, 250 mg/l calcium and 15 mg/l magnesium at 60 °C.

Recently, it was shown that sodium nitride interacts synergistically with sodium molybdate [21]. Figure 16.2-4 shows the synergistic effect on the corrosion rate. The synergistic interaction of the two inhibitors is evident at all of the weight ratios of MoO_4^{-2}/NO_2^-, with optimum synergism occurring at inhibitor ratios ranging from 50/450 to 250/250 mg/l. The PPC of MoO_4^{-2}/NO_2^- system were studied and it was found that the current densities in each of the passive regions were lower than the corresponding passive current densities with either molybdate or nitride ions used separately. The primary passive region near -500 mV is attributed to molybdate, while the secondary passive region near 0 mV results from nitride.

16.2.1.3. Stress-corrosion cracking

During stress-corrosion cracking (SCC), a metal is virtually unattacked over most of its surface while fine cracks progress through the bulk of the material. The alloy becomes brittle with little or no macroscopic plastic deformation. Although many alloys are susceptible to SCC in at least one environment, SCC does not occur in all environments. Moreover, an environment that induces SCC in one alloy does not necessarily induce SCC in another. Stress-corrosion cracking has serious consequences since it can occur at stresses within the range of typical design stresses. Stress-corrosion cracking can occur both in transgranular (across grains) or intergranular (between grains) modes. Intergranular stress-corrosion cracking (IGSCC) is found to be the dominant failure mechanism in sensitized austenitic stainless steels, while transgranular SCC (TGSCC) has been reported to occur primarily in ferritic and low-alloy steels [23]. Three requirements must be fulfilled simultaneously for SCC to occur: (1) the steel must be sensitized, (2) the steel must be under tensile stress, and (3) the environment must have specific corrosion properties (*e.g.*, oxygen).

The typical oxygen content in BWRs during full-power operation is about 200 to 400 ppb. The source of oxygen is the radiolysis of water in the reactor core. Oxygen contents that result in corrosion potentials below -300 mV have been shown not to produce any IGSCC [7]. This corresponds to an oxygen content of not more than 10 ppb at temperatures above 200 °C (Figure 16.2-3). Operating a BWR at full power with less

Table 16.2-V.

CORROSION RATE OF SAE 1010 STEEL[a]

Test Water[b]	Oxygen Concentration (mg/l)			
	0	1	2.5	5
Uninhibited	0.1 (0.00)	6.6 (0.17)	16.3 (0.41)	40.1 (1.02)
500 mg/l MoO_4^{-2}	0.1 (0.00)	5.0 (0.13)	12.8 (0.32)	1.7 (0.04)
1000 mg/l MoO_4^{-2}	0.1 (0.00)	4.1 (0.10)	7.6 (0.19)	1.9 (0.05)
500 mg/l NO_2^-	0.1 (0.00)	4.9 (0.12)	8.6 (0.22)	9.6 (0.24)
1000 mg/l NO_2^-	0.1 (0.00)	0.5 (0.01)	0.4 (0.01)	0.4 (0.01)

(*a*) Corrosion rates are given in mils per year and in mm/y (values in parenthesis).

(*b*) Uninhibited and inhibited test water at 60 °C and a pH of 9.

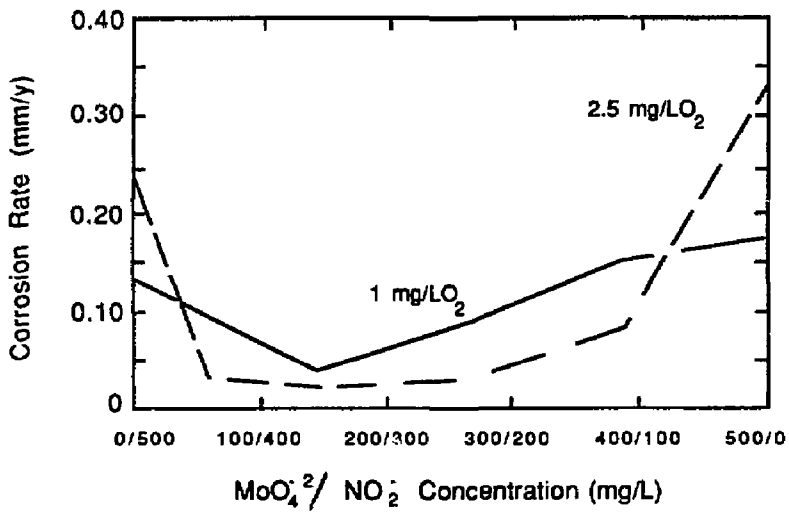

Figure 16.2-4. Corrosion rate of SAE 1010 steel in 60 °C test water showing the synergistic effect on corrosion inhibition with MoO_4^{-2}/NO_2^- combinations.

than 10-ppb oxygen content was achieved in the Swedish reactor OSKARSHAMM-2 [24]. The oxygen content was kept at 3 to 5 ppb by the addition of hydrogen to the feed water.

The Swedish researchers [23] were able to correlate IGSCC average crack-propagation rates to the corrosion potential at low strain rates ($5\times10^{-8}\,s^{-1}$). The tests were conducted on austenitic stainless steels at 275 °C. For oxygen contents of about 400 ppb, the crack-propagation rate was around 5×10^{-6} mm/s while for tests with oxygen contents less than 10 ppb, the propagation rate was as low as 10^{-7} mm/s. These measurements indicate a high sensitivity of IGSCC to the oxygen content of the coolant water.

Ljungberg *et al.* [23] tested 20 different steels including ferritic steels. Their results indicate that ferritic steels are sensitive to TGSCC under pure-water conditions (PWC). However, with hydrogenated water (alternate-water conditions, AWC), no TGSCC was observed (oxygen contents < 10 ppb). They concluded that TGSCC in ferritic and martensitic steels may be inhibited at a somewhat greater oxygen content in the reactor water than that needed for inhibiting IGSCC in sensitized stainless steel. The test results on ferritic and martensitic steels are summarized in Figure 16.2-5.

The fact that the AWC mitigates TGSCC in ferritic and martensitic steels with a somewhat broader margin of acceptable oxygen levels than for IGSCC in sensitized austenitic steels was also observed and reported by DRESDEN-2 experimentalists [25]. It should be noted that TGSCC of the type measured in the above experiments has never occurred in an operating BWR. Presumably, it is specific to the extreme mechanical conditions prevailing in the above-mentioned tests, with a constant extension rate such as the TGSCC observed in austenitic stainless steel with AWC.

Gordon *et al.* [26] also investigated the corrosion resistance of ferritic steels through hydrogen addition to BWR coolants. At a test temperature of 288 °C, the oxygen content was held close to 20 ppb by dissolving 125 ± 25 ppb hydrogen at a pressure of 8.69 MPa. Low-alloy- and carbon-steel samples were characterized by no crack growth under constant load-stress intensities of up to 50.9 MPa-$m^{1/2}$. Under cyclic loads, these samples showed a 7 to 20 times lower crack-propagation rate compared with samples exposed to nominal BWR environment (200 ppb oxygen). Furthermore, the addition of hydrogen to the test water did not show any evidence of hydrogen stress cracking or hydrogen embrittlement in low-alloy and high-strength, wrought martensitic stainless steels.

In addition to the control of the water chemistry, another remedy to SCC has been to develop alternative SCC-resistant materials. The most important materials of this type are the nuclear-grade stainless steels such as AISI 304 NG and 316 NG. These steels have a low carbon content (0.2 wt.%) to avoid sensitization, but contain nitrogen (between

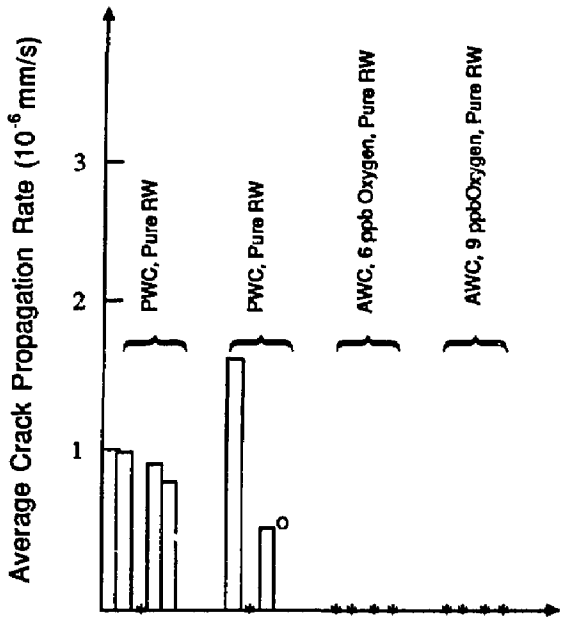

Figure 16.2-5. Summary of RINGHALS-1 CERT test results on ferritic and martensitic steels. For each test condition, the bars and symbols represent the result for the following alloys from left to right: A 204, SA 533, SA 508, and AISI 431. Symbol * denotes no cracking and symbol O denotes the result for the sample accidentally tested at constant load [23].

0.06 and 0.1 wt.%) to maintain the strength required by the ASME Boiler and Pressure Vessel Code. These nuclear-grade materials have been found to be much more IGSCC resistant than the regular AISI 304 and 316 stainless steels [27].

16.2.1.4. Corrosion in nitrates

Nitrates are known to be effective corrosion inhibitors (Table 16.2-IV) for stainless steels. In this section, the effects of nitrates on ferritics and austenitic steels are discussed.

Ferritic steels

In contrast to the voluminous literature on cracking in austenitic stainless steels, little information has been published concerning ferritic stainless steels. Until recently, it was

Table 16.2-VI.

THRESHOLD STRESSES (MPa) OF MILD STEELS IN BOILING NITRATE SOLUTIONS [30]

	Solution Concentration[a]			
Nitrate	8 N	4 N	2 N	1 N
NH_4NO_3	15.5	22.	54.	92.5
$Ca(NO_3)_2$	38.5	54.	92.5	177.5
$LiNO_3$	38.5	62.	146.5[b]	177.5
KNO_3	46.5	69.5	108.	185.5
$NaNO_3$	62.	146.5	170.	201.

(*a*) Normality, N, is in grams of solute per liter.

(*b*) Concentration was 2.5 N for this case.

more or less assumed that ferritic steels would not undergo SCC under similar environments which cause SCC in austenitic steels [28]. However, in the late 1960s, Bond [29] showed that the addition of nickel, copper, or cobalt can cause ferritics to become susceptible to SCC. In molybdenum-free steels, on the other hand, even 1.5-wt.% nickel did not produce susceptibility to SCC. The dependency of SCC on various interstitial components is very complex and strongly depends on the concentration of these components [28].

In an extensive study of SCC in low-strength ferritic steels, Parkins [30] investigated the susceptibility of low-carbon steels to SCC in the presence of a variety of nitrate solutions. Table 16.2-VI demonstrates the varying susceptibility of mild steels to cracking according to the nature of the cation and the concentration of the solution in boiling (atmospheric pressure) nitrate solution. The results show a marked reduction in the threshold stress as the solution concentration is increased. Table 16.2-VI also indicates a variation in the threshold stress with different cations at a constant concentration. According to this data, $NaNO_3$ is the least potent and NH_4NO_3 the most potent solution, with $LiNO_3$ somewhere between these two limits.

The effects of various cations in nitrate solutions have been related to the cation influence on the acidity of the solution. Recent studies have shown that acidic impurities accelerate the crack initiation, while essentially all impurities accelerate the crack growth rate which is governed by the concentration of the anion [31]. Therefore, the potency of the solution can be varied by changes in the pH value. Indeed, constant strain tests in 4 N $NaNO_3$ showed that acidification reduces the time-to-failure, while raising the pH value above 7 (*e.g.*, through addition of NaOH) causes marked increases in the time-to-failure [30 - 33]. This finding, although not substantiated for $LiNO_3$, would indicate an advantage in buffering the pH of the $LiNO_3$ solution to above neutrality to reduce SCC of ferritic steels. On the other hand, for a $Ca(NO_3)_2$ solution, a marked decrease in the time-to-failure below or above a pH value of 4 is observed [30]. Thus, a decrease or an increase in the pH value from a specific range could lead to an order-of-magnitude reduction in the time-to-failure.

An extensive investigation into ion-mitigating SCC of ferritic steel through the addition of various substances was performed by Parkins and Usher [32]. They concluded that oxidizing agents such as $KMnO_4$, $MnSO_4$, $NaNO_2$, and $K_2Cr_2O_7$ generally accelerate crack formation, while compounds such as Na_2CO_3, H_3PO_2, Na_2HPO_4, and $CO(NH_2)_2$ that form insoluble iron products, retard failure. This is an important point, since from a radiolytic point of view, oxidizing agents such as $KMnO_4$ have been shown to reduce the formation of molecular decomposition products such as H_2O_2, OH^-, and H_3O^+. Thus, in a nuclear environment, the two opposing effects of the addition of oxidizer agents to the aqueous coolants have to be optimized. Stress-corrosion cracking is minimized by removing oxidizing agents while radiolytic decomposition is reduced by adding oxidizers.

The effects of halide additions to nitrates have also been studied [34]. Fluoride additions showed no effect, while chlorides and bromides both increased the time-to-failure. Small amounts of chloride added to a 4 N $Ca(NO_3)_2$ solution increased the time-to-failure by orders of magnitude. Addition of chloride to NH_4NO_3 solution had little or no effect on the time-to-failure. The effects of chloride addition to $LiNO_3$ solutions have not been reported. Based on data reported in Table 16.2-VI, no marked effect is expected.

The effects of temperature on the cracking of steels in nitrate solutions follows a typical Arrhenius plot: a logarithmic dependence of failure time on the reciprocal of the temperature, as is seen in Figure 16.2-6 [35]. The slope of the Arrhenius plot is a measure of the activation energy of SCC. Values for the SCC activation energy vary, depending on the cation type and kind of steel used and are very sensitive to the nature of the films that form on the surface of the metals. Therefore, cracking does not depend only on temperature but also on precise electrochemical conditions which may in turn depend

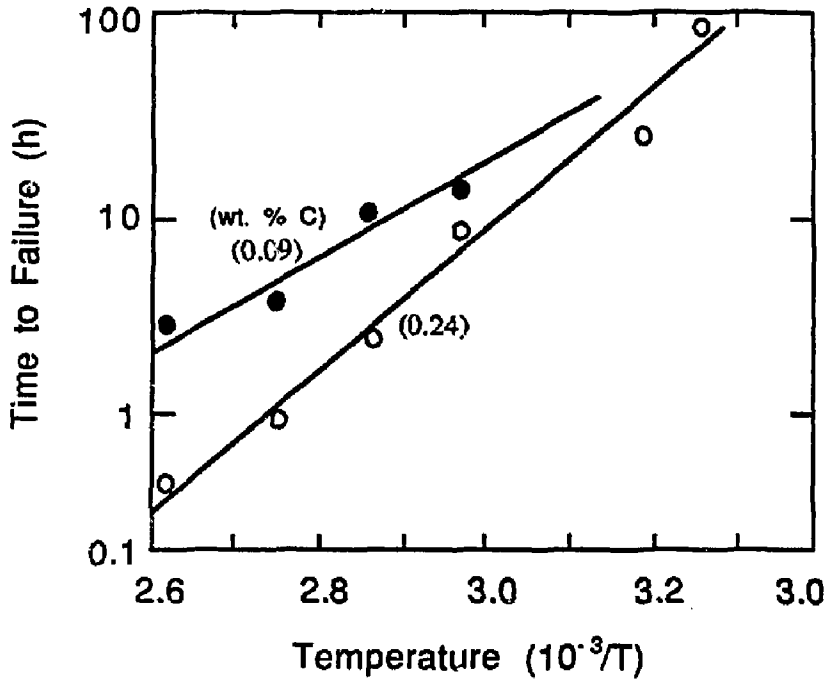

Figure 16.2-6. Effect of the temperature on the time-to-failure of carbon steels in a 60% $Ca(NO_3)_2$ + 3% NH_4NO_3 solution [35].

on the pressure and substances other than the NO_3^- ions. Szklarska *et al.* [33] point out that their measured activation energy for cracking agrees with the dissolution energy of iron in the corresponding nitrate solution. Because of discrepancies, the use of reported activation energies for cracking appears to be limited.

Austenitic steels

The main concern with the use of nitrates is SCC of unalloyed carbon steels. An extensive literature search was carried out by Waeben *et al.* [36] to determine the compatibility of lithium salts with steels as a function of water temperature and salt concentration. They note that no specific corrosion problems are reported for stainless steel in the presence of nitrate solutions, indicating no appreciable difficulties in practice with such systems. Their major findings on the effects of nitrates on corrosion are: (1) The threshold stress to cause failure decreases with an increase in the nitrate concentration.

(2) The failure times change logarithmically with the reciprocal of temperature. (3) The aggressiveness of nitrates with choice of cation decreases in the following order: NH_4, Ca, Li, K, and Na. (4) At a pH value above 7 to 8, the susceptibility of steel to SCC diminishes. (5) The susceptibility to SCC is the highest for steels with about 0.01 to 0.05-wt.% carbon content. (6) Alloying elements such as chromium and molybdenum show a beneficial effect on SCC, but nickel shows little or no effect.

Potentiodynamic polarization curves for 316 SS in water with $LiNO_3$ concentrations of 0.0296 and 0.296 g/cm^3 at 95 and 250 °C have been constructed by Waeben *et al.* [36]. The most significant finding was the lack of a marked transition between the primary and secondary passive regions which indicates that dissolution of a passive layer of alloying elements does not set in abruptly and, thus, a good passive behavior is observed over the entire potential range. Furthermore, the anodic currents are almost independent of the $LiNO_3$ concentration but are strongly temperature dependent. Microscopic examination of the 316 SS showed that a smooth oxide film was formed on the metal surface in $LiNO_3$ solution, with a roughness which was independent of solution concentration and temperature. Some crystallographic attack/deposit and small pits were found on both austenitic and martensitic stainless steels. The duration of the test was too short (200 h) to conclude that stainless steels are susceptible to pitting corrosion in $LiNO_3$ solutions.

16.2.1.5. Discussion

Fundamentals of the nature of corrosion were reviewed briefly to demonstrate that corrosion is primarily an electrochemical process. The electromagnetic environment of a fusion device can, therefore, have unforseen effects on the corrosion rates by the aqueous solution that are not experienced in conventional environments. The complexity of various environmental factors such as temperature, velocity, oxidizers, and other impurities was pointed out. The interdependence of these environmental factors is too great to allow any decisive conclusions regarding approximate corrosion rates. Lack of knowledge of the effects of irradiation and the effects of radiolytic decomposition products on corrosion mechanisms will undoubtedly further complicate the understanding and extrapolation of existing data.

Most recent experience with SCC in the nuclear environment was presented. The most significant finding was that a reduction of oxygen content through the addition of hydrogen to the coolant can reduce SCC in most ferritic and austenitic alloys. The effects of alloying elements on SCC were investigated. The high chromium content of the 9-C alloy (11.84 wt.%) is very helpful in reducing the susceptibility of this alloy to SCC.

The carbon content of the 9-C alloy (0.097 wt.%) is outside the range of highest SCC susceptibility but is high enough for sensitization to occur (> 0.02 wt.%) if the alloy is heated to temperatures above ~ 950 °C.

Experience with various aqueous nitrate-salt solutions shows that the choice of the cation will affect the degree of corrosion attack. The aggressiveness of nitrates decreases with choice of the cation in the following order: NH_4, Ca, Li, K, and Na. Thus for the $LiNO_3$ salt, the aggressiveness of NO_3^- ions is in the medium range. The effect of the cation choice on SCC has been related to the acidity of the solution. Investigations into buffering the $LiNO_3$ salt solutions to an optimum pH value could lead to marked reduction in the aggressiveness of the solution. Reduction of the oxidizing strength of the salt solution has been found to retard failure of test samples by SCC. On the other hand, an increase in the oxidizing power of the solution decreases radiolytic decomposition rates. An optimum oxidizing strength has to be established experimentally since the number of factors involved are too large to make analytical predictions.

Recent experiments [36] on the corrosion rates of $LiNO_3$ salt solutions with 316 SS and with a martensitic alloy at 95 and 250 °C show a lack of a marked transition between the primary and secondary passive regions. These data imply that a relatively stable passive layer is formed in this salt. Microscopic examination of the 316 SS showed that a smooth oxide film was formed on the metal surface in $LiNO_3$, with the roughness independent of solution concentration and temperature. Recently, electrochemical corrosion tests were performed for aqueous LiOH and $LiNO_3$ solutions in contact with AISI 316 L stainless steel [37]. It was found that stainless steels, particularly low-carbon steels, exhibit better corrosion resistance in an $LiNO_3$ solution than in LiOH.

It should be noted that most of the above experimental findings regarding corrosion and SCC of steels in $LiNO_3$ salt solutions were obtained without any control of the oxygen content of the solution which plays a significant role. In a fusion environment, the production of tritium will undoubtedly affect the oxygen content of the aqueous solution through recombination. Thus, breeding of tritium in the aqueous solution can potentially reduce corrosion and SCC of the structural material used in the FPC.

The investigation of the corrosion of ferritic steels in an aqueous $LiNO_3$ salt solution does not show unexpectedly high corrosion rates or high susceptibility to SCC. In addition, the latest experimental findings do not indicate any unforeseen catastrophic corrosion attack. However, an extensive research effort needs to be undertaken to confirm these observations. Furthermore, the effects of high-energy-neutron irradiation on corrosion mechanisms and rates should be examined.

16.2.2. Radiolysis of Aqueous Solutions

When water or aqueous solutions are used as the coolant in a fusion reactor, water will undergo extensive radiolysis because of the exposure to high levels of ionizing radiation. Various products such as H_2 and H_2O_2 will be formed, depending on the composition, temperature, pH, and impurities in the coolant. The radiolysis of water causes two major areas of concern. First, radiolysis can create large quantities of explosive gas mixtures. Second, the radiolytic decomposition products, in particular H_2O_2, can enhance the corrosion rate of structural materials.

The TITAN-II FPC is cooled by an aqueous $LiNO_3$ salt solution. The presence of lithium atoms undergoing (n,α) reactions in the coolant introduces high-energy α and tritium recoil ions. These energetic ions, together with neutrons, interact with the surrounding water molecules causing the decomposition of water molecules. Thus, contributions from both the ionizing radiation and the nuclear reactions in the aqueous solution should be included in the analysis.

It is desirable to quantify the radiolytic products as a function of water chemistry, impurity levels, temperature, and the characteristics of the radiation field. However, the complex interrelationship between environmental factors and the formation rates of the decomposition product makes this task very difficult. Furthermore, very little experimental data are available on production and recombination rates of radicals in aqueous $LiNO_3$ salt solutions.

In this section, an introduction to radiation chemistry is given (Section 16.2.2.1), followed by a qualitative description of radiolytic processes. Effects of $LiNO_3$ additions on radiolysis are reviewed. In conclusion, the findings and uncertainties due to the radiolysis of the salt solution are summarized.

16.2.2.1. Background

Ever since Roentgen discovered the X ray, the effects of nuclear radiation which cause chemical changes have been investigated as a branch of chemistry (radiation chemistry). During the 1960s, radiation chemistry received a great deal of attention and identified intermediate species in gases and liquids, the mechanism of energy loss of free-radical and ion-pair formation and distribution, and transient species. International conferences are still being held, mostly in Europe, with heavy contribution from eastern block scientists. While the literature of the 1960s is rich in research performed on various nitrate solutions,

$LiNO_3$ solutions have only been studied in the last decade and mostly by scientists in the USSR.

Interaction of highly energetic particles and photons with matter can be divided into two categories: light particles (electrons and photons), and heavy particles. It is important to note that the chemical effects produced in the water by this variety of radiation is much the same. The main difference lies in the geometrical distribution of the intermediate products that are formed by the interaction of the radiation with matter.

Photons

Photons produce free electrons by interacting with matter through three processes:

Photoelectric effect. All of the photon energy is given to one electron. The most tightly bound electron in water, the K-electrons of oxygen, requires 532 eV to become ionized and removed from the molecule. The excess energy of the photon will, therefore, appear as kinetic energy of one electron.

Compton effect. The photon only gives up part of its energy to an electron. The remainder is carried by a scattered photon of longer wavelength which eventually will be absorbed by the photoelectric effect.

Pair formation. For photons with energies above 1 MeV, the pair-formation process becomes significant. When a high-energy photon passes near an atomic nucleus, a pair of positive (positron) and negative electrons may be formed. The probability of pair formation is directly related to the charge of the nucleus. For water, the pair-formation process is negligible.

Electrons

The rate at which a moving electron loses energy, $-dE/dx$, is called "stopping power" by physicists and "linear energy transfer" (LET) by radiobiologists. For nonrelativistic electrons having energies below 50 keV the energy loss equation is [38]:

$$-\frac{dE}{dx} = \frac{2\pi e^4 NZ}{E} \ln\left(\frac{E}{I}\sqrt{\frac{\epsilon}{2}}\right), \qquad (16.2\text{-}3)$$

where e is the charge of the electron, E is the energy of the moving electron, NZ is the number of electrons per unit volume of irradiated material, $\epsilon = 2.71828$ is the base of natural logarithms, and I is a number characteristic of each material (sometimes called "stopping potential"). Parameter I depends on the atoms present in the material but is independent of the chemical bound of the atoms. For water, the value of I has been estimated between 66 [39] to 69 [40]. For $I = 66$, Equation 16.2-3 can be reduced to

$$-\frac{dE}{dx} = \frac{1019}{E} \log\left(\frac{E}{56.6}\right), \tag{16.2-4}$$

where $-dE/dx$ is in units of eV/Å. At higher energies, Equation 16.2-4 is modified to include the relativistic change of mass of the electron, resulting in a minimum value of $-dE/dx$ of 0.018 eV/Å for electron energies in the range of 1 to 2 MeV.

Another quantity of interest is the energy loss of the electron in each event. Although the probability of energy loss decreases exponentially with increasing electron energy, at low energies, the probability depends on the binding energy of the electron in the material and becomes difficult to calculate. Pollard [41] has determined the average energy loss per event to be 110 eV ± 30% in a low-pressure cloud chamber. The true value may be different in liquid water than in the gas cloud chamber.

If the electron energy greatly exceeds the ionization potential, another fast electron will be produced which is called a secondary or tertiary electron. These secondary electrons may carry enough energy to cause ionization along their path lying within a few Å of the primary ionization event and leading to the formation of a cluster of ions. These groups, referred to as "spurs," will form along the main track of the primary electron.

Figure 16.2-7 shows the LET for electrons in water as a function of electron incident energy. While passing through matter, electrons change direction frequently as a result of collisions with atomic nuclei. The loss of energy with distance refers to the actual distance traveled, not to the distance between beginning and end of path.

Heavy charged particles

Ions travel at slower speeds than an electron of equal energy because ions are much heavier. The LET equation for ions is similar to that for electrons, except that it also depends on the magnitude of ion charge:

$$-\frac{dE}{dx} = \frac{2\pi e^4 Z_i^2 NZ}{E} \frac{M}{m} \ln\left(\frac{4E}{I}\frac{m}{M}\right), \tag{16.2-5}$$

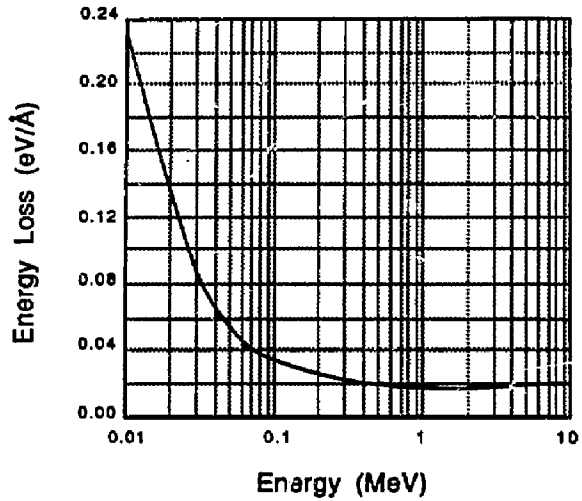

Figure 16.2-7. The LET for electrons in water [42].

where M and Z_i are, respectively, the mass and atomic number of the moving ion. Assuming $I = 66$ for water, the LET equation for protons reduces to:

$$-\frac{dE}{dx} = \frac{1.876}{E} \log\left(\frac{E}{0.0605}\right), \tag{16.2-6}$$

and for α particles to

$$-\frac{dE}{dx} = \frac{29.735}{E} \log\left(\frac{E}{0.1203}\right), \tag{16.2-7}$$

where E is units of MeV and $-dE/dx$ in units of eV/Å. The LET for helium ions (α particles) in water is shown in Figure 16.2-8.

Towards the end of the track, where the charged particle energy is reduced, it may capture electrons from the surroundings and become a fast-moving neutral atom (*e.g.*, for α particles with energies below ~ 0.5 MeV). As the neutral atom travels through the media, it may lose one, or all, of its electrons and recapture them a later time. The net energy loss of a neutral during these electron loss and capture processes is, therefore, much lower than that of a charged particle. The energy of the fast-moving neutrals is transferred primarily by direct collisions or "knock-ons" to the target nuclei.

Since the LET is proportional to the fourth power of the charge of the particle, α particles have small LET values. Therefore, an α particle retains its charge over a large part of the track, maintaining a fairly constant stopping power until it reaches the knock-on mode.

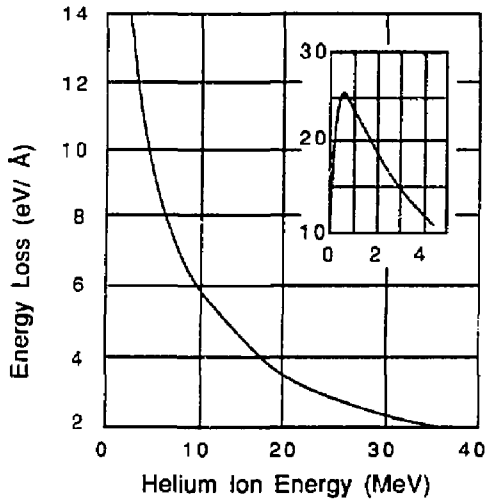

Figure 16.2-8. The LET for helium ions (α particles) in water [42].

Neutrons

Fast neutrons lose their energy by collision with the atoms in the material. In water, the hydrogen atom will take up most of the energy (on average, about half the energy of the neutron). The recoil hydrogen atom starts to travel at a very high velocity, is immediately stripped of its electrons, and becomes a fast proton. Therefore, irradiation by fast neutrons actually results in irradiation by fast protons.

16.2.2.2. Products of the radiolysis

The water decomposition products are often termed "molecular decomposition products" to distinguish them from the short-lived free radicals. The overall process can be broken up into three stages. During the first stage (lasting $\lesssim 10^{-13}$ s), mainly H_2O^+ ions and excited water molecules, H_2O^*, are produced. These products undergo a series of transformations during the second stage (lasting $\sim 10^{-11}$ s). These second stage transformations result in the formation of hydrogen atoms, hydrated electrons, OH radicals, and some H_2 and H_2O_2. Only during the third stage do the radicals undergo a variety of chemical reactions. If the radical concentration is high (*e.g.*, in or close to spurs),

radicals recombine to form molecular products H_2 and H_2O_2. This stage is completed within 10^{-9} to 10^{-8} s after irradiation. Radicals which do not recombine in the spurs will recombine in the bulk of the solution or, if present, with solutes. These reactions will be completed within 10^{-7} to 10^{-2} s [43].

In describing the system of reactions occurring during water decomposition, the hydrated electron is used. The solvated electron, called "hydrated" electron (e^-_{aq}), is trapped in a solvation shell. The discovery of hydrated electrons showed that electrons in water were chemical entities, as distinct from possessing purely physical characteristics. They have diffusion properties, size and sphere of influence, associated ion atmosphere, and reaction rate parameters, all comparable to normal chemical reagents [44]. The hydrated electron, e^-_{aq}, reacts with a hydrogen ion and produces a hydrogen atom:

$$e^-_{aq} + H^+ \rightarrow H\,. \tag{16.2-8}$$

Today it is widely accepted that the hydrated electron is the precursor for the formation of the hydrogen atom.

Interactions between the hydrated electron and water, and between the radicals constitute the following molecular product equations:

$$e^-_{aq} + e^-_{aq} + 2H_2O \rightarrow H_2 + 2OH^-\,, \tag{16.2-9}$$

$$e^-_{aq} + OH \rightarrow OH^-\,, \tag{16.2-10}$$

$$H + H \rightarrow H_2\,, \tag{16.2-11}$$

$$OH + OH \rightarrow H_2O_2\,, \tag{16.2-12}$$

$$H + OH \rightarrow H_2O\,. \tag{16.2-13}$$

The radicals that escape reactions with other radicals have a chance to diffuse away from the spurs and react with other molecular products. These reactions are denoted as "chain reactions" since they result in radicals that could again react with other molecules:

$$H_2O_2 + H \rightarrow H_2O + OH\,, \tag{16.2-14}$$

$$H_2 + OH \rightarrow H_2O + H\,. \tag{16.2-15}$$

Although some hydrogen and hydrogen peroxide is produced by direct association of water through

$$H_2O + H_2O^* \rightarrow H_2 + H_2O_2\,, \tag{16.2-16}$$

it has been established that most of the H_2 and H_2O_2 is formed by the radical recombination reactions (Equations 16.2-11 and 16.2-12). The molecule H_2O^* denotes an excited water molecule.

Oxygen is found among the water decomposition products, although it seems to be formed not directly from water but as a result of action of the radicals on hydrogen peroxide. Thus, the radiation decomposition of water is generally described in terms of the amounts of molecular H_2 and H_2O_2, the free radicals H and OH, and the free-radical decomposition products such as O_2 and HO_2. The HO_2 molecule forms mostly with heavy-particle irradiation and has to be included as another quantity to be considered. When solutes are present, subsequent reactions of these entities with the dissolved material are also included.

It is important to note that although the free radicals are generally denoted as H and OH, their actual molecular constitution is not absolutely known. It is clear that H is a powerful oxidizing agent while OH is a powerful reducing agent, and that they can react with each other to form H_2 and H_2O_2. In a polar medium (*i.e.*, water), solutes are often found to exist in acidic or basic forms. The radical OH might be present in its basic form (O^-) or in its acidic form (H_2O^+), and the H radical may actually exist as a solvated electron (basic form of H) or acidic form H_2^+ (loss of a proton is termed "basic," gain of a proton is termed "acidic"). So the ionization process of a water molecule results in a free electron and an H_2O^+ ion. This ion is the "basic" form of the H radical or the "acidic" form of the OH radical.

16.2.2.3. Molecular and radical yields in water

Reaction yield for a product, P, is denoted by $G(P)$ and refers to the number of radicals or molecules which are produced by radiation and determined by chemical analysis. Reaction yields expressed in this manner are different from the number of molecules and radicals which are produced directly by the radiation because these products may decompose further by reacting with the free radicals. Reaction yields are expressed in terms of numbers of molecules or radicals produced per 100 eV of energy absorbed by the media.

Gamma rays

Highly pure water irradiated with X or γ rays appears to be stable, showing no decomposition at all. The apparent stability arises from the reaction of free radicals with

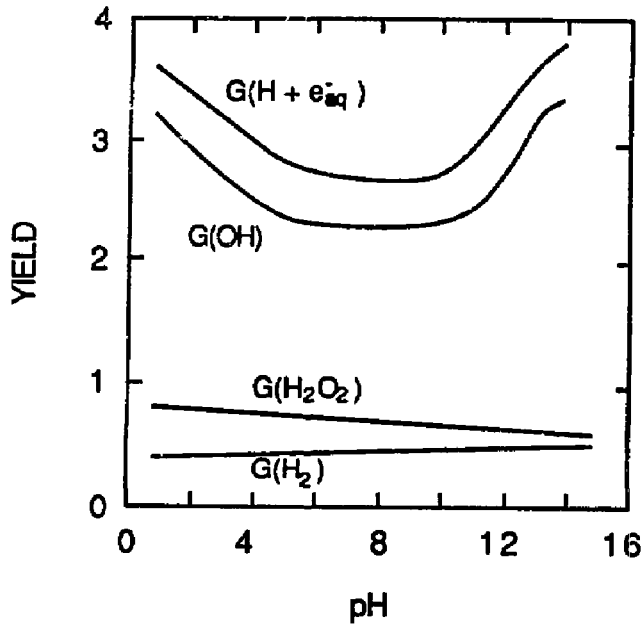

Figure 16.2-9. Variation of the primary yields of γ-irradiated water with the pH value.

molecular products (H_2 and H_2O_2) leading to recombination back to water. The net stability of water is seen to depend on whether the hydrogen gas is retained in the water to be acted on by the radicals, or allowed to escape. This was shown through experiments in which the hydrogen gas could escape to evacuated volumes [45].

The effect of pH on γ-ray yields of ordinary water has been well documented [42,43]. Figure 16.2-9 shows that the primary yields for gamma irradiation varies little in the pH range of 4.5 to 10.5 [46].

Alpha particles

When pure water is irradiated with α particles (high LET), the number of molecular decomposition products formed is too great to be converted back into water, resulting in a continuing net decomposition of water. Heavy-particle radiation, therefore, leads to extensive decomposition of the water into hydrogen gas, hydrogen peroxide, and oxygen, while the effect on dissolved solutes is considerably less for a given energy than with the light-particle radiation [47].

As early as 1913, a careful study of the decomposition of water in three phases (ice, liquid, and steam) by α particles from radon was published by Duane and Scheuer [48]. They reported considerable formation of hydrogen peroxide, oxygen, and hydrogen. More recently, Lefort [49] showed that the hydrogen yield from the action of α particles on a larger number of solutions to be about the same, with value of $G(H_2) \simeq 1.7$. Since the OH radicals are the prime radicals that convert the molecular hydrogen back to water, the α-particle yield of free OH must be very small. One explanation is that the free radicals must be produced so densely in the track of the α particle that nearly all undergo initial recombination to form H_2 and H_2O_2, or to go back to water [50].

Since the track density (of radicals) is directly related to the LET, the ratio of radicals to molecular yield should increase with decreasing LET. Another possible reaction in dense tracks is the encounter of an H_2O_2 with a third OH radical:

$$OH + H_2O_2 \rightarrow H_2O + HO_2 . \qquad (16.2\text{-}17)$$

Consequently, for particles of high LET, there are five primary yields: G_H, G_{OH}, G_{H_2}, $G_{H_2O_2}$, and G_HO_2. Quick estimates for high-LET radiation can be found from curves that display yields as a function of initial LET. Figure 16.2-10 shows typical yield curves for neutral solutions [50].

Jenks [51] has estimated the LET and the associated yields for γ rays, fast neutrons, and α particles from $^{10}B(n,\alpha)^7Li$ reactions. These values are summarized in Table 16.2-VII together with estimates for α-particle yield from $^6Li(n,\alpha)T$ reaction, derived from Figure 16.2-10.

16.2.2.4. Molecular and radical yields in concentrated solutions

Gamma rays

Over the past decade, considerable information has been accumulated on γ-ray yields in concentrated solutions, particularly for solutions containing nitrates such as $NaNO_3$, $LiNO_3$, $Ca(NO_3)_2$, and KNO_3. Until recently, no satisfactory (i.e., quantitatively and qualitatively self-consistent) account could be given of the radiolytic behavior of these systems [50]. In order to explain radiolysis mechanisms of concentrated solutions, Kiwi and Daniels [52] progressively measured the yields of various nitrated solutions as a function of solute concentrations under γ irradiation. The radiolysis of nitrate solutions is characterized by a yield of nitrite ions (NO_2^-), increasing continuously with nitrate concentration up to the solubility limit and the occurrence of O_2 as a major product.

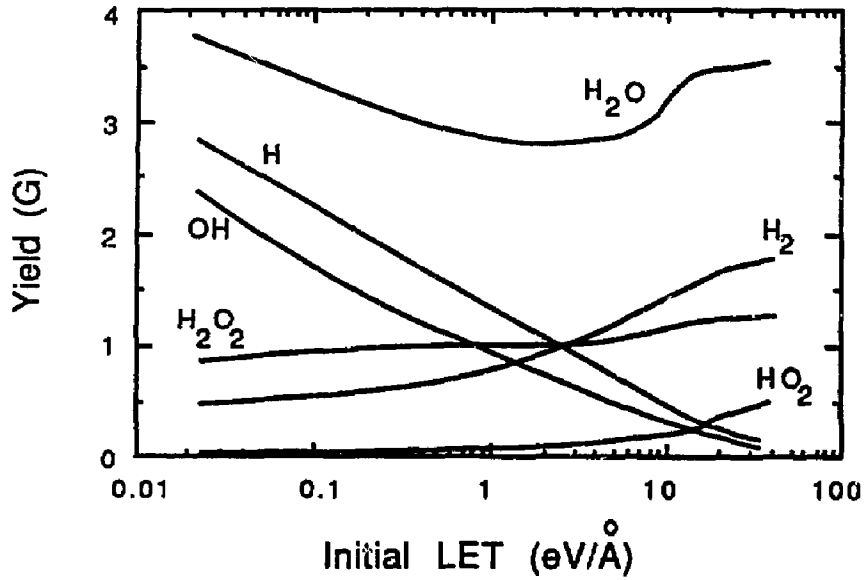

Figure 16.2-10. Water-decomposition yields in neutral solution as a function of initial LET of α particles [50].

Table 16.2-VII.

YIELDS AND LET FOR GAMMA RAYS, FAST NEUTRONS, AND ALPHA PARTICLES IN WATER [51]

Energy Source	Initial LET (eV/Å)	Yields (No./100 eV)				
		H_2	$H + e^-_{aq}$	H_2O_2	OH	HO_2
γ ray	0.02	0.44	2.86	0.70	2.34	0.00
Neutrons	4.0	1.12	0.72	1.00	0.47	0.17
$^{10}B(n,\alpha)^7Li$	24.	1.70	0.20	1.30	0.10	0.30
$^6Li(n,\alpha)T$ (a)	4.	1.2	0.7	1.0	0.4	0.2

(a) Estimated based on the data of Figure 16.2-10.

Nitrites are formed via the reaction of nitrate ions with reducing radicals [43]:

$$NO_3^- + H \rightarrow NO_2 + OH^- , \quad (16.2\text{-}18)$$

$$NO_3^- + OH \rightarrow NO_3 + OH^- , \quad (16.2\text{-}19)$$

$$NO_3^- + e_{aq}^- \rightarrow NO_3^{2-} , \quad (16.2\text{-}20)$$

$$2NO_2 + H_2O \rightarrow NO_2^- + NO_3^- + 2H^+ , \quad (16.2\text{-}21)$$

$$2NO_3^{2-} + H_2O \rightarrow NO_2^- + NO_3^- + 2OH^- . \quad (16.2\text{-}22)$$

While the above reactions are termed "indirect" reactions, "direct" reactions can also occur:

$$2NO_3^- \rightarrow 2NO_2^- + O_2 , \quad (16.2\text{-}23)$$

$$NO_3^- \rightarrow NO_2^- + \frac{1}{2}O_2 . \quad (16.2\text{-}24)$$

Kiwi and Daniels [52] have measured the yields for H_2, H_2O_2, O_2, and NO_2. The experimental data are difficult to explain because nitrite is formed indirectly (Equations 16.2-18 to 16.2-22) and directly (Equations 16.2-23 to 16.2-24). Kiwi and Daniels were able to explain and distinguish between the direct and indirect yields using an electron fraction model [50]. They concluded that for all of the nitrate solutions such as $NaNO_3$, $LiNO_3$, $Ca(NO_3)_2$, and KNO_3, and with more than 1 molar concentration, the major products are nitrite, peroxide, and oxygen. Table 16.2-VIII lists the various yields as a function of salt concentration in $LiNO_3$ solutions. Figures 16.2-11 and 16.2-12 present these results and show that, as the molarity of the solution increases, $G(H_2O_2)$ and $G(H_2)$ decrease drastically, while $G(NO_2^-)$ and $G(O_2)$ values stay fairly flat, increasing only slightly with increasing salt concentration.

The experimental yields were explained by assuming that the phenomena characteristic of concentrated solutions originates independently of water radiolysis [50]. Hence, the yield for a product (P), formed both in dilute and concentrated solutions, can be written as:

$$G(P) = G(P)_{H_2O} \times f_{H_2O} + G(P)_{NO_3^-} \times f_{NO_3^-} , \quad (16.2\text{-}25)$$

where $G(P)$ is the measured yield and $G(P)_{H_2O}$ and $G(P)_{NO_3^-}$ are constant yield characteristics of dilute and concentrated solutions, respectively. The values of the weighting coefficients are estimated to be 0.331 and 0.342 for $f_{NO_3^-}$ and 0.646 and 0.635 for f_{H_2O} for $LiNO_3$ solution with 7 and 7.2 mol/liter concentration, respectively [50]. No yields for

Table 16.2-VIII.

YIELDS FOR GAMMA RADIATION IN $LiNO_3$ SOLUTIONS [a] [52]

Molarity[b]	H_2O_2	H_2	NO_2^-	O_2
1	0.63	0.15	1.4	0.35
2	0.53	0.09	1.5	0.75
3	0.45	0.05	$\sim$ 1.55	$\sim$ 0.8
5	0.35	0.03	$\sim$ 1.6	$\sim$ 0.85
7	0.33	$<$ 0.01	$\sim$ 1.7	$\sim$ 0.6
9	0.26	$<$ 0.01	$\sim$ 1.8	–

(*a*) In units of No./100 eV.

(*b*) Molarity, M, is defined in units of mol/liter of $LiNO_3$.

OH as a function of molarity were reported, since it was shown that $G(OH)$ will be fairly independent of the concentration of the nitrate solutions [50]. Thus, for all practical purposes, the corresponding value for water can be used.

Scavenging

For concentrated solutions, it is found that oxidizing agents will gradually decrease the H_2 yield as the concentration of the oxidant is increased, and reducing agents will decrease the H_2O_2 yield [53]. This effect is expected, because solute molecules that are present in the spur may react with the radicals before they have a chance to encounter a radical of the same kind. Thus, the probability of molecular product formation decreases as the solute concentration increases. The process of picking up and destroying radicals by solutes is referred to as "scavenging." Some experience has been gathered in the fission industry by using copper as a scavenger to reduce the molecular-product yield [54].

The scavenger effects on the molecular-product yields for γ rays has been studied closely since the mid-1950s [53,55,56]. Sworski [55] measured the hydroxide peroxide

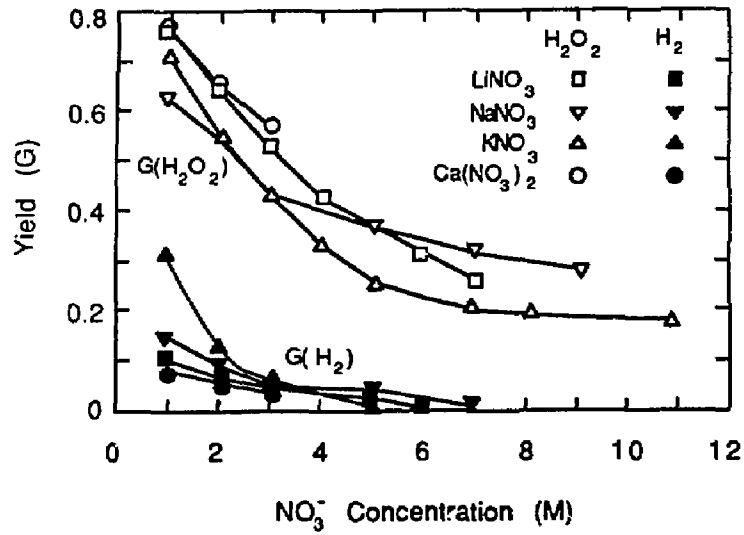

Figure 16.2-11. Yields of hydrogen, $G(H_2)$, and hydrogen peroxide, $G(H_2O_2)$, as functions of molarity (mol/liter) of the nitrate salt solution.

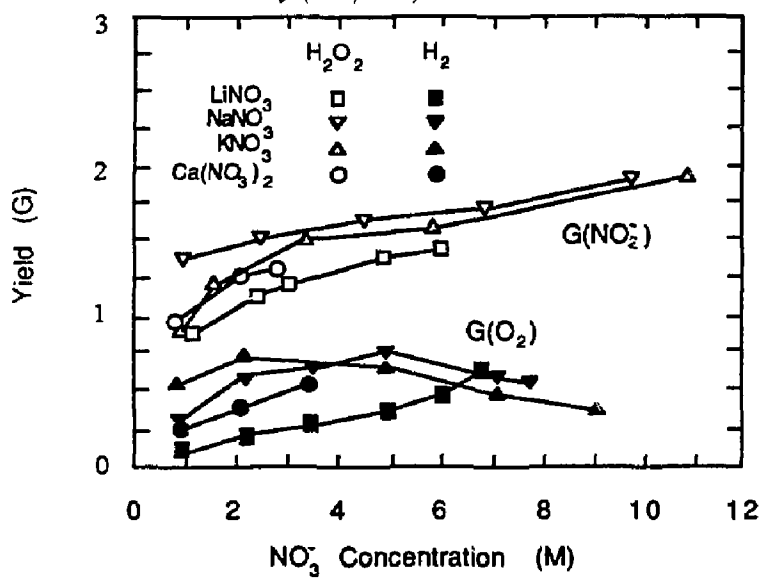

Figure 16.2-12. Yields of oxygen, $G(O_2)$, and nitrate ion, $G(NO_2^-)$, as functions of molarity (mol/liter) of the nitrate salt solution.

yield, $G_{H_2O_2}$, in aerated acid solutions as a function of bromide concentration (X). As the bromide concentration increased, $G_{H_2O_2}$ decreased linearly in the cube root of the bromide solution, or:

$$G_{H_2O_2}(X) \simeq G^{\circ}_{H_2O_2} + G_c \times (X)^n , \qquad (16.2\text{-}26)$$

where $n = 1/3$ for γ-ray irradiation, G° is the molecular yield (molecules/100 eV of radiation absorbed in very dilute solutions), G_c is a constant, and X is the concentration (molarity) of the solution. Schwarz [53] discovered that the hydrogen yield and the peroxide yield could be greatly reduced by concentrations of potassium nitrite and copper sulfate.

Nitrate ions at high concentrations were found to reduce the H_2 yield under nuclear reactor radiation to values less then 0.05 [57]. This result verifies that molecular hydrogen does not form directly by splitting of the hydrogen from the water molecule by

$$H_2O + e^-_{aq} \rightarrow H_2 + O^- , \qquad (16.2\text{-}27)$$

but by the combination of H atoms. Ferric ions are among other scavengers that reduce G_{H_2} in acid solutions [53]. In general, substances that react readily with H atoms reduce G_{H_2}, while those reacting with OH reduce $G_{H_2O_2}$.

Alpha particles

While the γ-ray yields are well known as a function of $LiNO_3$ salt concentration, the α and tritium recoil yields have not been studied to this extent. The effect of scavenger concentrations was investigated by Burton and Kurien [58]. They concluded that: for γ rays, the exponent n of Equation 16.2-26 is about 1/3; for 50-keV X rays, $n \sim 0.26$; and for 3.4-MeV α particles, $n \sim 0.15$. These results indicate that higher LET radiation yields are more sensitive to solute concentrations than are low LET radiation yields. H_2 and H_2O_2 yields can be approximated as a function of nitrate concentration by:

$$G^{(3.4\,MeV\ \alpha)}_{H_2,H_2O_2}(X) \simeq G^{\circ}_{H_2,H_2O_2} + G_{c1} \times X^{0.15} . \qquad (16.2\text{-}28)$$

Unfortunately the power law has not been investigated for yields of H, OH, and HO_2. The effect of scavenger concentration on these yields can be estimated using a mass balance equation resulting in:

$$G^{(3.4\,MeV\ \alpha)}_{H,OH}(X) \simeq G_{H,OH} \times (2X)^{-0.15} , \qquad (16.2\text{-}29)$$

$$G^{(3.4\,MeV\ \alpha)}_{HO_2}(X) \simeq G_{HO_2} \times (3X)^{-0.15} . \qquad (16.2\text{-}30)$$

Using Equations 16.2-28 through 16.2-30 and the water decomposition yields from Figure 16.2-10, the various yields as a function of salt concentration for the high LET radiation from ^{6}Li(n,α)T reactions can be estimated. Table 16.2-IX shows these estimated values.

16.2.2.5. Temperature effects

In general, the stability of non-boiling water to radiolysis increases as the temperature is increased, caused by the increase in the reaction rates between various radicals. Burns [59] has estimated the temperature dependance of reaction rate constants, k,

$$k(T) = k(T_o) \exp\left[-Q\left(\frac{1}{T_o} - \frac{1}{T}\right)\right], \qquad (16.2\text{-}31)$$

where T is temperature in K, T_o is the room temperature, and Q is the activation energy. Equation 16.2-31 can be used to estimate reaction-rate constants at higher temperatures.

Most of the experimental data of nitrate solutions reported in this section do not include the effect of temperature on various yields. However, Cohen points out that

Table 16.2-IX.

YIELDS FOR ^{6}Li(n,α)T REACTIONS IN $LiNO_3$ SOLUTION[a]

Molarity[b]	H_2	H_2O_2	H	OH	HO_2
0	1.2	1.	0.7	0.4	0.2
2	1.08	0.9	0.57	0.32	0.15
3	1.00	0.85	0.53	0.31	0.14
5	0.95	0.79	0.50	0.28	0.13
7	0.90	0.75	0.47	0.27	0.13
9	0.86	0.72	0.45	0.26	0.12

(*a*) Yields (No./100 eV) are based on the power-law measurement by Burton [58].

(*b*) Molarity, M, is defined in units of mol/liter of $LiNO_3$.

experiments in the High-Flux Irradiation Facility (HFIR) show a decrease of about an order of magnitude in yields for H_2 and H_2O_2, and about a factor of two decrease for HO_2 and O_2 yields as the temperature rises from room temperature to 200 °C [46]. In high-temperature coolants of power reactors, oxygen cannot be detected until hydrogen concentrations fall below the normally maintained levels of 25 cm^3/kg.

16.2.2.6. Tritium issues

The breeding of tritium in the coolant of a fusion reactor will lead to high-LET radiation which forms HO_2 molecules. These molecules are precursors of free-oxygen formation. Experiments with power reactors have shown that if oxygen is added to the coolant at high-power levels, rapid recombination with the existing hydrogen will occur [46]. Out-of-pile experiments with stainless-steel tubes at 260 °C have shown that excess oxygen will disappear with characteristic half-life of about 1.5 h, independent of hydrogen concentration [60], most probably reacting on the metal surface. Therefore, although the aqueous solution containing $LiNO_3$ salt will produce more oxygen than the salt-free coolants of fission power reactors, the production of tritium should enhance oxygen-hydrogen recombination under non-boiling conditions.

The nuclear reaction $^6Li(n,\alpha)T$ causes tritium atoms to recoil with 2.73 MeV of energy. Tritium atoms have been shown to react chemically while still possessing some of the kinetic energy. The high-energy tritium, "hot hydrogen," is believed to undergo a hydrogen abstraction reaction:

$$T + HOH \rightarrow HT + OH\,, \tag{16.2-32}$$

or an isotopic exchange reaction:

$$T + HOH \rightarrow TOH + H\,. \tag{16.2-33}$$

The activation energies for reactions 16.2-32 and 16.2-33 are, respectively, energies of 24 kcal/mol and 18 kcal/mol.

Thermal hydrogen atoms (low-energy tritium) will undergo reactions with the H and OH radicals to form HT or TOH by:

$$T + H \rightarrow HT\,, \tag{16.2-34}$$

$$T + OH \rightarrow TOH\,. \tag{16.2-35}$$

Table 16.2-X.

HT/HTO RATIOS OF NEUTRON-IRRADIATED SOLUTIONS [61]

Solution	HT/HTO Ratio
1.5 M $LiNO_3$, 0.1 M NaOH	0.06
1.5 M $LiNO_3$, 0.1 M NaOH	0.08
0.6 M LiOH	0.04
0.7 M LiCl, pH 14	0.048
1.0 M LiCl, 1 M NaOH	0.07

Kambara *et al.* [61] have made a detailed study of the HT/HTO ratio formed during neutron irradiation of various lithium-containing solutions. They studied aqueous solutions of $LiNO_3$, LiOH, and LiCl at pH values ranging from 1 to 11 irradiated to a total flux of 10^{14} to 10^{15} neutrons/cm^2. They found all HT/HTO ratios fall in the range of 0.04 to 0.12 with an average ratio of 0.10 ± 0.01. Table 16.2-X shows the HT/HTO ratios of some of the solutions studied.

An LiCl solution saturated with $KMnO_4$ showed an HT yield of zero. The NO_3^- ion is known to be an excellent scavenger for thermal hydrogen atoms through the following reaction:

$$H + NO_3^- \rightarrow NO_2 + OH^- . \qquad (16.2\text{-}36)$$

In fact, nitrate scavenging of thermal hydrogen atoms competes very successfully with hydrogen-atom recombination. Sowden [57] has shown that a 15.9-M $CaNO_3$ solution irradiated by fast neutron and γ rays shows a 75-fold reduction in hydrogen yield, $G(H_2)$, compared to that observed in water. However, it can be seen from Table 16.2-X that LiCl and LiOH also introduce strong H scavengers into solution. Thus the choice of lithium salt will have little effect on the HT/HTO ratio.

16.2.2.7. Discussion

Radiolysis of pure water and of aqueous $LiNO_3$ salt solutions by light and heavy particles was investigated. Gamma-ray radiolysis yields of $LiNO_3$ salt solutions are known as a function of salt concentration. At high concentrations, the H_2 yields are very small and the H_2O_2 yield decreases by a factor of about 3 relative to pure water. Oxygen yields of light-particle radiation are fairly independent of the salt concentration.

Energetic α particles (3.4 MeV) are produced by nuclear reactions with lithium in the aqueous $LiNO_3$ salt solution. Reaction yields were estimated as a function of salt concentration based on the power-law measurements of 3.4-MeV α particles. The oxygen production by heavy-particle radiation increases while the yields of H_2, H_2O_2, H, OH, and HO_2 all decrease with increasing salt concentration. The increase in oxygen production due to radiolysis may be balanced by the production of tritium atoms. It has been shown that oxygen added to non-boiling fission-reactor coolants at high-power levels rapidly combines with any hydrogen present. The decrease in the yield of free radicals in concentrated $LiNO_3$ solutions makes this salt more favored than LiOH solutions.

The effect of elevated temperature on radiolysis was investigated. From experience gained in the fission industry with pure water, it can be ascertained that the stability of non-boiling water to radiolysis increases as temperature increases. The apparent stability is actually caused by an increase in radical recombination rates at elevated temperatures.

In conclusion, although many uncertainties remain and much research is required in the area of radiolysis, the use of a highly concentrated, aqueous $LiNO_3$ salt solution should not lead to the formation of volatile or explosive gas mixtures. The effects of radiolytic decomposition products on corrosion, however, remain uncertain and experimental data on the behavior of radiolytic decomposition products in a fusion environment are needed.

16.2.3. Properties of $LiNO_3$ Solutions

The physical properties of concentrated solutions of $LiNO_3$ at high temperatures differ from those of pure water. Therefore, a fairly detailed investigation of the physical properties of the aqueous solutions was made, including an extensive literature survey, to ensure that reliable data were used in analyzing the performance of the TITAN-II FPC. The physical properties of $LiNO_3$ solutions as functions of temperature and salt concentration are given in the following subsections. During the TITAN-II design period, it proved convenient for the neutronics analysis to specify the salt concentration as the

atomic percentage of Li atoms present. As other measures of concentration are also commonly used, the relationships between the molality of the solution, m (the number of moles of solute per 1 kg of solvent), and the weight percentage of the solute, W, as a function of the atomic percentage of Li, A_{Li}, are given in the following equations:

$$m = \frac{3000 A_{Li}}{M_w(100 - 5A_{Li})}, \tag{16.2-37}$$

$$W = \frac{300 A_{Li} M_s}{3A_{Li} M_s + M_w(100 - 5A_{Li})}, \tag{16.2-38}$$

where M_w and M_s are the molecular masses of the water (18.02) and of the solute (68.94 for natural $LiNO_3$), respectively. Figure 16.2-13 shows these relationships over the concentration range of interest.

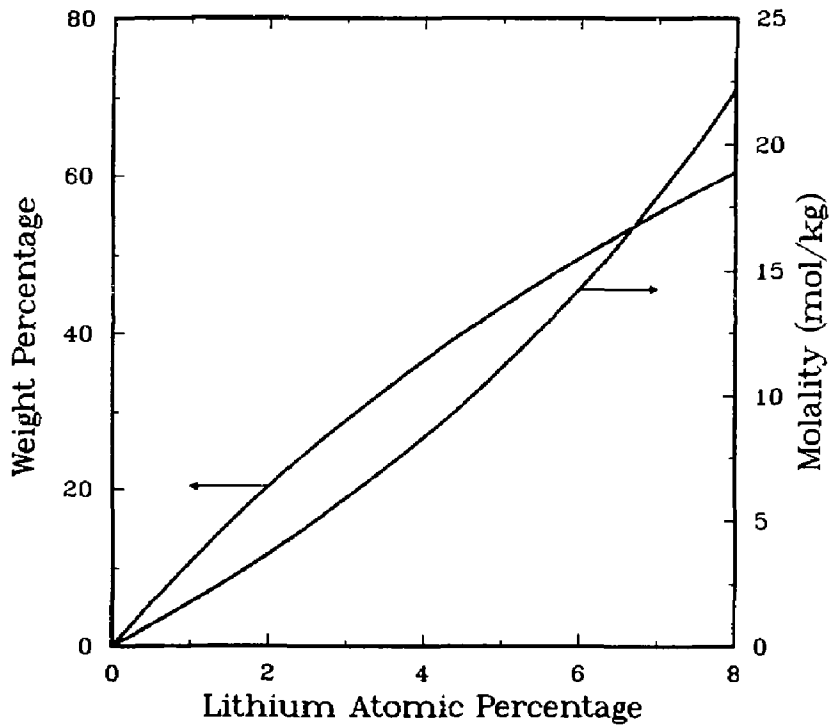

Figure 16.2-13. Relationship between molality and weight percentage of solute as a function of atomic percentage of Li for $LiNO_3$ solutions.

In many cases, experimental data for some physical properties of interest for $LiNO_3$ solutions are not available at high temperatures. Where this is the case, and reasonable extrapolations cannot be made, the corresponding data for NaCl solutions have been used because the NaCl–H_2O system has been much more widely studied than any other solution and many solutions of 1-1 electrolytes (*e.g.*, NaCl, KBr, and $LiNO_3$) have similar properties at the same concentrations. It is expected that such estimates should be accurate to about 20% [62], which is adequate for a worthwhile assessment of the thermal performance of the blanket.

16.2.3.1. Density

A full experimental data set is available for the density of $LiNO_3$ solutions for temperatures up to 350 °C and for concentrations from pure water to pure $LiNO_3$ [63,64]. In Reference [63], an expression is fitted to experimental data for weight percentages up to 40% and for temperatures up to 300 °C, the fit being accurate to better than 1.5% throughout the range. This data fit for the density, ρ, in g/cm^3 as a function of temperature, T (°C), is reproduced in the equation below:

$$\begin{aligned}\rho = \quad & 1.003 + 5.765 \times 10^{-3} W + 3.750 \times 10^{-5} W^2 \\ & - \left(1.898 \times 10^{-4} + 1.096 \times 10^{-5} W + 9.375 \times 10^{-9}\ W^2\right) T \\ & - \left(2.497 \times 10^{-6} - 6.500 \times 10^{-8} W + 4.229 \times 10^{-10} W^2\right) T^2 . \quad (16.2\text{-}39)\end{aligned}$$

In Reference [64], experimental data are given for weight percentages from 40% to 100% $LiNO_3$ and for temperatures up to 350 °C. To yield a smooth set of data over the entire range of temperatures and compositions under consideration, the fit has been used for the lower concentrations and the experimental data for the higher concentrations, with the data being slightly smoothed in the transition range between the two data sets. Figure 16.2-14 shows the density as a function of temperature for various values of the lithium-atom percentage. This figure shows that for the higher concentrations, density is significantly increased from the pure-water value, the difference being a factor of about two for a lithium-atom content of 8%.

No pressure dependence for the density was given in either of these references because the measurements were taken for saturation pressures. But the pressure dependence of the density is expected to be weak because the density of pure water rises by only ~ 3% as the pressure increases from 8.6 MPa (saturation) to 20 MPa.

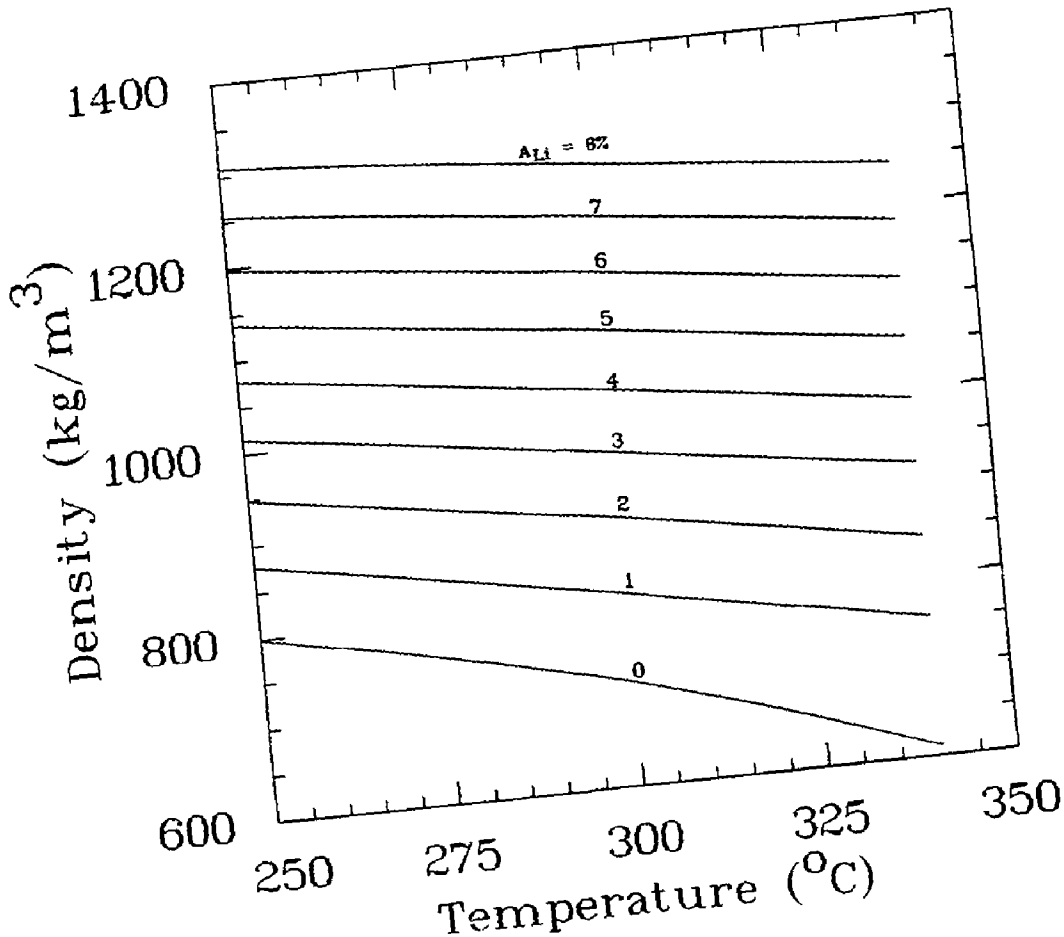

Figure 16.2-14. Density of $LiNO_3$ solutions at various temperatures and for a range of lithium-atom percentages.

A final point arising from these papers is that the authors note that $LiNO_3$ and H_2O are completely miscible at temperatures above the melting point of $LiNO_3$ (253 °C). This implies that there is effectively no upper limit to the salt concentration for high temperatures from solubility considerations.

16.2.3.2. Viscosity

The same Russian group that has published data concerning the density of $LiNO_3$ solutions at high temperatures has also reported measurements of the viscosity of these solutions. References [65,66] give experimental results for the viscosity of $LiNO_3$ solutions for temperatures up to 275 °C and for concentrations up to 10 mol/kg (~ 4.5% Li), and provide fits to these data. They quote a fit to the viscosity of the solution, η, relative to that of pure water, η_0, of the form

$$\ln\left(\frac{\eta}{\eta_0}\right) = \frac{AN}{1 - BN}, \qquad (16.2\text{-}40)$$

where A and B are temperature-dependent constants and N is the mole fraction of $LiNO_3$. Similar to the quoted fits for the density, no dependence of the viscosity on pressure was given, but since there is only an ~ 5% variation in the viscosity of pure water as the pressure changes from saturation to 20 MPa at 300 °C, it appears reasonable to ignore this effect.

The fit is said to be valid [65,66] only for mole fractions up to 0.1 ($m \sim 6$ mol/kg, or $A_{Li} \sim 3\%$), although it reproduces the experimental data well up to 10 mol/kg. The relative viscosity at the high temperatures relevant to fusion blankets is almost constant with varying temperature for a given concentration. Equation 16.2-40 has therefore been applied throughout the concentration and temperature ranges of interest, using the values of $A = 4.10$ and $B = -1.8$ (for 250 °C), and the results are shown in Figure 16.2-15.

According to this fit, there is about a factor of 6 increase in the viscosity of the 8% $LiNO_3$ solution compared with that of pure water. This large change can have a significant effect on the thermal performance of the coolant, although some of the change is reduced by differences in other properties. As the data fit has been used well outside its quoted range of validity, it is important to recognize that there is a large degree of uncertainty associated with these values. However, the general trend in the values should be correct, and until better experimental data become available it is reasonable to use these estimates to assess the potential of $LiNO_3$ solutions as fusion-blanket coolants.

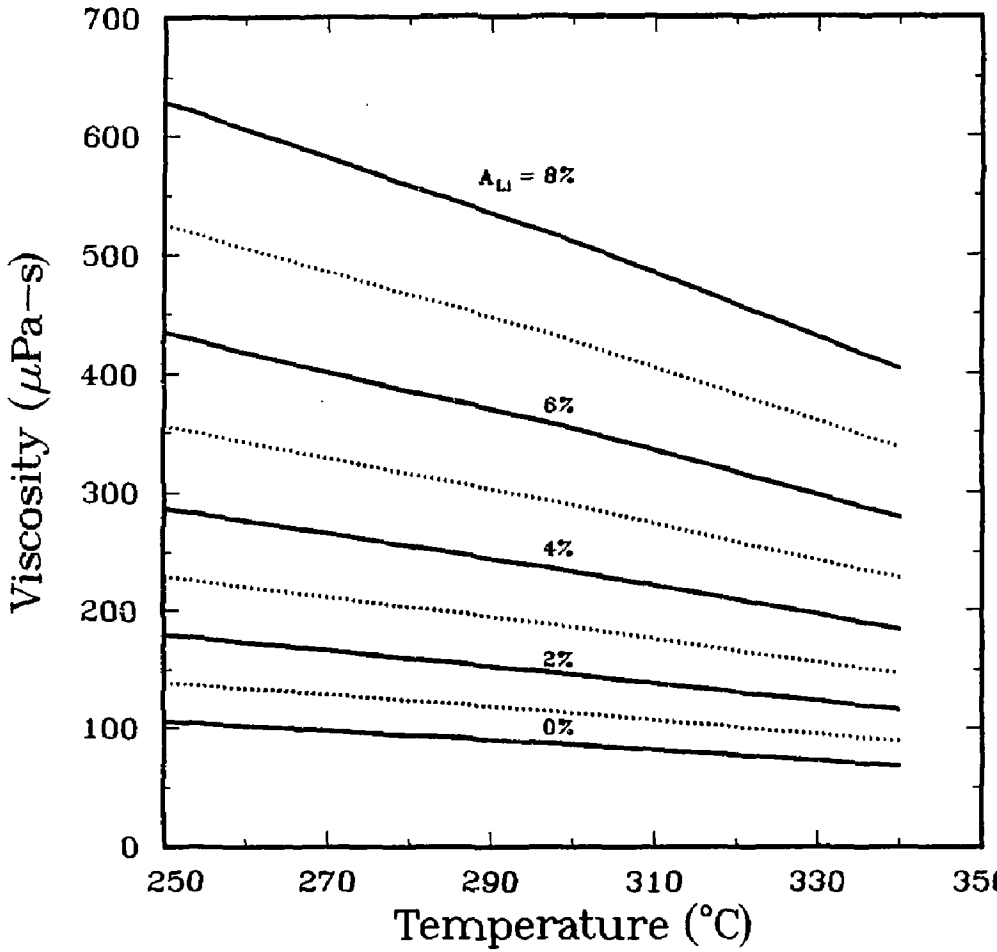

Figure 16.2-15. Viscosity of $LiNO_3$ solutions at various temperatures and for a range of lithium-atom percentages.

16.2.3.3. Specific heat capacity

The specific heat capacity is a more difficult quantity to predict by using a polynomial-type equation or by simply relating it to the value for pure water at the same temperature. The difficulty arises because the specific heat capacity of pure water becomes infinite as the critical point (374 °C and 22.1 MPa) is approached. The addition of even small quantities of a salt changes the critical temperature and pressure quite significantly. Therefore, the specific heat capacity of the solution can vary markedly from that of pure water at the same conditions. Wood and Quint have proposed a very simple way of estimating the specific heat capacity for aqueous salt solutions using a "corresponding-states" method [67]. In this method, the properties of the solution are approximated by the properties of water at the same "relative" conditions with respect to the critical point. The expression for the specific heat capacity of the solution, c_p, at temperature, T, and pressure, p, is

$$c_p(T,p) = W_0\left[c_{p0}(T',p') - c_{p0}(T',0) + c_{p0}(T,0)\right], \qquad (16.2\text{-}41)$$

where c_{p0} is the specific heat capacity of water, W_0 is the weight fraction of water, and T' and p' are, respectively, the reduced temperature and pressure and are given by

$$T' = \left(\frac{T}{T_c}\right) T_{c0}, \qquad (16.2\text{-}42)$$

$$p' = \left(\frac{p}{p_c}\right) p_{c0}. \qquad (16.2\text{-}43)$$

Here T_c and p_c are, respectively, the critical temperature and pressure of the solution and the subscript 0 refers to the properties of the pure water.

This approximation was tested for NaCl solutions up to 330 °C and 3 mol/kg and was found to give excellent agreement with experimental data, the largest error being about 3% at the highest temperatures and for the most concentrated solutions [67]. However, it should be noted that the heat capacity of the salt in the solution has been ignored in the calculation, which is likely to introduce a larger error for more concentrated solutions.

In order to use this method to estimate the specific heat capacity for $LiNO_3$ solutions, the critical temperature and pressure of the solution must be known as a function of concentration. No measurements for $LiNO_3$ salt appear to have been made, but data are available for many other salt solutions [68] and it has been found that many 1-1 electrolytes have very similar critical temperatures at the same molality. Since an extensive

data set is available for NaCl [69], these data have been used as a reasonable approximation for $LiNO_3$, although a large extrapolation has been made from the highest NaCl concentrations studied (6 mol/kg) to the most concentrated $LiNO_3$ solutions proposed.

Figure 16.2-16 shows the estimated critical temperature and pressure for $LiNO_3$ solutions. A rapid increase in the critical temperature and pressure with increasing salt concentration is evident from Figure 16.2-16, although the large extrapolation made for the higher concentrations makes these values rather uncertain. The possibility of operating an aqueous blanket at high temperatures (greater than 400 °C) is suggested by the increase in critical temperature, if the higher pressures can be tolerated and if suitable materials can be found for these conditions.

The data from Figure 16.2-16 have then been used to yield specific heat capacities of the aqueous salt solution, as illustrated in Figure 16.2-17. These data were evaluated for a pressure of 10 MPa, but the specific heat capacity varies by less than 1% for pressures up to 16 MPa, except for the case of pure water. Figure 16.2-17 shows an initial dramatic reduction in specific heat capacity as the salt is added to pure water, although there is little additional effect as the concentration is increased. The change in c_p is also offset somewhat by the associated increase in the density of the solution. It must be recognized that there is a large element of uncertainty in the specific-heat-capacity estimates, especially for the higher concentrations. This uncertainty is caused not only by the extrapolation made for the critical properties of the solution, but also by neglecting the contribution of the dissolved salt to c_p salt in the calculation. At low concentrations, this has little effect on the heat capacity of the solution, but as the weight fraction increases the contribution from the $LiNO_3$ becomes significant. The estimates presented here are, therefore, expected to be low for the higher concentrations.

16.2.3.4. Thermal conductivity

There appear to be no extensive experimental measurements of the thermal conductivity of $LiNO_3$ solutions for the temperature range of interest for fusion blankets. Data for NaCl are available, however, and Reference [70] gives smoothed values of experimental data for temperatures up to 330 °C and for concentrations up to 5 mol/kg. These data were extrapolated to 11 mol/kg ($A_{Li} \sim 5\%$) and a simple fit to the data was made. For higher concentrations, curve fits were used as the simple fit breaks down. The thermal conductivity of the solution, k ($W/m\,K$), is approximately given by

$$k = k_0 - (a - bm)m\,, \qquad (16.2\text{-}44)$$

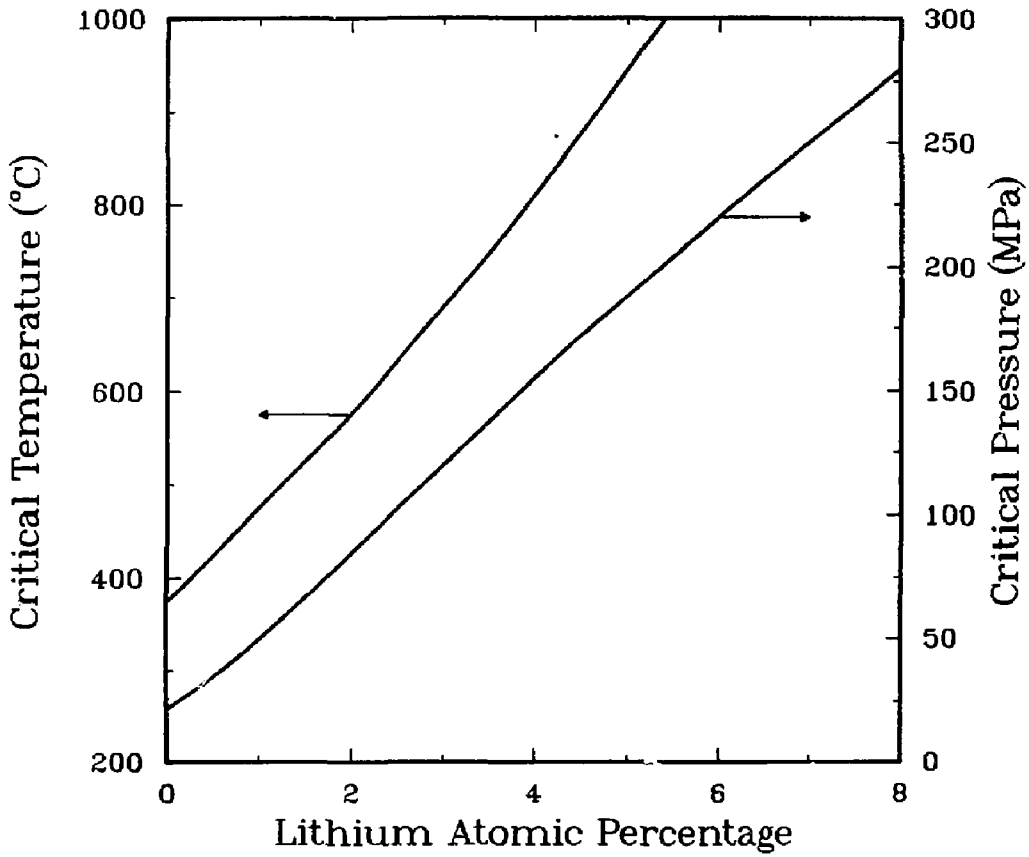

Figure 16.2-16. Critical temperature and pressure for $LiNO_3$ solutions as estimated from measurements for NaCl solutions.

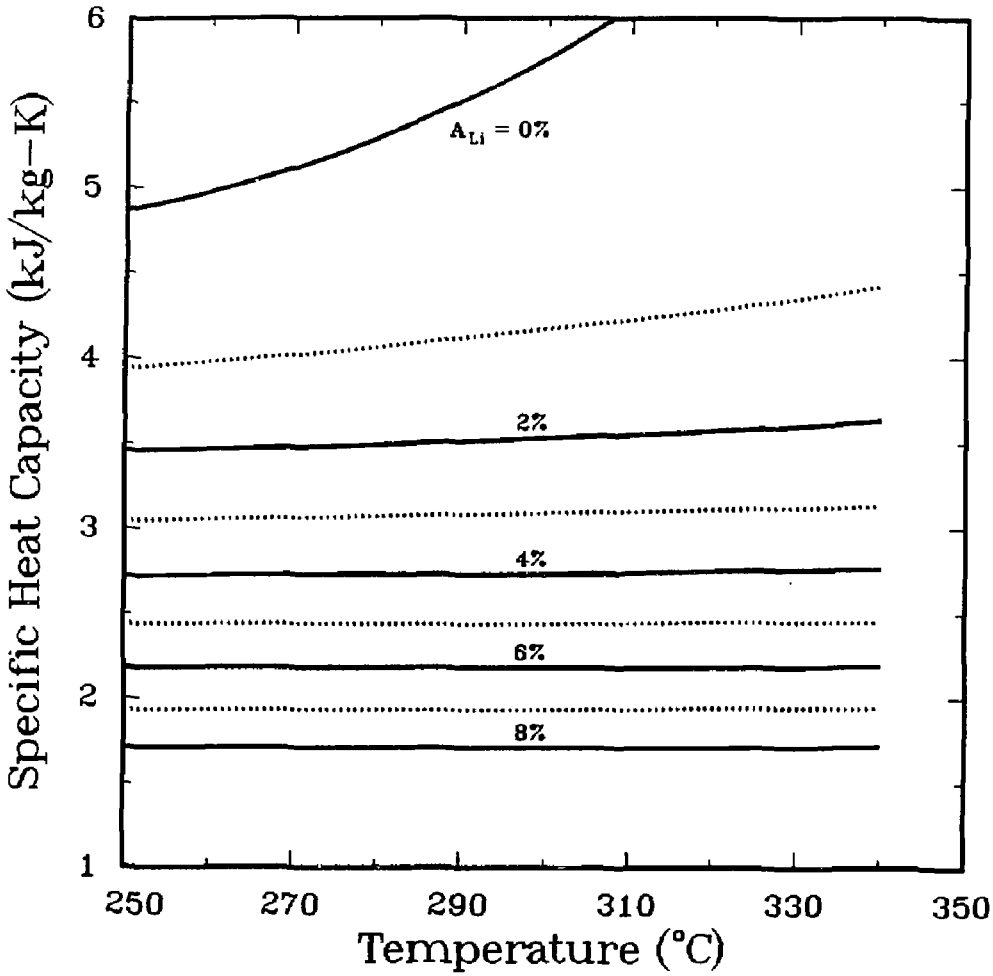

Figure 16.2-17. Specific heat capacity of $LiNO_3$ solutions at various temperatures and for a range of lithium-atom percentages.

$$a = 4.75 + 1.5 \times 10^{-2} T, \quad (16.2\text{-}45)$$

$$b = 0.185 + 5.0 \times 10^{-4} T, \quad (16.2\text{-}46)$$

where k_0 is the thermal conductivity of pure water, m is the molality in mol/kg, and T is the temperature in °C.

Estimates for the thermal conductivity are shown in Figure 16.2-18. These estimates suggest that the difference in the thermal conductivity of the solution compared with that of pure water is not as marked as for other properties. However, as the original NaCl data are not precise, and these results have been extrapolated to higher concentrations and applied to $LiNO_3$ solutions, the values shown here should be taken as indicative of the expected trends for the property rather than precise measurements. Further experimental data are required for a more exact assessment of the thermal performance of the coolant.

16.2.3.5. Boiling point

Reference [71] reported measurements of the vapor pressure of $LiNO_3$ solutions for concentrations up to 24 mol/kg and for temperatures up to 110 °C. Their results showed that the relative vapor pressure (the ratio of the vapor pressure of the solution to that of pure water) for a given concentration remained approximately constant, independent of changes in temperature. It has been assumed that this relationship is valid for higher temperatures, in the absence of relevant experimental data. The boiling point of the solution is then evaluated by finding the temperature at which the vapor pressure is equal to the applied pressure. Figure 16.2-19 shows these results for pressures ranging from 4 to 16 MPa. These estimates of the boiling point indicate that the boiling point of the $LiNO_3$ solution should be significantly higher than of pure water. For a lithium-atom percentage of 5%, the increase is 40 to 50 °C, which has a major effect on the thermal design of the fusion blanket.

Once again, a note of caution is necessary because the accuracy of these estimates is uncertain since an extrapolation was made from the lower temperature results. For example, LiOH solutions show a saturation in the boiling-point elevation with increasing concentration at higher temperatures [46], although this is caused by the association of the ions into LiOH molecules which is not expected to occur with $LiNO_3$. Further experimental data are clearly required.

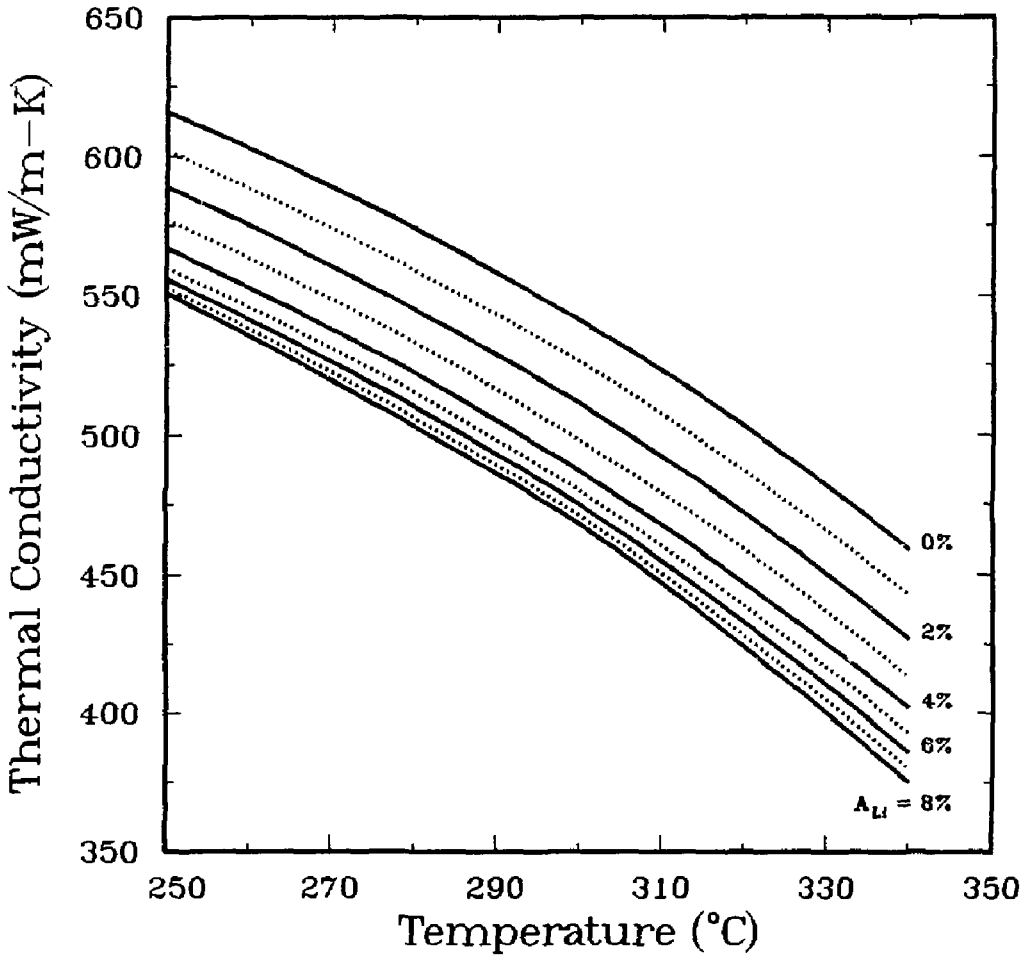

Figure 16.2-18. Thermal conductivity of $LiNO_3$ solutions at various temperatures and for a range of lithium-atom percentages.

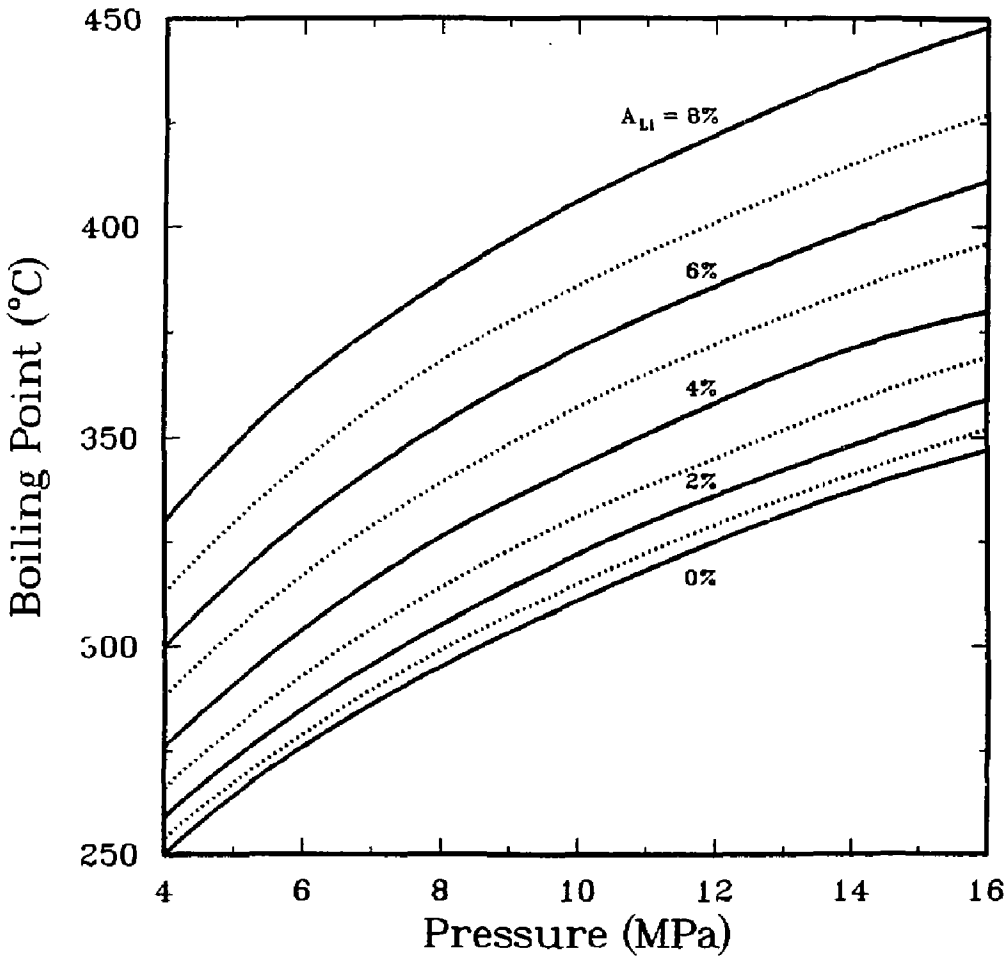

Figure 16.2-19. Boiling temperatures of $LiNO_3$ solutions at various pressures and for a range of lithium-atom percentages.

16.2.3.6. Discussion

The above estimates of the properties of $LiNO_3$ solutions at high temperatures exhibit marked differences from the properties of pure water. Therefore, the exact coolant conditions should be considered in designing the blanket. The thermal-hydraulic design of an aqueous salt blanket can be very different from that of a water-cooled design, and advantage can be taken of the differences in properties by, for example, reducing the coolant pressure or increasing the temperature without incurring an increased risk of burnout.

However, many of the estimates are extrapolations from experimental data or have been obtained from the results for other salt solutions. Although these predictions should give good indications of the expected trends for the various properties, a much expanded experimental data base is required for the salts and conditions proposed before the thermal performance of an aqueous salt blanket at high temperature can be confidently predicted.

16.2.4. *Structural Material*

One of the goals of the TITAN study has been to satisfy Class-C waste-disposal criteria [72] and achieve a high level of safety assurance. Among the low-activation candidate vanadium alloys, V-3Ti-1Si (the structural material for the TITAN-I design) had to be ruled out because of its poor water-corrosion resistance. Other vanadium alloys which contain chromium (*e.g.*, V-15Cr-5Ti) show excellent resistance to corrosion by water coolant but their properties are inferior to those of ferritic steels when helium-embrittlement effects are taken into account [73] (Section 10.2). Therefore, various steels were considered as TITAN-II structural material.

Irradiation of commercial steels in a fusion environment produces long-lived radioactive isotopes. Acceptable levels of activation for near-surface burial have been established by the U. S. Nuclear Regulatory Commission (U. S. – NRC). These limits are published in the U. S. Code of Federal Regulations, 10CFR61 [72]. The 10CFR61 list was compiled to establish concentration limits (Ci/m^3) for fission-reactor waste streams. In recent years, the 10CFR61 list of radionuclide concentrations have been augmented to include radionuclides important to fusion [74,75]. A list of limiting-specific activities for near-surface burial of all radionuclides with atomic numbers less than 84 was recently compiled by Fetter [76]. One should note that some discrepancies exist between Fetter's evaluations and those of 10CFR61. Furthermore, Fetter's evaluations includes nuclides

Table 16.2-XI.

10CFR61 CLASS-C DISPOSAL LIMITS OF SELECTED ALLOYING ELEMENTS OF STEELS [77]

Element	Product	Half-Life (y)	Disposal Limit (Ci/m^3)
N	^{14}C	5730	80
Ni	^{59}Ni	76000	220
	^{63}Ni	100	7000
Nb	^{94}Nb	20000	0.2
Mo	^{94}Nb	20000	0.2
	^{93}Mo	3500	30
W	^{192}Ir	241	1
	^{193}Pt	50	200000

not covered by the 10CFR61 code (Sections 13.7 and 19.5). Disposal limits of the major alloying elements used in commercial steels such as N, Ni, Nb, Mo, and W are listed in Table 16.2-XI [77].

Effort has been made to develop low-activation alloys by replacing those alloying elements that would not qualify for Class-C waste disposal with more suitable ones, without compromising mechanical properties. As a result of these reduced-activation-alloy studies, three steels have been produced: (1) Ti-modified 316 austenitic steels, (2) $2\frac{1}{4}$ Cr ferritic/bainitic steels, and (3) 9- to 12-Cr ferritic/martensitic steels. A major advantage of the ferritic steels over austenitics is their excellent resistance to void swelling. Figure 16.2-20 shows a comparison of the relative swelling rates of austenitic alloys with those of ferritic steels [78]. Furthermore, ferritic steels have a higher thermal-stress resistance compared to austenitic steels [77]. These characteristics prompted the choice of a ferritic steel as the structural material for the TITAN-II design.

Currently three major research institutions in the U. S. are developing and evaluating low-activation ferritic alloys [79]: Oak Ridge National Laboratory (ORNL), General

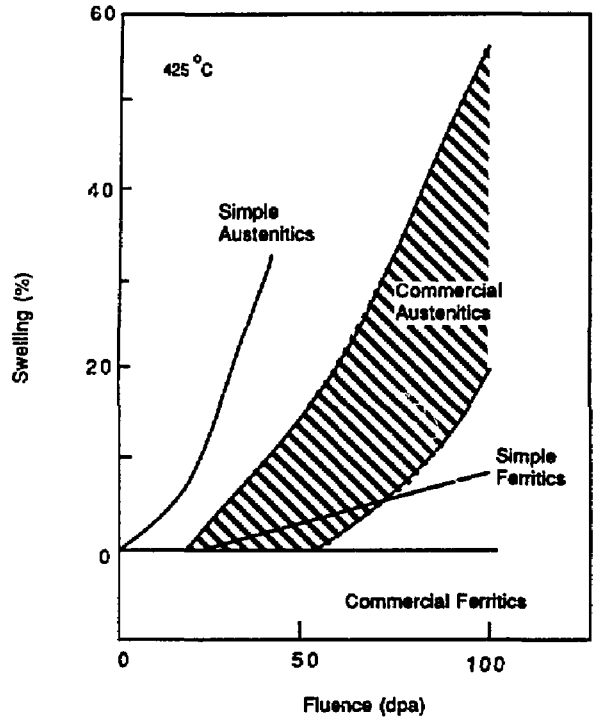

Figure 16.2-20. Comparison of swelling behavior of austenitic and ferritic steels [78].

Atomics (GA), and Hanford Engineering Development Laboratory (HEDL). The ORNL program has developed a series of low-chromium and 9%-12% Cr ferritic alloys termed fast-induced-radioactivity-decay alloys (FIRD). In the FIRD alloys, molybdenum is replaced by tungsten, which is in the same group as molybdenum. About 0.25 wt.% of vanadium is also added to increase the strength through vanadium-carbide formation. The low-chromium and 9-Cr steels were all 100% martensitic, while the 12-Cr steel contained about 26% delta-ferrite. The 12-Cr steel is, therefore, expected to have a lower hardness and a higher ductile-to-brittle transition temperature (DBTT) than the 100% martensitic steels. Tensile-behavior tests have verified the strengthening effect of vanadium and tungsten. The effects of irradiation on tensile properties of FIRD steels are being evaluated in specimens irradiated in the Fast-Flux Test Facility (FFTF) [79].

The GA program has concentrated on 9% and 12%-Cr ferritic alloys, referred to as GA3X and GA4X, respectively. Various combinations of Cr-W-V-C were developed and evaluated. The tungsten additions are as high as 2.5% and vanadium content is about

0.3%. A low-carbon concentration, below 0.15%, was chosen to ensure weldability. The low-vanadium concentration resulted in high $M_{23}C_6$ precipitate formation in tempered-steel samples. Generally, precipitate formation results in a decrease in elongation; the total elongation of the GA3X was found to be about 50% lower than that of its commercial counterpart alloy 9Cr-1Mo-V-W [80].

The emphasis of the HEDL program has been in replacing molybdenum with vanadium rather than with tungsten. These alloys are sometimes referred to as low-activation ferritic steels. To avoid delta-ferrite formation, manganese is added to the high-chromium alloys and carbon contents are kept very low (< 0.1 wt.%). To compensate for the effects of carbon as a solute strengthener, the manganese content had to be increased substantially ($\sim 6.5\%$ Mn). Compared with $2\frac{1}{4}$Cr-1Mo, the low-chromium bainitic alloy ($2\frac{1}{4}$Cr-V) has a lower yield strength, a slightly lower ultimate tensile strength, and a much higher elongation [79]. On the other hand, the 12-Cr martensitic alloys show a higher strength with comparable elongation when compared with commercial 12Cr-1Mo-V-W steels [79].

The effects of irradiation on the low- and high-chromium alloys were also investigated [2] and the latter alloys were found to be superior. Under irradiation, the $2\frac{1}{4}$Cr-V alloys showed an increase in strength and a reduction in elongation, while the 9 to 12Cr-Mn-V-W alloys exhibited only small changes in strength and elongation after irradiation at 420 °C and damage doses up to 10 dpa [2]. The radiation-hardening resistance of high-chromium alloys is also significantly different from commercial high-chromium ferritic steels such as 9Cr-1Mo-V-Nb and 12Cr-1Mo-V-W (HT-9) [79,81].

Some data on irradiation behavior of the low-activation ferritic steels are available. Specimens were irradiated up to 14 dpa in the FFTF and post-irradiation tests were performed at room temperature. Figure 16.2-21 shows a comparison of the yield strength and total elongation of low-activation ferritic steels as a function of irradiation temperature (values on the vertical axis corresponding to the unirradiated specimen). Figure 16.2-21 shows that $2\frac{1}{4}$Cr-V alloys experience an increase in strength of about 200 MPa when irradiated at 420 °C. At 585 °C, however, these alloys show a reduction of strength compared with unirradiated alloys. The high-chromium alloys show much smaller irradiation-hardening effects at 420 °C. A reduction in strength at 585 °C is also experienced by the high-chromium alloys, but the decrease is not as much as that of the low-chromium alloys. The 12Cr-0.3V-1W-6.5Mn martensitic steel shows the smallest degree of irradiation hardening and the lowest decrease in strength of all tested alloys. Figure 16.2-21 also shows the total elongation of the tested specimen. Again 12Cr-0.3V-1W-6.5Mn martensitic steel shows the smallest fluctuations in total elongation among all tested alloys.

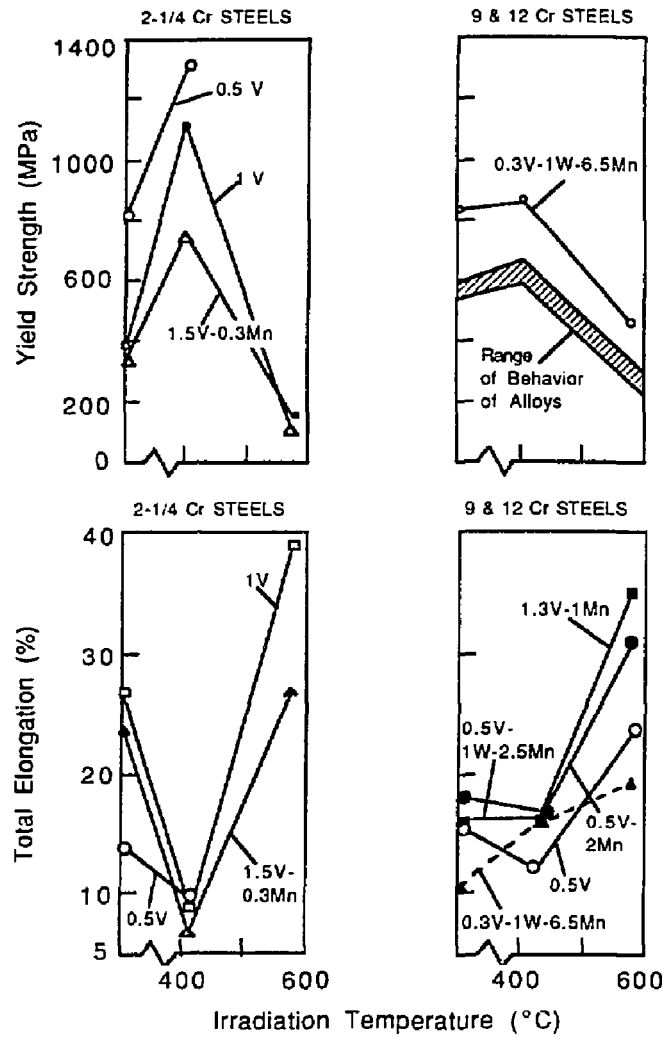

Figure 16.2-21. Results of uniaxial-tensile tests of HEDL low-activation ferritic alloys [79]. The yield strength and the total elongation are plotted as a function of the irradiation temperature. The values on the vertical axis denote the corresponding values for an unirradiated specimen.

The ductile-to-brittle transition temperature (DBTT) of some ferritic alloys may be a potential problem. The DBTT is the temperature at which the fracture stress is reached during loading of a specimen prior to the onset of the yield. When a specimen is loaded at a temperature below the DBTT, a brittle-type cleavage fracture occurs, while at temperatures above the DBTT the metal undergoes yielding before fracture occurs. Figure 16.2-22 shows changes in DBTT of 9Cr-1Mo-W-Nb and 12Cr-1Mo-W-V (HT-9) irradiated to damage levels of up to 30 dpa as a function of irradiation temperature. The change in DBTT is highest at low irradiation temperatures, and vanishes when irradiation temperatures exceed 600 °C. The commercial 9-Cr alloy shows overall smaller increases in DBTT when compared with HT-9. Recently, Lechtenberg [82] investigated the DBTT of the reduced-activation 9Cr-2W-0.15C stabilized martensitic steel. The DBTT of the unirradiated specimen was -24 °C. When irradiated at 356 °C to damage dose of 10.5 dpa, the DBTT increased to about 0 °C. The measured increase on DBTT of 24 °C is the

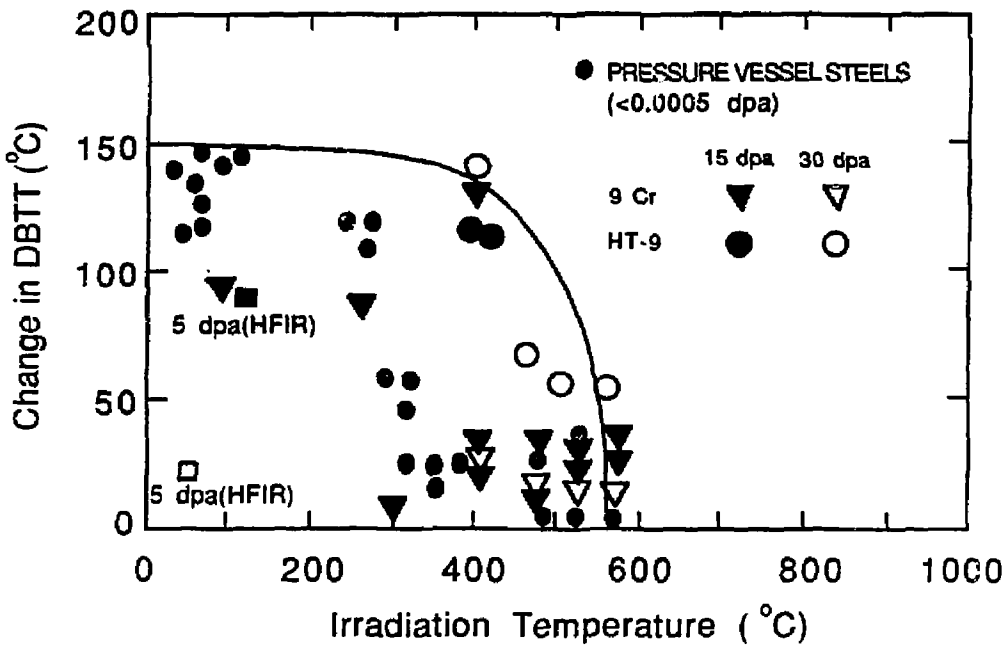

Figure 16.2-22. Change in the DBTT as a function of irradiation temperature for 9Cr-1Mo-W-Nb and HT-9 ferritic steels [82].

smallest increase reported among all the low-activation ferritic alloys studied. The DBTT of tested ferritics clearly indicates a potential problem. Until alloy-development efforts alleviate this problem, operating conditions must be chosen to minimize the rise in DBTT of ferritic steels.

16.2.4.1. Discussion

The TITAN-II FPC is cooled by a aqueous lithium-salt solution which also acts as the breeder material [1]. Among the low-activation candidate vanadium alloys, V-3Ti-1Si (the structural material for the TITAN-I design) had to be ruled out because of its poor water-corrosion resistance. Other vanadium alloys which contain chromium (*e.g.*, V-15Cr-5Ti) show excellent resistance to corrosion by water coolant but their properties are inferior to those of ferritic steels when helium-embrittlement effects are taken into account [73] (Section 10.2). Therefore, various steels were considered as TITAN-II structural material.

Reported results of the low-activation ferritic-steel development program indicate that a reduced-activation alloy can be developed without compromising mechanical properties, primarily by replacing Mo with W. However, recent evaluations of radionuclides produced from tungsten alloys indicate that W may be a potential activation-limited element [83]. Nevertheless, it should be possible to develop low-activation ferritic steels.

For the TITAN-II reactor, the HEDL/UCLA 12Cr-0.3V-1W-6.5Mn alloy (9-C) has been chosen as the structural material, primarily because of its high strength and good elongation behavior after irradiation as compared with other low-activation ferritic steels. The high-chromium content of this alloy ensures an excellent corrosion resistance, as is discussed in detail in Section 16.2.1. The low carbon content of this alloy results in good weldability, high sensitization resistance (Section 16.2.1.1), and a reduction of hydrogen-embrittlement susceptibility (Section 16.2.5). Furthermore, alloy 9-C has a low tungsten content ($< 0.9\%$) which reduces the waste-disposal concerns of the production of the radionuclide ^{186m}Re by fusion-neutron reaction with W. The high concentration of manganese in 9-C prevents the formation of delta-ferrite phases, which is responsible for high DBTT and low hardness

Table 16.2-XII shows selected properties of the 9-C alloy which was used throughout the TITAN-II study. The composition (wt.%) of the 9-C alloy was determined by the vendor as: 11.81Cr, 0.097C, 0.28V, 0.89W, 6.47Mn, 0.11Si, 0.003N, $<$ 0.005P, and 0.005S with balance in iron.

Table 16.2-XII.

PHYSICAL AND MECHANICAL PROPERTIES OF ALLOY 9-C LOW-ACTIVATION FERRITIC STEEL [2]

Property	Temperature (°C)				
	RT	300	400	500	600
Young's modulus (GPa)	225	200	193	180	150
Poisson ratio	0.4	0.4	0.4	0.4	0.4
Shear modulus (GPA) [a]	83	75	72	68	-
Tensile strength (MPa)	1002	-	810[a]	942[b]	749[c]
Yield strength (MPa) [c]	810	810	820	650	531
Total elongation (%) [c]	10.1	13.8	15.0	17.0	19.4
Thermal-expansion coefficient (10^{-6}/°C)	9.5	10.5	11.0	11.5	12.0
Specific heat (J/kg-°C)	450	570	600	680	780
Electric resistivity ($\mu\Omega$ m)	0.6	0.82	0.9	0.99	1.05
Thermal conductivity (W/m-K)	25	26.5	26.7	27.2	27.6
DBTT at 15 dpa (°C) [a]	-	-	100	25	0
DBTT at 30 dpa (°C) [a]	-	-	140	50	55

(*a*) Data unavailable, corresponding values for HT-9 were used.

(*b*) Values at irradiation temperatures after 6 dpa.

(*c*) Values at irradiation temperatures after 14 dpa.

16.2.5. Hydrogen Embrittlement

Interaction of hydrogen with metals can lead to one of the many forms of failures collectively termed "hydrogen damage." The term "hydrogen embrittlement" has been used freely in the past to describe any one of the many forms of hydrogen damage. Specific types of hydrogen damage have been categorized by Craig [84] based on the following property degradation processes.

Hydrogen environment embrittlement. This failure mode occurs during the plastic deformation of stressed alloys exposed to hydrogen-bearing gases or during hydrogen-producing corrosion reactions. Experiments show that steels, nickel-base alloys, and titanium alloys are most susceptible to this mechanism when the strain rate is low and the hydrogen pressure and purity is high.

Hydrogen stress cracking. Normally, ductile alloys can fail by brittle fracture under sustained loads in the presence of hydrogen. Hydrogen stress cracking starts by absorption of hydrogen. The hydrogen then diffuses into regions of high triaxial stresses. The diffusion and agglomeration manifests itself in a delayed time-to-failure (incubation time). Furthermore, this failure mode is often characterized by a threshold stress below which hydrogen stress cracking does not occur. The threshold stress generally decreases as the yield strength and tensile strength of an alloy increase. Thus, hydrogen stress cracking is not seen very often in low-strength alloys.

Loss in tensile ductility. Lower-strength alloys exposed to hydrogen can show a marked reduction in area (*i.e.*, loss of ductility during tensile-stress tests). The extent of loss in ductility is a direct function of the hydrogen content of the metal.

Hydrogen attack. Hydrogen may enter the steel and react with carbon to form volatile methane gas. The alloy undergoes decarburization and shows marked crack formations. This form of hydrogen damage is a high-temperature (T >200 °C) process that occurs in carbon and low-alloy steels exposed to high-pressure hydrogen. Although the limits of alloy content for certain groups of steels are not well defined, it is assumed that a "low-alloy" steel is one having less than 12% total alloy content; above that level the term *stainless steel* is used [85].

Blistering. In low-strength alloys, atomic hydrogens can be trapped at internal defects and consequently form molecular hydrogen (H_2). Localized plastic deformation can occur when the pressure of the H_2 gas reaches a large value, leading to blistering and can cause rupture.

Shatter cracks. Melts of alloys possess a higher hydrogen solubility than the solids. Therefore, during forging, welding, and casting, hydrogen pickup is increased. When the melt cools down, the solubility of hydrogen decreases and results in an agglomeration of hydrogen at internal trap sites. The effects of this process are similar to those of blistering.

Micro-perforation. Steels exposed to very high hydrogen pressures at near room temperature often show the formation of networks of fissures. Consequent exposure to gases or liquids will result in a rapid permeation of the alloy.

Degradation in flow properties. The interaction of atomic hydrogen with dislocations can enhance the dislocation motion and also create dislocations at surfaces or crack tips, leading to softening of the material on a localized scale. This enhanced plastic flow has been found at ambient temperatures for iron and steels and is observed as an increase in the steady-state creep rate.

Hydride formation. Atomic hydrogen can react with metals to form corresponding hydrides (MH_x). Precipitation of metal-hydride phases results in the degradation of the mechanical properties and cracking in magnesium, tantalum, niobium, vanadium, uranium, thorium, zirconium, titanium, and their alloys. Hydride formation is enhanced under stress and leads to an increase in hydrides around the crack tip, resulting in a degradation of ductility near crack-tip regions.

Hydrogen embrittlement encompasses only the first three of the above-mentioned processes: hydrogen environment embrittlement, hydrogen stress cracking, and loss in tensile ductility. Hydrogen embrittlement is caused primarily by the atomic, diffusible, or nascent hydrogen (H) content, and not by those processes caused by the total hydrogen content which may also include molecular hydrogen (H_2). In a non-nuclear environment, there are three sources of hydrogen: steel manufacturing, corrosion in aqueous solutions

(cathodic reactions generate hydrogen atoms at the metal surface), and in-service environment. A fourth source of hydrogen is added when metals and alloys are exposed to neutron irradiation. Hydrogen is generated as a result of (n,p) nuclear reactions. Furthermore, the metal or alloy must also be under an externally applied stress for a specific type of hydrogen damage to be termed hydrogen embrittlement. There are three sources of stress: applied stress, residual stress from heat treatment, and residual stress from welding or plastic deformation. These sources of stress further complicate the identification of a specific cause of hydrogen embrittlement.

To minimize hydrogen embrittlement, the following classification is helpful: (1) internal, reversible hydrogen embrittlement, and (2) hydrogen-reaction embrittlement [86]. For hydrogen embrittlement to be fully reversible, it must occur without the hydrogen undergoing any type of chemical reaction within the lattice. By relieving the applied stress and by aging steels at room temperature, ductility can be restored if micro-cracks have not yet developed. Hydrogen-reaction embrittlement, on the other hand, is generally not reversible by aging at room temperature. After having been absorbed, hydrogen can react near the surface or diffuse further into the lattice before undergoing a reaction. Hydrogen can react with itself to form H_2, with the matrix to form a metal hydride (MH_x), or with foreign elements in the matrix to form a gas (CH_x). In carbon and low-alloy steels, the primary gas formed is methane (CH_4). The volatility of the methane gas leads to the process known as decarburization. Hydrogen can also react with oxygen to form steam (H_2O) inside the matrix. Copper alloys are highly susceptible to steam formation which results in blistering and porous metal components [86].

Much confusion exists in the relationship between stress-corrosion cracking (SCC) and hydrogen embrittlement because the crack-growth mechanism of both processes is the same. For SCC to occur, the crack has to be in contact with the aqueous solution. During the corrosion process in aqueous solutions, atomic hydrogen is generated and is then absorbed by the crack tip. Stress-corrosion cracking is, therefore, a special case of hydrogen embrittlement in which hydrogen is produced by the corrosion process occurring inside the crack.

16.2.5.1. Hydrogen embrittlement of ferrous alloys

During 1960s, the National Aeronautics and Space Administration (NASA) experienced failure of ground-based hydrogen-storage tanks. Because of these failures and the anticipated use of hydrogen in advanced rocket and gas turbines, hydrogen environment embrittlement was recognized as a serious problem and NASA initiated research efforts

in these areas. Conferences on the subject of hydrogen embrittlement are held frequently, mostly sponsored by the National Association of Corrosion Engineers (NACE) and published under the International Corrosion Conference series [87]. As a result of the research efforts over the past decades, factors influencing hydrogen embrittlement in various alloys have been identified. The following is a summary of important factors in ferrous alloys. More detailed discussions are given in References [84-90].

The primary factors that affect the behavior of ferrous alloys in a hydrogen-bearing environment are: (1) hydrogen concentration, (2) temperature, (3) heat treatment, (4) microstructure, (5) stress level, and (6) environment. The tendency for hydrogen embrittlement to occur increases with hydrogen concentration in the metal. Figure 16.2-23 shows that after a given length of time, cracking occurs at successively higher stresses as the hydrogen content in the metal is reduced by the baking treatment [91]. In general, increasing the concentration of hydrogen in an alloy will reduce the time-to-failure and the stress levels at which failure occurs [84].

Hydrogen concentration inside the alloy is generally a function of many factors such as the approximate concentration of hydrogen at the surface exposed to the environment, hydrogen-adsorption characteristics of the surface, and amount of trapped hydrogen inside the matrix. Trapping occurs by binding hydrogen to impurities or structural defects. Structural traps may be mobile (*e.g.*, dislocations and stacking faults) or they can be stationary (*e.g.*, voids, grain boundaries, carbide particles, and solute atoms). The trapping at structural defects is believed to be the major cause of increased hydrogen embrittlement in heavily cold-worked ferritic steels. The microstructure of the alloy can have a profound effect on the resistance of steels to hydrogen embrittlement. A quenched and tempered fine-grain microstructure is more resistant to cracking than a normalized steel [92]. The effect of the grain size on the resistance to hydrogen embrittlement is illustrated in Figure 16.2-24 which shows that as the grain size of an alloy is reduced, the resistance to hydrogen damage is increased.

Another microstructural feature which affects hydrogen embrittlement is the concentration of precipitate particles (trap sites) dispersed in the alloy. Measurements of the effective diffusion coefficient of hydrogen as a function of precipitate particles (Figure 16.2-25) show a marked decrease in the diffusion of hydrogen with an increased concentration of particles [93]. The apparent diffusion coefficient is an indirect measure of the trapping strength of the matrix since, once trapped, a diffusing species must undergo de-trapping before diffusion can proceed. In general, the most resistant microstructure is a highly tempered martensitic structure with equiaxed ferrite grains and spheroidized carbides evenly distributed throughout the matrix [84].

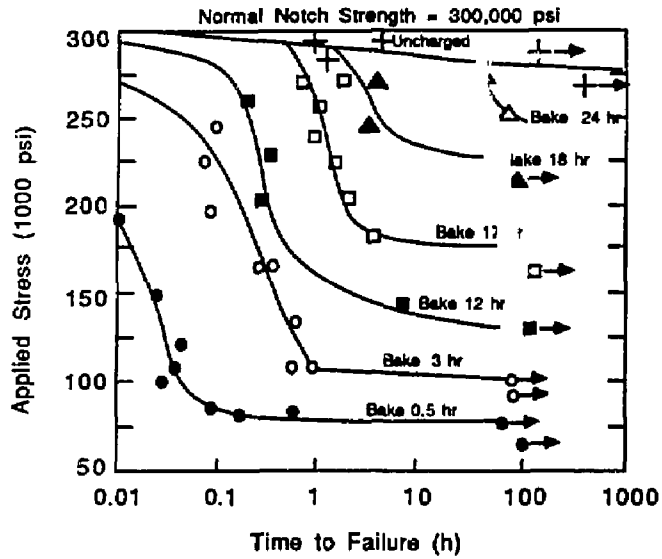

Figure 16.2-23. Static fatigue curves of AISI 4340 steels for various hydrogen concentrations obtained by different baking times at 150 °C. Arrows indicate very long time-to-failure [91].

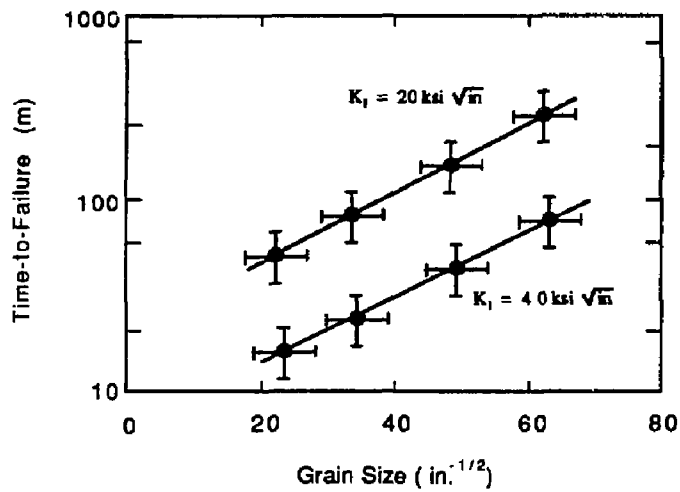

Figure 16.2-24. Effects of grain size on the resistance of AISI 4030 steels to hydrogen failure [92].

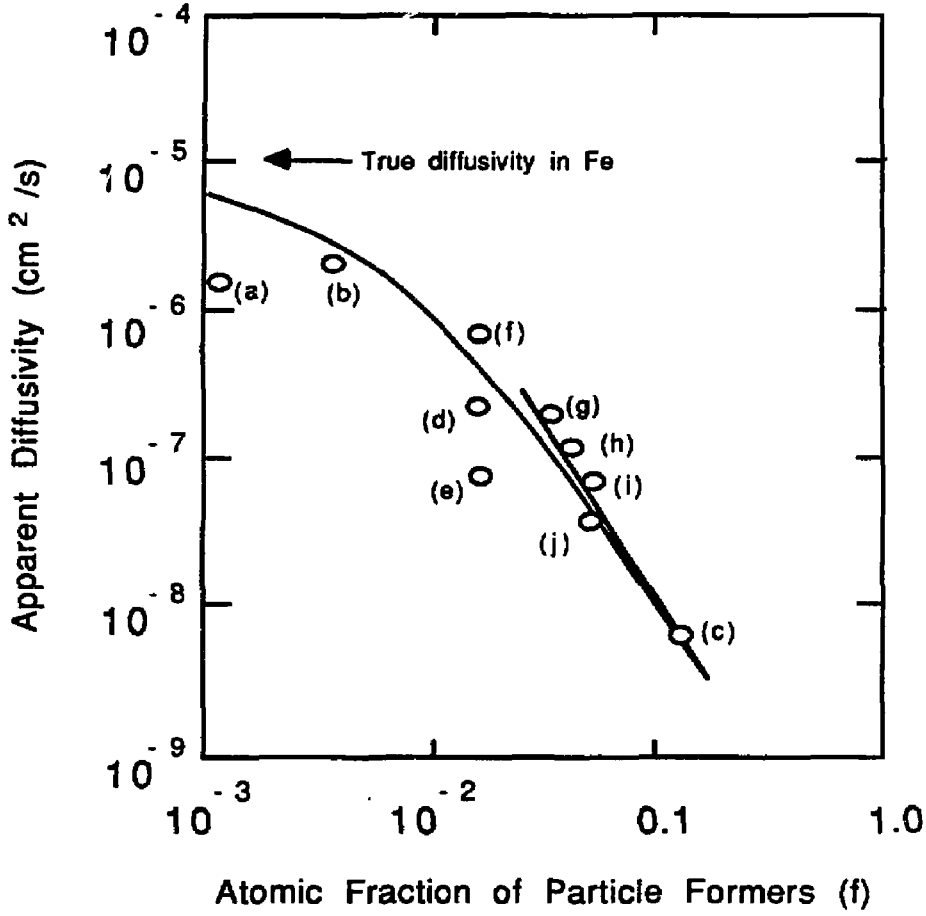

(a)	Fe-5.6% Cr	(f)	Ni-Cr-Mo
(b)	Fe-1.5% Mn	(g)	4340
(c)	Fe-0.73% C	(h)	HP-9Ni-4Co
(d)	Fe-1.1%Mn	(i)	D6aC
(e)	Fe-1.1%Mn	(j)	H-11

Figure 16.2-25. The apparent hydrogen diffusivity of various alloys as a function of the fraction of precipitate particles [93].

The effects of various elements on hydrogen embrittlement have also been studied in great detail. In general, elements such as carbon, phosphorus, sulfur, manganese, and chromium increase the susceptibility of low-alloy steels to hydrogen embrittlement. For stainless steels (high alloys), large amounts of elements such as chromium, nickel, and molybdenum are needed for manufacturing. The atom fractions of these elements in stainless steels are large enough to change the crystal structure, microstructure, and the heat treatment requirements. Since hydrogen embrittlement is sensitive to the microstructure, stainless steels with large atom fractions of Cr, Ni, and Mo, such as 15Cr-25Ni, also show almost no loss in ductility while 304 L stainless steels are the most susceptible to loss of tensile ductility when exposed to hydrogen environments [84].

The susceptibility of stainless steels to hydrogen embrittlement is also directly related to its strength. Stainless steels show extremely low resistance to hydrogen embrittlement with increasing yield strength as shown in Figure 16.2-26 for AISI 4340 steel in aqueous and gaseous hydrogen [94]. Data in Figure 16.2-26 indicate that the threshold stress intensity for crack growth generally decreases with increasing yield strength. The reason for this stress behavior is not entirely clear but it has been related to a change in hydrogen-assisted failure modes, with blistering becoming the dominant failure mechanism for low-strength steels.

Ferritic steels show an excellent resistance to hydrogen embrittlement because of their enhanced ductility and lower strength characteristics [28]. By examining a wide range of ferritic alloys that had undergone different heat treatments, Bond *et al.* [28] concluded that ferritic steels can be embrittled only after severe and extensive hydrogen charging from aqueous solutions. Furthermore, they concluded that cracking is intensified by welding, high-temperature heat treatment, and cold working. The chemical composition of the alloys was found to be less important under conditions of hydrogen charging.

The effect of temperature on hydrogen embrittlement has been investigated in detail. Hydrogen embrittlement has been observed in ferrous alloys over a wide range of temperatures, −100 to +700 °C. However, the most severe embrittlement in steels occurs around room temperature [96 - 99]. The temperature dependence of the tensile strength of a high-strength steel is shown in Figure 16.2-27. At very low (−100 °C) or very high (700 °C) temperatures, the tensile strength of a hydrogen-charged steel approaches the values of a hydrogen-free sample [95]. This temperature dependence can be explained by noting that at high temperatures, thermal agitation may cause de-trapping of a hydrogen atom which will then diffuse rapidly through the matrix. The combination of these two effects, a higher de-trapping rate and a higher mobility, results in a low hydrogen concentration at high temperatures. At very low temperatures, on the other hand, the

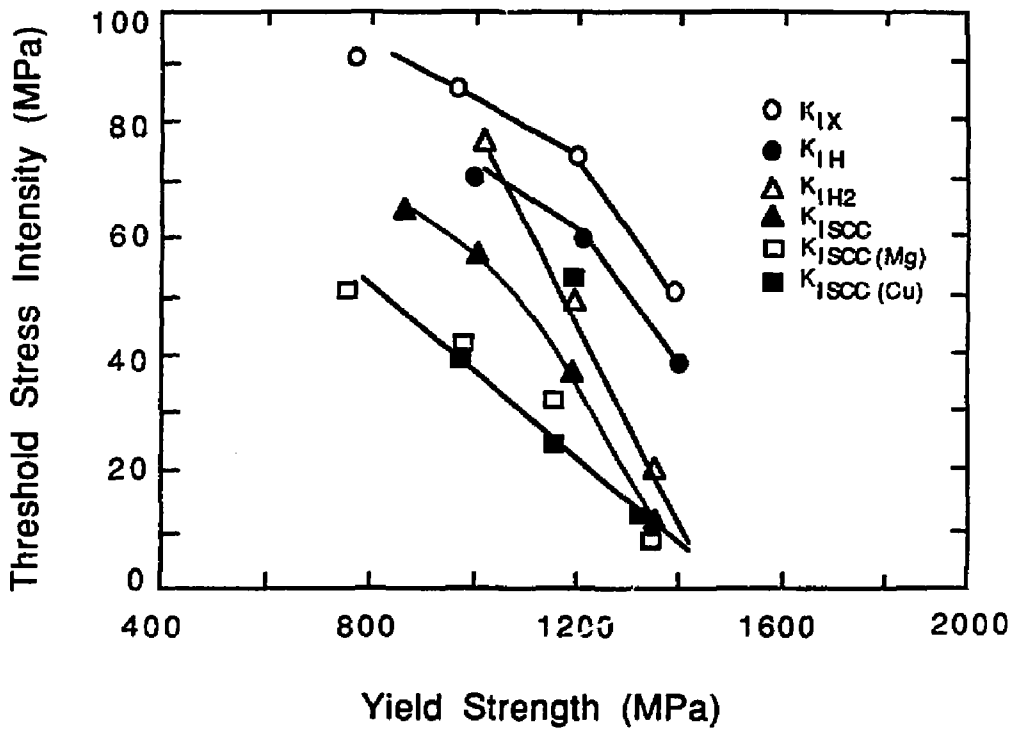

Figure 16.2-26. Effect of yield strength on some threshold stress intensity parameters for crack growth in a commercial AISI 4340 plate [94]. Here, K_{Ix} is the threshold stress intensity measured in air, K_{IH} and K_{IH_2} are for tests in gaseous hydrogen atmosphere, K_{Iscc}, K_{Iscc} (Mg), and K_{Iscc} (Cu) are for tests in aqueous solutions which are contact free, or are in contact with magnesium or copper, respectively.

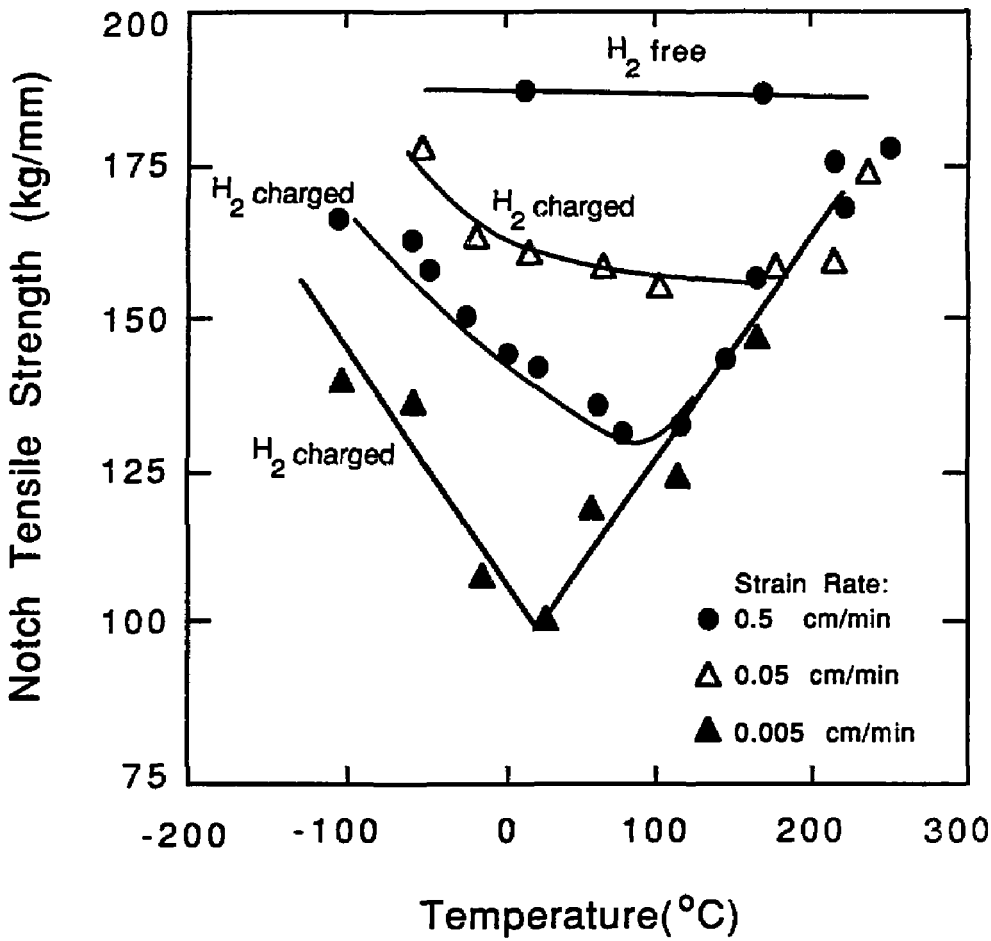

Figure 16.2-27. Tensile strength of a high-strength steel as a function of testing temperature for three strain rates [95].

diffusivity of hydrogen atoms is reduced to such a small value that trap sites would not be filled.

Figure 16.2-27 also shows that hydrogen embrittlement is highly sensitive to the strain rate. At a very high strain rate, the cracking proceeds without the assistance of hydrogen. The hydrogen mobility is not sufficient to maintain a hydrogen atom cloud around the moving dislocations. At a low strain rate, crack propagation is slow enough to keep the hydrogen concentration around the moving dislocations at levels that influence cracking. Cracking that is influenced by the presence of hydrogen falls into the category of stress-corrosion cracking (SCC). The tendency of an alloy to undergo SCC decreases with increasing temperature and drops significantly above 70 °C. Except in corrosion reactions involving hydrofluoric acid or hydrogen sulfide, SCC is usually not a problem with steels having a yield strength below 1,000 MPa [100].

16.2.5.2. Hydrogen-embrittlement prevention

The main cause of hydrogen embrittlement is the penetration of hydrogen into a metal or alloy. Techniques for in-service hydrogen-embrittlement prevention generally focus on either eliminating the source of hydrogen or minimizing stresses to below the threshold values necessary to cause cracks. For nuclear components, however, the hydrogen source from (n,p) reactions can never be totally eliminated. Nevertheless, hydrogen embrittlement may be mitigated or prevented by application of one or more of the following preventive measures.

Reducing corrosion rates. Corrosion of metals or alloys in aqueous solutions is always accompanied by the evolution of hydrogen at the surface of the metal. Corrosion-prevention measures are discussed in detail in Section 16.2.1.2. These include changes in the corrosive medium such as removing oxides or adding carefully selected inhibitors. Table 16.2-IV includes a reference list of corrosion inhibitors.

Baking. Hydrogen embrittlement is an almost fully reversible process, especially in low-carbon steels, if no hydrogen damage has yet occurred. If the hydrogen is removed, the mechanical properties of the treated material are only slightly different from those of hydrogen-free steels. Although a common way of removing hydrogen is by baking at relatively low temperatures (200 to 300 °F), high service temperatures will also ensure minimal hydrogen entrapment inside the matrix. Trapping of hydrogen atoms decreases

as the service temperature is increased above 200 °C. High-temperature hydrogen attack (*i.e.*, decarburization due to volatile CH_4 formation) is a major concern only for high-carbon or low-alloy steels.

Alloy selection. Hydrogen embrittlement strongly depends on the strength of the alloy and high-strength steels are the alloys which are most susceptible to hydrogen embrittlement. Low-strength alloys ($\sigma_Y < 1000$ MPa) are the least susceptible to hydrogen embrittlement. Furthermore, alloying elements such as nickel and molybdenum reduce the susceptibility to hydrogen embrittlement [3].

Reduction of SCC by deaeration of boiler water. Experiments with the addition of hydrogen to water in BWRs has shown that SCC can be reduced markedly (Section 16.2.1.3).

In summary, aeration (the presence of dissolved oxygen in a liquid medium) may have profound influence on the corrosion rate of metals. Some metals and alloys are more rapidly attacked in the presence of oxygen, whereas others may show better corrosion resistance. For example, deaeration of boiler water results in a marked decrease in the corrosion of steels and cast irons. The addition of hydrogen results in a deaeration or reduction of oxygen content of the water, leading to a decrease in corrosion rate [13, 23-26]. These experiments demonstrate the different effects between nascent (monatomic, adsorbed, and diffusible) hydrogen and molecular (H_2) hydrogen. While nascent hydrogen increases SCC, molecular hydrogen decreases SCC because of recombination with dissolved oxygen.

Petrochemical plants expose metals to high temperatures and high hydrogen pressures (hydrogenation processes). The dissociation of molecular hydrogen under conditions of high pressure and high temperature is a major source of diffusible hydrogen. The reaction of hydrogen with carbon has been identified as the main cause of hydrogen embrittlement in hydrogenation processes. The petrochemical industry has adopted a practical solution to this problem by using low-alloy steels. These steels contain carbon stabilizers such as chromium, molybdenum, tungsten, vanadium, titanium, and niobium. In addition to altering the microstructure of the alloy, these alloying elements also reduce the reactivity of carbon with absorbed hydrogen. Experience in the petrochemical industry has resulted in the development of "Nelson curves" [101] which prescribe the acceptable limits of temperature and hydrogen partial pressure for common low-alloy steels. An example of these curves is shown in Figure 16.2-28. It can be seen that a higher chromium content

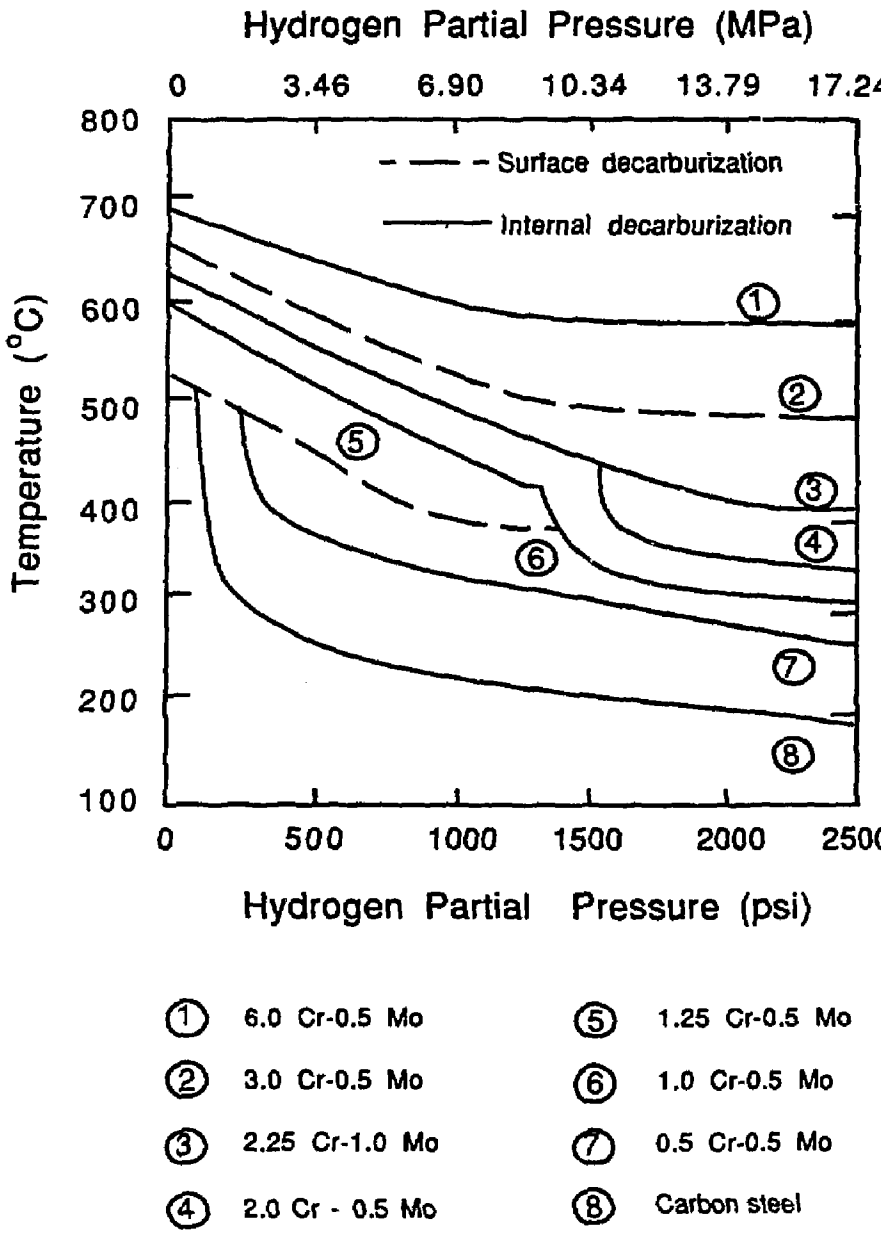

Figure 16.2-28. Operating limits (Nelson curves) for steels in hydrogen service [100].

allows higher temperatures and higher hydrogen partial pressures. The worst case is that of regular carbon steel.

16.2.5.3. Discussion

Hydrogen embrittlement is an important phenomena caused mainly by the trapping of absorbed hydrogen in metals under applied stresses. The main factor influencing hydrogen embrittlement is the hydrogen content which depends strongly on the temperature, microstructure, and strength of the alloy. Hydrogen content can be reduced by minimizing the source of nascent hydrogen (mostly due to corrosion) and by operating at high temperatures ($> 200\,^{\circ}C$), provided that a low-carbon steel is used. High concentrations of chromium, nickel, or molybdenum (> 10 wt%) increase the resistance of ferrous alloys to hydrogen damage. Microstructural features such as a fine-grained and annealed alloy with minimum cold work further reduce susceptibility to hydrogen embrittlement. B cause of the lower strength and higher ductility of ferritic steels, these alloys are generally less susceptible to hydrogen embrittlement than austenitic steels.

The low-activation, ferritic steel 9-C is chosen as the reference structural material for the TITAN-II FPC (Section 16.2.4). The 9-C alloy contains very small amounts of carbon (≤ 0.097 wt.%), but has a high concentration of carbon-stabilizing elements (≥ 11 wt.% Cr, 6 wt.% Mn, 0.28 wt.% V, and 0.89 wt.% W). Furthermore, the addition of nitrate salts to the aqueous solution reduces the corrosion rate of ferrous alloys (Section 16.2.1.2), resulting in a reduction in the production of hydrogen atoms on the surfaces, thus reducing the nascent hydrogen content.

The production of hydrogen by nuclear reactions and by plasma-driven permeation through the first wall of a fusion device increases the hydrogen content inside the alloy matrix which may lead to unacceptable hydrogen embrittlement of the structure for operation at or near room temperature (the highest susceptibility of high-strength alloys to hydrogen embrittlement is at or near room temperature [100]). But the TITAN-II structural material operates at high temperatures ($> 400\,^{\circ}C$), minimizing the effective trapping of hydrogen inside the matrix. Experiments show that above $\sim 200\,^{\circ}C$, hydrogen embrittlement of ferrous alloys is reduced markedly [3]. Furthermore, the Nelson curves indicate that 2.0 Cr-0.5 Mo steel can operate at $400\,^{\circ}C$ with a hydrogen partial pressure of 17 MPa without internal decarburization and hydrogen embrittlement (Figure 16.2-28).

Based on the above discussion, the ferritic alloy 9-C is expected to exhibit a high resistance to hydrogen embrittlement. The number of factors influencing hydrogen embrittlement are numerous and their interdependence is a complex function of the specific

microstructure and operating conditions of an alloy. Therefore, experimental data are needed in order to perform a complete evaluation of hydrogen embrittlement of the 9-C alloy under TITAN-II operating conditions.

16.2.6. Neutron-Multiplier Material

Beryllium is chosen as the neutron-multiplier material for the TITAN-II design mainly because of low activation. Concerns associated with beryllium are toxicity, resource limitation, and radiation damage. In this section, properties of beryllium are presented (Section 16.2 6.1) and the available data on corrosion of beryllium by the aqueous solution is reviewed (Section 16.2.6.2). Section 16.2.6.3 discusses the irradiation behavior of beryllium.

16.2.6.1. Properties

Selected properties of beryllium are given in Table 16.2-XIII. Mechanical properties of beryllium at elevated temperatures depend on the microstructure and composition (purity). Ultimate tensile and yield strengths of typical commercial beryllium (low purity) are given in Table 16.2-XIV. The average grain size of the tested beryllium was 16 μm with the principle impurities being: 200 appm oxygen, 620 appm argon, 1380 appm iron, 500 appm silicon, and 220 appm titanium.

16.2.6.2. Beryllium corrosion

The two areas of concern regarding beryllium in a fusion environment are swelling and corrosion. Beryllium that is clean and free of surface impurities (in particular carbonates and sulfates) has exceedingly good resistance to attack in low-temperature, high-purity water [102], with typical corrosion rates of less than 1 mil/y [103]. In a slightly acidic demineralized water of a nuclear test reactor, beryllium has performed without problems for over 10 years [104,105].

Beryllium exposed to chloride and sulfate-contaminated aqueous solutions is susceptible to attack. Development of corrosion-protective coatings for beryllium has been extensive [104]. Extremely thin (100 Å) chromate coatings produced by simple dip treatments have shown to hold up under 5% salt spray tests for a period of 120 h [106]. With anodized coatings, no corrosion was detected after 2000-h exposure in ASTM salt-spray

Table 16.2-XIII.

SELECTED PROPERTIES OF BERYLLIUM[a] [102]

Atomic weight	9.01
Density (g/cm^3)	1.85
Crystal structure	
T<1254°C	h.c.p.
T>1254°C	b.c.c.
Melting temperature (°C)	1283
Boiling temperature (°C)	2484
Heat of fusion (J/g)	1083
Heat of vaporization (J/g)	24,790
Heat capacity (J/g-°C)	
500 °C	2.25
1000 °C	2.92
1500 °C	3.59
Coefficient of thermal expansion (1/°C)	
25– 100 °C	11.6×10^{-6}
25– 500 °C	15.9×10^{-6}
25–1000 °C	18.4×10^{-6}
Thermal conductivity (W/m-K)	
50 °C	150
300 °C	125
600 °C	90
Electrical resistivity ($\mu\Omega$cm)	
50 °C	5
300 °C	12
600 °C	23
Bulk modulus (GPa)	115.8
Shear modulus (GPa)	157.7
Young's modulus (GPa)	278.5
Poisson ratio	0.2
Fracture mode	cleavage
Ductility	poor

(a) Properties are at room temperature except as indicated.

Table 16.2-XIV.

ULTIMATE TENSILE STRENGTH AND 0.2% YIELD STRENGTH OF A TYPICAL BERYLLIUM SHEET [102]

Temperature (°C)	Yield Strength (MPa)	Ultimate Tensile Strength (MPa)
300	180	360
500	140	260
700	100	170
900	80	120
1073	10	25

tests [104]. Uniform and adherent anodized coatings on beryllium are produced either by solutions of 50% HNO_3 with a current density of 0.20 A/ft^2 for 5 minutes, or by solutions of 7.5% NaOH with a current density of 10 A/ft^2 for 20 minutes. It is conceivable to develop an in-situ anodizing mechanism to coat beryllium in an aqueous self-cooled blanket. In particular, the TITAN-II blanket coolant contains both NO_3 and OH ions. Extensive research into this area will be required to establish the feasibility of in-situ anodizing methods.

16.2.6.3. Swelling

Irradiation-induced swelling is a major concern associated with beryllium in a fusion environment. Swelling of beryllium under neutron irradiation is mostly caused by helium-gas generation from (n,α) reactions. Helium atoms are insoluble in metals and consequently they will rapidly diffuse through the metal until they become immobilized at trap sites such as thermodynamically and irradiation-produced dislocations, cavities, and grain boundaries. This phenomena is responsible for the nucleation and growth of bubbles. Bubbles can also migrate through the matrix or along grain boundaries and coalesce to form bigger bubbles (increased swelling). The temperature has to be high enough to allow bubble migration and coalescence.

The threshold temperature below which swelling of beryllium is insignificant was determined in early post-irradiation experiments [107 - 110]. For fluences resulting in a few appm of helium-atom concentration in beryllium, the threshold temperature is around 700 °C while for fluences creating more than 50 appm of helium, swelling threshold temperature drops to about 500 °C. Beryllium located behind the first wall of a fusion device will have a helium generation rate of about 10,000 helium appm per 1 MW y/m^2. Because of these high helium-generation rates, suppression of beryllium swelling through operation at low temperatures is not feasible in a fusion blanket.

High-temperature (1000 °C), post-irradiation anneal experiments showed a maximum swelling of 30%. This maximum in swelling was attributed to interconnecting bubbles which resulted in a release of trapped helium from the bulk. The minimum swelling necessary to produce an interconnecting network of helium bubbles for gas venting was theoretically determined to be 5% to 10% [111]. Thus, beryllium exposed to high levels of fast-neutron irradiation will swell a minimum of about 10% and a maximum of 30% at high temperatures (> 750 °C).

Phenomenological swelling equation

Because it is believed that swelling has its microstructural origin in helium behavior, a swelling equation based on the following gas-behavior assumptions has been developed: (1) Van der Waal's equation of state is used, (2) all retained gas is trapped in bubbles, (3) all bubbles are of the same size, (4) bubbles are in mechanical equilibrium with the solid, and (5) irradiation-induced re-solution is neglected.

The Van der Waal's equation of state, commonly used to describe the thermodynamic state of fission gas bubbles, is:

$$p\left(\frac{1}{\rho_g} - B\right) = kT\,, \tag{16.2-47}$$

where p is the pressure of the gas of molecular density ρ_g at temperature T. The Van der Waal parameter, B, can be regarded as an expression for the volume occupied by a single gas atom. Using the mechanical-force balance on a bubble, $p = 2\gamma/R$ yields:

$$\frac{1}{\rho_g} = B + \frac{kT}{2\gamma}R\,, \tag{16.2-48}$$

where γ is the surface tension of a bubble with a radius R.

Assuming that all retained helium atoms are trapped inside bubbles of equal size, the fractional increase in volume caused by the bubbles is:

$$\frac{\Delta V}{V} = \frac{4\pi}{3} R^3 N . \tag{16.2-49}$$

The bubble number density, N, is related to the number of gas atoms per bubble, m, and the helium generation rate, $\dot{G}_{He}$:

$$m N = f_R \dot{G}_{He} t , \tag{16.2-50}$$

where f_R is the fraction of helium atoms retained in the bulk of the material and t is the time of irradiation. Using Equation 16.2-48, the number of gas atoms contained inside a bubble of radius R is:

$$m = \frac{4\pi}{3} R^3 \rho_g = \frac{4\pi}{3} \frac{R^3}{B + (kT/2\gamma)R} . \tag{16.2-51}$$

Combining Equations 16.2-49 through 16.2-51 and assuming bubbles have radii greater than 1000 Å (ignoring B) results in:

$$\frac{\Delta V}{V} = \left(\frac{3}{4\pi}\right)^{1/2} \left[\left(\frac{kT}{2\gamma}\right)\left(\frac{f_R \dot{G}_{He} t}{N^{1/3}}\right)\right]^{3/2} . \tag{16.2-52}$$

Note that the swelling rate scales as $t^{1.5}$, which is commonly found experimentally. To use Equation 16.2-52, it is necessary to know the surface tension of bubbles in beryllium, the fraction of retained helium atoms, and the bubble number density.

Recently, Beeston [112,113] measured beryllium swelling as a function of temperature and helium content. The helium content was about 30,000 appm. Beryllium was irradiated in ETR and ATR test reactors up to 3.5×10^{22} n/cm^2 by fast neutrons ($E > 0.1$ MeV). The number densities of helium bubbles were measured at annealing temperatures between 400 and 600 °C [113]. An empirical equation, given by Beeston, for the number density as a function of temperature is:

$$N = 1.4 \times 10^{14} \exp\left(\frac{0.41}{kT}\right) , \tag{16.2-53}$$

where N is given in bubbles per cm^3, k is Boltzmann constant ($k = 8.618 \times 10^{-5}$ eV/K), and T is the temperature in Kelvin. Since the effects of high-fluence 14-MeV neutrons are not known at the present time, this model should be used with caution.

No measurements for the fraction of retained helium atoms are reported. Therefore, for the purpose of using Equation 16.2-52, it is conservatively assumed that all helium

atoms produced during irradiation are trapped ($f_R = 1$). Beryllium surface-energy measurements have been performed and the values quoted range from 1 to $2\,J/m^2$ [114 - 117]. In calibrating the swelling Equation 16.2-52 to Beeston's data, a surface tension value of $1.6\,J/m^2$ leads to the best agreement between the model and the data. Table 16.2-XV shows a comparison of the experimental data with predictions of Equation 16.2-52. For the temperature range between 300 and 500 °C, good agreement between the model and measured swelling data is apparent.

To estimate the swelling of the TITAN-II beryllium rods, it is assumed that high density beryllium, which retains most of the generated helium, is used. Table 16.2-XVI shows the estimated beryllium swelling after one full-power year (FPY) of operation. The beryllium was assumed to have an average temperature of 500 °C. It can be seen that with conservative assumptions, the maximum swelling of beryllium should not be higher than $\sim 15\%$ at 0.5 cm behind the first wall.

Swelling of porous beryllium

The estimated swelling values of Table 16.2-XVI were calculated assuming no loss of helium atoms from the matrix. Loss of helium through open pores and helium trapped in closed pores affects the rate of swelling. A realistic model of beryllium swelling has to account for helium released through open pores and for the fraction that is retained in closed pores.

First, the amount of helium trapped in closed pores needs to be approximated. At high temperatures (> 250 °C), the helium bubbles will be in mechanical equilibrium ($p = 2\gamma/R$). For an average-sized closed pore of $R = 2.5\,\mu m$, the amount of helium trapped is

$$n = \frac{8\,\gamma\,\pi\,R^2}{3\,k\,T} \simeq 1.96 \times 10^9 \text{ (atom per pore)} . \qquad (16.2\text{-}54)$$

The total helium produced during 1 FPY of operation in beryllium located just behind the first wall of the TITAN-II reactor is about 6.6×10^{21} He/cm^3. Starting with a beryllium matrix having a density of about 70% theoretical density (70% TD or 30% open porosity), and assuming a 50% pore closure by self welding, the fraction of helium trapped inside closed pores after 1 FPY is estimated to be

$$\frac{1.96 \times 10^9 (\text{He/pore})}{8.2 \times 10^{-12} (\text{cm}^3/\text{pore})} \times (0.3) \times (0.5) = 3.1 \times 10^{19} (\text{He/cm}^3) . \qquad (16.2\text{-}55)$$

Table 16.2-XV.

EXPERIMENTAL[a] AND ESTIMATED[b] SWELLING VALUES OF BERYLLIUM

Temperature (°C)	$\Delta V/V$ (%)	
	Experiments[a]	Estimated[b]
200	1.2	0.36
300	1.5	1.29
400	3.	3.17
500	6.	6.69

(*a*) Specimen contained about 30,000 appm helium (3.7×10^{21} He/cm^3) [112,113].

(*b*) Estimated using Equation 16.2-52.

Table 16.2-XVI.

SWELLING OF SOLID BERYLLIUM IN THE TITAN-II REACTOR[a]

Distance from First Wall (cm)	Total Helium (appm)	$\Delta V/V$ (%)
0.5	53,400	14.5
4.9	34,000	7.4
9.5	20,300	3.4
14.5	11,900	1.5

(*a*) After 1 FPY of operation at 18 MW/m^2 neutron wall loading.

This rough estimate shows that only about 0.5% of the total generated helium is trapped inside closed pores. Only at very low temperatures can the amount of helium trapped inside closed pores be a fairly large fraction of the total amount produced.

Estimating the amount of helium that reaches open surfaces through interconnected open pores is best determined empirically. However, because of the lack of experimental data, only a rough estimate can be made. Diffusion of helium through beryllium can be estimated using self-diffusion coefficients given by [118]:

$$D_{\perp} = 0.52 \exp\left(\frac{-1.63}{kT}\right), \tag{16.2-56}$$

$$D_{\parallel} = 0.62 \exp\left(\frac{-1.71}{kT}\right), \tag{16.2-57}$$

where $D_{\perp}$ and $D_{\parallel}$ are, respectively, the diffusion coefficients perpendicular and parallel to the C-axis (in units of cm^2/s) and kT is in units of eV. Assuming an average diffusion path to open pores of $10\,\mu m$ and an average temperature of 500 °C, Equations 16.2-56 and 16.2-57 predict that it would take a helium atom from 1 to 3 days to reach the pore, depending on the crystal orientation. Thus, at elevated temperatures, a substantial fraction of untrapped helium atoms can reach open pores within a short time. If 30% of all generated helium atoms escape to open pores, about 1.9×10^{21} He/cm^3 will be vented resulting in $f_R \simeq 0.7$. Based on this estimate for f_R, the maximum beryllium swelling at 0.5 cm behind the first wall of TITAN-II is about 8.5%. The above calculations assume that the pores in the beryllium rod remain open and do not sinter during operation; sintering must be minimized to avoid pore closure and excessive swelling.

A smear density of 70% TD can be achieved using sphere-packed beryllium. The maximum operating temperature must be kept below 660 °C to prevent sintering of the spheres. Beeston [119] has conducted experimental investigations of grain growth of beryllium which indicate open porosity below 661 °C. The thermal conductivity of 70% TD beryllium at 600 °C is about 44 W/m-°C [120].

Strength

Most metals undergo hardening when exposed to neutron irradiation. Similarly, beryllium is expected to experience an increase in yield strength with irradiation [121]. Miller *et al.* [122] analyzed the effects of irradiation on the strength and fracture toughness of beryllium. Figure 16.2-29 shows the effects of temperature and irradiation on the strength of beryllium at a fluence of 1.2×10^{22} n/cm^2. Irradiation increases the strength

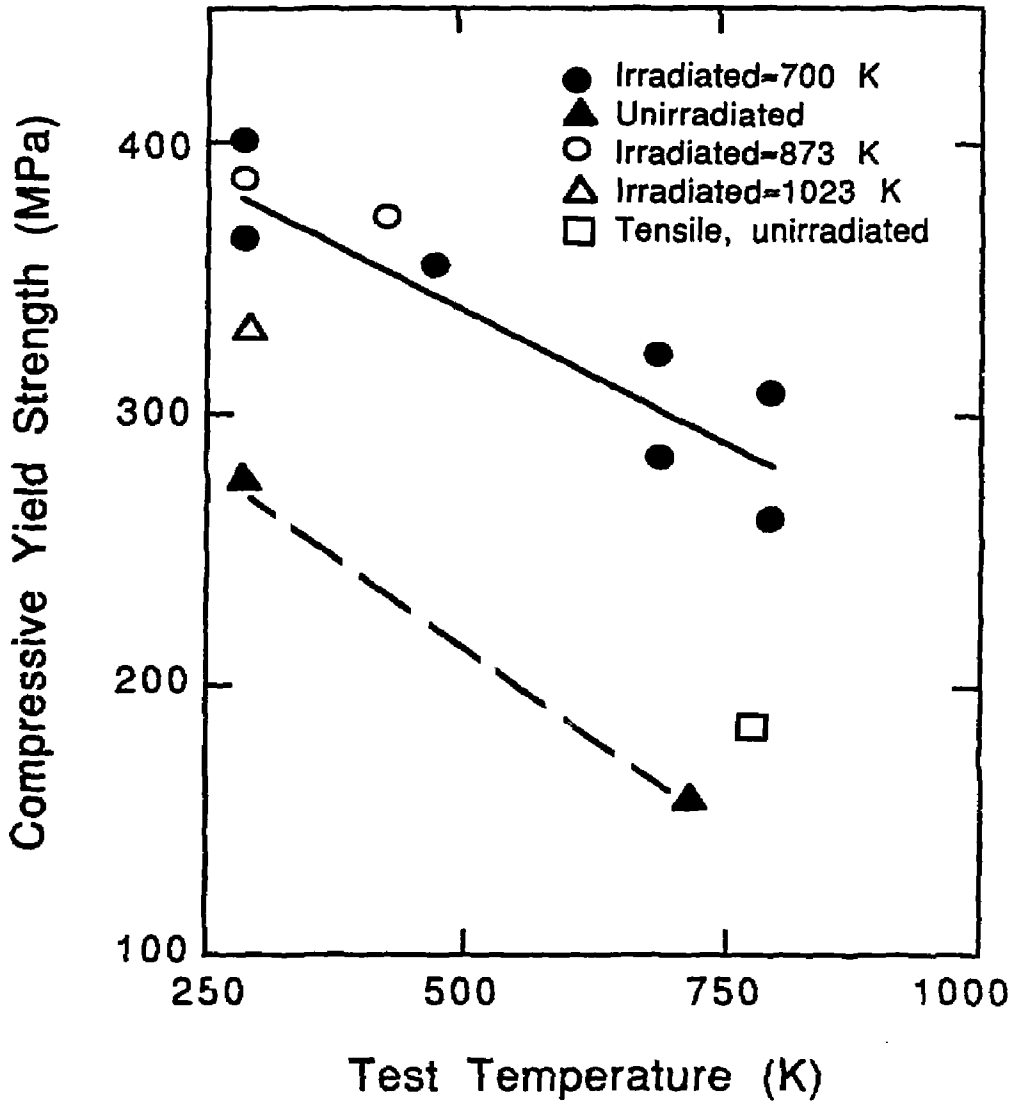

Figure 16.2-29. Compressive yield strength of beryllium as a function of test temperature under irradiation with a fluence of 1.2×10^{22} n/cm^2 [122].

of beryllium by a factor of ~ 2 at temperatures between 300 and 600 °C. Although the data base of irradiated beryllium is sparse, the irradiated strength measurements indicate adequate retention of the compressive strength. Irradiation experiments to measure the ductility of beryllium are needed to understand and model lifetime-limiting effects.

16.2.6.4. Discussion

Corrosion of beryllium in aqueous solutions is a function of the cleanliness of the beryllium surface and of solution impurities. Beryllium surfaces should be free of carbonates and sulfates and the water should have minimum chlorate and sulfate impurities to assure minimum corrosion rates. Coatings to protect beryllium against attack have been developed and their effectiveness has been demonstrated in a neutron-free environment.

Swelling levels of above $\sim 10\%$ will most likely result in a network of interlinking helium bubbles, thus promoting helium release. This means that swelling will stop temporarily until large enough temperature gradients cause sintering of open channels. The sintering temperature for beryllium has been estimated to be around 660 °C. The ongoing process of closing and opening of porosity will ultimately lead to an equilibrium helium-venting rate with an associated maximum swelling value. Realistic prediction of this process is currently not feasible because of the lack of experimental data. A phenomenological swelling equation for beryllium is developed which predicts a maximum swelling value between 9% and 15% depending on the amount of retained helium atoms. A swelling value of 10% is taken as the basis for design calculations. Swelling may be accommodated, to a degree, by using beryllium with low TD ($\sim 70\%$). This density can easily be achieved by using sphere-packed beryllium. The maximum operating temperature must be kept below 600 °C to prevent sintering of the spheres.

Two methods for accommodating the high rate of swelling in beryllium are available: (1) using a very fine grain beryllium operating at temperatures above 750 °C to ensure interlinkage of bubbles to vent the helium gas into the plenum of the cladding tube; and (2) using low-TD beryllium (sphere packed to a TD of $\sim 70\%$) to accumulate helium inside the porosity. The latter approach, however, results in a lower neutron multiplication and a reduction of thermal conductivity.

Irradiation data on the strength of beryllium are sparse. Irradiation hardening does occur at temperatures above 300 °C. McCarville *et al.* [123] predict that thermal creep may help extend the lifetime by relieving stresses caused by differential swelling, with irradiation-creep effects being negligible.

16.2.7. Discussion

In the TITAN-II design, tritium breeding is accomplished in a lithium salt which is dissolved in the primary-water coolant. Issues of corrosion and radiolysis, therefore, greatly impact the choice of the dissolved lithium salt and the structural material.

Two candidate lithium salts, lithium hydroxide (LiOH) and lithium nitrate ($LiNO_3$), are considered because they are highly soluble in water. The $LiNO_3$ salt was selected as the reference salt material for two main reasons. First, LiOH is more corrosive than $LiNO_3$ (Section 16.2.1). Recently, electrochemical corrosion tests were performed for aqueous LiOH and $LiNO_3$ solutions in contact with AISI 316L stainless steels [37]. It was found that stainless steels, particularly low-carbon steels, exhibit better corrosion resistance in $LiNO_3$ solution than in LiOH. Second, from the point of view of radiolysis, $LiNO_3$ solutions are also preferable. Radiolytic decomposition of water results in the formation of free radicals that will ultimately form highly corrosive hydrogen peroxide and OH ions. In an $LiNO_3$ solution, nitrate ions (NO_3) act as scavengers and reduce the probability of survival of highly reactive radicals in the water during exposure to radiation.

The most drastic effect of adding $LiNO_3$ to the coolant water is the elevation of the boiling point of the solution. This implies that the thermal-hydraulic design of such an aqueous salt blanket will be different from that of a pure-water-cooled design. A lower coolant pressure or a higher operating temperature can therefore be chosen.

The low-activation ferritic alloy, 9-C, was chosen from among other reduced-activation ferritics because of its good strength and elongation behavior after irradiation. The high chromium content (11 wt.%) of this alloy should provide good resistance to corrosion in an aqueous solution. The low-carbon content (0.09 wt.%) reduces the risk of hydrogen embrittlement. Although no data on the ductile-to-brittle transition temperature (DBTT) is available, it is believed that the high manganese content (6.5 wt.%) of 9-C will prevent the formation of delta-ferrite phases which are primarily responsible for increases of DBTT. The data base for corrosion of ferritics in $LiNO_3$ solutions is very limited. Indications are, however, that a high-concentration $LiNO_3$ solution does not exhibit unacceptable corrosion problems.

Stress-corrosion cracking (SCC) is a major concern in the nuclear industry. Most recent experiences with SCC in a nuclear environment clearly show that SCC can be suppressed by reducing the oxygen content through the addition of hydrogen to the coolant. The production of tritium in an aqueous $LiNO_3$ solution is seen as an SCC-controlling mechanism. The proper choice of structural material can further reduce the

probability of SCC. In particular, a high chromium content coupled with a low carbon content (as in the ferritic alloy, 9-C) are shown to reduce SCC.

Another form of attack on structural material in an aqueous environment is hydrogen embrittlement. The main factors influencing hydrogen embrittlement are the hydrogen content and the temperature of the structural alloy. Reducing the amount of atomic hydrogen available for solution in the structure and operating at high temperatures are the most effective means of reducing hydrogen attack. Atomic hydrogen is produced on metal surfaces during corrosion processes. Thus, minimizing corrosion also reduces hydrogen embrittlement of the structure. The production of tritium in the coolant does not necessarily result in an increased hydrogen attack because of rapid recombination to form molecular hydrogen or water molecules. In fact, the Nelson curves, used by the petrochemical industry as guidelines, show that chromium steels can operate at 400 °C with a hydrogen partial pressure of 17 MPa without experiencing hydrogen embrittlement [100].

Radiolytic decomposition of aqueous solutions exposed to a radiation environment is always cause for concern. Experimental data indicate that light-particle radiation (e, γ, and X rays) of concentrated $LiNO_3$ solutions results in a decrease of decomposition products compared with regular water. Heavy-particle radiation (n, p, α, and T) on concentrated $LiNO_3$ solutions also shows a decrease in the formation of radiolytic products, excepting oxygen. However, the production of tritium effectively reduces the oxygen content of the coolant by forming water molecules. Furthermore, the elevated operating temperature of the coolant is shown to be effective in reducing formation of decomposition products in non-boiling nuclear systems. More experimental data are required so that the radiolytic behavior of concentrated salt solutions can be predicated with a higher degree of confidence.

The TITAN-II design requires a neutron multiplier to achieve an adequate tritium-breeding ratio. Beryllium is the primary neutron multiplier for the TITAN-II design. Investigation of the swelling behavior of beryllium shows the necessity of using either low-density, sphere-packed or high-density, fine-grained beryllium. Depending on the type of beryllium chosen, different operating conditions must be satisfied to ensure minimum swelling and retention of structural integrity. Beryllium corrosion by an aqueous solution was also investigated. Past experience shows that minimizing carbonates, sulfates, and chlorates in solution reduces corrosion of beryllium. Coatings have also been developed and their effectiveness has been demonstrated. However, since most of the coatings were developed for radiation-free environments, research is needed to develop coatings that can withstand harsh radiation environments. For the TITAN-II design, a cladding of 9-C alloy surrounds the beryllium rods.

16.3. NEUTRONICS

Neutronics calculations for the TITAN-II design were performed with ANISN [124], a 1-D neutron and gamma-ray transport code, using a P_3S_8 approximation in cylindrical geometry. The nuclear data library, ENDF/B-V-based MATXS5 was used. The library was processed with the NJOY system at Los Alamos National Laboratory [125]. The energy group structures in this library are 30 groups for the neutron cross sections and 12 groups for the gamma-ray cross sections.

The TITAN-II design is cooled by an aqueous lithium-nitrate solution. The structural material is a low-activation ferritic-steel alloy, 9-C [2]. The TITAN-II blanket requires neutron-multiplier material to achieve an adequate tritium-breeding ratio (TBR). Beryllium is chosen as the multiplier, mainly because of its low-activation property.

This section describes the neutronics studies for the TITAN-II design. Scoping studies are reported in Section 16.3.1 and include an assessment of the blanket performance if heavy water (D_2O) is used as the coolant, and the impact of beryllium density on the blanket performance. The neutronics performance of the TITAN-II reference design is described in Section 16.3.2.

16.3.1. Scoping Studies

Neutronics scoping studies are performed with the configurational parameters based on the mechanical and thermal-hydraulic design of the TITAN-II FPC. The first wall is 12.5-mm thick and is composed of 16.7% structure, 61.8% coolant, and the balance is void (in this section, all material compositions are in volume percentages, except as otherwise noted). The blanket zone composition is 9% structure, 32% coolant, and 59% beryllium. The thickness of the blanket is a variable in the scoping studies. The blanket is followed by a metallic shield composed of 90% structure and 10% coolant. Two shield thicknesses of 0.2 and 0.25 m are considered.

A 50-mm-thick zone is located behind the shield to simulate the toroidal-field (TF) coils. The material composition of this zone is 10% structure, 10% spinel insulator ($MgAl_2O_4$), 10% coolant (pure water), and 70% copper conductor. The ohmic-heating (OH) coils of the TITAN-II design are located 0.78 m from the first wall in the scoping studies. The material compositions of the OH coils are identical to the TF coils. The space between the TF and OH coils contains pure water (the low-pressure water pool).

For the scoping studies, it is assumed that the aqueous coolant contains $LiNO_3$ salt and ordinary water (H_2O) with 1:5 molecular ratio. This aqueous $LiNO_3$ solution has

Table 16.3-I.

BERYLLIUM ZONE THICKNESSES TO ACHIEVE DIFFERENT TRITIUM-BREEDING RATIOS IN THE TITAN-II BLANKET[a]

	Tritium-Breeding Ratio					
	1.1			1.2		
^{6}Li enrichment (%)	7.42	30.	60.	7.42	30.	60.
Be zone thickness (m)	0.20	0.12	0.09	0.23	0.14	0.11
Blanket energy multiplication [b]	1.41	1.30	1.26	1.43	1.33	1.29

(*a*) For a 0.2-m-thick shield with 18 MW/m^2 neutron wall loading.

(*b*) Including all nuclear energy deposited in the first wall, Be zone, and shield.

a density of 1.07 g/cm^3 and contains 5 at.% of lithium. The blanket tritium breeding is strongly affected by ^{6}Li enrichment in the lithium salt. Three ^{6}Li enrichment cases were considered in the scoping studies: 7.42% (natural abundance), 30%, and 60%.

In the initial phase of the scoping studies, we varied the beryllium zone thickness from 0.1 to 0.3 m while keeping the shield thickness at 0.2 m. It was found that the TBR ranged from 0.76 for natural ^{6}Li enrichment (7.42%) and 0.1-m-thick beryllium zone to TBR of 1.66 for 60% ^{6}Li enrichment and 0.3-m-thick beryllium zone.

Next, for a given TBR, the thickness of the beryllium zone was estimated. Table 16.3-I presents the estimated thickness of the beryllium zone to achieve TBR of 1.1 or 1.2 for different ^{6}Li enrichment of 7.42%, 30%, and 60%. The resultant blanket-energy multiplications for these blanket systems are also given. Table 16.3-I shows that: (1) the blanket energy multiplication ranges from 1.25 to 1.43 as the beryllium zone thickness varies from 0.09 to 0.23 m; and (2) ^{6}Li enrichment can be adjusted, for example, from 7.42% to 60% ^{6}Li, to obtain the desirable TBR.

The neutron fluence at the location of TF coils was also examined. After 3 full-power years (FPY) of operation at 18.1 MW/m^2 neutron wall loading, the maximum fast-neutron ($E_n \geq 0.1$ MeV) fluence was found to be insensitive to ^{6}Li enrichment. For beryllium zone thicknesses of 0.1, 0.2, and 0.3 m, the maximum fast-neutron fluences

Table 16.3-II.

IMPACT OF ^{6}Li ENRICHMENT ON BLANKET PERFORMANCE[a]

^{6}Li Enrichment (%)	7.42	30.	60.
Tritium-breeding ratio	0.982	1.269	1.361
Blanket energy multiplication, M	1.42	1.37	1.35
Fraction (% of M) of nuclear energy in			
First wall	8.3	8.8	9.0
Beryllium zone	63.4	66.2	67.1
Shield	28.3	25.0	23.9
Energy leakage (% of M)	2.5	2.5	2.4
Maximum fluence[b] at TF coils (n/cm^2)	8.8×10^{22}	8.7×10^{22}	8.7×10^{22}

(*a*) For 0.15-m Be zone and 0.25-m shield designs at 18 MW/m^2 neutron wall loading.

(*b*) Fast-neutron fluence ($E_n \geq 0.1$ MeV) for 30 FPY of operation.

at the TF coils are, respectively, 2.3×10^{23}, 9×10^{22}, and 3.3×10^{22} n/cm^2. Since the fast-neutron-fluence limit to the spinel insulators is determined to be 2×10^{23} n/cm^2 (Section 10.2.3), a beryllium zone thicker than 0.15 m will be adequate to ensure a 30-FPY lifetime for the TF coils. Note that a single-piece maintenance procedure is envisioned for the TITAN-II design (Section 20). The complete FPC, including the TF coils, is replaced each year during the scheduled maintenance. The used TF coils are separated from the replaced FPC and are reused on a new reactor torus.

Further scoping studies were performed for a 0.15-m-thick beryllium zone and a 0.25-m-thick shield (for a total blanket and shield thickness of 0.4 m). Table 16.3-II summarizes the results of neutronics calculations for three different ^{6}Li enrichments of 7.42%, 30%, and 60%. The case of natural enrichment does not yield adequate tritium breeding and for enrichments above 30% the blanket performance is rather insensitive to the enrichment levels. From the results shown in Table 16.3-II, a set of preliminary performance parameters can be obtained: (1) a blanket energy multiplication of about

Table 16.3-III.

COMPARISON OF NEUTRONICS PERFORMANCE OF BERYLLIUM MULTIPLYING BLANKETS[a] WITH H_2O AND D_2O-BASED LITHIUM-NITRATE COOLANTS

	Coolant Type			
	H_2O		D_2O	
^{6}Li enrichment (%)	7.42	30.	7.42	30.
Tritium-breeding ratio	0.982	1.269	0.936	1.217
Blanket energy multiplication	1.42	1.37	1.44	1.39
TF-coil heating rate (W/cm^3)	4.6	4.2	7.2	6.7

(a) For 0.15-m Be zone and 0.25-m shield designs at 18 MW/m^2 neutron wall loading.

1.38 for a TBR of 1.2; (2) the nuclear energy deposited in the TF coils, the pool water, and the OH coils is about 2.5% of the total nuclear energy deposited in the first wall, blanket, and shield; (3) the maximum fast neutron fluence at the TF coils is less than 1×10^{23} n/cm^2; and (4) the needed ^{6}Li enrichment is 30% or less for obtaining a TBR of 1.2 in the full-coverage 1-D analysis.

Heavy water (D_2O) as the coolant

The option of using heavy water (D_2O) as the coolant for the TITAN-II design was considered because D_2O has a lower neutron-absorption cross section than ordinary water (H_2O). Furthermore, deuterium has a significant (n,2n) cross section of about 0.1 barn at 14 MeV. It is also of interest to investigate whether D_2O can be used without any beryllium in the TITAN-II concept.

Two additional neutronics calculations were performed for the 0.15-m-thick beryllium zone blanket of Table 16.3-II. In these calculations, H_2O was replaced by D_2O while all other blanket parameters remained the same. Table 16.3-III compares the results of these calculations with those obtained with H_2O as the coolant. The results show

that the ordinary-water blanket is able to breed more tritium than the heavy-water one, within the range of blanket parameters used, because hydrogen has a better neutron-moderation capability than deuterium. As a result, the neutron-leakage rate into the TF coils is expected to be higher in the D_2O blanket than in the H_2O blanket, as is seen in Table 16.3-III. The D(n,2n) reactions do not significantly contribute to tritium breeding, since beryllium is the major neutron multiplier with a multiplication factor of 15 or more higher than that of the heavy water under the specified blanket parameters.

The need for the beryllium multiplier in the TITAN-II design is demonstrated by considering four different designs without Be:

1. 0.3-m blanket and 0.1-m shield, D_2O coolant, 60% ^6Li,
2. 0.6-m blanket and no shield, D_2O coolant, 30% ^6Li,
3. 0.6-m blanket and no shield, D_2O coolant, 60% ^6Li, and
4. 0.6-m blanket and no shield, H_2O coolant and 60% ^6Li.

The compositions in the above blankets are identical to those in the previous study, except that beryllium is replaced by either D_2O or H_2O with the corresponding $LiNO_3$ content of the solution.

Table 16.3-IV summarizes the results for these four cases. It is clear that without beryllium, both D_2O and H_2O $LiNO_3$ blankets have insufficient TBRs. Marginal breeding ratios can be achieved for a blanket with a structural content of about 1% or 2% and with D_2O as the coolant.

The fast-neutron fluence at the TF coils for the first blanket considered (total thickness of 0.4 m) is about the same as the blanket design containing beryllium (Table 16.3-II). The latter indicates that water (either light or heavy water) itself is a very good neutron moderator, but lacks adequate neutron-multiplication capability.

Effect of beryllium density factor

Scoping studies were performed to assess the impact of the beryllium zone thickness and density factor on optimized blanket-energy multiplication and beryllium utilization. The blanket composition in this set of calculations includes a 15-mm-thick first wall with 16.7% structure, 61.8% coolant, and a balance of void. A variable-thickness beryllium

zone was considered consisting of 12.2% structure, 58.7% beryllium, and 29.1% coolant, according to a more up-to-date mechanical design of the FPC. Two beryllium density factors, 1.0 and 0.8, were considered. A 0.15-m-thick breeder/reflector zone with 9% structure and 91% aqueous coolant and a 0.1-m-thick shield with 90% structural metal and 10% aqueous coolant are located behind the Be zone.

Figure 16.3-1 shows the Be (n,2n) reaction rate as a function of beryllium zone thickness which indicates that for a 0.3-m-thick beryllium zone, the reaction rate is about saturated for both density factors of 1.0 and 0.8. When the beryllium zone thicknesses are 0.1, 0.15, and 0.2 m, the corresponding Be (n,2n) reaction rates relative to the value

Table 16.3-IV.

NEUTRONICS PERFORMANCE OF D_2O- AND H_2O-BASED $LiNO_3$ BLANKETS[a] WITHOUT BERYLLIUM NEUTRON MULTIPLIER

	Case 1	Case 2	Case 3	Case 4
Blanket thickness (m)	0.3	0.6	0.6	0.6
Shield thickness (m)	0.1	0.0	0.0	0.0
Coolant [b]	D_2O	D_2O	D_2O	H_2O
^6Li enrichment (%)	60.	30.	60.	60.
Tritium-breeding ratio	0.850	0.987	0.993	0.880
Blanket energy multiplication	1.12	1.16	1.15	1.13
D (n,2n)	0.130	0.140	0.140	N/A
TF-coil heating rate (W/cm^3)	7.7	3.4	3.2	2.5
Fluence[c] at TF coils (n/cm^2)	1.0×10^{23}	2.5×10^{22}	2.2×10^{22}	1.8×10^{22}

(a) For designs with 9% ferritic-steel structure and 18 MW/m^2 neutron wall loading.

(b) The coolant is an aqueous $LiNO_3$ solution containing 5 at.% lithium.

(c) After 30 FPY of operation.

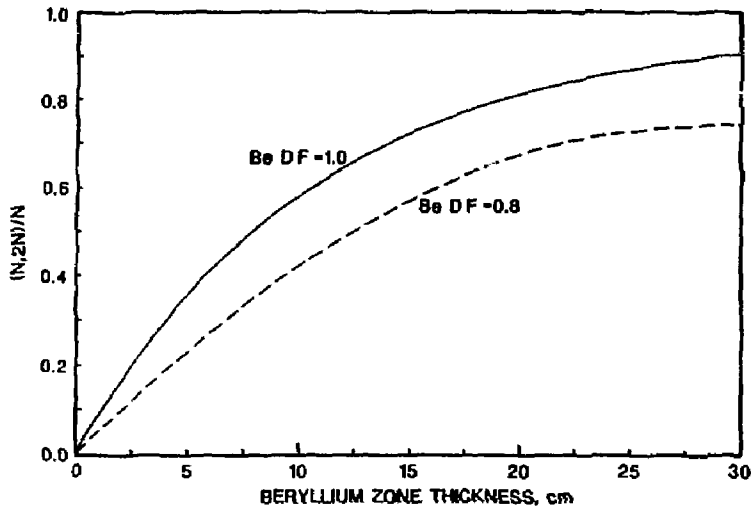

Figure 16.3-1. Beryllium neutron-multiplication factor in the TITAN-II design as a function of beryllium zone thickness for beryllium density factors (D.F.) of 0.8 and 1.

at 0.3 m are 0.64, 0.77 and 0.9, respectively. The Be (n,2n) reaction rate is almost directly proportional to the beryllium density factor (packing fraction) used. Hence, a beryllium design with a 0.8 density factor will produce a 20% lower neutron-multiplication factor than a design with a density factor of 1.0.

The ultimate impact of a lower-density beryllium on the neutronics performance of the TITAN-II design is a lower blanket energy multiplication (M) when the TBRs in these designs are fixed at 1.2 by adjusting the ^{6}Li enrichment. A preliminary design study was performed using a 0.15-m-thick beryllium zone as the base blanket for the design analysis. Two beryllium zone compositions were considered in the preliminary structural design study: Case A with 12.2% structure, 29.1% coolant, and 58.3% beryllium; and Case B with 15% structure, 20.5% coolant, and 64.5% beryllium. For each case, two beryllium density factors of 0.8 and 1.0 were considered. Natural lithium in the aqueous coolant is used when the beryllium density factor is 1.0, while 20% ^{6}Li enrichment is used for the designs when the beryllium density factor is 0.8. These ^{6}Li enrichments were chosen primarily to make sure that these preliminary designs result in reasonable TBRs (> 1).

Table 16.3-V shows the neutronics performance for these blankets with these two beryllium zone compositions. For a beryllium density factor of 0.8, both cases have equal

Table 16.3-V.

COMPARISON OF NEUTRONICS PERFORMANCE OF PRELIMINARY TITAN-II BLANKET DESIGNS[a]

	Case A		Case B	
Compositions of Be zone (%)				
Beryllium	58.7		64.5	
Coolant	29.1		20.5	
Structure	12.2		15.0	
Beryllium density factor	1.0	0.8	1.0	0.8
^{6}Li enrichment (%)	7.4	20.	7.4	20.
Tritium-breeding ratio	1.06	1.19	1.01	1.18
Blanket energy multiplication, M	1.38	1.31	1.43	1.34
Be(n,2n) reaction rate	0.684	0.573	0.740	0.624
Nuclear energy leakage (% of M)	2.8	3.3	2.6	3.1

(*a*) All calculations were obtained with the following system:
First wall (15 mm): 16.7% structure, 61.8% coolant, and 21.5% void;
Beryllium zone (0.15 m): Two variable compositions as shown;
Breeder/reflector zone (0.15 m): 9% structure and 91% coolant;
Shield (0.1 m): 90% structure and 10% coolant; and
Coolant: aqueous (H_2O) $LiNO_3$ solution containing 5 at.% lithium.

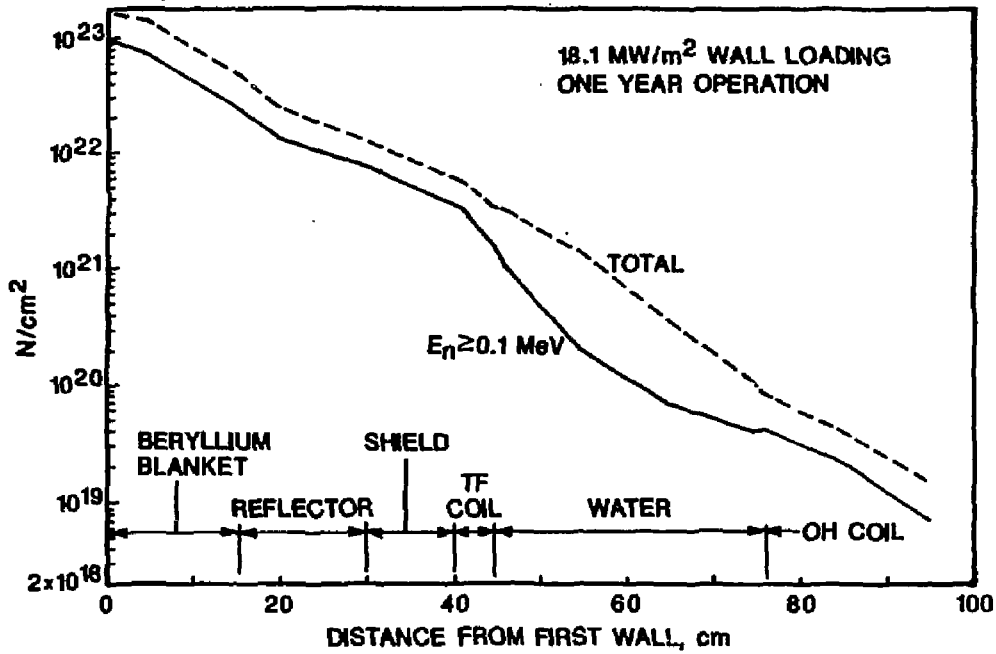

Figure 16.3-2. Total and fast-neutron ($E_n \geq 0.1$ MeV) flux distributions in TITAN-II components as a function of distance from the first wall.

TBRs of 1.2 and roughly equal M (1.31 for Case A and 1.34 for Case B). For a Be density factor of 1.0, M increases to 1.38 and 1.43, respectively, for Cases A and B. However, the TBRs are reduced to 1.06 and 1.01. If the TBRs are adjusted to about .2 by increasing the ^{6}Li enrichment in lithium, M will decrease slightly to about 1.36 and 1.40. This study suggests that the reduction of the beryllium density factor from 1.0 to 0.8 will cause M to decrease by about 4%.

Figure 16.3-2 shows the neutron-flux distribution as a function of distance from the first wall for Case A with a beryllium density factor of 0.8 and a ^{6}Li enrichment of 20%. The maximum fast-neutron fluence at the TF coils is about 3×10^{21} n/cm^2 after 1 FPY of operation at 18.1 MW/m^2 neutron wall loading. Therefore, TF and OH coils can be used for the lifetime of the power plant with no replacement, since the fast-neutron fluence after 30 FPY is about a factor of 2 to 3 below the radiation-damage limit to the spinel insulator. This margin may provide an incentive to move the OH coils closer to the blanket system in order to improve the coupling between the OH coils and the plasma.

16.3.2. Reference Design

Based on the above scoping studies, the following parameters were selected for the TITAN-II reference design: a 0.2-m-thick beryllium zone with a beryllium density factor of 0.9 (a maximum value when beryllium swelling is considered); a 0.1-m-thick breeder/reflector zone; and only a 50-mm water gap region between the TF and OH coils, bringing the OH coils closer to the blanket system by 0.3 m. Also, a higher $LiNO_3$ concentration (6.4 at.%) in the aqueous coolant is used because of heat-transfer considerations. The ^6Li enrichment level is chosen to achieve a TBR of 1.2. The schematic and materials composition of the TITAN-II reference design are illustrated in Figure 16.3-3.

The neutronics performance of the reference design is summarized in Table 16.3-VI and compared to three alternate designs with no breeder/reflector zones and 0.3-m-thick beryllium zones. The TBR is calculated to be 1.22 for the reference design when the ^6Li enrichment is 12%. The corresponding ^6Li enrichment for the alternate designs with thicker beryllium zones is also 12%. The blanket energy multiplication for the reference design is 1.36 and 1.40 for the alternate design because of its thicker beryllium zone. The nuclear energy leakages to the TF coil, water, and OH coils are also given in Table 16.3-VI, and are very similar in these designs with a 2.8% total leakage of the blanket energy from the high-temperature zones. The volumetric nuclear-heating rates in the reference and alternate (12% ^6Li enrichment) designs are displayed, respectively, in Figures 16.3-4 and 16.3-V.

16.4. THERMAL AND STRUCTURAL DESIGN

The TITAN-II design uses an aqueous salt solution ($LiNO_3$ in ordinary water) as the primary coolant. Major parameters of the TITAN-II design are given in Table 16.1-I. The configuration of the first wall, blanket, and shield is shown in Figures 16.1-1 through 16.1-4. The coolant channels are in the poloidal direction. The coolant enters at the bottom and exits at the top of the torus. One set of coolant channels runs along the outboard side of the torus and another set along the inboard side. The geometry of the coolant channels is shown in Figure 16.4-1. The cross section of the first wall is a semicircular channel with the convex side facing the plasma. The outer diameter is 3 cm and the wall thickness is 1.5 mm, including a 0.25-mm erosion allowance.

The blanket is made of rectangular-cross-section lobes attached to the first-wall coolant channels. The outer dimensions of the blanket lobes are 3 cm toroidally and

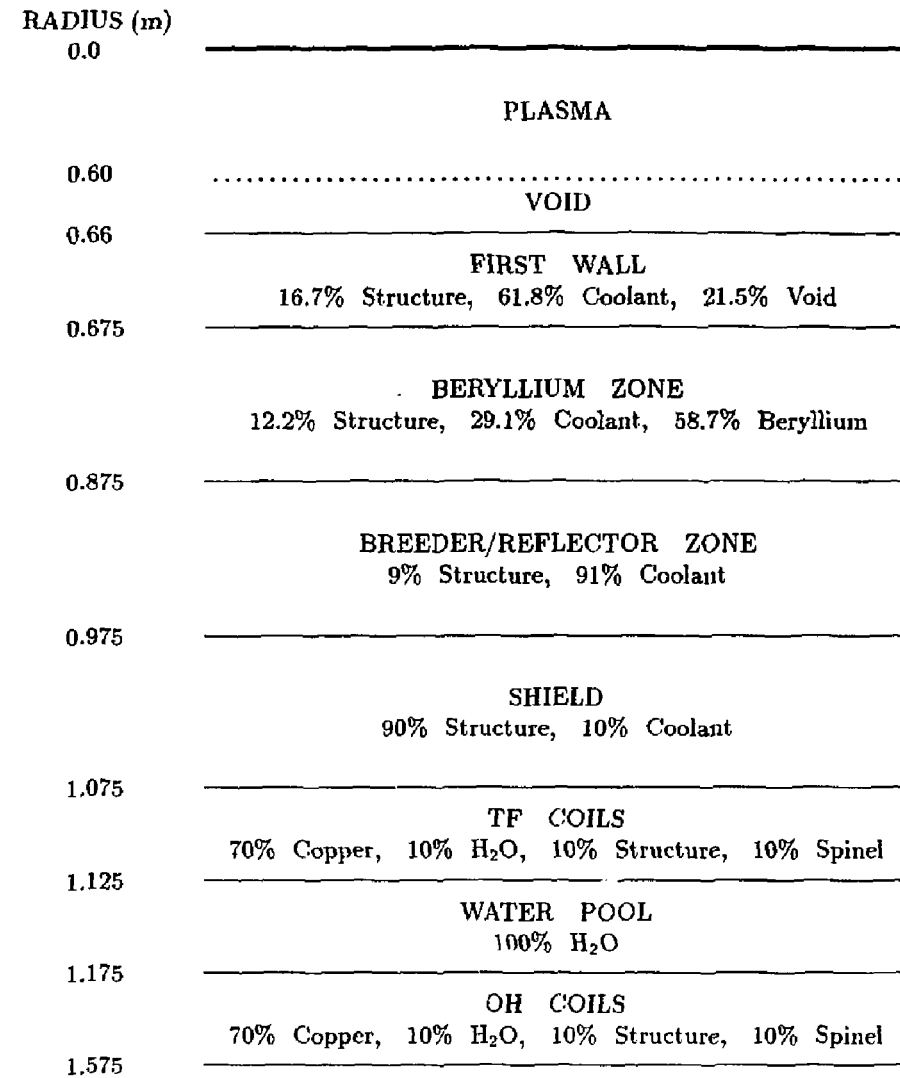

Figure 16.3-3. Schematic of the blanket and shield for the TITAN-II reference design. The coolant is an aqueous $LiNO_3$ solution (6.4 at.% Li) and beryllium density factor is 90%.

Table 16.3-VI.

NEUTRONICS PERFORMANCE OF THE TITAN-II REFERENCE AND ALTERNATE BLANKET DESIGNS

	Reference Design	Alternate Designs		
Beryllium zone thickness (m)	0.2	0.3		
Breeder/reflector zone thickness (m)	0.1	0.0		
Shield thickness (m)	0.1	0.1		
^{6}Li enrichment (%)	12.	7.42	12.	15.
Tritium-breeding ratio	1.22	1.08	1.20	1.25
Blanket energy multiplication, M	1.36	1.42	1.40	1.39
Fraction (% of M) of nuclear energy in				
First wall	12.4	11.8	12.1	12.2
Beryllium zone	69.2	81.0	81.5	81.5
Breeder/reflector zone	12.7	–	–	–
Shield	5.7	7.2	6.4	6.3
Energy leakage (% of M) to				
TF coils	1.27	1.43	1.40	1.38
Water pool	0.31	0.30	0.30	0.30
OH coils	1.09	1.11	1.11	1.12
TOTAL:	2.67	2.84	2.81	2.80

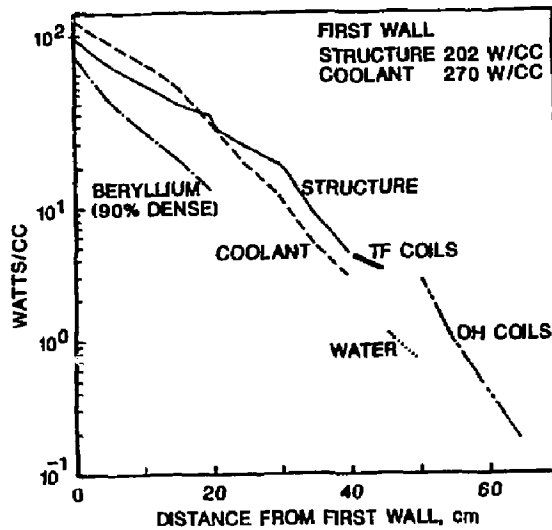

Figure 16.3-4. Volumetric nuclear heating rates in the reference TITAN-II design (18.1 MW/m^2 neutron wall loading) as a function of distance from the first wall.

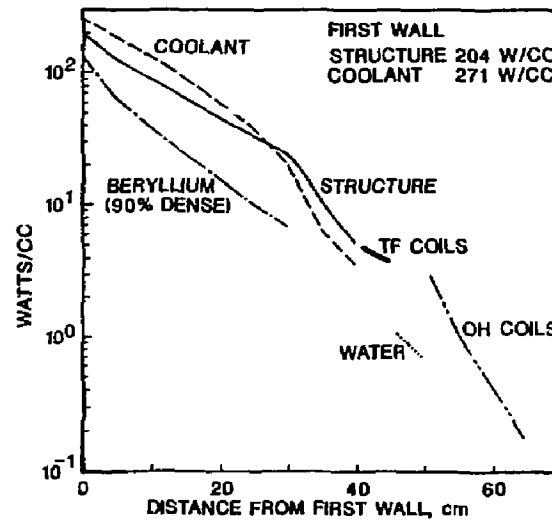

Figure 16.3-5. Volumetric nuclear heating rates in the alternate TITAN-II design (12% ^{6}Li enrichment and 18.1 MW/m^2 neutron wall loading) as a function of distance from the first wall.

30 cm radially. The lobe wall thickness is 1.4 mm. The first 20 cm of the blanket lobe (the multiplier zone) contains 7 rows of beryllium rods clad in 9-C, with a diameter of 2.6 cm. The thickness of the clad is 0.25 mm. The multiplier zone contains 12% structure, 59% beryllium, and 29% coolant (all by volume). Nuclear-heating rate in the blanket decreases away from the first wall. Therefore, to ensure proper coolant velocity, poloidal flow separators are placed behind the 2nd, 4th, and 7th rows of beryllium rods to form channels which have individual orifices. The remaining 10 cm of the blanket lobe (the breeder/reflector zone) does not contain beryllium and consists of 9% structure and 91% coolant (by volume). Behind the breeder/reflector zone, there is a 10-cm-thick shield. The shield contains two rows of circular coolant channels. The volume percentages of structure and coolant in the shield are 90% and 10%, respectively.

A review of the thermal analysis of the TITAN-II FPC is given in Section 16.4.1. The thermal-hydraulic parameters of the reference design are summarized in Section 16.4.2. The structural design of the FPC is presented in Section 16.4.3.

16.4.1. Thermal Analysis

The design peak heat flux on the first wall due to plasma radiation is 4.6 MW/m^2, corresponding to a plasma radiation fraction of 0.95. The coolant is an aqueous $LiNO_3$ solution with a lithium concentration of 6.4 at.% and a base pressure of 7 MPa. The inlet and exit temperatures of the coolant are, respectively, 298 and 330 °C. The resulting exit subcooling is 17 °C and, at moderate coolant velocities, nucleate boiling will take place

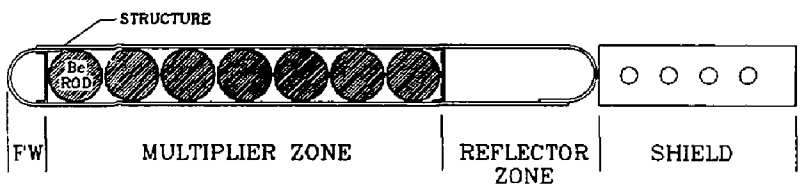

Figure 16.4-1. Geometry of the first-wall, blanket, and shield coolant channels.

in the first-wall coolant channels because of the high heat flux. Therefore, the mode of heat transfer in the first-wall coolant channels will be subcooled flow boiling (SFB). On the other hand, the heat load in the blanket and shield coolant channels is by volumetric nuclear heating only. The resulting heat flux on the coolant surface is smaller than that on the first wall. The maximum heat flux is less than $1\,MW/m^2$. Therefore, at these coolant velocities in the blanket and shield coolant channels, boiling will not take place and non-boiling, forced-convection heat transfer is sufficient to remove the heat.

16.4.1.1. Subcooled flow boiling

The maximum value of the average coolant temperature is always less than the boiling point by at least 17°C. Any boiling will, therefore, be subcooled boiling. When the wall temperature exceeds the saturation temperature, boiling begins. Bubbles form at nucleation sites, grow, and detach from the wall. In the bulk of the coolant, where the temperature is lower than the boiling point, the bubbles collapse. Flow boiling is a highly efficient mode of heat transfer. The boiling process suffers a drastic reduction in heat-transfer capability when the heat flux exceeds a certain limiting value termed critical heat flux. Beyond the critical heat flux, the boiling process changes from nucleate boiling to film boiling and the heat transfer capability is much less than that of the critical heat flux. If the surface heat flux is not correspondingly reduced in such a case, the wall temperature will drastically increase and may result in melting of the wall material. This is more likely to happen in designs with a constant heat flux.

Three important parameters govern boiling heat transfer: the incipience of boiling, the wall superheat corresponding to a given surface heat flux, and the critical heat flux for the given coolant and flow conditions. Complete physical understanding of the boiling phenomena and theoretical solutions to different problems are not available at present. However, extensive experiments have been performed with different types of boiling heat transfer, mainly with pure liquids, and many empirical correlations are available. Since pure water (without additives) is used as coolant in many boiling heat-transfer applications, most of the boiling heat-transfer data are for water. It is expected that when additives are mixed with water, as is the case for TITAN-II, the boiling heat-transfer capability as measured by the critical heat flux will increase. However, only very limited data are available in this area. Therefore, the correlations for boiling heat transfer of pure water are used for the aqueous coolant of TITAN-II with appropriate corrections for changes in coolant properties resulting from the addition of the salt (Section 16.2.3).

Incipience of boiling

A semi-empirical correlation for the heat flux for incipience of boiling at a given wall superheat is provided by Bergles and Rohsenow [126]. Conversion to more convenient SI units yields

$$q_i'' = 0.0155\,p^{1.156}\left[\frac{9}{5}(T_w - T_{sat})\right]^{2.047/p^{0.0234}}, \qquad (16.4\text{-}1)$$

where q_i'' is the incipient heat flux (MW/m^2), p is the pressure (MPa), and T_w and T_{sat} are, respectively, the wall and saturation temperatures (°C). This correlation is valid for all velocities and represents the numerical data for water quite accurately over a pressure range of 0.1 to 14 MPa (15 to 2000 psia).

Equation 16.4-1 can be used to determine if boiling will take place or if the heat-transfer mechanism will remain purely convective at a given flow velocity, pressure, and heat flux. If the wall temperature obtained from the assumption of pure forced-convection heat transfer is greater than that given by Equation 16.4-1, then boiling will take place. In this case, the wall temperature should be calculated from the boiling equations given below.

Wall superheat in subcooled-flow-boiling heat transfer

Several correlations are available for calculating wall superheat corresponding to a given heat flux in fully developed, forced convection, nucleate-boiling heat transfer. The following three equations (converted to SI units) are by Jens and Lottes [127], Weatherhead [128], and Thom *et al.* [129], respectively:

$$T_w - T_{sat} = \frac{100}{3}\left(\frac{q''}{3.152}\right)^{1/4}\exp\left(-\frac{p}{6.207}\right), \qquad (16.4\text{-}2)$$

$$T_w - T_{sat} = (47.74 - 0.127\,T_{sat})\left(\frac{q''}{3.152}\right)^{1/4}, \qquad (16.4\text{-}3)$$

$$T_w - T_{sat} = 40\left(\frac{q''}{3.152}\right)^{1/2}\exp\left(-\frac{p}{8.690}\right), \qquad (16.4\text{-}4)$$

with temperature in °C, pressure in MPa, and the heat flux in MW/m^2.

Equations 16.4-2 and 16.4-3 are based on the assumption that the surface characteristics do not significantly influence the position of the fully developed boiling curve in

forced convection. Equation 16.4-4 appears to be in better agreement with experimental data. At higher heat fluxes, Equation 16.4-4 by Thom *et al.* [129] predicts highest wall superheat among the three equations and, therefore, will give a conservative estimate for the wall temperature of the first-wall coolant channel. Hence, Equation 16.4-4 is used in the thermal-hydraulic design of the TITAN-II FPC.

Critical heat flux

In any application of boiling heat transfer, it must be ensured that the maximum possible heat flux is less than the critical heat flux (CHF) by a certain safety margin. A large amount of data for internal flow boiling CHF for pure liquids, especially for water, is available and many empirical correlations for the CHF exist. Because of the scatter in the data, these correlations are generally accurate to $\pm 20\%$ over the applicable range of the data. Therefore, the CHF given by the different correlations may vary by as much as 40% [130].

The particulars about boiling in the first-wall coolant channels of TITAN-II are: the heat flux varies circumferentially, the flow is upward, and the coolant is an aqueous salt solution (not pure water). Since boiling is a localized phenomenon, circumferential variation of heat flux is not likely to affect the CHF. This has been shown to be the case by an experiment conducted at Oak Ridge National Laboratory [131].

It has been shown by Hasan *et al.* [132] that the direction of flow relative to gravity does not affect the CHF at high flow velocities in external flow boiling. They found that in subcooled or near-saturation boiling of methyl and ethyl alcohols flowing across a horizontal cylinder, the flow direction does not have any effect on the CHF for velocities in excess of about 1 m/s. The coolant velocity in the first-wall coolant channel is about 20 m/s. Therefore, the flow direction is not expected to have any effect on the CHF in the first-wall coolant channels of TITAN-II.

Several correlations for critical heat flux (q''_{CHF}) in flow boiling of pure liquids are available. The following correlation (converted to SI units) is by Jens and Lottes [127] and is based on the data for water only:

$$q''_{CHF} = C\left(\frac{G}{1356}\right)^{m}(\Delta T_{sub})^{0.22}, \qquad (16.4\text{-}5)$$

where G is the mass velocity of the coolant ($= \rho v$) in kg/m^2-s, the factor 1356 aries from the conversion of units, ΔT_{sub} is the local subcooling in °C, and q''_{CHF} is in MW/m^2.

Constants C and m depend on the pressure, p (MPa), through

$$C = 3.00 - 0.102\,p\,, \tag{16.4-6}$$

$$m = \frac{p}{30} + 0.04\,. \tag{16.4-7}$$

Data used in deriving the above CHF correlation was limited to maximum values of CHF of 38 MW/m^2, water velocity of 17 m/s, pressure of 13.6 MPa, and local subcooling of 90 °C.

A subcooled empirical correlation for the CHF developed by Tong [133], has the following form (after conversion to SI units):

$$q''_{CHF} = (0.725 + 1.93 \times 10^{-4}\,G) \times (3.0 + 0.018\,\Delta T_{sub}) \times (0.435 + 1.23\,e^{-0.0093\,L/d_h}) \times (1.7 - 1.4\,e^{-a})\,. \tag{16.4-8}$$

The parameter, a, is given by

$$a = 0.532 \left(\frac{h_{sat} - h_{in}}{h_{fg}}\right)^{3/4} \left(\frac{\rho_f}{\rho_v}\right)^{1/3}\,. \tag{16.4-9}$$

The length and hydraulic diameter are denoted by L and d_h, respectively. The inlet enthalpy is h_{in} and the saturation enthalpy is h_{sat}. The heat of vaporization is h_{fg}, ρ_f is water density, and ρ_v is vapor density. Data used in deriving the above correlation were limited to maximum values of CHF of 12.6 MW/m^2, water velocity of 110.6 m/s, pressure of 19 MPa, local subcooling of 127 °C, and L/d_h of 365. Because the data for this correlation were obtained from uniform-heat-flux test sections, it is not clear whether the CHF predicted by Equation 16.4-8 is a local CHF or an average heat flux up to the critical point.

Another empirical correlation of CHF data in up-flow of water through vertical tubes was provided by Katto and cited in Reference [130]:

$$q''_{CHF} = q''_o \left(1 + K\,\frac{\Delta h_{sub}}{h_{fg}}\right)\,, \tag{16.4-10}$$

where parameters K, q''_o, and the Weber number, We, are given by:

$$K = 0.416 \left(\frac{\rho_v}{\rho_f}\right)^{0.133} We^{0.433} \left(0.0221 + \frac{d_h}{L}\right) \left(\frac{d_h}{L}\right)^{0.27}\,, \tag{16.4-11}$$

$$We = \frac{G^2\,L}{\sigma\,\rho_f}\,, \tag{16.4-12}$$

$$q''_o = 9.8 \times 10^{-8}\,G\,h_{fg} \left(\frac{\rho_v}{\rho_f}\right)^{0.133} We^{-0.433}\,\frac{(L/d_h)^{0.27}}{1 + 0.0031\,L/d_h}\,, \tag{16.4-13}$$

with σ being the surface tension of water and L being the length of the channel. The ranges of velocity and CHF are rather small for this correlation.

Of the three correlations, the Jens-Lottes correlation (Equation 16.4-5) is the simplest and has the range of parameters for boiling heat transfer which is close to those of the first-wall coolant channel of TITAN-II. In the region of high heat flux, the predictions of Equations 16.4-5 and 16.4-8 are close, but the prediction by Equation 16.4-10 is too small, probably because the equation is not applicable at high heat flux. For example, at 13.8 MPa, water velocity of 10 m/s, and exit subcooling of 20 °C, the predictions of critical heat fluxes for the first-wall channel of TITAN-II by the above three correlations are 6.8, 5.8, and 3.8 MW/m^2, respectively.

As explained before, correlation 16.4-8 probably underestimates the CHF. References cited in [130] show that the CHF is increased by about 40% with an aqueous solution of ethanol over pure water. Therefore, if the maximum heat flux is kept within 60% of that predicted by the correlation of Jens and Lottes, an adequate safety margin for CHF is available. Any increase in the CHF due to the lithium-salt content will add to the safety margin. The Jens-Lottes correlation (Equation 16.4-5) is used to check for CHF in the first-wall coolant channel in TITAN-II.

16.4.1.2. Maximum temperature of the first wall

The maximum structure temperature in the first-wall coolant channel is given by

$$T_{w,max} = T_{ex} + \Delta T_w + \Delta T_f , \qquad (16.4\text{-}14)$$

where T_{ex} is the mixed-coolant exit temperature and ΔT_w and ΔT_f are the wall and film temperature drops, respectively. The maximum temperature drop across the wall is obtained from a 1-D, cylindrical-geometry heat conduction at the point of maximum radiation heat flux on the first wall. The maximum wall temperature drop is given by:

$$\Delta T_w = \frac{q''_o a}{k_s} \ln\left(\frac{b}{a}\right) + \frac{q'''_w b^2}{2k_s} \ln\left(\frac{b}{a}\right) - \frac{q'''_w (b^2 - a^2)}{4k_s} , \qquad (16.4\text{-}15)$$

where q''_o is the maximum radiation heat flux, q'''_w is the volumetric heating rate in the channel wall, a and b are the inner and outer radii, respectively, and k_s is the thermal conductivity of the wall material. The film temperature drop, ΔT_f, is the result of subcooled flow boiling (Section 16.4.1.1) and can be written as $\Delta T_f = (T_w - T_{sat}) + \Delta T_{sub,ex}$, where $\Delta T_{sub,ex}$ is the subcooling at the channel exit. The wall superheat, $(T_w - T_{sat})$, is calculated from Equation 16.4-4 using the maximum radiation heat flux on the first-wall coolant channel.

16.4.1.3. Analysis of blanket and shield

In the multiplier and breeder/reflector zones of the blanket lobe and in the shield, the heat flux removed by the coolant is very low. The flow is turbulent in the channels of these regions. Forced-convective heat transfer is adequate to remove the heat without raising the wall temperature to the level which would initiate nucleate boiling. Therefore, the maximum structure temperatures in the blanket and shield are calculated under the condition of non-boiling, forced-convective heat transfer.

The film temperature drop is calculated from the forced-convection, turbulent-flow Nusselt number, Nu, which is given by the Dittus-Boelter equation:

$$Nu = 0.023\,(Re)^{0.8}\,(Pr)^{1/3}\,, \tag{16.4-16}$$

where $Re = \rho_f V d_h/\mu_f$ is the Reynolds number, $Pr = c_p\mu_f/k_f$ is the Prandtl number, and ρ_f, μ_f, c_p, and k_f are the density, viscosity, specific heat capacity, and thermal conductivity of the coolant, respectively. The coolant velocity is denoted by V and d_h is the hydraulic diameter of each zone. The film temperature drop is then obtained from:

$$\Delta T_f = \frac{q'' d_h}{Nu\, k_f}\,. \tag{16.4-17}$$

The heat flux, q'', at the wall-coolant interface is determined from the volumetric nuclear-heating rates.

The important temperatures in the blanket and shield are those at the center of the beryllium rods, the clad, the channel wall, and the maximum temperature in the shield region. These temperatures should not exceed the design limits. The maximum temperatures are obtained by adding the film temperature drop and the temperature drops across the structural material and gap resistance to the coolant exit temperature. One-dimensional heat conduction is used to find the temperature drops in the structural material. The maximum center-line temperature of a beryllium rod, $T_{c,max}$, is given by:

$$T_{c,max} = T_{ex} + \Delta T_f + \Delta T_{clad} + \Delta T_{gap} + \Delta T_{Be}\,, \tag{16.4-18}$$

where ΔT_{clad}, ΔT_{gap}, and ΔT_{Be} are the temperature drops across the clad, gap, and the beryllium rod (from center to the surface), respectively:

$$\Delta T_{clad} = \frac{q'''_s\,(b^2 - a^2)}{4k_s} - \frac{(q'''_s - q'''_{Be})\,a^2}{2k_s}\,\ln\left(\frac{b}{a}\right)\,, \tag{16.4-19}$$

$$\Delta T_{gap} = \frac{q'''_{Be}\,a}{2h_{gap}}\,, \tag{16.4-20}$$

$$\Delta T_{Be} = \frac{q'''_{Be}\,a^2}{4k_{Be}}\,, \tag{16.4-21}$$

where q_s''' and q_{Be}''' are the volumetric nuclear-heating rates in the structure (cladding) and beryllium rod, respectively. The thermal conductivities of the structural material and beryllium are, respectively, k_s and k_{Be}, and the heat-transfer coefficient for the gap is h_{gap}.

The maximum blanket-lobe wall temperature, $T_{w,max}$, is given by:

$$T_{w,max} = T_{ex} + \frac{q_s''' t^2}{2k_s} + \frac{q_s''' t\, d_h}{Nu\, k_f}, \qquad (16.4\text{-}22)$$

where t is the wall thickness.

The maximum temperature in the shield region, $T_{s,max}$, is given by:

$$T_{s,max} = T_{ex} + \frac{q_s'''(R^2 - r^2)}{Nu\, k_f} + \frac{q_s''' R^2}{2k_s} \ln\left(\frac{R}{r}\right) - \frac{q_s'''(R^2 - r^2)}{4k_s}, \qquad (16.4\text{-}23)$$

where R is the radius of the shield region surrounding a coolant channel of radius r. The thermal-hydraulic design should ensure that none of the above three maximum temperatures, $T_{c,max}$, $T_{w,max}$, and $T_{s,max}$, exceeds the corresponding design-limit temperatures.

16.4.1.4. Pressure Drops

The pressure drop in the coolant circuit is caused by the friction in the coolant channel and bends, and by sudden contraction and expansion at the inlet and outlet. In the first-wall coolant channel, the pressure drop will be increased because of the two-phase flow which results from subcooled flow boiling. In the blanket- and shield-coolant channels, the friction pressure drop is given by:

$$\Delta p_f = f \frac{\rho_f V^2}{2d_h} L, \qquad (16.4\text{-}24)$$

where f is the friction factor which is a function of the Reynolds number and the wall roughness parameter for turbulent flow. The friction factor is given in the Moody diagram available in texts on fluid dynamics [134].

Friction pressure resulting from sudden expansion and contraction or occurring at a 90° bend is given by:

$$\Delta p_f = \alpha \frac{\rho_f V^2}{2g}, \qquad (16.4\text{-}25)$$

where g is the gravity acceleration. The factor α is equal to $0.5(1 - 1/n)$ for a sudden contraction and is equal to $(1 - 1/n)^2$ for sudden expansion with n being the ratio by which the flow area suddenly decreases or increases. For a circular channel with a 90° bend, the factor α depends on the ratio of the radius of curvature to the channel radius. When the ratio is 1, $\alpha = 0.6$ and when it is 5, $\alpha = 1.4$.

The pressure drop in subcooled flow boiling in the first-wall-coolant channel can be calculated from the following equation [135].

$$\left(\frac{dp}{dz}\right)_{SFB} = \left(\frac{dp}{dz}\right)_f \exp\left[\frac{2.65}{p}\left(\frac{q''_o}{q''_{SPL}} - 1\right)\right], \qquad (16.4\text{-}26)$$

where p is the pressure in MPa, $(dp/dz)_f$ is the pressure drop for single-phase flow and can be obtained from Equation 16.4-24 for unit channel length, and

$$q''_{SPL} = \frac{\Delta T_{sub,in} + \Delta T_{sat}}{(4L/G\,c_p\,d_h) + (d_h/Nu\,k_f)}. \qquad (16.4\text{-}27)$$

Here $\Delta T_{sub,in} = T_{sat} - T_{in}$ is the subcooling at the inlet and L is the channel length. The wall superheat, $\Delta T_{sat} = T_w - T_{sat}$, is given by Equation 16.4-4. Nusselt number, Nu is obtained from Equation 16.4-16 for purely convective heat transfer.

16.4.2. Reference Design

Figure 16.4-1 shows the cross sections of the first-wall, blanket, and shield coolant channels. The nuclear-heating rates in the FPC components are given in Figure 16.3-4. The input parameters relevant to the thermal-hydraulic design are given in Table 16.4-1. In the TITAN-II design, pressure drop and pumping power are not as limiting as the structure temperature and the base pressure of the coolant. The coolant base pressure is 7 MPa and the inlet and exit temperatures of the coolant are, respectively, 298 and 330 °C. The primary-coolant pressure has been selected to be lower than the steam-generator pressure (7.2 MPa) so that any leakage in the steam-generator tubes does not result in leaks of the tritium-containing primary coolant to the steam cycle. The necessity for an intermediate heat exchanger is thereby avoided. The coolant inlet and exit temperatures are selected to match the primary-coolant temperatures of a typical PWR power cycle, thus eliminating a full-scale power-cycle analysis.

The thermal-hydraulic design must ensure that the maximum structure temperatures, coolant velocities, and pressure drops do not exceed the design limits. The structure temperatures are determined by using the equations presented in Section 16.4.1. The coolant

velocities are determined by energy balance. The nuclear-heating rates in the structure, coolant, and beryllium rods are obtained from the neutronics analysis (Figure 16.3-4). The thermal-hydraulic reference design of TITAN-II first wall, blanket, and shield are given in Tables 16.4-II through 16.4-V.

The thermal-hydraulic design of TITAN-II is conservative in that the structure temperatures are well within the design limits. The critical heat flux in the first-wall channel is 8.34 MW/m^2 which is 63% higher than the peak heat flux crossing the coolant film (5.1 MW/m^2). The pumping power is 49 MW, nearly equal to that for TITAN-I. For coolant circulation, pumps supplying a head of 1 MPa are used. Because the coolant flows in parallel through the first wall, multiplier, reflector, and shield zones, orifices are used to reduce the pressure as necessary for each channel. Separate coolant supplies for each of the flow channels (or zones) would alleviate the need for orifices and reduce the pumping power considerably. However, the added complexity of more coolant systems and hydraulic separation of the flow channels does not justify this change.

16.4.3. Structural Analysis

The first wall and blanket of the TITAN-II design are integrated in the form of blanket lobes. The construction procedure for each blanket lobe is shown in Figure 16.4-2. Each

Table 16.4-I.

THERMAL-HYDRAULIC DESIGN PARAMETERS

First-wall heat flux	4.6	MW/m^2
Coolant inlet temperature	298	°C
Coolant exit temperature	330	°C
Coolant pressure	7	MPa
Structure temperature limit	550	°C
Pressure stress limit	200	MPa
Thermal stress limit	400	MPa

Table 16.4-II.

THERMAL-HYDRAULIC DESIGN OF TITAN-II FIRST WALL

Channel outer diameter, b	30.0	mm
Channel inner diameter, a	27.0	mm
Wall thickness, t	1.5	mm
Erosion allowance	0.25	mm
Structure volume fraction	0.17	
Coolant volume fraction	0.62	
Void volume fraction	0.21	
Volumetric heating (structure)	202	MW/m^3
Volumetric heating (coolant)	270	MW/m^3
Total thermal power	770.2	MW
Coolant inlet temperature, T_{in}	298	°C
Coolant exit temperature, T_{ex}	330	°C
Maximum wall temperature, $T_{w,max}$	503	°C
Coolant pressure, p	7	MPa
Maximum primary stress	98	MPa
Maximum secondary stress	363	MPa
Coolant flow velocity, U	22.6	m/s
Mass flow rate	1.15×10^4	kg/s
Volumetric flow rate	10	m^3/s
Pressure drop, Δp	0.5	MPa
Total pumping power	12.5	MW
Reynolds number, Re	1.49×10^6	
Nusselt number, Nu	2360	
Prandtl number, Pr	16.5	
Critical heat flux, q''_{CHF}	8.3	Mw/m^2
Subcooling at exit, $T_{ex,sub}$	17	°C

Table 16.4-III.

THERMAL-HYDRAULIC DESIGN OF TITAN-II BERYLLIUM ZONE

Zone radial thickness	200	mm
Zone toroidal extent	30	mm
Wall thickness	1.4	mm
Structure volume fraction	0.12	
Coolant volume fraction	0.29	
Beryllium volume fraction	0.59	
Volumetric heating (structure)[a]	180	MW/m^3
Volumetric heating (coolant)[a]	240	MW/m^3
Volumetric heating (beryllium)[a]	140	MW/m^3
Total thermal power	1753.6	MW
Coolant inlet temperature	298	°C
Coolant exit temperature	330	°C
Maximum beryllium temperature	573	°C
Mass flow rate	2.6×10^4	kg/s
Volumetric flow rate	22.6	m^3/s
Coolant flow velocity[a]	14	m/s
Pressure drop[a]	1.0	MPa
Total pumping power	28.2	MW
Reynolds number[a]	2.7×10^5	
Nusselt number[a]	601	

(a) Values for the first cell of multiplier zone.

Table 16.4-IV.

THERMAL-HYDRAULIC DESIGN OF TITAN-II BREEDER/REFLECTOR ZONE

Zone radial thickness	100	mm
Zone toroidal extent	30	mm
Wall thickness	1.4	mm
Structure volume fraction	0.09	
Coolant volume fraction	0.91	
Volumetric heating (structure)	40	MW/m^3
Volumetric heating (coolant)	40	MW/m^3
Total thermal power	314.3	MW
Coolant inlet temperature	298	°C
Coolant exit temperature	330	°C
Maximum wall temperature	348	°C
Mass flow rate	4.66×10^3	kg/s
Volumetric flow rate	4.1	m^3/s
Coolant flow velocity	1	m/s
Pressure drop	5.0×10^{-4}	MPa
Total pumping power	5.1	MW
Reynolds number	1.5×10^5	
Nusselt number	376	

Table 16.4-V.

THERMAL-HYDRAULIC DESIGN OF TITAN-II SHIELD

Shield radial thickness	100	mm
Structure volume fraction	0.90	
Coolant volume fraction	0.10	
Total thermal power	159.8	MW
Coolant inlet temperature	298	°C
Coolant exit temperature	330	°C
Mass flow rate	2.44×10^3	kg/s
Volumetric flow rate	2.1	m^3/s
Total pumping power	2.6	MW
First Row of Channels		
Channel inner diameter	12.7	mm
Volumetric heating (structure)	22	MW/m^3
Volumetric heating (coolant)	10	MW/m^3
Maximum wall temperature	409	°C
Coolant flow velocity	6.5	m/s
Pressure drop	2.2×10^{-2}	MPa
Reynolds number	3.3×10^5	
Second Row of Channels		
Channel inner diameter	19.0	mm
Volumetric heating (structure)	9	MW/m^3
Volumetric heating (coolant)	5	MW/m^3
Maximum wall temperature	427	°C
Coolant flow velocity	3.7	m/s
Pressure drop	4.7×10^{-3}	MPa
Reynolds number	2.8×10^5	

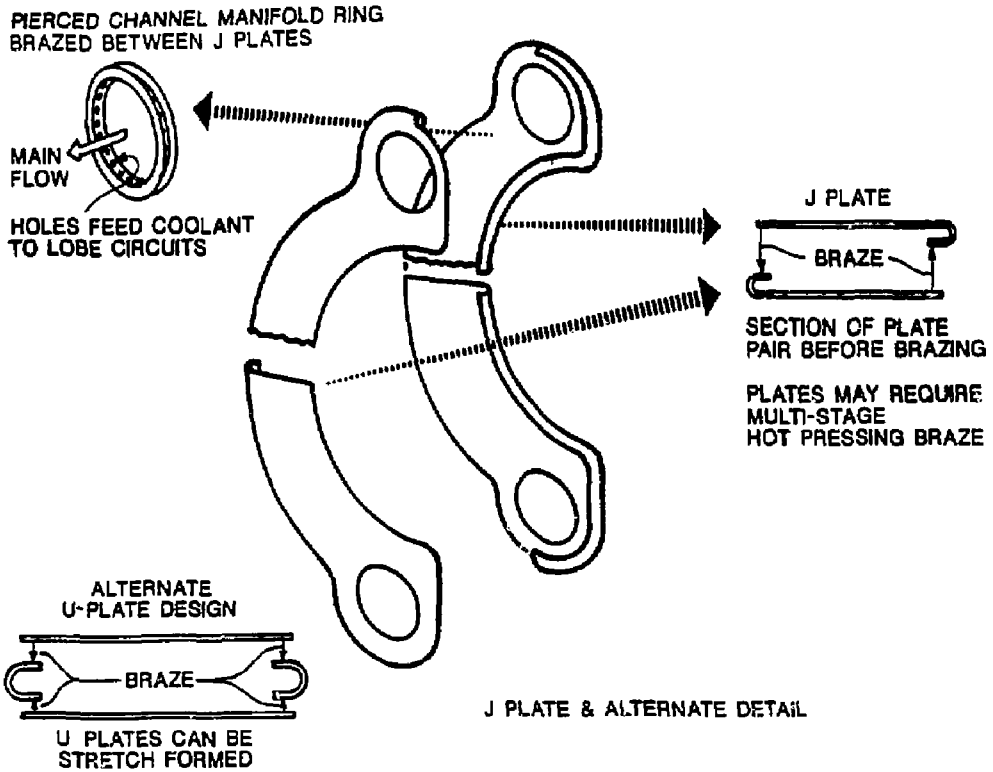

Figure 16.4-2. The TITAN-II blanket lobe, J-plate design.

blanket lobe is made of two plates, called "J-plates" because one edge of each plate is rolled to the appropriate radius to form a J-section. Both J-plates are made of the low-activation, high-strength ferritic steel, 9-C [2]. The first-wall plate is thicker than the other plate, since it is subject to erosion. Two plates are then brazed or welded together to form a complete blanket lobe. A channel manifold ring completes the lobe and allows the coolant and breeder mixture to flow. This configuration will require a multistage pressing operation, perhaps even hot-pressing to achieve this shape.

An alternate design, also shown in Figure 16.4-2, is the U-plate design. The advantages of this design are that the thin material can be used for both sides, and the edge U members are easier to make than the J-plates. However, acceptance of either configuration would depend on detailed investigation of the thick braze or weld area to ensure there is no focusing of thermal radiation or other heat-transfer problems.

Seventy blanket lobes are then stacked side-by-side to form a blanket module. The structural details of a blanket module are shown in Figure 16.4-3. This arrangement is structurally a membrane pressure vessel with balancing forces, derived from identical neighboring lobes, maintaining its flat sides. This configuration requires an external constraining structure to keep it pressed into oval form, which is readily derived from the shield as discussed below. The advantage of this design is that the structural fraction in the important near-first-wall radial zone is nearly as low as ideally possible, giving good tritium-breeding performance. This configuration also has a much lower void fraction when compared to a tubular design, giving a minimum-thickness blanket. The assembly technique for each blanket module is expected to be multistage brazing with intermediate leak checking. Since the lobes only require constraint in the blanket toroidal direction and because they are soft structurally in this direction, high precision is not necessary.

For the first wall, the structural-material temperature limit is taken at the centerline. The allowable peak, midline temperature of the 9-C alloy is 550 °C. The allowable primary stress, S_{mt}, for 9-C is 200 MPa. The coolant base pressure is 7 MPa. With the 4.6 MW/m^2 of surface heat loading, the lobe radius is conservatively selected at 1.5 cm. The first-wall thickness at the beginning of life (BOL) is selected at 1.5 mm. The plasma side of the first wall is designed with an erodible thickness of 0.25 mm. The BOL first-wall maximum surface temperature is 650 °C. The BOL midline temperature of 503 °C is 47 °C below the allowable temperature.

The primary stress, S_p, due to coolant pressure, is:

$$S_p = \frac{pr}{t} = 98.6 \text{ MPa}, \qquad (16.4\text{-}28)$$

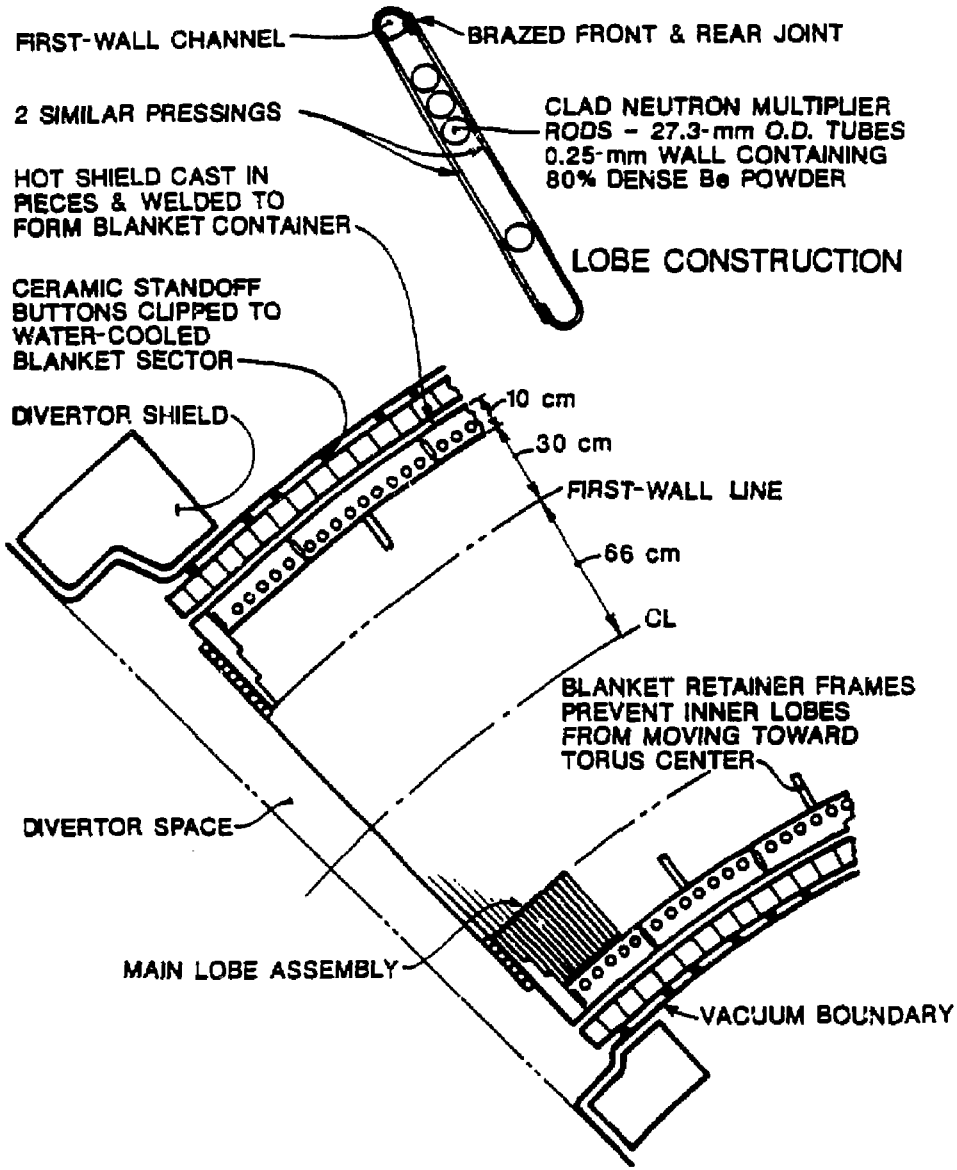

Figure 16.4-3. Equatorial-plane cross section of a TITAN-II blanket module.

where $r = 14.175\,\text{mm}$ is the lobe centerline radius and $t = 1.15\,\text{mm}$ is the wall thickness at the end of life.

The temperature stress, under these conditions, is a secondary stress with an allowable value of $2 \times S_{mt} = 400\,\text{MPa}$. The temperature stress in the TITAN-II first wall is estimated at:

$$S_{th} = \frac{\Delta T}{2} \frac{\alpha E}{1-\nu} = 363\ \text{MPa}, \tag{16.4-29}$$

for the temperature drop across the first wall of $\Delta T = 265\,°\text{C}$, a coefficient of thermal expansion for 9-C alloy of $\alpha = 1.11 \times 10^{6}\,/\,°\text{C}$, a Young's modulus of $E = 172\,\text{GPa}$, and Poisson ratio of $\nu = 0.3$. The lobed wall in the classical hoop-tension configuration (Figure 16.4-3) has a very high structural efficiency (ratio of mean stress under maximum loading to the allowable stress) and good swelling tolerance.

The split at the top and bottom of the torus divides the blanket and the shield into inner and outer half shells which are structurally independent. The tendency of the lobe flat sides to blow out has to be resisted by what are, in effect, the divertor walls (Figure 16.4-3). These wall are 12-cm-thick cantilever beam members which also derive some of their strength from their torsional stiffness and will require internal cooling. These walls are anchored to the 10-cm-thick shield shell by welds at the inside and outside of the shield. The shield is made of cast half-ring sectors, welded together at the inside edge (Figure 16.4-3).

Welding of the main body of the shield to give a 2.5-cm-thick continuous, semicircular member between divertors gives a sufficiently strong beam to prevent "concertina" expansion of the blanket lobes. The shell on the inside of the vertical split includes 15×3-cm retainer frames at about 0.5-m intervals which are welded into the shield. Each 0.5 m of the inner assembly has a force trying to increase its major radius. The magnitude of this expanding force:

$$\begin{aligned} F_{exp} &= \text{Blanket axial area} \times \text{Subtended angle} \times \text{Pressure} \\ &= \tfrac{\pi}{2}(0.96^2 - 0.66^2) \times \sin(10°) \times 7.0 \times 10^{6}\ \text{N} \\ &= 927{,}950\ \text{N}. \end{aligned} \tag{16.4-30}$$

Each inner assembly presses against both of the retainer frames with a total force of 1,317,866 N. Thus, given a coefficient of friction (ratio of the expanding to retainer forces) greater than 0.16, the lobe assembly will retain itself against "concertina" expansion sideways, ensuring that no outer shell force is required for stability of the inner shell. The 0.16 figure will need to be confirmed by experiment for use in the final design.

It should be pointed out that the present design is relatively flexible and a few of the parameters can easily be adjusted for the final design.

Immediately behind the shield there is a 5-cm-thick zone occupied by the toroidal field (TF) coil which is a multi-turn copper coil held in position by ceramic standoffs from the shield (Figure 16.4-3). The design of the standard elements to support the TF coils is comparatively straightforward since the TF coil has only gravitational and magnetic position stabilizing forces carried externally.

The vacuum boundary is a continuous, 5-mm-thick metal shell immediately outside the TF coil. Because of the large toroidal radius of 5.06 m, such a shell cannot withstand the atmospheric and water-pool pressures totalling about 3 atm without buckling. Accordingly, since the working stress is only about 7 MPa, nonconducting stabilizers similar to those used for the 5-cm-thick TF coil can be used. If necessary, the vacuum boundary can be electrically insulated in the toroidal direction by alternate layers of soft aluminum and hard, anodized 7075 aluminum-alloy sheets. The soft aluminum provides a deformable vacuum seal, and the anodized layer provides the electrical insulation. The two vacuum boundary skins can then be held together by 15-mm-thick stainless-steel, insulator-lined swagged clamps. Details of this method of vacuum-vessel insulation will still need to be demonstrated.

A number of electrically insulated penetrations of the vacuum shell also have to be made for the TF-coil leads. It is envisaged that the technology of automotive spark plugs can be developed to do this task which consists of embedding a precision ceramic insulator in soft metal (usually copper) gaskets. This technique is presently available for diameters an order of magnitude larger than spark plugs, and its extension to sizes relevant to TITAN-II appears feasible. This will also need to be developed.

A skirt, welded to the lower header system and extended to the pool bottom, will support the entire removable first wall, blanket, and shield assembly. This skirt will be of open-frame form to allow free circulation of the pool.

16.4.4. Discussion

The TITAN-II design uses an aqueous salt solution as the coolant. The coolant circulation is essentially loop-type, similar to that for TITAN-I, although the geometry of the blanket-coolant channels is very different. The aqueous salt solution has two advantages as coolant. First, the coolant can act as tritium breeder. Second, the salt content elevates the boiling point of the coolant which can be utilized to reduce primary-coolant pressure below the pressure in the steam generator, eliminating the need for

intermediate heat exchangers. Pressure reduction in a pure-water system cannot be realized because of the lower saturation temperature and the resulting lower critical heat flux.

Among other effects of the salt content, the specific heat capacity is reduced by a factor of about two while the density increases only by 15% which result in a significant reduction in the heat capacity of the coolant. The temperature rise of the primary coolant is 32 °C. Therefore, although the coolant pressure drop is only 1 MPa, the large coolant volume flow rate ($39\,m^3/s$) results in a pumping power of 49 MW, which is very close to that for TITAN-I.

The thermal-hydraulic design of TITAN-II is expected to have adequate safety margins. The maximum heat flux on the first-wall channel is 60% lower than the critical heat flux. The maximum temperature at the mid-plane of the first wall is 503 °C which is less than the allowable limit of 550 °C. The structure temperatures in the blanket and shield coolant channels have even greater safety margins. The maximum pressure stress is less than 50% of the allowable and the thermal stress is below its limit.

16.5. POWER-CYCLE ANALYSIS

The selection of the inlet and exit temperatures of the primary coolant (respectively, 298 and 330 °C) is motivated by the possibility of using a typical fission, pressurized-water-reactor (PWR) power cycle. The lithium-salt content of the TITAN-II aqueous coolant (6.4 at.%) elevates the boiling point of the coolant from 285 °C for pure water to 347 °C at a primary-coolant pressure of 7 MPa. With a primary-coolant pressure of 7 MPa, a higher steam pressure in the steam generator can be selected. During normal operation, if there is any steam-generator tube leakage, the primary coolant will not leak into the steam side. Therefore, the necessity for an intermediate heat exchanger (IHX) can be avoided, resulting in an increase in the power cycle efficiency. Somewhat higher steam temperatures can be obtained with higher primary-coolant pressure, but at the cost of additional expense and complexity associated with IHX and more robust primary piping. Therefore, the TITAN-II reference design uses a power cycle without an intermediate heat exchanger. The steam conditions are similar to those of an existing PWR-type power cycle.

The parameters of a typical PWR power cycle are readily available. The STARFIRE report [136] has a detailed discussion on PWR-type power cycles. That report also discusses some possible improvements which can raise the gross thermal efficiency by

Table 16.5-I.

COMPARISON OF SOME PWR POWER CYCLES

	STARFIRE PWR	Typical PWR
Primary coolant (water):		
Inlet temperature (°C)	280	298
Exit temperature (°C)	320	330
Coolant pressure (MPa)	13.8	15.5
Saturation temperature (°C)	335	345
Exit subcooling (°C)	15	15
Throttle steam conditions:		
Temperature (°C)	299	308
Pressure (MPa)	6.3	7.2
Saturation temperature (°C)	279	289
Gross thermal efficiency	0.34	0.346

one or two percentage points. Other nuclear steam supply systems and power cycles have been reported [137] which are applicable to the TITAN-II design. Table 16.5-I summarizes the parameters for PWR-type power cycles from these two references. These data show that with pure water as the primary coolant, gross thermal efficiency of 34% to 36% can be realized. Further increase of the primary-coolant pressure beyond 15 MPa will not increase the efficiency significantly.

Using an aqueous salt solution as the primary coolant allows the exit temperature of the primary coolant to be significantly increased at the same pressure as that for pure water. However, if the primary coolant pressure is higher than the steam generator pressure (about 7 MPa), then an IHX will be necessary for safety reasons. This reduces some of the benefits of higher primary-coolant exit temperatures. In addition, the use of IHXs increases the capital cost and complexity of the system. By designing for an over-pressure in the steam side, TITAN-II does not need an IHX under normal conditions to

isolate the primary coolant circuit. At 7 MPa pressure and a lithium content of 6.4 at.% in TITAN-II coolant, the primary coolant inlet and exit temperatures can be made equal to those for the typical PWR power cycle given in Table 16.5-I. The primary coolant pressure of 7 MPa is less than the steam generator pressure of 7.2 MPa for this cycle and considerably less than the 15 MPa required in a typical PWR. The parameters of TITAN-II reference power cycle are given in Table 16.5-II which has the same steam cycle parameters as found in Reference [137]. The estimated gross thermal efficiency of the TITAN-II power cycle is 35%.

16.6. SUMMARY AND CONCLUSIONS

The TITAN-II design uses an aqueous solution as the primary coolant and breeder. Two candidate lithium salts, lithium hydroxide (LiOH) and lithium nitrate ($LiNO_3$), were considered because they are highly soluble in water. The $LiNO_3$ salt was selected as the reference salt material for two main reasons. First, LiOH is more corrosive than $LiNO_3$ (Section 16.2.1). Recently, electrochemical corrosion tests were performed for aqueous LiOH and $LiNO_3$ solutions in contact with AISI 316L stainless steels [37]. It was found that stainless steels, particularly low-carbon steels, exhibit better corrosion resistance in $LiNO_3$ solution than in LiOH. Second, from the point of view of radiolysis, $LiNO_3$ solutions are also preferable. Radiolytic decomposition of water results in the formation of free radicals that will ultimately form highly corrosive hydrogen peroxide and OH ions. In an $LiNO_3$ nitrate solution, nitrate ions (NO_3) act as scavengers and reduce the probability of survival of highly reactive radicals in the water during exposure to radiation.

The low-activation ferritic alloy, 9-C, was chosen from among other reduced activation ferritics because of its good strength and elongation behavior after irradiation. The high chromium content (11 wt.%) of this alloy should provide good resistance to corrosion and stress corrosion cracking in an aqueous solutions. The low carbon content (0.09 wt.%), reduces the risk of hydrogen embrittlement. Although no data on the ductile-to-brittle transition temperature (DBTT) is available, it is believed that the high manganese content (6.5 wt.%) of the 9-C alloy will prevent the formation of delta-ferrite phases which are primarily responsible for increases of DBTT. The data base for corrosion of ferritics in $LiNO_3$ solutions is very limited. Indications are, however, that a high-concentration $LiNO_3$ solution does not exhibit unacceptable corrosion problems.

Stress-corrosion cracking (SCC) is a major concern in the nuclear industry. Most recent experiences with SCC in a nuclear environment clearly show that SCC can be

Table 16.5-II.

TITAN-II REFERENCE POWER CYCLE

Primary coolant (water):		
Total thermal power	3027	MW
Inlet temperature	298	°C
Exit temperature	330	°C
Coolant pressure	7	MPa
Saturation temperature	347	°C
Exit subcooling	17	°C
Mass flow rate	4.5×10^4	kg/s
Total pumping power	49	MW
Throttle steam conditions:		
Temperature	308	°C
Pressure	7.2	MPa
Saturation temperature	289	°C
Degree of superheat	19	°C
Gross thermal efficiency	0.35	

suppressed by reducing the oxygen content through the addition of hydrogen to the coolant. The production of tritium in an aqueous lithium-salt solution is seen as an SCC-controlling mechanism. The proper choice of structural material can further reduce the probability of SCC. In particular, coupling a high chromium content with a low carbon content is shown to reduce SCC. The ferritic alloy, 9-C, fulfills both requirements.

Another form of attack on structural material in an aqueous environment is hydrogen embrittlement. The main factors influencing hydrogen embrittlement are the hydrogen content and temperature of the structural alloy. Reducing the amount of atomic hydrogen available for solution in the structure and operating at high temperatures are the most effective means of reducing hydrogen attack. Atomic hydrogen is produced on metal surfaces during corrosion processes. Thus, minimizing corrosion also reduces hydrogen embrittlement of the structure. The production of tritium in the coolant does not necessarily result in an increased hydrogen attack because of rapid recombination to form molecular hydrogen or water molecules. In fact, the Nelson curves, used by the petrochemical industry as guidelines, show that chromium steels can operate at 400 °C with a hydrogen partial pressure of 17 MPa without experiencing hydrogen embrittlement [101].

Radiolytic decomposition of aqueous solutions exposed to a radiation environment is always cause for concern. Experimental data indicate that light-particle radiation (e, γ, X rays) of concentrated $LiNO_3$ salt solutions results in a decrease of decomposition products compared with regular water. Heavy-particle radiation (n, p, α, T) on concentrated $LiNO_3$ solutions also shows a decrease in the formation of radiolytic products, excepting oxygen. However, the production of tritium effectively reduces the oxygen content of the coolant by forming water molecules. Furthermore, the elevated operating temperature of the coolant is shown to be effective in reducing the formation of decomposition products in non-boiling nuclear systems. More experimental data are required so that the radiolytic behavior of concentrated salt solutions can be predicated with a higher degree of confidence.

Neutronics scoping studies resulted in a TITAN-II reference design with a total blanket thickness of 41.5 cm including the first wall, 20 cm of beryllium multiplier zone, 10 cm of ferritic steel breeder/reflector, and 10 cm of shield. With a ^6Li enrichment of 12% in the $LiNO_3$ solution, the tritium-breeding ratio (TBR) is estimated at 1.2 and the blanket energy multiplication at 1.36.

Neutronics scoping studies have shown that the TITAN-II design requires a neutron multiplier to achieve an adequate TBR. Beryllium is the primary neutron multiplier for the TITAN-II design. Investigation of the swelling behavior of beryllium shows the need

for using either low-density, sphere-packed or high-density, fine-grained beryllium. Depending on the type of beryllium chosen, different operating conditions must be satisfied to ensure minimum swelling and retention of structural integrity. Beryllium corrosion by an aqueous solution was also investigated. Past experience shows that minimizing carbonates, sulfates, and chlorates in solution reduces corrosion of beryllium. Coatings have also been developed and their effectiveness has been demonstrated. However, since most of the coatings were developed for radiation-free environments, research is needed to develop coatings that can withstand harsh radiation environments. For the TITAN-II design, a cladding of the 9-C alloy surrounds the beryllium rods.

The primary coolant contains 6.4 at.% lithium with a ^{6}Li enrichment of 12%. Estimated properties of this solution were used in the thermal-hydraulic calculations. Compared to water, this aqueous solution has a higher density, a lower specific heat capacity, and a higher boiling point. This implies that the thermal-hydraulic design of such an aqueous salt blanket will be different from that of a pure-water-cooled design. A lower coolant pressure or a higher operating temperature can be chosen.

Taking advantage of the elevated boiling point of the solution, the reference TITAN-II design operates at a coolant pressure of 7 MPa, with inlet and outlet temperatures of 298 and 330 °C, respectively. The design can handle a first-wall heat flux of 4.6 MW/m^2 using subcooled-flow-boiling heat transfer. The beginning-of-life first-wall midline temperature is 503 °C, which is below the temperature limit for alloy 9-C (550 °C). The primary-coolant pressure has been selected to be lower than the steam-generator pressure (7.2 MPa) so that any leakage in the steam-generator tubes does not result in leaks of the tritium-containing primary coolant to the steam cycle. The necessity for an intermediate heat exchanger is thereby avoided. Pressure reduction in a pure-water system cannot be realized because of the lower saturation temperature and the resulting lower critical heat flux. This power conversion system has a gross thermal efficiency of 35%.

The engineering design study of the TITAN-II FPC indicates that this design is technically feasible. Design approaches to address different critical design areas have been identified. However, experimental investigations and design improvements in several areas are needed to confirm the findings. In the materials area, experimental measurements of the effects of corrosion, hydrogen embrittlement, and radiolysis in aqueous-coolant/ferritic-steel systems are needed. Experimental data to confirm the estimated physical properties of nitrate solution, confirmation of the $LiNO_3$ subcooled-flow-boiling heat transfer, critical heat flux, and pressure drop are essential.

REFERENCES

[1] D. Steiner *et al.*, "A Heavy Water Breeding Blanket," in *Proc. 11th Symp. on Fusion Engineering*, Austin, Texas (1985).

[2] D. S. Gelles, N. M. Ghoniem, and R. W. Powell, "Low Activation Ferritic Alloys Patent Description," University of California Los Angeles report UCLA/ENG-87-9/PPG-1049 (1987).

[3] M. G. Fontana and N. D. Greene, *Corrosion Engineering*, McGraw-Hill International Book Company, Singapore (1978).

[4] J. C. Danko, "Corrosion in the Nuclear Power Industry," *Metals Handbook*, 9th edition, **13** (1987) 927.

[5] H. R. Copson, *Corrosion Resistance of Metals and Alloys*, F. L. LaQue and H. R. Copson (Eds.), American Chemical Society, Reinhold Publishing Corporation, New York (1963) p. 72.

[6] P. A. Akolzin, "The Role of Temperature in the Electrochemical Corrosion of Steel," *Proc. High Temperature High Pressure Electrochemistry in Aqueous Solutions*, sponsored by Central Electricity Research Laboratory, England, National Association of Corrosion Engineers, USA, University of Surrey, England (January 7-12, 1973) 414.

[7] M. E. Indig and A. R. McIree, "High Temperature Electrochemical Studies of the Stress Corrosion of Type 304 Stainless Steel," *Corrosion* **35** (1979) 288.

[8] M. J. Povich and D. E. Broecker, "The Stress Corrosion Cracking of Austenitic Stainless Steel Alloys in High Temperature Air Saturated Water," *Mater. Performance* **18** (1979) 41.

[9] Y. Park, J. R. Galvelle, A. K. Agrawal, and R. W. Staehle, "Stress Corrosion Cracking and Anodic Behavior of AISI 304 Stainless Steel, Inconel 600, and Incoloy 800 Straining in Boiling NaOH Solutions," *Corrosion* **34** (1978) 413.

[10] W. Schoch, H. Wiehn, E. Richter, and H. Schuster, *VGB-Mitteilungen* **52** (1972) 288.

[11] W. H. M. Huijbregts, *KEMA Scientific and Technological Report* **3** (1985) 33.

[12] W. Kastner, K. Roedle, and H. Tratz, *VGB-Kraftwerktechnik* **64** (1984) 452.

[13] J. B. Lee, A. K. Agrawald, and R. W. Staehle, "Corrosion and Corrosion Cracking of Materials for Water-Cooled Reactors," Electric Power Research Institute (EPRI) report NP-1741 (1981).

[14] G. A. A. Van Osch and W. H. M. Huijbregts, "Corrosion Potential Measurements in Boiler Water: The Influence of Oxygen Content," *Corrosion* **42** (1986) 120.

[15] M. G. Fontana and N. D. Greene, *Corrosion Engineering*, McGraw-Hill International Book Company, Singapore (1978) p. 104.

[16] K. N. Nesmeyanova, E. B. Matzevich, and V. G. Kasatkina, in *Proc. 3rd Int. Conf. Metallic Corrosion*, Moscow (1966).

[17] T. Maekawa, M. Kagawa, and N. Nakajima, "Corrosion Behavior in High-Temperature Water and Steam," *J. Japan Inst. Metals* **31** (1967) 1213.

[18] G. Ito, Y. Shimidzu, and T. Usuki, *Corrosion Eng.* **17** (1968) 440.

[19] T. Fujii, T, Kobayashi, and G. Ito, "The Influence of Dissolved Oxygen on the Electrochemical Behavior of Mild Steel and Stainless Steel in Aqueous Solution at Temperatures above 100°C," *Proc. High Temperature High Pressure Electrochemistry in Aqueous Solutions*, sponsored by Central Electricity Research Laboratory, England, National Association of Corrosion Engineers, USA, University of Surrey, England (January 7-12, 1973) 416.

[20] M. G. Fontana and N. D. Greene, *Corrosion Engineering*, McGraw-Hill International Book Company, Singapore (1978) p. 200.

[21] T. R. Weber , M. A. Stranick, and M. S. Vukasovich, "Molybdate Corrosion Inhibition in Deaerated and Low-Oxygen Waters," *Corrosion* **42** (1986) 542.

[22] M. A. Stranick, "The Corrosion Inhibition of Metals by Molybdates, Part 1: Mild Steel," *Corrosion* **40** (1984) 296.

[23] L. G. Ljungberg, D. Cubicciotti, and M. Trolle, "Material Behavior in Alternate (Hydrogenated) Water Chemistry in the RINGHALS-1 Boiling Water Reactor," *Corrosion* **42** (1986) 263.

[24] B. M. Gordon, W. L. Clarke, M. E. Indig, A. E. Pickett, and M. T. Wang, *Corrosion/81*, Paper No. 20, National Association of Corrosion Engineers, Houston, TX (1981).

[25] R. L. Gowan *et al.*, "Assessment of Operation of the Dresden-2 Nuclear Power Station Under Hydrogen Water Chemistry," prepared by General Electric for Nuclear Energy Business Operation (July 1984).

[26] B. M. Gordon, C. W. Jewett, A. E. Pickett, and M. E. Indig, "Corrosion Resistance Improvement of Ferritic Steels through the Hydrogen Addition to the BWR Coolant," *Proc. of Topical Conference on Ferritic Alloys for Use in Nuclear Energy Technologies*, AIME, Snowbird, UT (June 19-23, 1983) 65.

[27] A. McNinn, "Stress Corrosion of High-Chromium Nickel-Base Metals and AISI 316 Nuclear Grade Stainless Steel in Simulated Boiler Water Reactor Environment," *Corrosion* **42** (1986) 682.

[28] A. B. Bond and H. J. Dundas, "Stress Corrosion Cracking of Ferritic Stainless Steels," *Proc. of Stress Corrosion Cracking and Hydrogen Embrittlement of Iron Base Alloys*, R. W. Staehle, J. Hochmann, R. D. McCright, and J. E. Slate (Eds.), Unieux-Firminy, France (June 12-16, 1973) 1136.

[29] A. B. Bond and H. J. Dundas, "The Effects of Composition on the Stress Corrosion Cracking of Ferritic Steels," *Corrosion* **24** (1968) 344.

[30] R. N. Parkins, "Environmental Aspects of Stress Corrosion Cracking in Low Strength Ferritic Steels," *Proc. of Stress Corrosion Cracking and Hydrogen Embrittlement of Iron Base Alloys*, R. W. Staehle, J. Hochmann, R. D. McCright, and J. E. Slate (Eds.), Unieux-Firminy, France (June 12-16, 1973) 601.

[31] P. L. Andresen, " The Effects of Aqueous Impurities on IGSCC of Sensitized Type 304 Stainless Steel," Electric Power Research Institute (EPRI) report NP-3384 (1983).

[32] R. N. Parkins and R. Usher, *Proc. 1st Int. Congr. Metallic Corrosion*, Butterworths, London (1961) 289.

[33] Z. Szklarska-Smialowska, "Effect of Potential of Mild Steel on Stress Corrosion Cracking in Ammonium Nitrate Solutions," *Corrosion* **20** (1964) 198.

[34] W. Radeker and H. Grafen, *Stahl und Eisen* **76** (1956) 1616.

[35] H. Mazille and H. H. Uhlig, "Effect of Temperature and Some Inhibitors on Stress Corrosion Cracking of Carbon Steels in Nitrate and Alkaline Solutions," *Corrosion* **28** (1972) 427.

[36] R. Waeben, W. Bogaert, and M. Embrecht, "Initial Corrosion Evaluation of Candidate Materials for an ASCB Driver Blanket for NET," *Proc. IEEE 12th Symp. Fusion Engineering*, Monterey, CA (October 12-16, 1987) 1332.

[37] W. F. Bogaerts, M. J. Embrechts, and R. Waeben, "Application of the Aqueous Self-Cooled Blanket Concept to a Tritium Producing Shielding Blanket for NET," University of Leuven (Belgium) report EUR-FU/XII-80/87/75 (1987).

[38] H. A. Bethe and J. Ashkin, *Experimental Nuclear Physics*, E. Serge (Ed.), John Wiley & Sons, Inc., New York (1953) p. 166.

[39] R. H. Schuler and A. O. Allen, "Radiation Chemistry Studies with Cyclotron Beams of Variable Energy: Yield in Aerated Ferrous Sulfate Solutions," *J. Am. Chem. Soc.* **79** (1957) 1565.

[40] P. R. Burch, *Radiat. Res.* **6** (1957) 289.

[41] E. Pollard, *Advances in Biological and Medical Physics* **3** (1953) 153.

[42] A. O. Allen, *The Radiation Chemistry of Water and Aqueous Solutions*, D. Van Nostrand Company, Inc., New Jersey (1961).

[43] A. K. Pikaev, in *Pulse Radiolysis of Water and Aqueous Solutions*, E. J. Hart (Ed.), Indiana University Press, Bloomington & London (1967).

[44] D. C. Walker, "Hydrated Electrons in Chemistry," in *Radiation Chemistry, Vol. 1*, R. F. Gould (Ed.), American Nuclear Society, Washington D. C. (1968).

[45] P. Gunther, "Helium-bildung aus α-Strahlern," *Z. Phys. Chem.* **185** (1939) 367.

[46] P. Cohen, "Water Coolant Technology of Power Reactors," American Nuclear Society (1980).

[47] W. M. Dale, L. H. Gray, and W. J. Meredith, *J. Phil. Trans.* **A242** (1949) 33.

[48] W. Duane and O. Scheuer, *Le Radium* **10** (1913) 33.

[49] M. Lefort, "Radiochimie Des Solutions Aqueouses," *J. Chem. Phys.* **51** (1954) 351.

[50] M. Daniels, "Radiolysis and Photolysis of the Aqueous Nitrate System,"in *Radiation Chemistry, Vol. 1*, R. F. Gould (Ed.), American Nuclear Society, Washington D. C. (1968).

[51] G. H. Jenks, "Effects of Reactor Operation on HFIR Coolant," Oak Ridge National Laboratory report ORNL-3848 (1985).

[52] J. T. Kiwi and M. Daniels, "On the Radiolysis of Concentrated Alkaline and Calcium-Nitrate Solutions," *J. Inorg. Nucl. Chem.* **40** (1978) 576.

[53] H. A. Schwarz, "The Effect of Solutes on the Molecular Yields in the Radiolysis of Aqueous Solutions," *J. Am. Chem. Soc.* **77** (1955) 4960.

[54] J. A. Lane, H. G. MacPherson, and F. Maslan, "Fluid Fuel Reactors," in *Atoms for Peace*, Addison-Wesley Publishing Company, Inc., New York (1958).

[55] T. J. Sworski, "Yield of Hydrogen Peroxide in the Decomposition on Water by Cobalt γ-Radiation. I: Effect of Bromide Ion," *J. Am. Chem. Soc.* **76** (1954) 4687.

[56] A. O. Allen and R. A. Holroyd, "Peroxide Yield in the γ-Irradiation of Air-saturated Water," *J. Am. Chem. Soc.* **77** (1955) 5852.

[57] R. G. Sowden, "The Effect of Nitrate Ion on the Yield of Hydrogen from Water Radiolysis," *J. Am. Chem. Soc.* **79** (1957) 1263.

[58] M. Burton and K. C. Kurien, "Effects of Solute Concentration in Radiolysis of Water," *J. Phys. Chem.* **63** (1959) 899.

[59] W. G. Burns and P. B. Moore, "The Radiation Chemistry of High Temperature (300-400 °C) Water," Harwell Laboratory report AERE-R9516, England (1980).

[60] R. F. S. Robertson and P. G. Anderson, "Out-Reactor Test of HTP Loop," National Research Council of Canada report CRDC-596 (June 1955); also issued as Atomic Energy of Canada, Ltd. report AECL-195.

[61] T. Kambara, R. M. Whites, and F. S. Rowland, "The Reactions of Recoil Tritium Atoms in Aqueous Solution," *J. Inorg. Nucl. Chem.* **21** (1961) 210.

[62] R. H. Wood, University of Delaware, Newark, personal communication, August 1987.

[63] L. V. Puchkov and V. G. Matashkin, "Densities of $LiNO_3$–H_2O and $NaNO_3$–H_2O Solutions at Temperatures in the Range 25 – 300 °C," *J. App. Chem. USSR* **43** (1970) 1864.

[64] L. V. Puchkov, V. G. Matashkin, and R. P. Matveeva, "Density of Aqueous Lithium Nitrate Solutions at High Temperatures (up to 350°C) and Concentrations," *J. App. Chem. USSR* **52** (1979) 1167.

[65] L. V. Puchkov and P. M. Sargaev, "Viscosities of Lithium, Sodium, Potassium, and Ammonium Nitrate Solutions at Temperatures up to 275°C," *J. App. Chem. USSR* **46** (1973) 2367.

[66] L. V. Puchkov and P. M. Sargaev, "Dependence of Viscosity of Electrolyte Solutions on Temperature and Concentration," *J. App. Chem. USSR* **47** (1974) 280.

[67] R. H. Wood and J. R. Quint, "A Relation between the Critical Properties of Aqueous Salt Solutions and the Heat Capacity of the Solutions Near the Critical Point Using a Single-Fluid Corresponding-States Theory," *J. Chem. Thermodynamics* **14** (1982) 14.

[68] W. L. Marshall and E. V. Jones, "Liquid-Vapor Critical Temperatures of Aqueous Electrolyte Solutions," *J. Inorg. Nucl. Chem.* **36** (1974) 2313.

[69] S. Sourirajan and G. C. Kennedy, "The System H_2O–NaCl at Elevated Temperatures and Pressures," *Am. J. Sci.* **260** (1962) 115.

[70] H. Ozbek and S. L. Phillips, "Thermal Conductivity of Aqueous Sodium Chloride Solutions from 20 to 330°C," *J. Chem. Eng. Data* **25** (1980) 263.

[71] G. A. Sacchetto, G. G. Bombi, and C. Macca, "Vapor Pressure of Very Concentrated Electrolyte Solutions," *J. Chem. Thermodynamics* **13** (1981) 31.

[72] "Standards for Protection Against Radiation," U. S. Nuclear Regulatory Commission, Code of Federal Regulations, Title 10, Part 0 to 199 (1986).

[73] D. N. Braski, "The Effect of Neutron Irradiation on the Tensile Properties and Microstructure of Several Vanadium Alloys," in *Proc. ASTM Conf. on Fusion Reactor Materials*, Seattle, WA (1986).

[74] W. E. Kenedy, Jr. and F. M. Mann, "Potential Low-Level Waste Disposal Limits for Fusion Radionuclides," *Trans. Am. Nucl. Soc.* **45** (1983) 51.

[75] F. M. Mann, "Reduced Activation Calculations for the Starfire First Wall," *Fusion Technol.* **6** (1984) 273.

[76] S. A. Fetter, "Radiological Hazards of Fusion Reactors: Models and Comparisons," Ph. D. Thesis, University of California Berkeley (1985).

[77] D. G. Doran, A. F. Rowcliffe, and F. M. Mann, "Prospects for Reduced Activation Alloys," *J. Nucl. Mater.* **141-143** (1986) 1074.

[78] T. Lechtenberg, "Irradiation Effects in Ferritic Steels," *J. Nucl. Mater.* **133-134** (1985) 149.

[79] R. L. Klueh, D. S. Gelles, and T. A. Lechtenberg, "Development of Ferritic Steels for Reduced Activation: The U. S. Program," *J. Nucl. Mater.* **141-143** (1986) 1081.

[80] C. Y. Hsu and T. A. Lechtenberg, "Alloy Development for Irradiation Performance, ADIP Semiannual Progress Report," U. S. Department of Energy report DOE/ER-0045/15 (Sept. 30, 1985) 137.

[81] J. M. Vitek and R. L. Klueh, "Alloy Development for Irradiation Performance, ADIP Semiannual Progress Report," U. S. Department of Energy report DOE/ER-0045/12 (March 31, 1984) 110.

[82] T. A. Lechtenberg, General Atomics, San Diego, CA, private communication, March 1987.

[83] E. T. Cheng and R. W. Conn, "Waste Disposal Ratings in the TITAN RFP Reactor," *Proc. IEEE 12th Symp. on Fusion Engineering*, Monterey, CA (October 12-16, 1987) 913.

[84] B. Craig, "Hydrogen Damage," *Metals Handbook*, 9th edition **13** (1987) 163.

[85] H. Howarth, "The Oxidation Resistance of Low-Alloy Steels," *Corrosion: Metal/Environment Reactions*, L. L. Shreir (Ed.), Newnwe-Butterworth, London (1977) 7:13.

[86] L. Raymond, "Evaluation of Hydrogen Embrittlement," *Metals Handbook*, 9th edition **13** (1987) 283-290.

[87] R. W. Staehle, J. Hochmann, R. D. McCright, and J. E. Slate (Eds.), *Proc. of Stress Corrosion Cracking and Hydrogen Embrittlement of Iron Base Alloys*, Unieux-Firminy, France (June 12-16, 1973).

[88] P. Azou (Ed.), *Third International Congress on Hydrogen and Materials*, Pergamon Press (1982).

[89] C. D. Beachem (Ed.), *Hydrogen Damage*, American Society for Metals (1977).

[90] I. M. Bernstein and A. W. Thompson (Eds.), *Hydrogen Effects in Metals*, American Institute of Mining, Metallurgical, and Petroleum Engineers (1981).

[91] H. H. Johnson, E. J. Schneider, and A. R. Troiano, *Trans. American Inst. Mining Engineers* **212** (1958) 5.

[92] R. P. M. Procter and H. W. Paxton, *Trans. Amer. Soc. Metals* **62** (1969) 989.

[93] W. W. Gerberich, "Effect of Hydrogen on High Strength and Martensitic Steel," in *Hydrogen in Metals*, I. M. Bernstein and A. W. Thompson (Eds.), American Society for Metals (1974) 115.

[94] G. Sandoz, "A Unified Tl eory for Some Effects of Hydrogen Source, Alloying Elements and Potential on Crack Growth in Martensitic AISI 4330 Steel," *Metall. Trans.* **3** (1972) 213.

[95] B. A. Graville, R. G. Baker, and F. Watkinson, *Br. Weld J.* **14** (1967) 337.

[96] D. H. Zhon, W. X. Zhon, and Z. L. Xu, "Hydrogen Degradation of 21-6-9 and Medium Carbon Steels by Disk-Pressure Test," *J. Nucl. Mater.* **141-143** (1986) 503.

[97] H. R. Gray, "Testing for Hydrogen Environment Embrittlement: Experimental Variables," *Hydrogen Embrittlement Testing*, American Society for Testing and Materials (ASTM STP 543), Philadelphia (1974) p. 133.

[98] J. P. Fidelle, R. Borudeur, C. Rowx, and M. Rapin, "Disk Pressure Testing of Hydrogen Environemnt Embrittlement," *Hydrogen Embrittlement Testing*, American Society for Testing and Materials (ASTM STP 543), Philadelphia (1974) p. 221.

[99] W. T. Chandler and R. J. Walter, "Testing to Determine the Effect of High-Pressure Hydrogen Environments on the Mechanical Properties of Metals," in *Hydrogen Embrittlement Testing*, American Society for Testing and Materials (ASTM STP 543), Philadelphia (1974) p. 171.

[100] R. S. Treseder, "Guarding Against Hydrogen Embrittlement," *Chem. Eng.* **29** (1981) 105.

[101] "Steels for Hydrogen Service at Elevated Temperatures and Pressures in Petroleum Refineries and Petrochemical Plants," API Publication 941, 2nd edition (1971).

[102] D. Webster and G. J. London (Eds.), *Beryllium Science and Technology,* Plenum Press, New York and London (1979).

[103] J. N. Wanklyn and P. J. Jones, "The Aqueous Corrosion of Reactor Metals," *J. Nucl. Mater.* **63** (1962) 291.

[104] A. J. Stonehouse and W. W. Beaver, "Beryllium Corrosion and How to Prevent It," *Mater. Prot.* 4 (1965) 24.

[105] P. D. Miller and W. K. Boyd, "Beryllium Deters Corrosion - Some Do's and Don'ts," *Mater. Eng.* **68** (1968) 33.

[106] J. Brooker and A. J. Stonehouse, "Chemical Conversion Coatings Retard Corrosion of Beryllium," *Mater. Prot.* **8** (1969) 43.

[107] J. B. Rich and G. P. Walters, "The Effects of Heating Neutron Irradiated Beryllium," *J. Nucl. Mater.* **1** (1959) 96.

[108] C. E. Ells and E. C. W. Perryman, "Effects of Neutron-Induced Gas Formation on Beryllium," *J. Nucl. Mater.* **1** (1959) 73.

[109] J. R. Weir, "The Effects of High-Temperature Reactor Irradiation on Some Physical and Mechanical Properties of Beryllium," *Proc. of Int. Conf. Metallurgy of Beryllium,* Institute of Metals, London (October 1961) 362.

[110] J. B. Rich and R. S. Barnes, "Mechanical Properties of Some Highly Irradiated Beryllium," *J. Nucl. Mater.* 4 (1961) 287.

[111] M. O. Tucker and R. J. White, "The Geometry in Interlinked Grain Edge Porosity," *Res Mechanica* **1** (1980) 21.

[112] J. M. Beeston, M. R. Martin, C. R. Brickman, G. E. Korth, and W. C. Francis, *Symp. on Materials Performance in Operating nuclear Systems,* Ames Laboratory report CNF-730801, Ames, IA (August 1978) 59.

[113] J. M. Beeston, L. G. Miller, E. L. Wood, and R. W. Moir, "Comparison of Compression Properties and Swelling of Beryllium Irradiated at Various Temperatures," Idaho National Engineering Laboratory report EGG-FT-6608 (1984).

[114] R. S. Barnes and G. B. Redding, "Neutron Lifetime Measurement in the Fast Reactors Zeus and Zephyr," *Nucl. Energy* **10** (1959) 22.

[115] J. B. Rich, "The Mechanical Properties of Beryllium Irradiated At 350 and 600 °C," *The Metallurgy of Beryllium*, Institute of Metals, Chapman and Hall, Ltd., London (1963) 135.

[116] L. E. Muir, *Interfacial Phenomena in Metals and Alloys*, Addison-Wesley Publishing Corp., Reading, MA (1975) 124.

[117] W. G. Wolfer and T. J. McGarville, "Swelling of Beryllium," in *Damage Analysis and Fundamental Studies*, U. S. Department of Energy report DOE/ER-0046/19 (November 1984).

[118] N. L. Peterson, "Self-Diffusion in Pure Metals," *J. Nucl. Mater.* **69 & 70** (1978) 3.

[119] J. M. Beeston, "Gas Release and Compression Properties in Beryllium Irradiated at 600 and 700 °C," *Effects of Irradiation on Structural Metals*, American Society of Testing and Materials (ASTM STP 426) (1967) 135.

[120] G. P. Marino, "The Porosity Correction Factor for the Thermal Conductivity of Ceramic Fuels," *J. Nucl. Mater.* **38** (1971) 178.

[121] C. E. Ells and J. R. Weir, "The Effects of Neutron Irradiation on the Plastic Deformation and Fracture of Beryllium," *J. Nucl. Mater.* **13** (1964) 49.

[122] L. G. Miller, J. M. Beeston, B. L. Harris, and C. P. C. Wong, "Special Topics Reports for the Reference Tandem Mirror Fusion Breeder: Beryllium Lifetime Assessment," Lawrence Livermore National Laboratory report UCID-20166 (1984).

[123] T. J. McCarville, D. H. Berwald, W. Wolfer, F. J. Fulton, J. D. Lee, *et al.*, "Technical Issues for Beryllium Use in Fusion Blanket Applications," Lawrence Livermore National Laboratory report UCID-20319 (1985).

[124] W. W. Engle, Jr., "A User's Manual for ANISN, A One-Dimensional Discrete Ordinates Transport Code with Anisotropic Scattering," Oak Ridge Gaseous Diffusion Plant, K-1693 (1967).

[125] R. MacFarlane, "Nuclear Data Libraries from Los Alamos for Fusion Neutronics Calculations," *Trans. Am. Nucl. Soc.* **36** (1984) 271.

[126] A. E. Bergles and W. M. Rohsenow, *J. Heat Trans.* **C86** (1964) 365.

[127] W. H. Jens and P. A. Lottes, "Analysis of Heat Transfer, Burnout, Pressure Drop and Density Data for High Pressure Water," U. S. Atomic Energy Commission report ANL-4627 (1951).

[128] R. J. Weatherhead, "Nucleate Boiling Characteristics and Critical Heat Flux Occurrence in Subcooled Axial Flow Water System," U. S. Atomic Energy Commission report ANL-6675 (1962).

[129] J. R. S. Thom, W. M. Walker, T. A. Fallon, and G. F. S. Reising, "Boiling in Subcooled Water During Flow in Tubes and Annuli," *Proc. Inst. Mech. Engr.* **3C** (1965-66) 180.

[130] R. D. Boyd, C. P. C. Wong, and Y. S. Cha, "Technical Assessment of Thermal-Hydraulics for High Heat Flux Fusion Components," Sandia National Laboratory report SAND-84-0159 (1985).

[131] S. L. Milora, S. K. Combs, and C. A. Foster, "A Numerical Model for Swirl Flow Cooling in High-Heat-Flux Particle Beam Targets and the Design of a Swirl-Flow-Based Plasma Limiter," Oak Ridge National Laboratory report TM-9183 (1984).

[132] M. Z. Hasan, M. M. Hasan, R. Eichhorn, and J. H. Lienhard, "Boiling Burnout During Crossflow Over Cylinders," *J. Heat Trans.* **C103** (1981) 478.

[133] L. S. Tong, *Boiling Heat Transfer and Two-Phase Flow,* Robert E. Krieger Publishing Co., New York (1975).

[134] H. Schlichting, *Boundary Layer Theory,* McGraw-Hill Book Co., New York (1979).

[135] J. G. Collier, *Convective Boiling and Condensation,* McGraw-Hill, London (1972).

[136] C. C. Baker, M. A. Abdou, R. M. Aron, *et al.*, "STARFIRE– A Commercial Tokamak Fusion Power Plant Study," Argonne National Laboratory report ANL/FPP-80-1 (1980).

[137] "Steam/Its Generation and Use," Babcock & Wilcox Co. (1978).

17. TITAN-II DIVERTOR ENGINEERING

Patrick I. H. Cooke
Richard L. Creedon
Charles C. Bathke
Steven P. Grotz
Shahram Sharafat
James P. Blanchard
Mohammad Z. Hasan

Contents

17. TITAN-II DIVERTOR ENGINEERING

17.1. INTRODUCTION

This section describes the engineering design of the divertor of TITAN-II, including the thermal and mechanical design of the divertor components, materials selection, and fabrication issues. The design of the impurity-control system poses some of the most severe problems of any component of a DT fusion reactor. For TITAN, the divertor design represents (perhaps together with the design of the oscillating-field current-drive system, described in Section 7) the most critical engineering and physics issues for the reactor.

The two main design issues for the divertor system are to achieve heat loadings on the divertor collector plate (or target) that do not exceed the maximum acceptable level, while simultaneously ensuring that the sputtering erosion rate does not lead to an early failure of the component. These two aims tend to conflict, because the high heat loadings which inevitably occur on the divertor target require the use of thin structures to minimize temperature differences and thermal stresses, while a thick structure is necessary to give a long life against erosion.

The background behind the toroidal-field-divertor design for TITAN-I was given in Section 11; the considerations for TITAN-II are the essentially the same. An account of the magnetics analysis for the divertor is contained in Section 4.4 and the edge-plasma and neutral-particle modeling, which had a strong bearing on the engineering of the divertor, are described in Sections 5.4 and 5.5, respectively.

As discussed in Section 4.4, the TITAN divertor uses an "open" configuration in which the divertor target is located close to the null point, facing the plasma, rather than in a separate chamber. This positioning takes advantage of the increased separation between the magnetic field lines (flux expansion) in this region, which tends to reduce the heat loading on the divertor plate because the plasma flowing to the target is "tied" to the field lines. The high plasma density in front of the divertor target ensures that the neutral particles emitted from the surface have a short mean free path; a negligible fraction of these neutral particles enter the core plasma (Section 5.5).

The magnetic design (Section 4.4) focussed on maximizing the achievable degree of flux expansion in order to minimize the peak heat flux on the divertor target while

minimizing the divertor-coil currents and reducing the joule losses in the divertor coils. The toroidal-field-coil design for TITAN-II, which consists of copper coils as opposed to the integrated blanket coils (IBCs) of TITAN-I, prompted a new divertor magnetic design. The final magnetic design, similar to that of TITAN-I, includes three divertor modules, located 120° apart in the toroidal direction. An equatorial-plane cross section of a quadrant of the TITAN-II fusion power core including one of the divertors is shown in Figure 17.1-1. The magnetic field lines are diverted onto the divertor plate using one nulling and two flanking coils which localize the nulling effect. No divertor-trim coils are required for the TITAN-II design. The use of copper coils reduces the joule losses in the TITAN-II divertor coils to 9.8 MW which are much smaller than that of the TITAN-I IBC divertor coils (120 MW).

The results of the magnetic design of TITAN-II divertor (*e.g.*, field-line connection length) were not sufficiently different from the results for TITAN-I to warrant a separate edge-plasma analysis. A summary of the results of the edge-plasma modeling for TITAN-I, which are also used for the TITAN-II design, is given in Table 17.1-I and are described in detail in Section 5.4. The plasma power balance is controlled by the injection of a trace amount of a high atomic-number impurity (xenon) into the plasma, causing strong radiation from the core plasma, the scrape-off layer (SOL) plasma, and the divertor plasma. About 95% of the steady-state heating power (alpha particle and ohmic heating) can be radiated to the first wall and divertor plate, with about 70% being radiated from the core plasma (*i.e.*, inside the separatrix). This intense radiation reduces the power deposited on the divertor target by the plasma to an acceptably low level. Preliminary experimental results suggest that beta-limited RFP plasmas can withstand a high fraction of power radiated without seriously affecting the operating point (Section 5.3); this behavior contrasts with that observed in tokamaks, in which a high radiation fraction appears to lead to a plasma disruption. The radiative cooling also reduces the electron temperature at the first wall and divertor target (also assisted by recycling) which, in turn, reduces the sputtering erosion problem.

The final TITAN-II divertor design represents the results of extensive iterations between edge-plasma analysis, magnetic design, thermal-hydraulic and structural analyses, and neutronics. The remainder of this section is devoted to the engineering aspects of this integrated design. In many cases, there are strong similarities with the TITAN-I design. The major difference between TITAN-I and TITAN-II divertor designs is the use of an aqueous-salt solution as the coolant for the TITAN-II divertor (as opposed to liquid lithium for TITAN-I). The use of a nonconducting coolant eliminates the concerns of excessive MHD pressure drops. As a result, the divertor target can be shaped more freely,

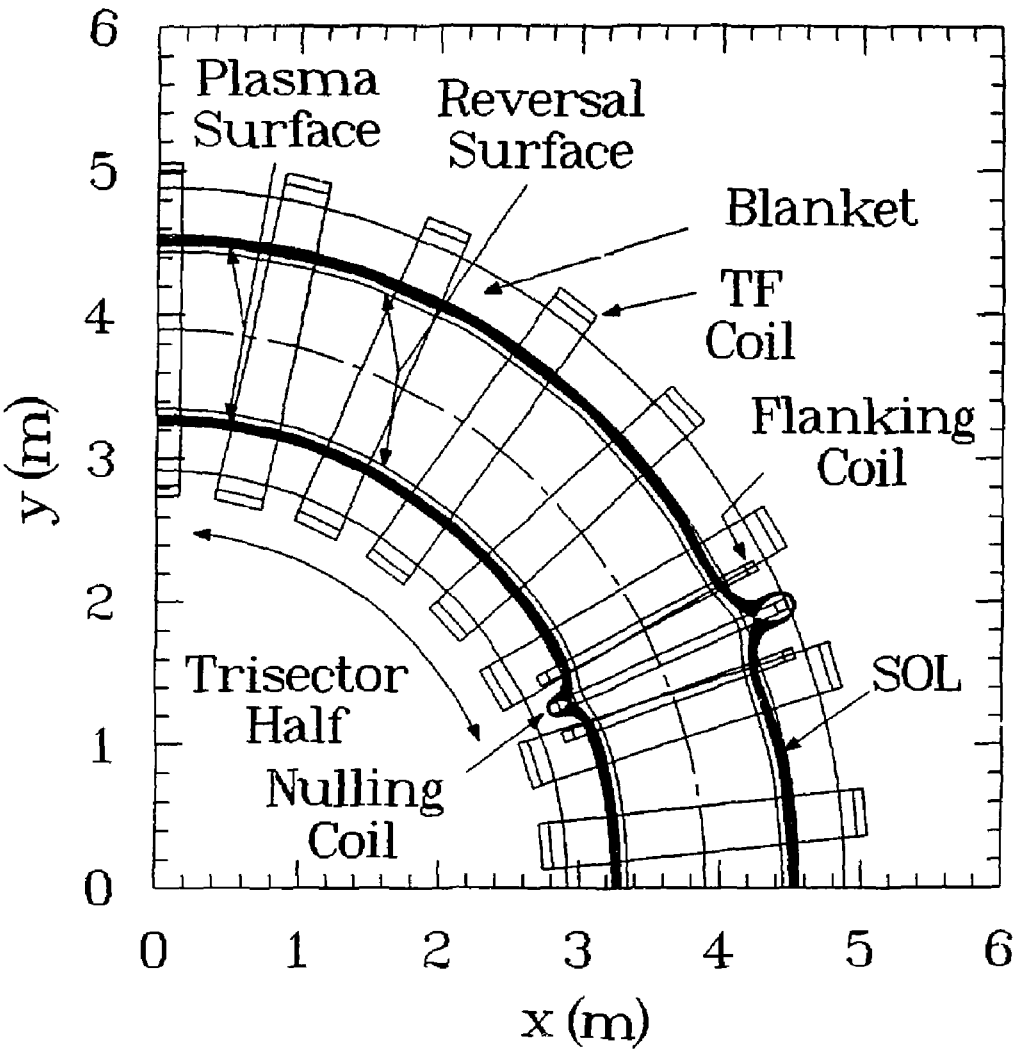

Figure 17.1-1. Equatorial-plane view of divertor coils and magnetic field lines for TITAN-II.

Table 17.1-I.

SUMMARY OF TITAN-II EDGE-PLASMA CONDITIONS

Number of divertors	3	
Scrape-off layer thickness	6	cm
Peak edge density	1.7×10^{20}	m^{-3}
Peak edge ion temperature	380	eV
Peak edge electron temperature	220	eV
Plasma temperature at first wall	1.7	eV
Peak divertor density	6×10^{21}	m^{-3}
Peak divertor plasma temperature	4.5	eV
Divertor recycling coefficient	0.995	

resulting in a rather lower peak heat flux for the TITAN-II divertor. Furthermore, the coolant for the TITAN-II divertor can be routed in the radial/toroidal direction, making the divertor performance less sensitive to the exact location of the plasma. Lastly, a single structural material (tungsten alloy) can be used both for the divertor armor and the divertor-coolant channels, easing the divertor-target design and fabrication.

17.2. MATERIALS

17.2.1. Plasma-Facing Material

In order to reduce the erosion of the divertor armor by the plasma, a high atomic-number (Z) material must be used for the surface of the divertor plate. This conclusion is based on the estimates of sputtering rates of various candidate materials (described in Section 5.5). The threshold energy for sputtering is sufficiently high for high-Z materials that the erosion rate of the divertor target under the expected conditions for TITAN designs (Table 17.1-I) is acceptable.

The requirements for the plasma-facing material are identical to those described for TITAN-I in Section 11.2. Thus, the same alloy of tungsten and rhenium, W-26Re, as was used for TITAN-I, has been chosen for the TITAN-II divertor armor. The properties of this alloy are described in Section 11.2 and are summarized in Table 11.2.-I.

17.2.2. Divertor-Target Coolant

It is advantageous to use the same coolant for all components of the fusion power core (FPC). Therefore, an aqueous-$LiNO_3$ solution (as used in the blanket) is chosen as the divertor-target coolant for TITAN-II. Pure water was also considered because of the eased corrosion and radiolysis problems, but these concerns appear to have been accounted for in the blanket-coolant analysis (Section 16.2). Also, there is a large uncertainty in the thermal and physical properties of the salt solution (Section 16.2), but the indications are that the changes relative to pure water should improve the thermal performance (*e.g.*, by allowing operation at a lower pressure and increasing the critical heat flux). The choice of an $LiNO_3$ solution as the TITAN-II divertor-target coolant, therefore, allows an assessment of the potential of aqueous-salt solutions, but it is recognized that certain issues cannot be fully resolved until more experimental data are available. The concentration of the coolant is the same as for the blanket (6.4 at.% Li), but because of the higher loadings on the divertor, different inlet and outlet conditions have to be used. In particular, as described in Section 17.4, the higher pressure used for the divertor coolant allows a higher outlet temperature. This permits the heat deposited into the divertor-target coolant to be extracted via a heat exchanger with the blanket inlet coolant, and avoids the need for a complete separate cooling circuit.

17.2.3. Substrate Material

Using a single structural material for the divertor target avoids the problems of bonding dissimilar materials and stress concentrations which can occur at the interface of the two materials (Section 11.5). Such a construction was not possible for TITAN-I because of MHD pressure-drop considerations, but has been chosen for TITAN-II in order to compare the two approaches. Therefore, the coolant tubes for the divertor target are also made from the W-26Re alloy which was selected for the divertor armor. The complex geometry of the target plate does not allow the structure to be fabricated from one piece, so the sputtering-resistant armor plate is bonded to the coolant tubes, as described in Section 17.3.

17.3. TARGET FABRICATION

In the TITAN-II divertor, the divertor-target coolant is routed in the radial/toroidal direction, in order to make divertor performance less sensitive to the exact location of the plasma (Section 17.4). A schematic view of the TITAN-II divertor geometry is presented in Figure 17.3-1 and shows the coolant-flow paths and headers. Because of the double curvature of the divertor plate, the cross section of the coolant tubes must vary along their length in order for the tubes to continue to touch. To avoid severe difficulties in the fabrication of the tungsten-rhenium tubes with variable cross sections, the reference design for the TITAN-II divertor plate uses constant-cross-section tubes, with coolant tubes arranged to touch only at the apex of the target (the location of minimum minor radius), with a slight gap between adjacent tubes at other points (Figure 17.3-1). This choice is made because the thermal penalties associated with this approach appear manageable (Section 17.5).

Various procedures which were considered for the fabrication of the divertor plate are discussed in Section 17.3.1. As an alternate design, methods of manufacturing tubes of variable cross section have been examined, and are described in Section 17.3.2

17.3.1. Reference Design

The reference fabrication procedure for the TITAN-II divertor plate follows fairly closely that of TITAN-I (Section 11.4). The first step involves the production of a 3- to 4-mm-thick W-26Re plate using powder-metallurgy techniques. After allowances have been made for thermal-expansion effects between the bending temperature and the operational temperature, the plate is bent to accord with the specified target shape. Grooves for the coolant channels are then formed in the plate using a numerically controlled milling procedure. This leaves a minimum plate thickness of 1 mm at the apex of the coolant tube, with a greater thickness between tubes. The W-26Re coolant tubes (which are themselves manufactured using powder-metallurgy techniques) are then brazed into the grooves, using a CuPd18 braze alloy [1] with an application temperature of $\sim 1100\,^{\circ}C$. The ends of the W-26Re tubes are interconnected by brazing them to poloidal headers at the inlet and outlet (Figure 17.3-1).

Another approach to the fabrication of the armor is to use chemical-vapor deposition (CVD) to deposit the armor onto the bank of coolant tubes. At conventional deposition rates of between 1 to 3 mm/h, this process would not take a long time. After completion of the deposition, the resulting uneven surface is ground to yield the necessary flat,

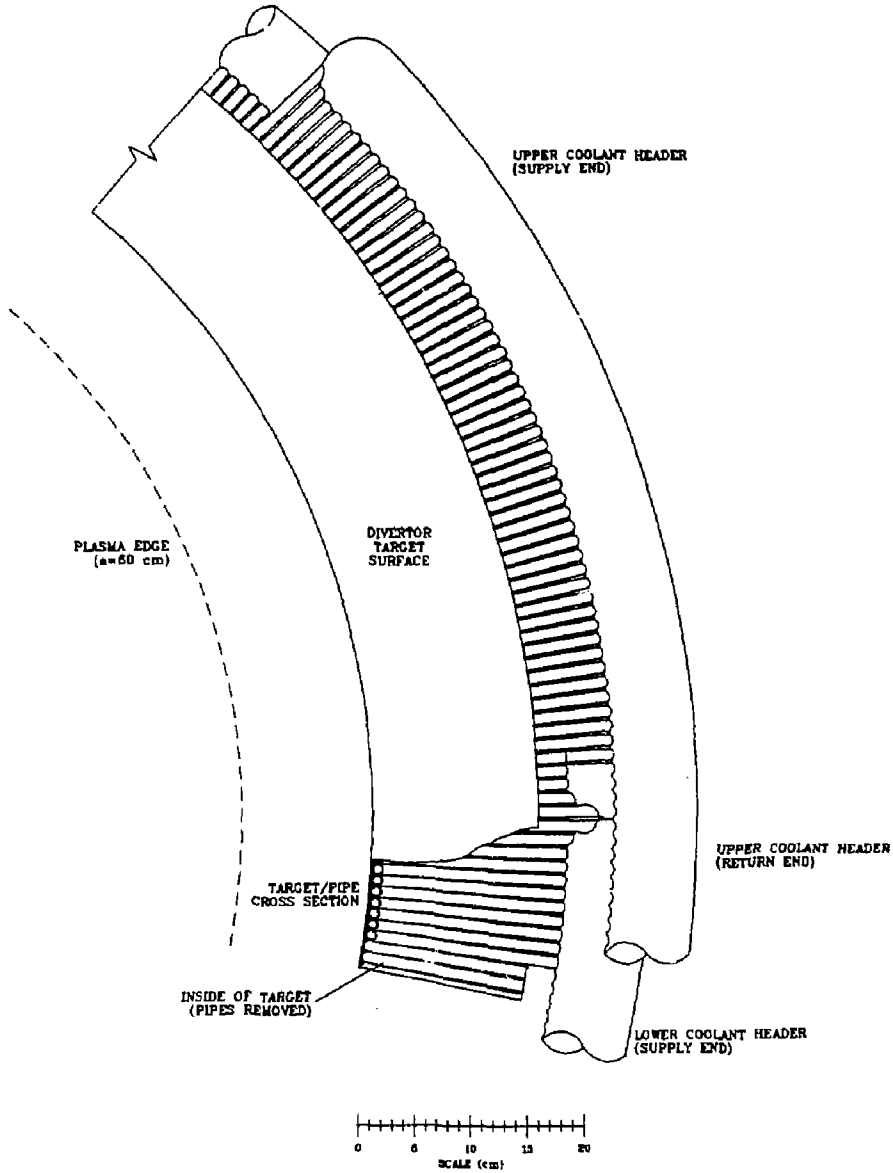

Figure 17.3-1. Schematic view of the divertor geometry, showing the divertor target, coolant-flow paths, and headers.

smooth surface. Silicon carbide wheels with grain sizes of 100 to 120 μm have proven useful for most grinding applications [2].

17.3.2. Alternative Design

This subsection describes methods of manufacturing the divertor plate with variable-cross-section coolant tubes to eliminate the gaps between the coolant tubes. Two manufacturing processes have been identified to make such tubes: hydroforming and CVD. After individual tubes are manufactured, they are brazed together using the CuPd18 braze alloy (Section 17.3.1) and then joined to the poloidal ring headers. The free-standing structure of W-26Re tubes with headers constitutes the skeleton of the divertor plate. The divertor armor is then attached to the bank of tubes using the CVD method or by brazing (as discussed in Section 17.3.1).

17.3.2.1. Hydroforming

The high ductility of tungsten-rhenium alloys (Table 11.2-I) allows the fabrication of pre-bent tubes with variable cross sections by hydroforming. Hydroforming is particularly useful when tubes of variable cross section also need to be bent because it avoids the problem of distortion of the cross section which frequently arises with bending.

As an example, the space shuttle main engine (SSME) is made of a number of variable-diameter hexagonal tubes that resemble giant bows ($\sim$ 3-m high) for cooling purposes. These tubes are manufactured using the hydroforming technique. First, a mold is made of the final product in two halves. For the SSME, these molds have semi-hexagonal grooves in the shape of the bow. A circular tube (Inconel) is bent to fit more or less into the groove. The mold halves are closed and the tube is pressurized. Plastic deformation of the tube would produce the variable cross section and the overall bend with very close tolerances. The nonuniform hexagonal bowed tubes are then welded together to form a channel-walled Venturi tube for the SSME [3].

Hydroforming of tungsten-rhenium alloys at temperatures above 1000 °C is particularly attractive because of the high ductility of these alloys ($\sim$ 70% at 1500 °C). The great advantage of using hydroforming is that the variable-cross-section tubes eliminate the gaps between the tubes that may be caused by sharp bends.

17.3.2.2. Chemical-vapor deposition of tungsten

Chemical-vapor deposition (CVD) is another process which can be used to manufacture variable-cross-section tungsten-rhenium tubes. The CVD technique (Section 11.4) involves the deposition of target material onto a hot substrate (400 to 1000 °C). The CVD of tungsten has been investigated more thoroughly than CVD of any other metal, and is widely used in various industries for many important applications [4]. The most frequently used CVD process is the hydrogen reduction of the halides WF_6 and WCl_6. An example of the overall hydrogen reduction of hexafluoride to tungsten is:

$$WF_{6(g)} + 3H_{2(g)} \rightarrow W_{(s)} + 6HF_{(g)} . \qquad (17.3\text{-}1)$$

The versatility of the CVD process and the control over the end-product characteristics is reflected in the number of papers that have been published on chemical-reaction parameters, kinetics, thermodynamics, pressure and temperature factors, substrate effects, deposit orientation, and industrial applications. In particular, numerous articles on the CVD of tungsten and tungsten-rhenium alloys appear in the literature [5 - 9]. Free-standing structural components are routinely manufactured using CVD of tungsten and tungsten-rhenium for high-temperature applications [10 - 20]. The tungsten alloy is chemical-vapor deposited onto a mandrel which is later removed, either by chemical etching or by melting. Mandrels of variable-cross-section coolant tubes would have to be manufactured for each tube individually.

The mechanical properties of tungsten-rhenium tubes produced by the CVD process have been studied and compared with those produced by the powder-metallurgy technique since the late 1960s [13 - 19]. Early samples of CVD tungsten showed a high degree of columnar grains and voids in the direction of deposition. It was shown that the low-temperature mechanical properties of the early CVD tungsten samples were comparable to those of tungsten produced by powder metallurgy [14]. However, creep-rupture tests at 1650 and 2200 °C clearly showed differences between the mechanical properties of the early CVD samples and powder-metallurgy tungsten [13].

An extensive study of tungsten-rhenium deposition was later conducted by Holman and Huegel [15 - 17]. Their studies greatly elucidated the effects of temperature, pressure, gas mixture, and total gas-flow rates on the composition, deposition rate, and grain structure of the deposited tungsten-rhenium alloys. They developed a CVD technique that produced fine-grained tungsten-rhenium alloys with no preferential grain-growth direction and with densities of 98.5% to 99% of the theoretical density. These figures are higher than those obtained in samples produced by powder metallurgy or plasma

spraying [19]. The new deposition techniques include simple rubbing or brushing of the deposit surface during deposition with a tungsten-carbide rod or a tungsten-wire brush. Thirty-centimeter-long tubes of tungsten-rhenium alloys with various rhenium contents (up to 28% rhenium) were chemical-vapor deposited onto mandrels with an outer diameter of 1 cm, with deposition rates of up to 1 mil/m (1.5 mm/h). Using Holman and Huegel techniques, CVD tubing can be produced with mechanical properties equal to those obtained in wrought or powder-metallurgy tungsten-rhenium alloys.

17.3.3. Discussion

Several fabrication methods have been identified for the TITAN-II divertor plates, and the reference-fabrication procedure is based on brazing a bank of constant-cross-section coolant tubes into the grooves milled on a powder-metallurgy-produced tungsten-rhenium plate. A particularly promising alternative method is the hydroforming process, which allows "bowed" tungsten-rhenium tubes with variable cross sections to be produced, followed by CVD of tungsten-rhenium armor to form the target plate. Although the individual processes involved in the manufacturing of the divertor plates are feasible and are used commercially, the viability of the total manufacturing process needs to be researched and be demonstrated. In particular, CVD furnaces large enough to hold the TITAN-II divertor plate need to be developed.

17.4. TARGET DESIGN

The details of the shaping of the surface and the overall thermal analysis are described in this section; a more extensive set of structural and thermal analyses using finite-element techniques is reported in Section 17.5.

Despite the intense radiation arising from the impurities injected into the plasma, careful shaping of the divertor target is required to maintain the heat flux at acceptable levels at all points on the plate. The target design for TITAN-II proceeds in much the same way as for TITAN-I (Section 11.4). This complex problem is handled by a modified version of the code described in Section 11.4. The differences arise from the use of an aqueous-salt solution as the coolant (eliminating the MHD effects), and using the tungsten-rhenium alloy as the structural material for the divertor-plate coolant tubes which allows for much higher temperatures in the tube walls.

The geometry of the TITAN-II divertor, representing the results of the iteration between the thermal analysis and the shaping code, is shown in Figure 17.4-1. This

geometry is very similar to that of TITAN-I with the following differences: (1) copper coils are used here rather than divertor IBCs; (2) the shape of the target is somewhat different because the use of a nonconducting coolant removes the MHD constraints on locating the target in regions of minimum magnetic field. Figure 17.4-2 shows the inclination angle of the target to the magnetic field lines and the flux-expansion factor as a function of distance along the target (measured from the apex of the target). A comparison with the corresponding figures for TITAN-I shows that the trends are similar. However, because the MHD constraints are removed, slightly lower inclination angles are possible for TITAN-II, allowing the area of the target to increase and a rather lower peak heat flux to be obtained.

For TITAN-II, the divertor-target coolant flows in the radial/toroidal direction, as opposed to the poloidal direction which was mandated for TITAN-I in order to avoid excessive MHD pressure drops. A disadvantage of the poloidal coolant routing (or, in general, the direction along the majority magnetic field) is that the heating rate can vary considerably from one tube to another. If the plasma should move slightly from its expected position, a coolant tube could receive a much greater heat load than it was designed for. With the coolant flowing in the direction perpendicular to the majority field, the total heat deposited on each tube is the same, and plasma motion will only alter the heat-flux distribution along the length of the tube. A problem with the toroidal/radial flow proposed for TITAN-II is that the length of the tubes is rather short, which can lead to a large volumetric flow rate of the coolant and a small inlet-to-outlet temperature rise. This problem, however, is avoided in TITAN-II design by using poloidal ring headers and a multi-pass coolant flow, as illustrated in Figure 17.3-1.

Because of the double curvature of the divertor plate, the cross section of the coolant tubes must vary along their lengths in order for the tubes to remain touching. Because of severe difficulties in the fabrication of the variable-cross-section tungsten-rhenium tubes, the reference divertor-plate design of TITAN-II uses constant-cross-section tubes, arranged to touch only at the apex of the target (the location of minimum minor radius), with a slight gap between adjacent tubes at other points (Figure 17.3-1). The effects of these gaps on the thermal and stress analyses are discussed in detail in Section 17.5, but the results of these more sophisticated analyses were incorporated into the overall design which is described here.

The diameter of each coolant tube was chosen to be as large as possible (to minimize the number of tubes and, hence, the likelihood of failure at the ends of the tubes where they are joined to the steel headers), taking into account pressure and thermal stress considerations. This process led to a coolant-tube design with an outer diameter

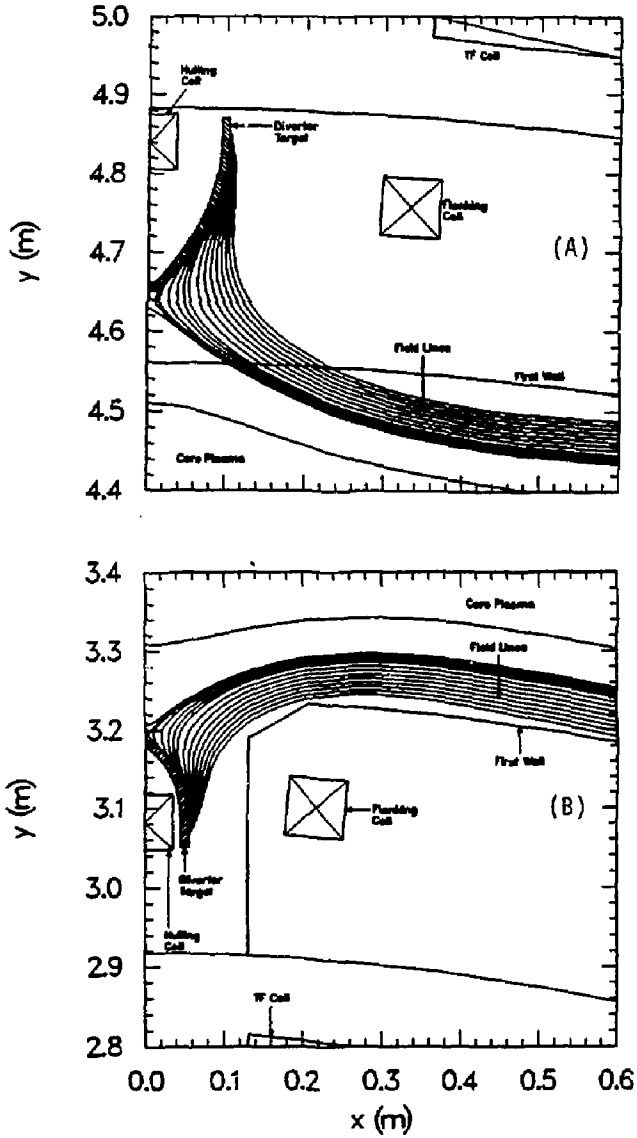

Figure 17.4-1. Outboard (A) and inboard (B) graph) equatorial-plane views of the divertor region for TITAN-II.

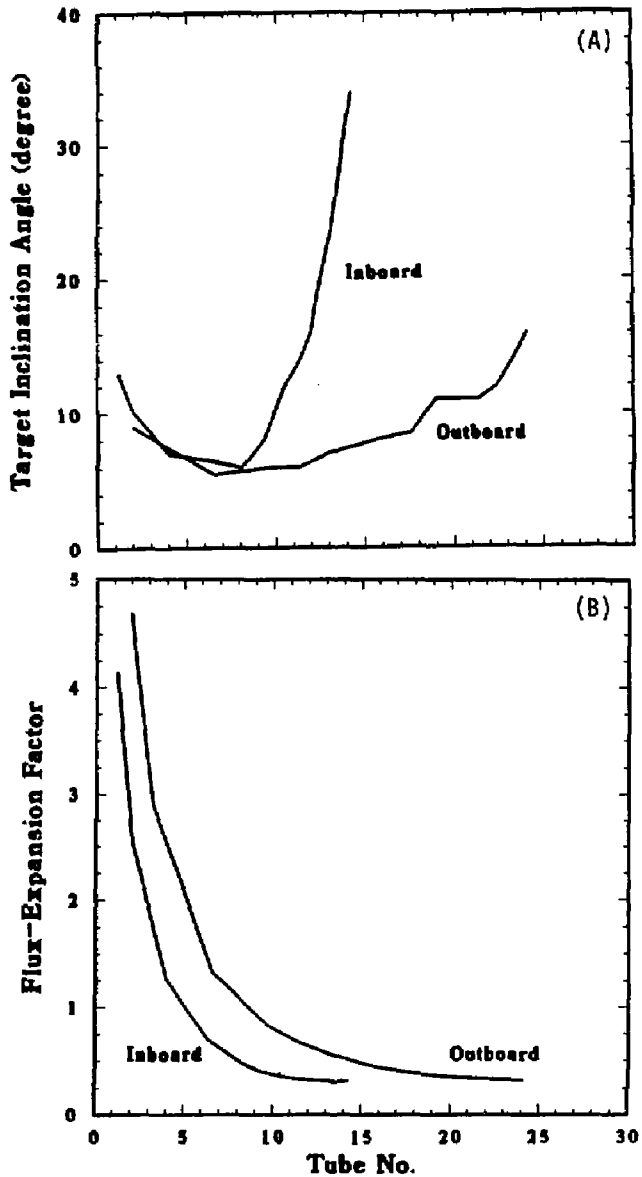

Figure 17.4-2. Target-inclination angle (A) and flux-expansion factor (B) as a function of position along inboard and outboard sections of TITAN-II divertor target. The distance is measured along the target from its apex.

of 10 mm and a wall thickness of 1 mm. Subsequent stress analysis (Section 17.5) indicated that with a 1-mm-thick W-26Re armor plate bonded to these tubes, the equivalent thermal stress on the inboard part of the target approached the design limit of 600 MPa. Therefore, total thickness of high-Z sputtering-resistant material is 2 mm, the same as for TITAN-I, although some of this layer performs a structural function. The detailed stress analysis, however, shows that the pressure stresses are well within the design limits, and a substantial fraction of the tube wall would have to be eroded before any failure occurred. As the erosion allowance was specified on the very conservative grounds of ignoring redeposition, which may be expected to be extensive, the TITAN-II design appears to be acceptable.

To accommodate the high heat loads on the divertor target, advantage is taken of the high heat-transfer coefficients possible in the subcooled-flow-boiling regime, as used in the first-wall cooling. At any point along the coolant tube, the heat-transfer coefficient is taken as the greater of the values predicted by the Dittus-Boelter (forced-convection) correlation and the Thom correlation for subcooled flow boiling.

The Dittus-Boelter correlation is given by

$$Nu = 0.023\, Re^{0.8}\, Pr^{0.4}, \tag{17.4-1}$$

where Nu, Re, and Pr are, respectively, the Nusselt, Reynolds, and Prandtl numbers. The Thom correlation for the tube-wall superheat, $T_w - T_{sat}$, in subcooled flow boiling is [21]

$$T_w - T_{sat} = 22.65 \sqrt{q''}\, e^{-p/8.69}, \tag{17.4-2}$$

where q'' is the heat flux into the coolant (MW/m^2) and p is the coolant pressure (MPa). These correlations can be used to determine the temperature of the inner wall of the coolant tube (tube-coolant interface) and a 1-D thermal analysis, as described in Section 11.4, is then used to evaluate the temperature distribution through the tube wall and armor.

For any water-cooled component, it is important that the heat flux into the coolant is maintained below the critical heat flux (CHF) for the particular conditions. In the absence of any CHF correlations specifically for high-temperature aqueous solutions, a general correlation, derived for water, has been used to assess the cooling performance of the TITAN-II divertor target. This correlation for the CHF, q''_{CHF}, was developed by Jens and Lottes [22]. Conversion to more convenient units of MW/m^2 yields

$$q''_{CHF} = C \left(\frac{G}{1356}\right)^m (\Delta T_{sub})^{0.22}, \tag{17.4-3}$$

where G is the mass velocity of the coolant ($= \rho v$) in kg/m^2 s, the factor 1356 arises from the conversion of units, and ΔT_{sub} is the subcooling in °C. Constants C and m depend on the pressure, p, through

$$C = 3.00 - 0.102p\,, \tag{17.4-4}$$

$$m = \frac{p}{30} + 0.04\,. \tag{17.4-5}$$

To allow for uncertainties in the correlations and to include a safety margin in the design, the allowable heat flux is generally assumed to be lower than the estimated CHF limit by a factor ~ 1.4 for water-cooled systems. For the TITAN-II design, the same factor has been used in the analysis, although the application of the water-derived CHF correlation to the salt-solution coolant increases the uncertainty.

A further factor in considering CHFs is the conduction of heat from the surface of the target into the coolant. In general, the heat flux tends to be concentrated from the value on the surface to a smaller area of the tube inner wall (Section 17.5). This peaking, which is augmented by the gap between the coolant tubes, is included in the analysis by using an approximate fit to the concentration factor found by the finite-element analysis (Section 17.5). Note that this concentration is only of importance for CHF considerations; for the lithium-cooled TITAN-I divertor, the only impact would be to increase the temperature drops across the structure by a small amount.

Figure 17.4-3 shows the distribution of heat flux along the divertor targets for the inboard and outboard locations shown in Figure 17.4-1. The distance along the target is measured in the direction of the coolant flow (*i.e.*, the center of the figure, where the heat flux drops, is at the apex of the target) facing directly into the core plasma. Figure 17.4-3 shows that the maximum total surface heat flux on the inboard target is 7.5 MW/m^2 with 5.8 MW/m^2 of the heat flux on the outboard target (compared with corresponding levels of 9.5 and 6.0 MW/m^2 for TITAN-I). This reduction in the divertor-plate surface heat flux for TITAN-II was made possible by the increased freedom in shaping the target, allowing it to be located in areas of higher magnetic field than would have been permitted for the liquid-metal-cooled TITAN-I. Figure 17.4-3 also shows an estimate of the concentration in the heat flux (*i.e.*, the difference between the total surface heat flux and the inner-wall heat flux).

Given the heat loadings on the divertor-plate cooling tubes, the coolant conditions are determined by the requirements of obtaining an adequate safety factor on CHF, and of allowing the heat deposited into the divertor-target-coolant loop to be removed by a heat exchanger with the inlet coolant for the blanket. Additional constraints were

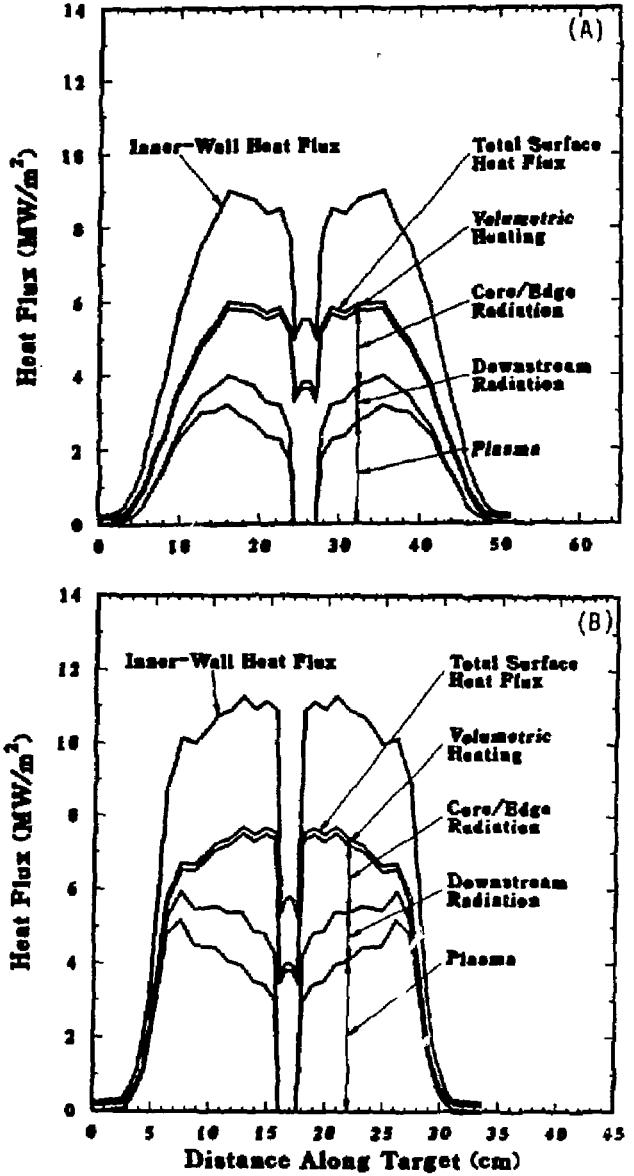

Figure 17.4-3. Heat flux distribution on outboard (A) and inboard (B) sections of divertor target. The CHF for TITAN-II divertor coolant is estimated at 16.2 MW/m^2 (Equation 17.4-3). Distance along target is measured in the direction of coolant flow.

that the coolant velocity should not exceed 20 m/s and that its composition should be the same as for the blanket (6.4 at.% Li). These considerations led to the selection of the coolant-outlet conditions of 345 °C and 14 MPa. At this pressure, the boiling point of a 6.4% $LiNO_3$ solution is 405 °C (Section 16.2), yielding a subcooling at the outlet conditions of 60 °C and a CHF of 16.2 MW/m^2, as predicted by the Jens and Lottes correlation (Equation 17.4-3). Figure 17.4-3 indicates that a safety factor in excess of 1.4 with respect to CHF is achieved at all points on the target; on the outboard target, where the heat fluxes are lower, the minimum safety factor is about 1.8.

Figure 17.4-4 shows the coolant and structure temperatures as a function of distance along the inboard and outboard divertor targets. The coolant-temperature rise along the tube is about 7 °C, while the saturation temperature remains virtually constant because the pressure drop along the tube is small. The heat removed from the divertor plate is deposited into the blanket-cooling circuit through a heat exchanger. In order to maintain a minimum temperature difference of 20 °C in the heat exchanger between the inlet divertor coolant and the inlet blanket coolant (298 °C), the divertor-coolant inlet temperature must be not less than 318 °C. For a divertor-coolant exit temperature of 345 °C and temperature rise of about 7 °C per pass, the TITAN-II divertor coolant passes four times across the target. The temperature of the inner wall of the coolant tube is governed by the local heat flux, and the abrupt change in slope in Figure 17.4-4 is caused by the onset of subcooled flow boiling, which prevents the wall temperature from rising to a level substantially above the saturation temperature.

The maximum temperature of the armor is estimated to be $\sim$ 660 °C. This is somewhat lower than the result from the finite-element thermal analysis, described below in Section 17.5, because of 2-D effects in the heat conduction and because the gaps between the the tubes have been ignored in this calculation.

17.5. THERMAL AND STRUCTURAL ANALYSES

The overall geometry of the TITAN-II divertor is very similar to that for TITAN-I, but there are two major differences: (1) the TITAN-II divertor is manufactured from a single material; (2) the coolant flow is in the radial/toroidal direction, rather than poloidal, thus destroying the axisymmetry of the TITAN-I design (Section 11.5) and requiring a somewhat different finite-element modeling. The finite-element analysis was performed for the inboard section of the divertor target where the heat loadings are the highest.

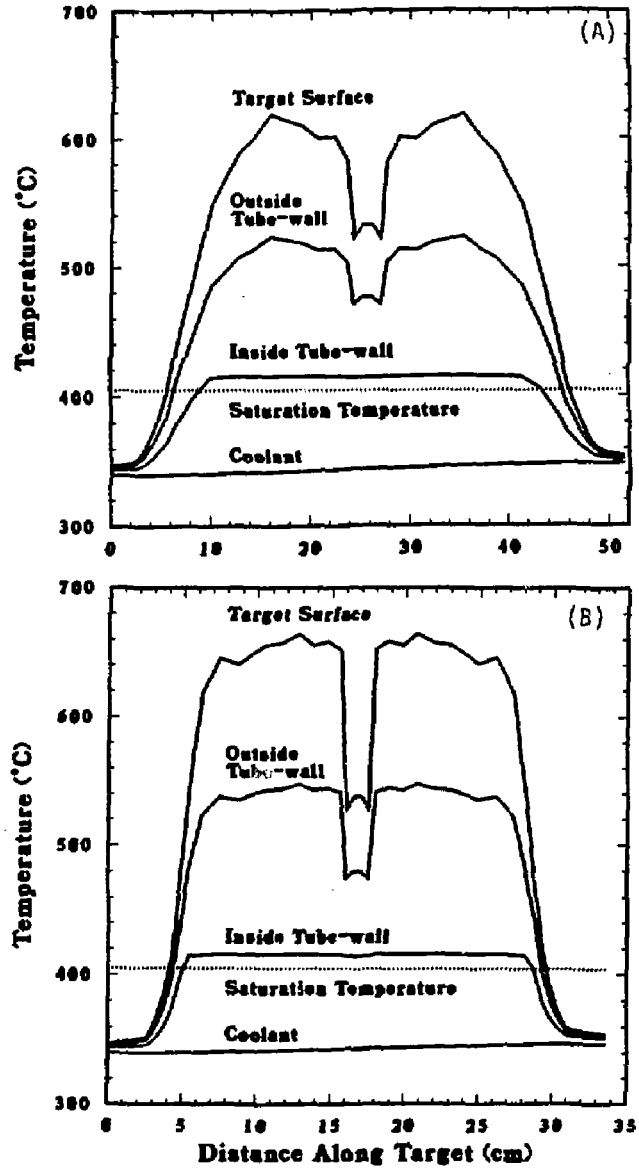

Figure 17.4-4. Coolant and structure temperature distribution on outboard (A) and inboard (B) sections of the divertor target. Distance along target is measured in the direction of coolant flow.

17.5.1. Thermal Analysis

The surface heat flux on the inboard section of the TITAN-II divertor target (distance measured from the apex in the toroidal direction) is shown in Figure 17.4-3. The surface heat flux shows a broad peak of 7.5 MW/m^2, covering about 8 cm of the inboard target. Because the thickness of the divertor plates (0.2 cm) is much smaller than the distance over which this heat flux changes appreciably, a detailed model such as that used for TITAN-I should be quite accurate (Section 11.5).

The finite-element model used for the thermal analysis is shown in Figure 17.5-1. The heat flux is assumed to be uniform over the plasma-facing surface and the lines of symmetry on the sides are assumed to be adiabatic. The heat-transfer coefficient at the interface between the tube wall and the coolant was set to be the greater of the two coefficients calculated from subcooled-flow-boiling and laminar-flow correlations. In other words, boiling is assumed to occur in regions of the tube where the subcooled-flow-boiling correlation predicts a higher heat-transfer coefficient than the forced-convection correlation. For the TITAN-II divertor, the Dittus-Boelter correlation (Equation 17.4-1) predicts a heat-transfer coefficient of 57 kW/m^2-K. For subcooled flow boiling, the heat-transfer coefficient was calculated from Thom's correlation [23] which, for 60 °C of subcooling and 14 MPa of coolant pressure, is

$$h = \frac{q}{60 + 4.54\sqrt{q}}, \qquad (17.5\text{-}1)$$

where q is the local heat flux (MW/m^2) and h is the heat-transfer coefficient (MW/m^2 K). This value for the heat-transfer coefficient has been normalized by the ratio of the subcooling to the film temperature drop, so it can be used in a finite-element code which assumes that the heat-transfer correlations are based on the film temperature drop.

Because the boiling heat-transfer correlation is based on the local heat flux which is not known, an iterative solution method is required. The local heat flux into the coolant along the inside wall of the coolant tube is first estimated, assuming it peaks at the apex of the tube (the point nearest to the plasma) and drops to zero at an angle of about 60° to either side of the peak. From this estimated local heat-flux distribution, the heat-transfer coefficient is calculated around the tube and input to the finite-element code. The resultant heat fluxes from the finite-element analysis are then used to update the heat-transfer coefficients and the problem is recalculated. This process is repeated until the desired accuracy is achieved. In practice, the local heat fluxes seemed to depend only on the geometry, rather than on the heat-transfer coefficient, so the local flux changed little after the initial run and convergence of this iterative process was rapid.

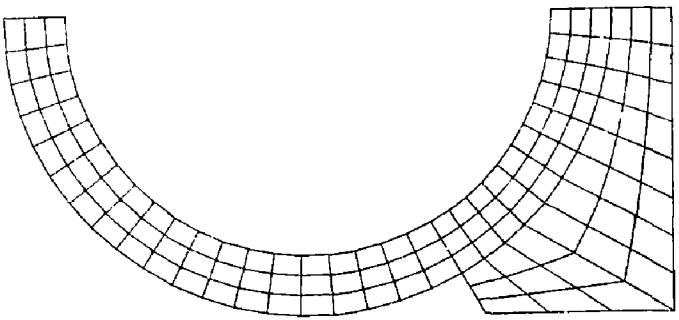

Figure 17.5-1. The finite-element model used for thermal and structural analyses of the TITAN-II divertor plate.

The temperature contours, for the coolant tubes touching each other, are shown in Figure 17.5-2. The peak temperature is 762 °C, located at the divertor-plate surface midway between two neighboring tubes. A crucial aspect of the thermal analysis for the TITAN-II divertor is that the maximum local heat flux into the coolant must be well below the CHF limit of $\sim 16\,\mathrm{MW/m^2}$. The maximum local heat flux is greater than the surface heat flux of $7.5\,\mathrm{MW/m^2}$ for two reasons:

1. The area available for transfer of heat into the coolant is less than the area facing the plasma. Assuming that only about 65° of the inner wall on either side of the apex actually conducts heat into the coolant (as indicated by the finite-element calculations), this effect would amplify the peak heat flux to over $8\,\mathrm{MW/m^2}$.

2. The heat tends to flow into the coolant along radial paths, rather than flowing perpendicular to the plasma-facing surface, thus resulting in the concentration of the heat flux towards the apex of the tube.

The distribution of the heat flux into the coolant (or at the inner wall of the coolant tube) is shown in Figure 17.5-3. One of the curves in this figure corresponds to the case of the heat flux on the top surface entering the tube with a pure cosine distribution, as would be expected for a thin-walled tube. This curve shows a peak heat flux of over $9\,\mathrm{MW/m^2}$, which is well above the surface heat flux of $7.5\,\mathrm{MW/m^2}$. This increase in the heat flux is a result of the decrease in the surface area caused by the difference between the outer and inner radii of the tube. For the TITAN-II divertor plate, the finite-element

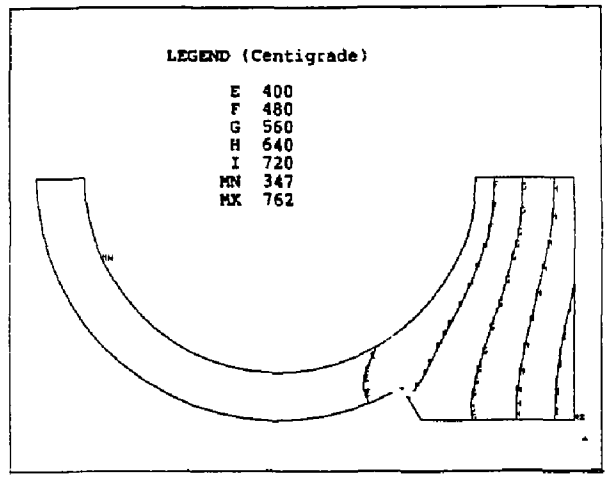

Figure 17.5-2. Temperature contours for the TITAN-II divertor plate from the finite-element analysis for a surface heat flux of 7.5 MW/m^2 and no gap between neighboring tubes.

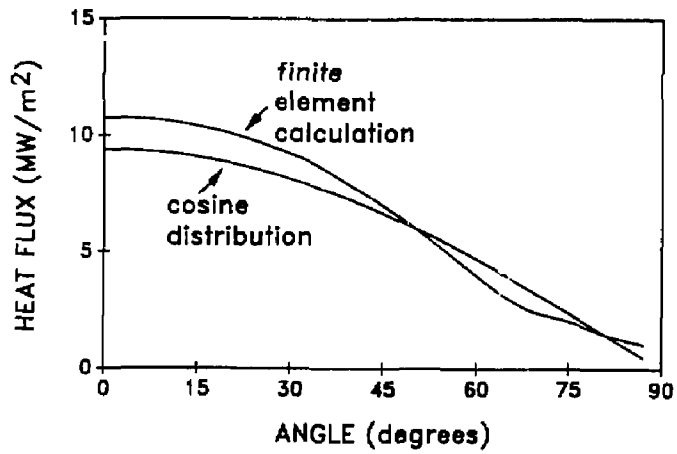

Figure 17.5-3. Distribution of the heat flux into the coolant along the inner surface of the coolant tube of the TITAN-II divertor from the finite-element analysis for a surface heat flux of 7.5 MW/m^2 and no gap between neighboring tubes.

calculations show that the enhancement in the heat flux at the point closest to the plasma is even more pronounced because the tube wall is effectively very thick at the plasma-facing surface (second curve in Figure 17.5-3). For this case, the peak heat flux into the coolant is 10.7 MW/m^2, thus providing a safety margin of about 1.5 with respect to the CHF (16.2 MW/m^2).

Because of the double curvature of the divertor target, there would be a gap between the constant-cross-section coolant tubes everywhere except at the apex (the points of minimum minor radius). At the points of the maximum heat flux, located 2 to 6 cm away from the apex in the radial/toroidal direction (Figure 17.4-3), there is a small gap (0.4 mm) between neighboring tubes, as can be seen in Figure 17.3-1. The presence of this gap increases the maximum heat flux into the coolant to 10.9 MW/m^2 and the peak structural temperature to 779 °C, again providing a safety margin of about 1.5 with respect to the CHF (16.2 MW/m^2).

17.5.2. Stress Analysis

As with the thermal analysis, the boundary conditions and global deformations have little effect on the pressure stresses in the divertor. Hence, the detailed finite-element model used previously can also be used to calculate the primary stresses induced by the 14-MPa coolant pressure. The equivalent stress contours are shown in Figure 17.5-4. The peak stress is 83 MPa. There is some bending in the tube wall, thus increasing the peak primary stress above the expected value of 56 MPa (from $\sigma = pr/t$). Also, the primary stress in the plasma-facing surface, which will be shown to be the location of the peak thermal stress, is essentially zero.

Because the coolant flow in the TITAN-II divertor plate is in the radial/toroidal direction, there is no poloidal axisymmetry in the structure, and the detailed model used for the thermal analysis cannot be used for calculating the thermal stresses which depend strongly on the imposed boundary conditions. Fortunately, the coolant tubes, themselves, have little effect on the thermal stress distribution (as indicated by preliminary analyses) so an axisymmetric model can be used to approximate the structural behavior of the divertor plate as a unit. This allows accurate treatment of the boundary constraints without a prohibitive loss of detail.

The finite-element model which is used to analyze the thermal stresses is shown in Figure 17.5-5. Half of the U-shaped cross section is modeled by using symmetry conditions to model the other half. The model consists of 600 axisymmetric quadrilateral

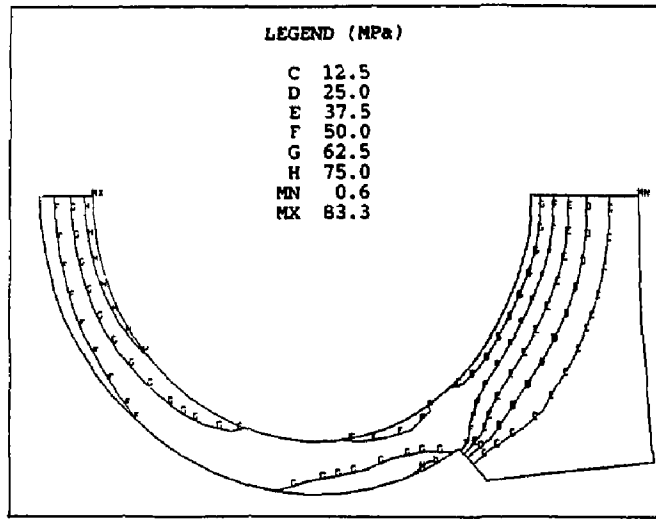

Figure 17.5-4. Equivalent pressure-stress contours from finite-element analysis of the TITAN-II divertor plate for a coolant pressure of 14 MPa.

elements. The heat flux was distributed along the surface of the divertor according to Figure 17.4-3 (also shown in Figure 17.5-6) and a constant heat-transfer coefficient of $200\,kW/m^2$ was assumed along the entire inner surface. The bulk temperature of the coolant was assumed to be 345 °C.

The maximum temperature is 615 °C and occurs at point A on Figure 17.5-5. The temperature drops across the divertor-plate structural material is 229 °C, which is 36 °C lower than the calculated value from the local analysis (265 °C). Hence, the global model will underestimate the in-plane stresses by roughly the same amount (15%). The out-of-plane stresses, though, tend to dominate the equivalent stresses in this problem, and they would be underestimated by less than 15% because these stresses depend on the overall temperature distribution, rather than just the local distribution.

The peak equivalent stresses in the TITAN-II divertor plate occur on the plate surface and are shown in Figure 17.5-6. The maximum equivalent stress, which occurs at the same location as the peak temperature, is 505 MPa. Since the pressure stress at this point is zero, the allowable stress at this location is $3S_{mt} = 600$ MPa for tungsten. Therefore, the TITAN-II divertor plate can withstand the very high heat fluxes expected during the normal operation.

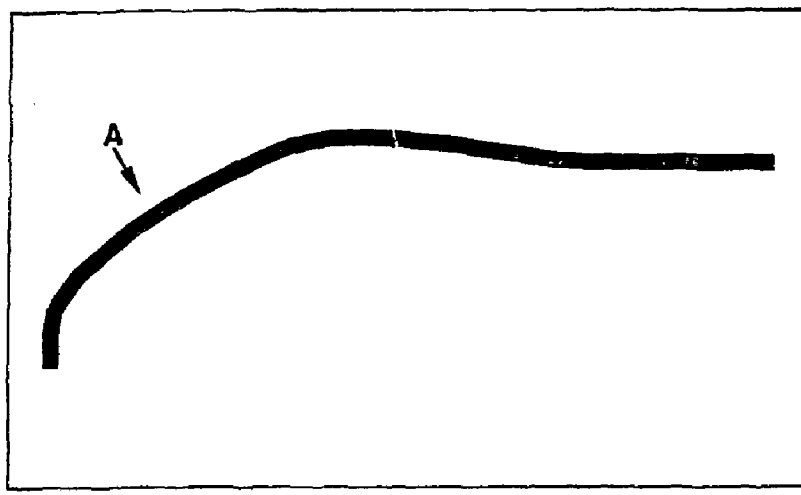

Figure 17.5-5. Finite-element model for determination of thermal stresses in the TITAN-II divertor plate.

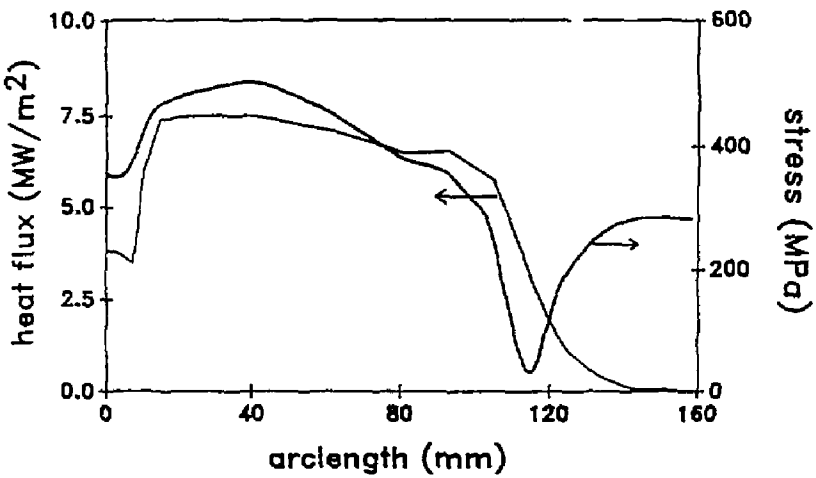

Figure 17.5-6. Surface heat flux and peak-equivalent thermal-stress distributions on the inboard section of the TITAN-II divertor. Distance along the target is measured in the radial/toroidal direction from the apex.

17.6. DIVERTOR-COIL ENGINEERING

The toroidal-field-coil design for TITAN-II, which consists of copper coils as opposed to the IBCs of TITAN-I, prompted a new divertor magnetic design (reported fully in Section 4.4). The final magnetic design, similar to that of TITAN-I, includes three divertor modules, located 120° apart in the toroidal direction. An equatorial-plane cross section of the divertor coils is shown in Figure 17.1-1. The magnetic field lines are diverted onto the divertor plate using one nulling and two flanking coils which localize the nulling effect. No divertor-trim coils are needed for the TITAN-II design. The use of copper divertor coils reduces the joule losses in the TITAN-II divertor coils to 9.8 MW which are much smaller than that of the TITAN-I design (120 MW).

The TITAN-II divertor coils are normal-conducting copper coils cooled by pure water with spinel insulator material. Because of the expected long life of the inorganic spinel insulator (Section 10.2.3), the TITAN-II divertor coils are expected to perform at the design level for the one-year lifetime of the divertor module. The nuclear heating in the divertor coils is not excessive and can easily be removed by the cooling circuit.

Forces on the divertor coils are of four types: (1) outward radial forces on each coil caused by the interaction of the coil current with the toroidal field, (2) centering forces resulting from the radial variation of the toroidal field, (3) overturning moments generated by the interaction between the vertical field and the coil current, and (4) out-of-plane forces caused by the spatial variation of the magnetic field especially in the divertor region. These electromagnetic forces also vary in time during the cycles of the oscillating-field current-drive (OFCD) system.

The forces exerted on the divertor coils are such that the maximum coil face pressure is of the order of 1.8 MPa. This constitutes only about 3% of the end forces generated by the blanket-coolant pressure (Section 16.4). Capturing the flanking coil against the end wall within the blanket scarcely alters the loading patterns in the blanket and the blanket-load paths can be easily strengthened to accommodate this small increase. Figure 17.6-1 shows the equatorial-plane view of the TITAN-II divertor module and the related structure. The structural support for the nulling coil is also explicitly shown. The nulling coil does not see any lateral forces.

The spine plate and shield block behind the nulling coil serve to maintain the shape of this coil and resist its tendency to translate outwards. This spine plate and shield block cover the entire divertor circumference but are restricted to the divertor-plate width on the outboard section to allow for the divertor pumping ducts. As illustrated in

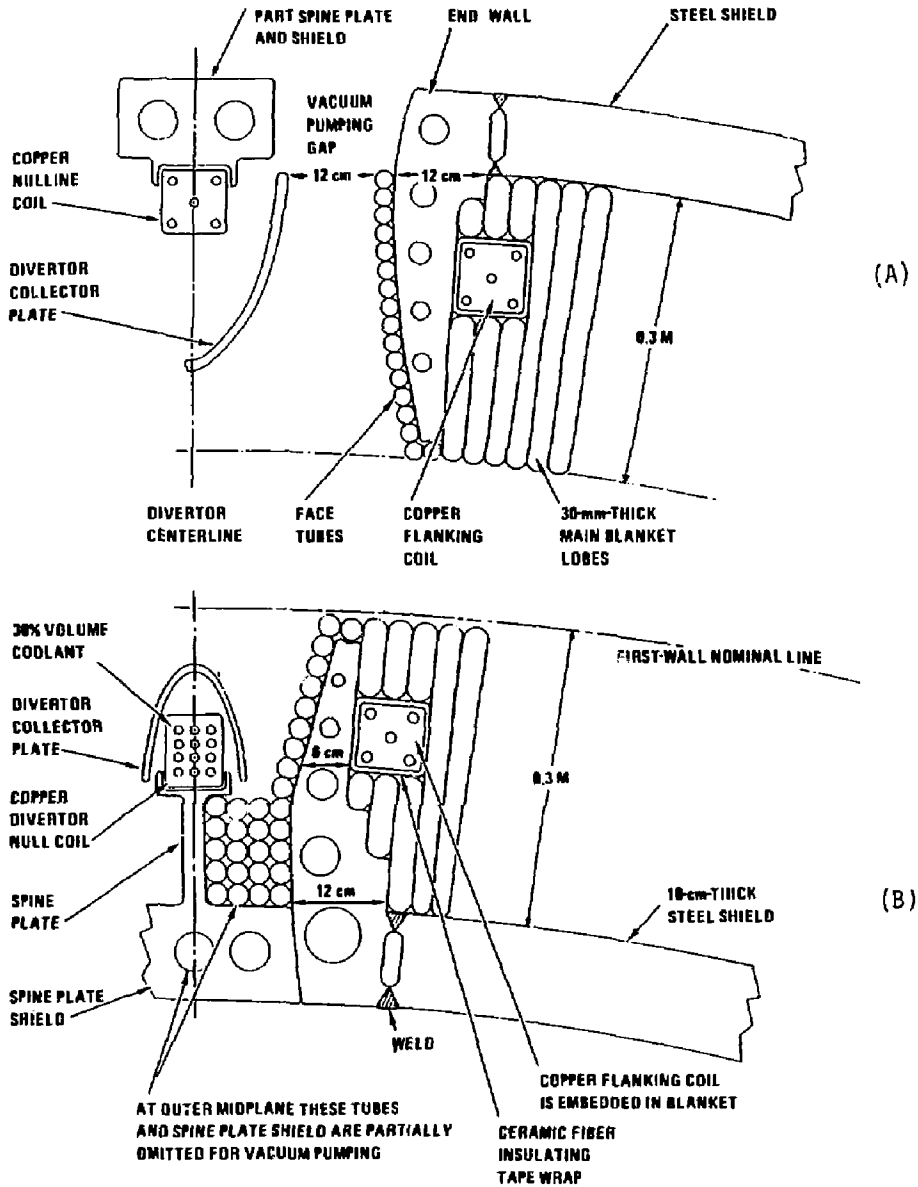

Figure 17.6-1. Equatorial-plane views of outboard (A) and inboard (B) cross sections of the divertor modules and the related support structure.

Figure 17.6-1, some face tubes are needed in the divertor module in order to handle the surface heat flux and also to fill in voids around the back of the divertor collector plates.

17.7. VACUUM SYSTEMS

The vacuum boundary in the TITAN-II design is behind the hot shield, as opposed to the TITAN-I design in which the entire fusion power core (FPC) is located inside a vacuum tank. Three vacuum-pumping ducts with large cross sections are connected to the outboard side of the three divertor modules of TITAN-II. The high-vacuum pumps are connected to these ducts and are located under the water pool surrounding the TITAN-II FPC to allow easy access for maintenance. This arrangement also minimizes the shielding requirements because the water pool surrounding the TITAN-II FPC also acts as a very good radiation shield. Detailed calculations for the pumping requirements of the TITAN-II design have not been performed but they are not expected to be very different from those of the TITAN-I design.

17.8. SUMMARY AND CONCLUSIONS

The design of the impurity-control system poses some of the most severe problems of any component of a DT fusion reactor. For TITAN-II design, the impurity-control system is based on toroidal-field divertors in order to minimize the perturbation to the global magnetic configuration, and to minimize the coil currents and stresses. Three such divertors are used as a compromise between the conflicting desires to minimize the joule losses in the divertor coils and maximize the total area of divertor plates.

To limit the heat flux on the divertor-target plate to a manageable level ($10\,MW/m^2$), the TITAN plasma is required to operate in a high-radiation regime, such that a total of about 95% of the steady-state heating power is radiated in the core, edge, and divertor plasmas. An "open" configuration, in which the divertor target is located close to the null point in the magnetic field, is used, rather than a "closed" configuration, which tends to produce large peaking factors in the heat-flux distribution. These features, together with careful shaping of the divertor-target surface, allow the maximum heat flux at the inboard location to be limited to $7.5\,MW/m^2$, with a peak outboard value of $5.8\,MW/m^2$.

To satisfy the requirement for a high-Z material for the plasma-facing surface of the divertor target, a tungsten-rhenium alloy, W-26Re, is used. The high rhenium content

provides the high ductility and high strength necessary for the severe loading conditions. A single structural material is used for the divertor target to avoid the problems of bonding dissimilar materials and of stress concentrations which occur at the interface of the two materials. The coolant tubes are, therefore, also made from W-26Re alloy.

The coolant for the divertor system is an aqueous-$LiNO_3$ solution, as used in the TITAN-II blanket. Advantage is taken of the predicted differences in the physical properties between this solution and pure water to obtain the high CHFs ($\sim 16\,MW/m^2$) necessary to provide an adequate safety margin against burnout. The divertor-plate coolant flows in the toroidal/radial direction to equalize the power deposited on each tube, although this causes gaps between adjacent tubes (if they are of constant cross section) because of the double curvature of the divertor plate. Fabrication of the divertor target is based on brazing of the tungsten-alloy plate (which is produced by powder-metallurgy techniques) to a bank of constant-cross-section coolant tubes, although alternative methods which allow tubes of variable cross section to be constructed have also been considered.

Two-dimensional, finite-element thermal and structural analyses were performed, which indicated that the maximum equivalent thermal stress is about 500 MPa, within the allowable level of 600 MPa for tungsten. The thermal analysis showed that geometric effects concentrate the heat flux from its value on the plate surface to a higher value at the tube-coolant interface, and that the effects of the gaps between adjacent tubes in elevating structural temperatures are acceptable.

In conclusion, at the present level of analysis, the toroidal-field divertor design for TITAN-II appears to represent a feasible design approach for the impurity-control and particle-exhaust system for a high-power-density reversed-field-pinch (RFP) reactor. A number of areas require further analysis and experimental investigation to confirm their potential as described in this report. Demonstration of good RFP operation with a toroidal-field divertor is clearly necessary, and operation with a highly radiative core plasma is central to the divertor design and also requires further experimental work.

The physical and heat-transfer properties of $LiNO_3$ solutions need to be better understood, although the present estimates suggest they should be favorable. The fabrication procedure proposed for manufacturing the large divertor plate from tungsten-rhenium alloy requires experimental verification, and the data base for the irradiated properties of the tungsten alloy requires considerable expansion. Additional work on the design of the support structure for the divertor modules and the divertor coils and the vacuum system is also needed.

REFERENCES

[1] "Tungsten-Rhenium Alloys," in *Refractory Metals and Special Metals*, Metallwerk Plansee GmbH, Austria (1987).

[2] "How to Make Time with Tungsten," in *A Practical Guide on the Various Uses of Tungsten*, Schwarzkopf Development Corporation, Holliston, MA (1987).

[3] G. Orient, Rockwell International, private communications (1987).

[4] W. Kern and V. S. Ban, "Chemical Vapor Deposition of Inorganic Thin Films," *Thin Film Processes*, Academic Press, New York (1978) p. 257.

[5] "Chemical Vapor Deposition of Refractory Metals, Alloys and Compounds," in *Proc. Am. Nucl. Soc.*, A. W. Shaffhauser (Ed.), Hinsdale, IL (1967).

[6] "Chemical Vapor Deposition - Second International Conference," in *Proc. Conf. Electrochem. Soc.*, J. M. Blocher, Jr. and J. C. Withers (Eds.), New York, NY (1970).

[7] "Chemical Vapor Deposition - Third International Conference," in *Proc. Conf. Electrochem. Soc.*, F. A. Glaski (Ed.), Hinsdale, IL (1972).

[8] "Chemical Vapor Deposition - Fourth International Conference," in *Proc. Conf. Electrochem. Soc.*, G. F. Wakefield and J. M. Blocher Jr. (Eds.), Princeton, NJ (1973).

[9] "Chemical Vapor Deposition - Fifth International Conference," in *Proc. Conf. Electrochem. Soc.*, J. M. Blocher, Jr., H. E. Hintermann, and L. H. Hall (Eds.), Princeton, NJ (1975).

[10] R. C. Svedberg and R. W. Buckman Jr., "W-Re Composite Tube Fabrication by Chemical Vapor Deposition for Application in an 1800 °C High Thermal Efficiency Fuel-Processing Furnace," *Thin Solid Films* **72** (1980) 393.

[11] J. I. Federer and A. C. Schaffhauser, "Chemical Vapor Deposition and Characterization of Tungsten-Rhenium Alloys," *Proc. Int. Conf. on CVD*, Salt Lake City, UT (April 1977) 242.

[12] F. A. Glaski, "A Report on the Current Role of Chemical Vapor Deposition as a Manufacturing Process," *Proc. Conf. CVD of Refractory Metals, Alloys and Compounds*, Gatlinburg, TN (September 1967) 276.

[13] H. E. McCoy and J. O. Stiegler, "Mechanical Behavior of CVD Tungsten at Elevated Temperatures," *Proc. Conf. CVD of Refractory Metals, Alloys and Compounds*, Gatlinburg, TN (September 1967) 391.

[14] A. C. Schaffhauser, "Low-Temperature Ductility and Strength of Thermochemically Deposited Tungsten and Effects of Heat Treatment," *Summary of 11th Refractory Composites Working Group Meeting*, AFML-TR-66-179 (July 1966) 261.

[15] W. R. Holman and F. J. Huegel, "CVD Tungsten and Tungsten-Rhenium Alloys for Structural Applications. Part Process Development," *Proc. CVD of Refractory Metals, Alloys and Compounds*, Gatlinburg, TN (September 1967) 127.

[16] W. R. Holman and F. J. Huegel, "CVD Tungsten and Tungsten-Rhenium Alloys for Structural Applications. Part II: Evaluation," *Proc. CVD of Refractory Metals, Alloys and Compounds*, Gatlinburg, TN (September 1967) 427.

[17] F. J. Huegel and W. R. Holman, "CVD Tungsten and Tungsten-Rhenium Alloys for Structural Applications. Part III: Recent Developments," *Proc. CVD of Refractory Metals, Alloys and Compounds*, Gatlinburg, TN (September 1967) 171.

[18] F. A. Glaski, "A Report on the Current Role of Chemical Vapor Deposition as a Manufacturing Process," *Proc. CVD of Refractory Metals, Alloys and Compounds*, Gatlinburg, TN (September 1967) 276.

[19] A. M. Shroff, "Vapor Deposition of Refractory Materials," *Proc. 6th Plansee Seminar* (1968) 845.

[20] L. W. Roberts, "The Properties of CVD Deposits of W and W-Re alloys," *Proc. 6th Plansee Seminar* (1968) 880.

[21] J. G. Collier, *Convective Boiling and Condensation*, McGraw-Hill, London (1972) p. 159.

[22] W. H. Jens and P. A. Lottes, "Analysis of Heat Transfer, Burnout, Pressure Drop and Density Data for High Pressure Water," U. S. Atomic Energy Commission report ANL-4627 (1951).

[23] J. R. S. Thom, W. M. Walker, T. A. Fallon, and G. F. S. Reising, "Boiling in Subcooled Water During Flow in Tubes and Annuli," *Proc. Inst. Mech. Engr.* **3C 180** (1965-66) 226.

18. TITAN-II TRITIUM SYSTEMS

Dai-Kai Sze
John R. Bartlit
Paul J. Gierszewski
Otto K. Kveton
Rodger C. Martin

Contents

18. TITAN-II TRITIUM SYSTEMS

18.1. INTRODUCTION

In this section, specific tritium-system design issues that relate to the use of the aqueous-salt blanket coolant in TITAN-II are considered. A critical issue is the need to recover and control tritium that is bred directly in the water coolant of the primary heat-transport system. In particular, tritium recovery from water is required on a scale larger than existing water-detritiation systems. However, there is considerable industrial experience with recovery of hydrogen and its isotopes from water, and some relevant process equipment is used on a larger scale in non-tritium applications.

The TITAN-II design considers higher tritium levels (50 Ci/kg) in the primary-coo ..t water relative to previous design studies (*e.g.*, 1 Ci/kg in the "Blanket Comparison and Selection Study," BCSS [1]) in order to minimize the cost of water-processing equipment required for tritium recovery. Design features which make this possible are: (1) lower pressure in the primary system resulting from an elevation of the fluid boiling point caused by the addition of the Li salt, (2) possible use of double-walled steam generators, (3) presence of the water pool which captures a large part of the tritiated-water leakage, (4) routine use of welded joints, and (5) removal of tritiated water to safe storage during major maintenance operations. Component leakage rates and air-drier technology are based on CANDU systems performance. The overall tritium-loss rate for the TITAN-II design is estimated at 50 Ci/d.

The reference design for the blanket tritium-recovery system is based on a tritium level of 50 Ci/kg in the primary water coolant. This system recovers 430 g/d of tritium, primarily through a five-stage vapor-phase catalytic-exchange (VPCE) system, which transfers the tritium from the water to hydrogen gas, and then by cryogenic distillation for isotope separation. The TITAN-II fusion power core is submerged in the pool of water to achieve a high level of safety. The water pool contains tritium from primary-coolant system leakage, which is maintained at 0.37 Ci/kg by water distillation, with the enriched tritiated water from the distillation columns mixed with the primary-coolant water for final tritium recovery. The water-feed rate to the VPCE system is about 4000 kg/h at 50 Ci/kg. The estimated installed cost of the TITAN-II tritium-recovery system is 130 M$ (1986), not including building, air-cleanup, and indirect costs. Although the water-feed rate is about 10 times larger than the Darlington Tritium-Removal Facility,

the cost is only 3 to 4 times larger because of the economy of scale, fewer VPCE stages, and the lower reflux ratio needed in the cryogenic columns by the light-water feed.

The other TITAN-II tritium-related systems and flow rates are also assessed. The fuel-processing systems are similar to those of TITAN-I, which are described in Section 12. Unique features include a redundant impurity-removal loop (rather than relying on large tritium storage capacity) and a small feed to the isotope-separation system because of the use of mixed DT fueling. Plasma-driven permeation is less important in TITAN-II than in TITAN-I because the first wall is at a lower temperature and is made of ferritic steel rather than vanadium (Section 18.2). Back diffusion of protium is significant but acceptable. The air-detritiation system has a larger drier (but not recombiner) capacity to recover most of the tritiated water leaking from primary-system components.

The analysis of the TITAN-II tritium systems is given in the subsequent sections. The tritium flow rates are estimated in Section 18.3. The blanket tritium-recovery system, the plasma-exhaust-purification system, and the room-air-cleanup system are discussed, respectively, in Sections 18.4 through 18.6.

18.2. PERMEATION

18.2.1. First Wall

The first wall of the TITAN-II design is made of a ferritic steel alloy (9-C) in contrast with vanadium-alloy first wall of TITAN-I. Ferritic alloys are more resistant to hydrogen permeation than vanadium, so plasma-driven permeation should be less of a concern for TITAN-II.

As described in Section 12, plasma-driven permeation is modeled by using the code TRIPOS [2] to estimate the depth of triton implantation into the first wall, and the DIFFUSE code [3] to model the ensuing diffusion through the first wall. Values for the activation energies and coefficients for diffusion and solubility of hydrogen in the 9-C alloy (or HT-9) have not been reported. Consequently, the stainless-steel properties are used since both stainless steel and 9-C have 12% chromium and, therefore, the stainless-steel properties should approximate those of 9-C. The plasma flux and energies incident on the first wall are similar to those of TITAN-I.

The first wall of TITAN-II consists of half-cylindrical channels separated from the blanket lobes, with the cylindrical face towards the plasma. The direct area facing

the plasma is 101.6 m^2, although the cylindrical shape increases the effective area for permeation. The first-wall channels are 30-mm wide and 1.5-mm thick at the beginning of life. The channel-wall temperature ranges from 638 to 345 °C on the plasma side, 370 to 335 °C on the coolant side, and varies by 32 °C from coolant inlet to outlet. For DIFFUSE calculations, a slab geometry with an effective area is used, with average temperatures of 530 and 240 °C, respectively, for the plasma and coolant side.

Diatomic-recombination boundary conditions are used for both sides of the first wall. The plasma-side calculations consider both a sputter-cleaned and dirty surface (recombination sticking coefficient of 1 or 0.01, respectively). Ferritic surfaces in contact with water coolant are known to form oxide layers which act as permeation barriers. A barrier factor of 100 was used for HT-9 in water in the BCSS [1] and is adopted here, although the effect of the lithium-nitrate solution on the oxide layer is uncertain.

The result is a permeation of tritium from the plasma into the coolant of 0.34 to 4 g/d, depending on the cleanliness of the plasma surface. Comparable amounts of deuterium also permeate. The recombination coefficient is not well known and lower values than assumed here would give higher permeation rates.

In an aqueous-salt-cooled system, the hydrogen over-pressure in the coolant may be significant, perhaps as much as several atmospheres. Such pressures raise the possibility of hydrogen permeation through the first wall from the coolant into the plasma. To estimate the size of hydrogen back-diffusion, DIFFUSE calculations are made assuming a Sievert's-law boundary condition on the coolant side of the first wall, and diatomic recombination on the plasma side (sticking coefficient of unity). The back permeation is found to be between 12 and 39 g/d, respectively, for over-pressures of 1 to 10 atm. If an oxide layer at the steel-water interface is assumed with a barrier factor of 100, then back permeation is reduced to tenths of a gram per day. Similar calculations assuming a dirty plasma-side surface (sticking coefficient of 0.01) result in comparable values.

18.2.2. Divertor

The TITAN-II divertor design is similar to that of TITAN-I. The divertor armor is made of a tungsten-rhenium alloy (W-26Re) and is 1-mm thick with 7.4-m^2 surface area. The armor is brazed onto W-26Re tubes with 10-mm outer diameter and 1-mm wall thickness which are cooled with an aqueous-$LiNO_3$ solution. Data for hydrogen diffusion are not available for the W-26Re alloy, so corresponding properties of pure tungsten are used for calculations.

The particle flux and energies incident on the divertor plates are similar to those for TITAN-I (Section 12). The TITAN-II divertor-plate temperature ranges from 675 to 870 °C on the plate surface, peaks at 360 °C on the coolant side of the tubes, and varies by 40 °C from coolant inlet to outlet. For DIFFUSE analysis, average temperatures of 730 and 340 °C are used, respectively, for the plasma side and coolant side of the divertor plate. For these conditions, a plasma-driven permeation of 0.035 to 0.07 g/d is calculated, depending on the cleanliness of the plasma-facing surface.

18.3. TRITIUM CONTROL

In this section, the tritium-release rates from the TITAN-II reactor are estimated as a function of the tritium levels in the water coolant. Previous fusion-reactor studies have used a tritium level of 1 to 10 Ci/kg in the primary coolant [1,4], but such a low level would require a very large water-detritiation system for TITAN-II. In fact, there is considerable utility operating experience with tritium levels above 1 Ci/kg in water coolant. For example, CANDU reactors are designed to accommodate up to 70 Ci/kg in the moderator and 2.5 Ci/kg in the primary circuit at equilibrium. In present CANDU reactors at Pickering and Bruce, the heavy-water moderator (70 °C and 0.1 MPa) contains 20 to 30 Ci/kg tritium while the heavy-water primary coolant (300 °C and 9 MPa) contains 1.5 to 2 Ci/kg [5]. With these tritium concentrations (and inventories of about 4 kg of tritium in the water), the release rates from CANDU power stations have averaged 30 to 50 Ci/d-reactor over the past several years [5]. For fusion, a tritium level of 10 to 100 Ci/d is generally considered acceptable [1]. Based on the CANDU experience, tritium levels in the range of 10 to 100 Ci/kg were considered and a level of 50 Ci/kg was selected for TITAN-II.

There are two generic pathways for tritium losses to the environment: water leakage and permeation across heat exchangers and steam generators, and air losses from the evaporation of water leaked from components. For TITAN-II with steel piping and aqueous solution at ≤ 350 °C, tritium permeation across the coolant piping is unimportant.

18.3.1. Tritium Losses to Power Cycle

Tritium losses across heat exchangers include both permeation and leakage. Heavy-water losses across the steam generators at Pickering (550 MWe) and Bruce (880 MWe) were, respectively, 4 and 0.5 kg/d, because of permeation and small leaks [5]. Large leaks

are not included in these values, as they are rare and are quickly repaired. Reference [1] (BCSS) reports a water-loss rate of 45 kg/d for light-water-reactor steam generators, 10 kg/d for CANDU reactors, and adopts 24 kg/d-GWe as a reference value. More recent data also support a low CANDU steam-generator leakage. For example, 0.02% of CANDU tubes were plugged or repaired (as of 1986) compared to the industry average of 2% [6]. This small percentage was achieved through care in design, fabrication, and operation, and is necessary because of the cost of lost D_2O (*e.g.*, a 1.6-mm hole in 24,000 m^2 of steam-generator area will be unacceptable). For TITAN-II, similar care would be necessary with the proposed tritium levels. If a water-loss rate of 1 to 10 kg/d by leakage and permeation is assumed, then the tritium-loss rate through the steam generator is 1 to 10 (Ci/d)/(Ci/kg).

Alternately, the permeation rate through the steam generator can be estimated directly. The permeating flux is proportional to the material permeability, area, inverse of the wall thickness, and square-root of up-stream minus down-stream pressures. A value of 2×10^{-10} N-cm^2/s-kPa$^{0.5}$ is reported in the literature for the permeability of the oxidized Inconel [5], with some CANDU data indicating somewhat lower values. Based on a heat-transfer area of 21,500 m^2 (Bruce uses 18,920 m^2 for 880 MWe), a tube thickness of 1.12 mm (Bruce uses 1.12 mm with 9-MPa primary and 4.3-MPa steam-side pressures), a conservative primary H_2 pressure of 10 MPa, and a negligible steam-side hydrogen pressure, the permeation rate for TITAN-II is about 3 (Ci/d)/(Ci/kg).

This permeation rate assumes that the T:H ratio in the gas phase is the same as that in the water. There is some evidence that about 5%-10% of the tritium is initially formed as HT gas [7]. This will eventually equilibrate with the HTO phase (about 16 appm T in H at 50 Ci/kg) such that the T:H ratio in the hydrogen gas phase would be three times less than that in the water phase. However, the rate of equilibration is normally slow at room temperature. In the presence of radiolysis, 300 °C water in contact with metals, an H_2 over-pressure, and recombiners, the level of HT partial pressure is not clear. If the HT partial pressure were much higher than the equilibrium levels, it could be used to aid tritium extraction.

These tritium-loss rates could be reduced by three system-design options:

1. Use of an intermediate heat exchange (IHX) loop,
2. Use of double-walled steam-generator tubes,
3. Use of equal or higher pressure on the steam side.

An IHX provides a good barrier between the steam side and the primary circuit. The intermediate loop could be maintained at a much lower tritium level so that subsequent losses into the steam generator contain a low tritium content. The lower tritium levels would be maintained by an additional flow to the primary-coolant tritium-recovery system. A particular advantage of the IHX is that it prevents the highly-tritiated primary water from reaching the steam circuit in the event of a major tube rupture. The disadvantages are: a lower thermal efficiency because of the loss of peak steam temperature, the capital cost of an extra heat-transport loop, extra load on tritium-recovery and room-air-detritiation systems because of the extra coolant loop, and increased leakage and maintenance due to the extra equipment.

Double-walled steam generators have been considered for use in sodium-cooled fission reactors and in some fusion studies (BCSS [1], MARS [8]). TITAN-II could use this concept to provide additional leak resistance (failure of one boundary need not propagate into the second boundary) and permeation resistance (interior-surface coatings inhibit transport). Estimates for MARS indicate a reduction in the tritium permeation of up to a factor of 10^5 is possible [8]. One experiment [9] reported no improvement over single-wall permeation rates, but it seems likely that a significant effect could be obtained with other interior-surface preparations. The double-walled steam-generator approach provides similar advantages as an IHX, but with less cost and complexity and reduced degradation of peak steam temperature.

The third approach, equal or lower primary-system pressure is possible for TITAN-II because the salt content of the primary circuit elevates the boiling point. Consequently, the primary-system pressure can be reduced while maintaining a high temperature, resulting in the elimination of the driving force for leakage. In the TITAN-II design, the primary-coolant system is at 7 MPa, about equal to that of the secondary side. Lower pressure in the primary system will also reduce the water-leakage rate from other components of the primary system and keep the leakage rates within the range of CANDU experience (primary system at 9 MPa).

In summary, the tritium-loss rate across a good but conventional steam generator is estimated to be about 1 to 10 (Ci/d)/(Ci/kg). With improvements such as equal primary and secondary pressures, increased thickness of tubing, double-walled tubes, or other concepts, it seems plausible that the leakage rates could be reduced an additional factor of ten. It is assumed here that a tritium-loss rate of 0.2 (Ci/d)/(Ci/kg) by permeation and leakage can be achieved.

18.3.2. Component Tritium Losses

Water leakage from components leads to losses of tritiated-water vapor generally up the stack. This loss is minimized by using leak-tight designs and components, segregating major systems, and the use of air-drier technology. Again, because of the economics of heavy water, CANDU reactors have developed leak-tight systems and efficient air driers. TITAN-II has the further advantages of no mechanical pressure-tube end fittings (eliminating a major water-loss pathway), and of the primary system being immersed in a water pool (capturing a large part of the tritiated-water leakage).

Characteristics of tritium leakage and recovery from several CANDU reactors are summarized in Table 18.3-I. Total tritium-escape rates (leakages) and loss rates are reasonably well-known because the air-drier water is monitored and any lost heavy water must be made up by external supplies. Uncertainty exists in leak rates from specific components or systems, and the data are not necessarily reported in a directly accessible form. Overall, however, the data indicate that operating power plants with tritium levels in the range 1 to 30 Ci/kg have demonstrated overall water leakage rates of 40 to 400 kg/d, loss rates of 5 to 16 kg/d, and air-recovery efficiencies of 75% to 96%.

Several possibilities exist for reducing water leakage from present CANDU levels. The improvements are being incorporated into the newer fission reactors, and could certainly be used in a fusion reactor. These include [5]:

- Minimizing piping joints and components and using welds where possible;
- Using live-loading and bellows seals on valves, taper-lock or equivalent fittings on flanges, and similar leak-tight components;
- High maintenance priority for the fixing of leaks;
- Better room sealing.

For TITAN-II, tritium leakage during maintenance is minimized by removing the tritiated water from the affected loop to a dump tank and replacing it with unpressurized, low-tritium water. In general, the routine use of remote welding and maintenance equipment as expected in fusion machines will encourage welded connections and on-line repair of leaky components.

In order to estimate the tritium losses, the TITAN-II water-blanket systems are divided into four major areas: the reactor vault, coolant-chemistry room, blanket tritium-recovery room, and main reactor hall, as is shown in Figure 18.3-1. The main steam

Table 18.3-I.

TRITIUM-RELEASE RATES FROM CANDU REACTORS

Unit(s)	Year	Escape Rate (kg/d-reactor)	Recovery (%)	Loss Rate (kg/d-reactor)
Pickering A (1-4)	1972-86	170[a]	94[a]	10[a]
Pickering A (3,4)	1985	360	96	16
Pickering B (5-7)	1985	290	95	15
Pickering B (5-8)	1983-86	82[a]	94[a]	4.8[a]
Bruce A (1-4)	1985	175	93	12
Bruce B (5,6)	1985	-	-	7
Cordoba	1984	36	85	5
Le Preau	1984	45	75	11
Le Preau	1985	98	89	11
Wolsung	1985	125	91	11

(a) Estimated values.

generator, the primary pumps, and the pool heat exchanger are located within the pool. Other components such as the primary-circuit ion-exchange resins and filters, which are gamma active, could also be placed in the pool.

A CANDU average of 200 kg/d leakage may be inferred from Table 18.3-I. The distribution of water leakage between CANDU systems is not known precisely, but it appears to be dominated by the hot primary-coolant system. Of this, a substantial amount is believed to be caused by the pressure-tube end fittings which are mechanical joints that are routinely accessed while on line. Taking 75% of the nominal CANDU leak rate to be from the primary system, and taking credit for the lack of end fittings in TITAN-II but recognizing that the primary loop is not easily accessible and the salt may affect leakage,

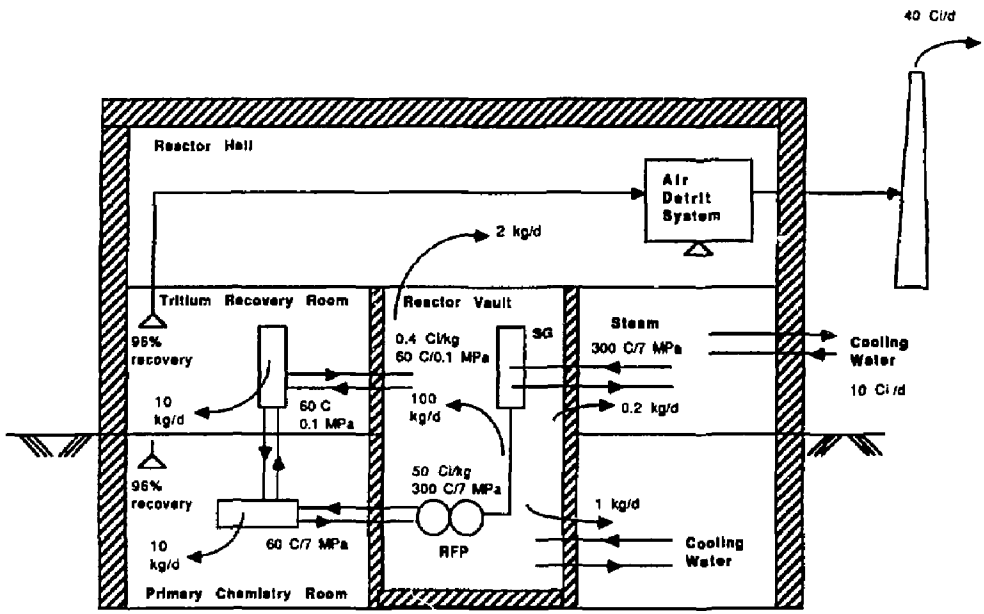

Figure 18.3-1. Water and tritium pathways within the TITAN-II reactor building, based on a 50 Ci/kg primary-system concentration. The net loss to the environment, allowing for the air-drier recovery efficiencies shown, is 50 Ci/d.

the estimated primary-system leakage rate in TITAN-II is 100 kg/d. Note that as this water leaks into the pool, the associated tritium is not released to the environment.

The remaining 25% of the nominal component water-leak rate occurs in other water-processing systems: the coolant-chemistry system and blanket tritium-recovery system in TITAN-II. It is assumed that welded joints and other procedures noted earlier are used, which reduce the leak rate by half to about 20 kg/d. A small loss also occurs from the pool, which is also sealed from the reactor hall. Figure 18.3-1 illustrates the general tritium levels and leakage pathways, based on a primary-coolant concentration of 50 Ci/kg.

It is further assumed that the equipment within the chemistry and tritium-recovery rooms is confined so that its environment can be efficiently dried at a 96% water-removal

rate. This rate represents the upper end of proven CANDU performance and implies use of room seals, segregation of leakage-prone equipment, and good drier capacity.

18.3.3. Tritium-Loss Rates

Based on the above permeation and leakage rates, the tritium-loss rates can be determined as a function of the tritium concentration in the primary coolant. In general, these releases linearly increase with tritium concentration. Clearly, the lower the tritium levels in the water, the lower the potential tritium-release-rate levels are. However, this must be balanced against the increasing cost of tritium extraction at low coolant concentration. These costs are evaluated in Section 18.4 with a tritium level of 50 Ci/kg selected as the TITAN-II design point.

From a maintenance viewpoint, the water temperature and tritium levels are of less concern than the air-tritium levels. In CANDU reactors, the moderator presently contains 20 to 30 Ci/kg without having a major impact on maintenance, and the design value is 70 Ci/kg. Under these conditions, workers would use plastic suits, system flushing, and automatic equipment to minimize the dose. In an accident where a worker was exposed to, for example, 10% direct skin wetting by 100 Ci/kg water, the committed dose is 15 rem. External dose from gamma-active corrosion products will also contribute and are much larger than the tritium dose (in present CANDU circuits). Overall, it is not expected that a tritium level of 50 Ci/kg will pose an unusual or unacceptable maintenance risk.

The TITAN-II reference design based on this trade-off has a tritium concentration of 50 Ci/kg in the primary-coolant system and 0.4 Ci/kg in the pool. The corresponding tritium-release rates to the environment are about 50 Ci/d total from the water-related systems. Based on the estimates for TITAN-I (Section 12), the additional contribution to the routine tritium releases from the remaining tritium systems, such as fuel cleanup and storage, are small.

18.4. BLANKET TRITIUM-RECOVERY SYSTEM

18.4.1. Tritium-Recovery Options

Some options for hydrogen-isotope separation are summarized in Table 18.4-I, with the hydrogen in the elemental or oxide (water) form. The effectiveness of the process is

Table 18.4-I.

THEORETICAL SEPARATION FACTORS FOR SOME ISOTOPE-ENRICHMENT PROCESSES [10]

Process	HD/H_2	HT/H_2	DT/D_2	H_20/D_20	HTO/H_2O	DTO/D_20	$^{235}U/^{238}U$
Distillation	1.5[a]	1.8	1.2[a]	1.05[a]	1.06	1.01	1.00002
H_2S exchange	NA	NA	NA	1.07[a]	–	–	NA
Gas diffusion	1.22	1.41	1.12	1.027	1.054	1.025	1.0043[a]
Gas centrifuge	1.051	1.10	1.051	1.038	1.078	1.038	1.16[a]
Laser	–	–	–	–	10,000[b]	–	–

(*a*) Processes in industrial use

(*b*) Tritium must be transferred into CF_3H molecule first.

roughly proportional to the separation factor, although there are other equally important parameters.

Distillation is widely used for hydrogen isotopes: cryogenic distillation at 20 K with elemental gas feed, and water distillation at 320 K with water feed (depending on the isotopes and concentrations). The bi-thermal hydrogen-sulfide (and the related ammonia) exchange process is used in industry for heavy-water extraction from ordinary water. This process would have good separation factors for tritiated water also, but would be difficult to use since it involves toxic and flammable gases. The newer technologies of gas centrifuge and laser enrichment offer particular advantages for uranium separation. Gas centrifuge offers reasonable theoretical separation for water, but not sufficiently better to justify replacing passive columns with high-speed rotating machinery. Laser separation offers very high separation factors in the laser stage, but requires substantial chemical processing as well as high-power lasers and optics. Laser separation has not proven better than the H_2S-exchange process for H_2O/HDO separation from natural water (at 150 ppm HDO). However, laser enrichment is still under development and may be effective for TITAN-II.

In the TITAN-II study, water and hydrogen distillation are considered the fundamental isotope-separation processes. These processes represent conventional technologies, have reasonable separation factors, and are mechanically fairly simple. Water distillation is used for pre-enrichment of the tritium, and cryogenic distillation is used for the final separation. A practical system involves other processes needed to transfer the tritium from the water into hydrogen gas. The options are vapor-phase catalytic exchange (VPCE), liquid-phase catalytic exchange (LPCE), direct electrolysis, or a combination of catalytic exchange and electrolysis. Some energy for electrolysis could be recovered by recombining the detritiated hydrogen with oxygen in a fuel cell. The water would be separated from the salt by flashing.

For the TITAN-II reactor, the tritium-production rate is 430 g/d. For an average tritium level in the primary heat-transport circuit of 50 Ci/kg, the water-feed rate to the tritium-recovery system would be about 4000 kg/h (200 kmol/h). For comparison, in other water-cooled blanket concepts in which the water tritium levels were deliberately kept lower than the levels considered here, maintaining 1 Ci/kg in water would require a 20-kmol/h water-detritiation system for 1-g/d tritium permeation into the water from the first wall or breeder [1,11].

Table 18.4-II summarizes some of the existing large hydrogen-separation facilities. Relative to TITAN-II with 50 Ci/kg coolant-tritium levels, VPCE, electrolysis, water distillation, and cryogenic distillation have been (or soon will be) demonstrated on a 1/10 scale with tritium; and electrolysis and H_2S exchange have been used in industry on a larger scale without tritium.

The effect of coolant-tritium levels on tritium-system cost is determined by considering a range of process designs at primary-coolant levels between 10 to 100 Ci/kg. Representative water-feed rates to the tritium-recovery system are given in Table 18.4-III as a function of the primary-system tritium content.

The water feed to the salt separator (flasher) is about 2.5 times the tritium-system feed assuming that 40% of the water is evaporated while going from the high-temperature, high-pressure feed conditions to the 0.1-MPa and 100 °C salt-free vapor. If the water-feed salt concentration is at 40% of its solubility limit, then the product is at 70% and precipitation should not occur. The pool is maintained at less than 0.5 Ci/kg in order to keep its tritium inventory acceptable. The tritiated water from the air-detritiation and other waste streams is estimated at about 6 kg/h (and several Ci/kg) based on the assumed leak and recovery rates. For comparison, these flow rates are much smaller than the coolant flow in the primary circuit (about 10^8 kg/h) and its flow through the chemistry-control system (10^5 kg/h).

Table 18.4-II.

PARAMETERS OF VARIOUS LARGE WATER ISOTOPE-SEPARATION SYSTEMS

Site	Feed Fluid	Product Fluid	Process[a]	Feed Rate (kmol/h)	Start-up Date
Darlington (Canada)	D_2O	T_2	VPCE/CD	18	1988
Grenoble (France)	D_2O	T_2	VPCE/CD	1	1972
Chalk River (Canada)	D_2O	T_2	LPCE/CD	1	1988
Mound Lab (US)	H_2O	T_2	CECE/CD	0.06	1986
Chalk River (Canada)	D_2O	T_2	DE	0.13	1985
Chalk River (Canada)	D_2O/HDO	D_2O	Elec. cascade	3-30	1950
Aswan Dam (Egypt)	H_2O	H_2	DE	1700	1984
Norsk Hydro (Norway)	H_2O	H_2	DE	180	1950
Bruce (Canada)	H_2O	D_2O	H_2S exchange	110,000	1975
Pickering (Canada)	D_2O/HDO	D_2O	WD	1-6	1972
Bruce (Canada)	H_2O/HDO	D_2O	WD	20	1975
Nangal (India)	H_2/HD	D_2	CD	223	1964
Los Alamos (US)	DT	T_2	CD	0.02	1985
Tokyo (Japan)	H_2	H_2O	FC	150	1984
TITAN at 50 Ci/kg	H_2O/HTO	T_2	–	220	20xx

(*a*) VPCE: Vapor-phase catalytic exchange;
LPCE: Liquid-phase catalytic exchange;
CD: Cryogenic distillation with H_2 or He refrigerant;
CECE: Combination of catalytic exchange and electrolysis;
DE: Direct electrolysis;
WD: Water distillation;
FC: Fuel cell.

Table 18.4-III.

REPRESENTATIVE WATER-DETRITIATION FEED RATES[a]

Coolant T Level (Ci/kg)	From Blanket Circuit To Flasher (kg/h)	From Blanket Circuit To Recovery (kg/h)	From Pool[b] (kg/h)	From Air Cleanup (kg/h)
100	5050	2020	930	6
70	7200	2880	650	6
50	10100	4040	460	6
30	16800	6730	280	6
10	50450	20180	90	6

(a) Based on 460 g/d of T recovered from blanket, with 90% detritiation per pass.

(b) Based on 0.5 Ci/kg in pool or 100 kg/d leakage of primary coolant from blanket.

For the TITAN-II water-detritiation system, several process options were considered. Light-water coolant is used in the final design, although heavy water was considered [12]. A heavy-water tritium-recovery system has more efficient phase transfer but less efficient cryogenic distillation, so it uses less steam but more electricity, and has more hydrogen gas but contains less tritium. The overall tritium system costs are comparable, but the cost of the heavy water itself makes light water the coolant of preference.

A simple model was developed containing correlations for water distillation, VPCE, electrolysis, and cryogenic distillation [13]. The model was developed for and calibrated against equipment at the Darlington or ITER scale (100 to 800 kg/h water-feed rate), so the extrapolation to TITAN-II conditions is approximate. The results of these scoping calculations are given in Table 18.4-IV at various blanket-coolant tritium levels. The costs are direct equipment costs and must be doubled to include installation.

The trade-off between tritium-recovery-system cost and tritium release as a function of coolant-tritium level is shown in Figure 18.4-1. Tritium-release rates increase linearly with blanket-coolant tritium levels, but the system costs decrease roughly as the inverse

Table 18.4-IV.

SCOPING EVALUATION OF SEVERAL TRITIUM-RECOVERY-SYSTEM DESIGNS (460 g/d RECOVERY AND 90% DETRITIATION PER PASS)

Coolant T Level (Ci/kg)	Process[a]			Maximum T Level (Ci/kg)	Process T Inventory (kg)	Process H Inventory (kmol)	Electrical Power (MWe)	Thermal Power (MWth)	Direct Cost (M$)
H_2O COOLANT:									
10	5WD	5VPCE	CD(H_2)	50	1.8	560	31	240	230
10	10WD	5VPCE	CD(He)	100	2.8	280	16	230	230
20		5VPCE	CD(H_2)	20	1.4	2100	28	51	125
20		5VPCE	CD(He)	20	1.4	1400	73	51	150
20		DE	CD(He)	240	12.0	280	78	0	190
20	10WD	5VPCE	CD(He)	200	2.8	140	8	120	125
50		5VPCE	CD(H_2)	50	0.9	860	12	21	73
50		5VPCE	CD (He)	50	0.9	580	32	21	89
50	5WD	5VPCE	CD(He)	250	1.3	110	7	48	63
50	10WD	5VPCE	CD(He)	500	2.6	60	4	50	62
50	5WD	5VPCE	CD(H_2)	250	1.4	170	3	50	60
50		DE	CD(H_2)	600	12.0	170	3	0	86
70		5VPCE	CD(H_2)	70	0.8	600	8.5	15	60
70	5WD	5VPCE	CD(H_2)	350	1.3	121	1.8	35	46
70	5WD	5VPCE	CD(He)	350	1.3	81	5	35	51
100		5VPCE	CD(H_2)	100	0.7	460	6.5	11	51
100	5WD	5VPCE	CD(H_2)	500	1.3	91	1.4	26	38
D_2O COOLANT:									
20		5VPCE	CD(H_2)	20	0.9	3800	51	38	118
50		5VPCE	CD(H_2)	50	0.6	1500	22	16	70
70		5VPCE	CD(H_2)	70	0.5	1100	16	11	57
100		5VPCE	CD(H_2)	100	0.4	820	12	8	49
34[b]		8VPCE	CD(H_2)	34	0.04	140	2	1.4	20

(*a*) nWD: Water distillation with enrichment by factor of n;
mVPCE: m-stage vapor-phase catalytic exchange;
DE: Direct electrolysis;
CD: Cryogenic distillation with H_2 or He refrigerant.

(*b*) Darlington Tritium Recovery Facility at 26 g/d of tritium and 97% detritiation per pass.

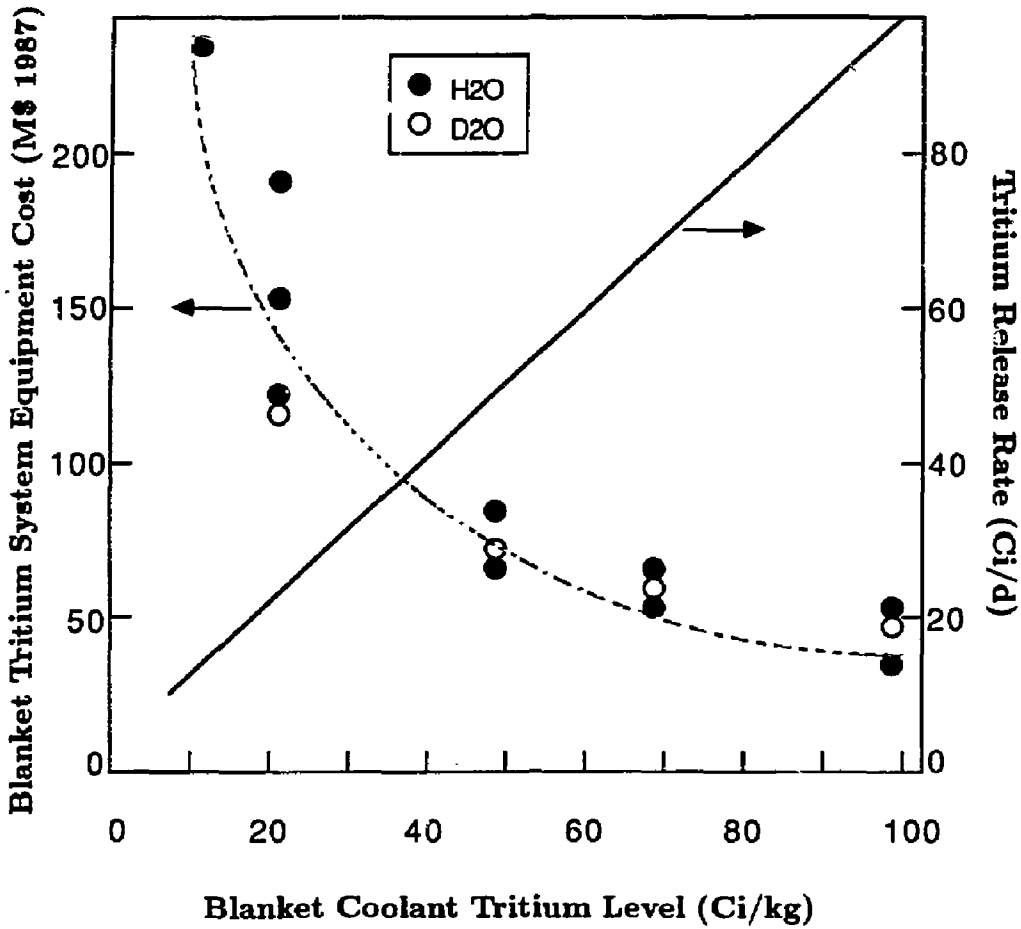

Figure 18.4-1. Comparison of direct cost of the tritium-recovery system and tritium-release rate as a function of blanket-coolant tritium levels. Design points are shown for the various tritium-system designs analyzed.

Table 18.4-V.

TITAN-II BLANKET TRITIUM-SYSTEM DESIGN REQUIREMENTS

Blanket:	
Volume	$274\,m^3$
Coolant	H_2O at 50 Ci/kg
Lithium content	6.4 at.% Li as aqueous-$LiNO_3$ solution ($98.5\,g$ $LiNO_3$ per $100\,g$ H_2O)
Conditions	330 °C, 7 MPa
Tritium-extraction rate	$\geq 430\,g/d$ of T
Tritium-extraction efficiency	$\geq 90\%$ per pass
Pool:	
Volume	$22{,}640\,m^3$
Tritium inventory	$\leq 1\,kg$ T
In-leakage from blanket coolant	100 kg/d at 50 Ci/kg
Tritiated Waste Water:	
Production rate	6 kg/h at 10 Ci/kg

of the tritium level. Beyond about 50 Ci/kg, the additional cost savings become relatively small while the tritium-release rates (and coolant-tritium inventory) continue to increase. At 50 Ci/kg, the estimated tritium-release rate is about 50 Ci/d, which is within the acceptable design range for fusion reactors (nominally 10 to 100 Ci/d), and is consistent with present CANDU performance.

The TITAN-II reference design must recover 430 g/d of tritium from 50-Ci/kg water. The system conditions are summarized in Table 18.4-V. Based on the scoping evaluations (Table 18.4-IV), the main options for tritium recovery are compared below.

VPCE versus LPCE versus electrolysis. The catalytic-exchange processes need more hydrogen gas because of the less efficient HTO/HT transfer, but they have much

smaller tritium inventories for the same peak process HTO concentration and are generally less expensive. The total power consumption is similar. A catalytic process is preferred for the TITAN-II scale. The LPCE has some advantages because of mechanical simplicity and lower temperature operation. However, VPCE is more efficient and thus less expensive. Therefore, the vapor-phase catalytic-exchange process is chosen for TITAN-II.

Hydrogen versus helium refrigerant. For TITAN-II, as with Darlington, the additional hydrogen gas for the refrigerant cycle should be less important (given the large amount already present as process gas) than the cost and power savings (a factor of three to five).

Water distillation. Distillation provides simple HTO enrichment, operating at 50 to 60 °C and 13 to 17 kPa using low-pressure steam. Equipment costs could potentially be reduced by 10M$ by using water distillation. However, the cost of the large building needed to house the towers (8 towers, each about 2.6 m in diameter and 30 to 40-m high, for 50-Ci/kg feed) and the high tritium levels in water should be considered, which appear to offset any cost savings. Distillation would be useful, however, for enriching the pool and waste water because of the lower feed rate and tritium content.

18.4.2. Blanket Tritium-System Design

Based on the scoping analysis, a reference design was selected based on:

- Water distillation for the detritiation and pre-enrichment of the low-tritium feed from the pool and air-cleanup systems,
- Five-stage VPCE for transferring tritium into the hydrogen gas phase from the primary coolant and enriched water-distillation output,
- Cryogenic distillation to separate the protium from the tritium.

A block diagram of the tritium-recovery system is shown in Figure 18.4-2, giving the overall mass balance and the flow rates of the main forward and recycle streams within the tritium system. This design is larger than necessary and could remove 465 g/d of tritium (rather than 430 g/d) at 50 Ci/kg.

Tritium levels in the pool are maintained at less than 0.5 Ci/kg by processing 465 kg/h through a single water-distillation tower. The tower returns the water with 90% detritiation, and forwards 5.4 kg/h at 50 Ci/kg for mixing with the blanket-coolant water

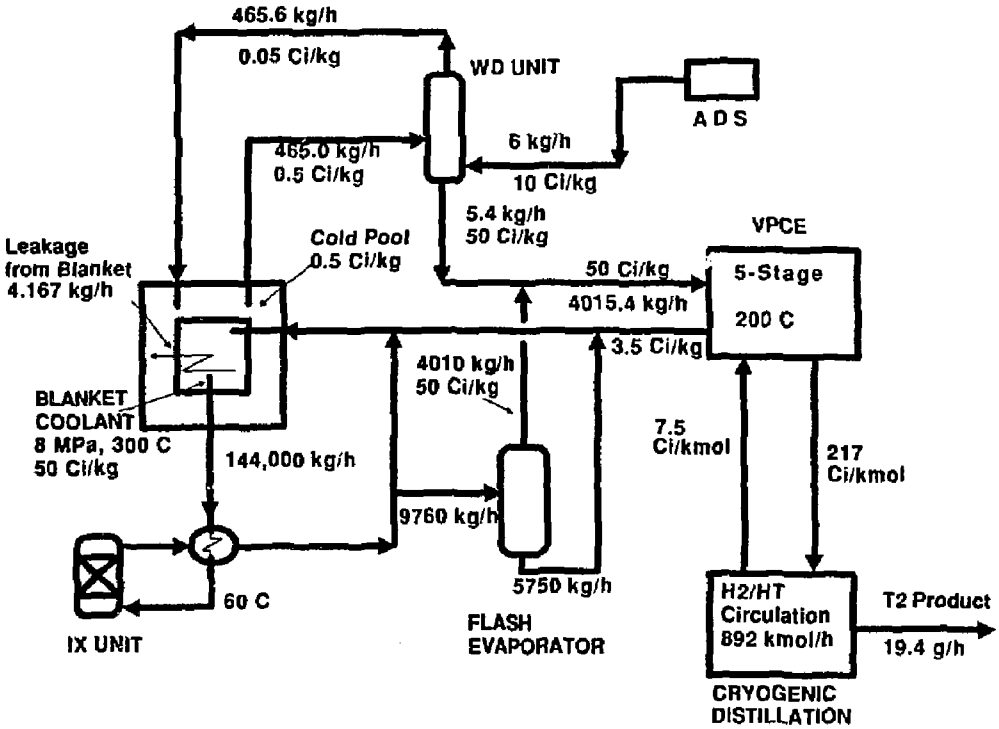

Figure 18.4-2. Blanket tritium-extraction system for TITAN-II showing water and hydrogen flow rates and tritium level in the flows, based on extracting 465 g/d of tritium at 50 Ci/kg.

for processing. This tower is about 2.6 m in diameter and 30- to 40-m high, about the size and duty of the heavy-water-upgrader distillation column at Darlington. The water-distillation system includes the tower with packing, reboiler, overhead condenser, vacuum system to provide a condenser pressure of 13 kPa, pumps, surge tanks, piping, control, and instrumentation. Accounting for tritium decay in the pool, the peak tritium levels would actually be 0.37 Ci/kg and would only be reached after several years of operation.

A purification unit is required to keep gamma levels low in the blanket coolant and to provide a clean feed stream to the tritium-recovery system. The purification unit uses high-pressure, low-temperature technology widely used in CANDU reactors: a heat exchanger, filters, and ion exchange (IX) columns to remove both cationic and anionic impurities. A bleed stream of 144,000 kg/h is withdrawn from the blanket-coolant loop and cooled to 60 °C to avoid thermal degradation of the IX resin. This flow rate re-

moves about 50% of the suspended impurities in the primary circuit each hour, typical of CANDU design. The filter vessels will have integral lead shielding and replaceable cartridge baskets. The IX columns contain a lithiated mixed-bed resin that will not remove lithium or nitrate ions. The IX columns will be located in pits provided with concrete shielding, and the resin will be slurried in and out of the columns.

The purified salt solution leaving the IX columns is reheated to 280 °C in the heat exchanger, and a fraction is diverted to a flash evaporator. The flashing of water from 8 MPa and 280 °C yields about 40% salt-free vapor at 0.1 MPa and 100 °C which is sent to the VPCE unit for tritium recovery. Liquid from the flash evaporator, concentrated in lithium salt but below the solubility limit, combines with the detritiated water from the VPCE and the main purification stream from the heat exchanger.

A five-stage VPCE unit provides a water-detritiation factor of 93% and reduces the hydrogen flow to the cryogenic distillation, which is then four times the molar feedwater rate. Each VPCE stage consists of an evaporator, superheater, catalyst bed, and condenser. The catalyst operates at 200 °C and slightly above atmospheric pressure. There are no valves in this equipment; the Grenoble VPCE system has operated reliably for many years.

The cryogenic-distillation unit receives mostly H_2/HT and separates the hydrogen isotopes into 99+% T_2 product and an almost pure H_2 stream. The cryogenic-distillation unit is a cascade of packed distillation columns, reboilers, condensers, heat exchangers, and catalytic equilibrators inside an insulated cold box. The feed gas from the VPCE is dried and purified to remove contaminants (*e.g.*, water vapor, nitrogen, and oxygen) and then compressed and cooled before entering the columns. Hydrogen refrigeration is used because it cools efficiently through the latent heat of vaporization. This leads to much reduced refrigeration power and smaller cryogenic cold boxes because of the smaller heat-exchange surface area.

The largest cost component in the cryogenic-distillation unit is the first column which separates the bulk H_2 from HT. With hydrogen refrigerant, the operating conditions of this first column are 0.2 MPa and 23 K. A 40-stage stripping section is adequate to provide a tritium-poor hydrogen-return stream at 10 Ci/kmol. The first column condenser heat load, which essentially determines the refrigeration requirement, is about 360 kW for 890-kmol/h feed. The tritium inventory is based on a scale-up of Darlington, accounting for differences in flow rate and reflux ratios, with a 25% reduction for an optimum design of the high-tritium cascade.

Table 18.4-VI.

TITAN-II BLANKET TRITIUM-SYSTEM CAPITAL COST AND TRITIUM INVENTORY (BASED ON EXTRACTING 465 g/d of T at 50 Ci/kg)

Process Unit	Equipment Cost (M$ 1987)	Tritium Inventory (g)
Purification	1.5	4.5
Flash evaporator	1.0	25.4
Water distillation	6.0	1.7
VPCE[a]	41.0	12.5
Cryogenic distillation[b]	20.0	550.0
TOTAL	69.5	594.1

(*a*) Cost includes driers, feed and return tanks, gas compressors, five-stage VPCE (catalytic beds, evaporators, superheaters, and condensers), low-tritium column-expansion tank, vacuum pumps, piping, controls, analyzers, and instrumentation.

(*b*) Cost includes hydrogen-refrigeration unit.

The characteristics of the TITAN-II blanket tritium system are given in Tables 18.4-VI and 18.4-VII. The process-equipment capital cost includes engineering but not site preparation, structures and foundations, site services, installation, commissioning, freight, taxes, or indirect costs such as corporate overheads.

The overall cost of TITAN-II tritium systems is estimated as 70 M$ (1987) for direct cost of the process equipment. Although the feed throughput is about a factor of 10 larger than Darlington and the process is similar, the costs are only about 3 to 4 times larger. This reduction reflects general economies of scale (the dominant equipment scales as the 0.7 power), fewer VPCE stages for TITAN-II because of the lower detritiation needs (5 rather than 8), and the lower reflux ratio (a factor of 3 to 5) in the first and largest cryogenic-distillation column by separating H_2/HT rather than D_2/DT.

Table 18.4-VII.

TITAN-II BLANKET TRITIUM-RECOVERY SYSTEM
(BASED ON EXTRACTING 465 g/d of T at 50 Ci/kg)

Maximum tritium concentration	50 Ci/kg in water
Tritium-extraction rate	465 g/d of T
Tritium inventory as water	44 g T
Tritium inventory as gas	550 g T
Blanket detritiation factor	93% per pass
Hydrogen-refrigeration power	5.7 MWe
Low-pressure steam to water distribution	5.7 MWth at 300 kPa
Low-pressure steam to VPCE	1.2 MWth at 600 kPa
High-pressure steam to VPCE	8.5 MWth at 2.5 MPa
Hydrogen-gas inventory	1500 kg
Building volume	36,000 m^3

The installed cost for the TITAN-II tritium system is estimated as 140 M$ (1987), based on doubling the direct cost of the equipment. The exact multiplier is not clear; installation costs for similar types of equipment have been quoted as 10% to 400% of the direct costs. A factor of two is roughly consistent with Darlington, if the building and air-cleanup systems are treated separately.

There are several factors which will reduce costs. First, the actual system is about 8% oversized relative to the final TITAN-II requirements. Second, the TITAN-II base year for costing is 1986. Consequently, the reference TITAN-II blanket tritium-system cost is estimated to be 130 M$ (1986).

Other factors are not explicitly included since their individual contributions are less than the overall accuracy of the cost estimate. First, TITAN-II is a commercial reactor so there will be economies of production. Engineering costs (10% of Darlington, roughly 25% of the process-equipment cost) can be shared over several reactors. Second, there will be

a learning curve which can reduce costs by 15% to 30% over 10 installed systems. Third, the VPCE equipment (boiler, superheater, catalyst, and condenser) can be combined into factory-assembled columns for each stage. This would complicate maintenance, but reduce water leakage and provide up to 30% savings per stage. Finally, the tritium-recovery system will reduce the natural deuterium present in the primary circuit, which will decrease the work load on the cryogenic columns and also provide some reactor deuterium needs (about 200 kg of deuterium is available, mostly in the pool). Another blanket tritium-system concept could allow higher tritium levels in the pool, and circulate the detritiated blanket-coolant water directly through the pool. This would eliminate the water-distillation column presently used on the pool, but would require more stages on the VPCE. This concept was not optimized, but with pool tritium levels of 1 to 1.2 Ci/kg (rather than the present 0.4-Ci/kg concept) there is little overall effect on the direct capital cost.

A substantial improvement in costs requires a new approach. Laser separation is under investigation, but it is not yet clear that this is attractive for water detritiation. Radiolysis may be useful if a large amount of the tritium stays in the HT form, and if the system can control the consequences of the associated O_2 production. One may imagine advances in technologies such as lasers, permeation membranes, or magnetic systems that take advantage of the large differences in mass, charge-to-mass ratios, nuclear moments, and molecular vibrational levels between the different water molecules. These differences have not been fully exploited in present hydrogen-separation systems.

18.5. PLASMA-EXHAUST-PURIFICATION SYSTEM

The plasma-exhaust-purification system is virtually identical to that of TITAN-I described in Section 12. Back diffusion of protium from the coolant into the plasma may occur if there is a substantial hydrogen over-pressure from the radiolysis. For an H_2 pressure of 1 to 10 bar, the permeation rate is 0.1 to 10 g/d of hydrogen. Assuming 1 g/d of H permeation, a fuel-feed rate of 10 kg/d of DT, and a flow to the fuel-isotope system of 1% of the main fuel flow, the resulting protium concentration in the plasma is about 2.5 at.%, which is acceptable. The present fuel-processing system is designed to handle up to about 5% protium. If necessary, the fuel-isotope system could be increased in size at small overall increase in cost, or the fuel-isotope system could be merged with the blanket-isotope system.

18.6. ROOM-AIR-CLEANUP SYSTEM

Air driers will be widely used in TITAN-II to recover HTO lost from component leakage. Air from rooms containing leakage-prone equipment will be segregated using CANDU-like confinement technology and ventilated through air driers. These driers are not needed for HT conversion duty so they do not have heaters, recombiners, or coolers. They are reliable and proven in CANDU service.

The overall building volume containing exposed primary-coolant circuit and blanket tritium-system equipment is roughly 40,000 m^3. In the TITAN-II reference design, 40 Ci/h of HTO escapes from this equipment and is recovered or lost. For a room decontamination factor of 100, this implies air tritium levels of about 1 MPCa averaged over the whole volume. In practice, the tritium levels will fluctuate and be higher during spills and maintenance. On the other hand, the most leakage-prone equipment will be segregated into smaller volumes which can be dried more effectively. A detailed layout has not been attempted, but if driers are used with several air changes per hour on average, then the cost for the installed drier system is estimated at 13 M$ for 200,000 m^3/h. In addition, some capacity is needed for other rooms (*e.g.*, the fuel-purification room). In TITAN-II, tritium is generally more in the water form and handled using the normal driers, so the additional emergency air-cleanup system has a capacity of 15,000 m^3/h at a cost of 2 M$.

18.7. SUMMARY

The TITAN-II tritium flow paths are shown in Figure 18.7-1. The tritium inventories and tritium-systems costs are given in Tables 18.7-I and 18.7-II, respectively.

The final design of the TITAN-II tritium system is based on 50 Ci/kg in the blanket-water coolant, and 0.37 Ci/kg in the pool. The TITAN-II tritium-release rates are dominated by those associated with leakage of HTO from the blanket-coolant systems and are estimated to be 50 Ci/d. The maximum tritium concentration in the blanket tritium-recovery system is also 50 Ci/kg since no enrichment is used in the present design. This level of tritium is only modestly beyond present utility experience, presents no unusual risks (*i.e.*, accidental splashing is not fatal), and may be handled using standard precautions such as protective suits.

The overall cost of the TITAN-II tritium system is 170 M$ (1986) installed. The costs of the TITAN-II tritium system (Table 18.7-II) are dominated by the blanket tritium-

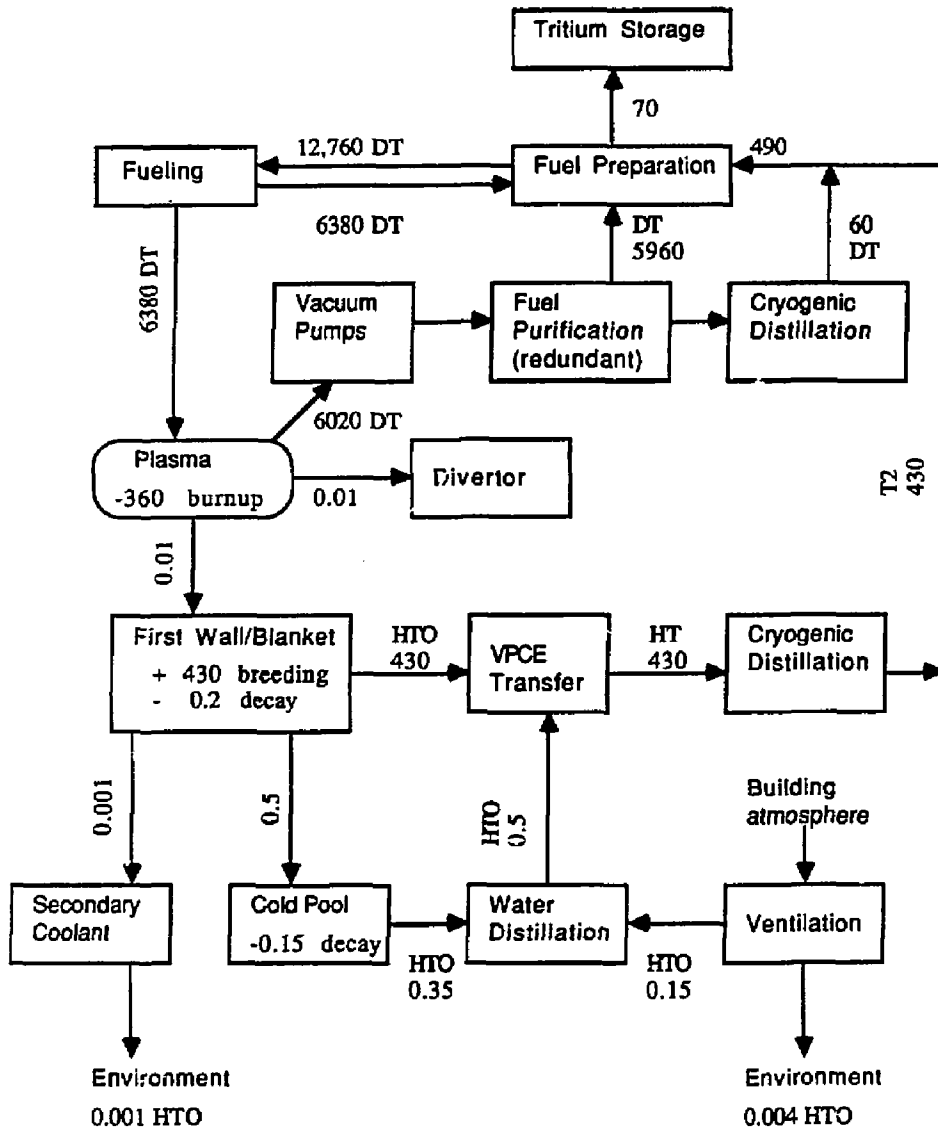

Figure 18.7-1. Overall tritium flow rates (g/d) and form in the TITAN-II reactor.

recovery system. Since tritium recovery in TITAN-II involves isotope separation of tritium from low concentrations in water, it is expected to be more expensive than for other fusion-blanket concepts. The present design approach is based on proven chemical exchange and distillation concepts. Costs for other tritium systems are similar to those for TITAN-I (note the larger air-drier capacity). Some costs are estimated from Reference [14].

The total tritium inventory in TITAN-II is 4 kg, roughly comparable to the inventory in some CANDU reactors at present. The largest inventory is in the primary circuit, which requires a larger blanket processing system.

Table 18.7-I.

TITAN-II TRITIUM INVENTORIES

System	T Inventory (g)	Form
Primary heat-transport coolant	1420[a]	HTO
Beryllium	10	T in metal
Piping and structure	< 1	T in metal
Plasma chamber and vacuum	5	DT
Fuel processing	20	DT
Blanket tritium recovery	44	HTO
	550	HT
Shield	< 10	HTO
Tritium storage	1000	Metal tritide
Pool	940[b]	HTO
TOTAL	4000	

(*a*) Based on 274 m^3 at 50 Ci/kg.

(*b*) Based on 22,640 m^3 at 0.4 Ci/kg.

A major reduction in the costs and tritium levels requires a new water-detritiation approach. At present, laser separation is under investigation, but probably improvements in the lasers and optical materials are required for this approach to be attractive. Radiolysis might be helpful if a high yield of HT is obtained (not clear from present experiments), and if the associated O_2 production is acceptable.

Relative to the TITAN-I tritium system (Section 12), the TITAN-II tritium system is more expensive, the total tritium inventory is larger, the overall tritium system is physically larger, and the chronic tritium releases are larger. However, the TITAN-II tritium inventory is much less at risk for major release because of the lack of reactive chemicals, the low temperatures and pressures of most of the tritiated water, and the pool surrounding the fusion power core. Plasma-driven permeation is not a concern for TITAN-II, although the amount of protium back-diffusing to the plasma is significant.

Table 18.7-II.

TITAN-II TRITIUM-SYSTEM INSTALLED COSTS

System	Installed Cost (M$ 1986)
Fuel processing	14
Blanket tritium recovery	130
Air detritiation	15
Fueling	4
Waste-water cleanup	2
Tritium storage	1
Tritiated-waste disposal	3
Primary-coolant-storage tanks	1
TOTAL	170

REFERENCES

[1] D. L. Smith, G. D. Morgan, M. A. Abdou, *et al.*, "Blanket Comparison and Selection Study, Final Report," Argonne National Laboratory report ANL/FPP-84-1 (1984).

[2] P. Chou and N. M. Ghoniem, "Precipitate Dissolution by High-Energy Collision Cascades," *J. Nucl. Mater.* **117** (1983) 55.

[3] M. I. Baskes, "DIFFUSE 83," Sandia National Laboratory report SAND-83-8231 (1983).

[4] S. Sood, O. K. Kveton, *et al.*, "Tritium Systems Concepts for the Next European Torus (NET)," Canadian Fusion Fuels Technology Project report CFFTP-G-86020 (1986).

[5] K. Y. Wong, T. A. Khan, F. Guglielmi, *et al.*, "Canadian Tritium Experience," Ontario Hydro report (1984).

[6] G. A. Pon, "Significant Engineering Developments," in *Proc. Eng. Centennial Conf.*, Montreal, Canada (May 1987).

[7] T. Kamara, R. M. White, and F. S. Rowland, "The Reactions of Recoil Tritium Atoms in Aqueous Solution," . *Inorg. Nucl. Chem.* **21** (1961) 210.

[8] B. G. Logan, C. D. Henning, *et al.*, "MARS, Mirror Advanced Reactor Study, Final Report," Lawrence Livermore National Laboratory report UCRL-53480 (1984).

[9] S. Sinharoy, A. R. Keeton, and W. J. Lange, "Permeation of Deuterium through Double Walled Croloy Tubes," Westinghouse report 86-7B6-HYPER-R1 (1986).

[10] M. Benedict, T. Pigford, and H. Levi, *Nuclear Chemical Engineering*, 2nd edition, McGraw-Hill, Toronto (1981).

[11] The NET Team, "NET Status Report," NET-51 (1985).

[12] A. Dombra, Chalk River Nuclear Laboratories, private communication (August 1986).

[13] A. Busigin and K. Kalyanam, "Water Detritiation System Module for ETR System Code," Ontario Hydro report (1987).

[14] M. Abdou, C. Baker, J. Brooks, *et al.*, "A Demonstration Tokamak Power Plant Study (DEMO)," Argonne National Laboratory report ANL/FPP/82-1 (1982).

19. TITAN-II SAFETY DESIGN AND RADIOACTIVE-WASTE DISPOSAL

Clement P. C. Wong
Edward T. Cheng
Steven P. Grotz
Shahram Sharafat
Kenneth R. Schultz

Contents

19. TITAN-II SAFETY DESIGN AND RADIOACTIVE-WASTE DISPOSAL

19.1. INTRODUCTION

Strong emphasis has been given to safety engineering in the TITAN study. Instead of an add-on safety design and analysis task, the safety activity was incorporated into the process of design selection and integration at the beginning of the study. The safety-design objectives of the TITAN-II design are: (1) to satisfy all safety-design criteria as specified by the U. S. Nuclear Regulatory Commission on accidental releases, occupational doses, and routine effluents and (2) to aim for the best possible level of passive safety assurance.

This section presents the safety design and evaluations of the TITAN-II reactor. The safety-design goals for the TITAN reactors are discussed in Section 19.2. To achieve a high level of safety assurance, the TITAN-II fusion power core (FPC) is submerged in a pool of low-temperature, low-pressure water. Various safety scenarios and the impact of the water pool are reviewed in Section 19.3. Detailed analyses of loss-of-flow and loss-of-coolant accidents in the TITAN-II FPC are reported in Section 19.4. Plasma-related accidents and plasma shutdown methods for TITAN-II are similar to those of TITAN-I (Section 13.6) and thus are not repeated here. Section 19.5 describes the radioactive-waste-disposal issues and ratings for the TITAN-II design. A summary of the TITAN-II safety design and analysis is given in Section 19.6.

19.2. SAFETY-DESIGN GOALS

Two main objectives have guided the TITAN safety design: (1) to satisfy all safety-design criteria as specified by the U. S. Nuclear Regulatory Commission (U. S. - NRC) on accidental releases, occupational doses, and routine effluents; and (2) to aim for the best possible level of safety assurance.

Although the accident scenarios and classification systems developed by the U. S. fission industry may not apply directly to fusion reactors, the dose guidelines used by the fission industry will probably either be directly applicable or serve as useful references in

defining the radiological safety requirements for fusion-reactor designs. The U. S. – NRC regulations covering fission reactors are described in the Code of Federal Regulations in Sections:

- 10CFR20 – Standards for Protection Against Radiation [1],
- 10CFR50 – Domestic Licensing of Production and Utilization Facilities [2],
- 10CFR100 – Reactor Site Criteria [3],
- 10CFR61 – Licensing Requirements for Land Disposal of Radioactive Waste [1].

Details of the present industry guidelines for satisfying the regulations and the corresponding numerical dose limits are presented in Section 13.2 and are summarized in Tables 13.2-I and 13.2.-II.

Recently, four levels of safety assurance were proposed to facilitate the preliminary evaluation of different designs [4,5]. While these levels are neither precisely defined licensing criteria nor rules for formal safety evaluation, they do provide a relatively simple guide for designers who can use these definitions of different levels of safety to evaluate their designs or to improve on their safety features when appropriate. The following summarize the interpretation of these four levels of safety assurance as suggested by Piet [4] (also see Reference [5]).

Level 1 – "Inherent safety." Safety is assured by inherent mechanisms of release limitation no matter what the accident sequence is. The radioactive inventories and material properties in such a reactor preclude a violation of release limits regardless of the reactor condition.

Level 2 – "Large-scale passive-safety assurance." Safety is assured by passive mechanisms of release limitation as long as severe reconfiguration of large-scale geometry is avoided, and escalation to fatality-producing reconfigurations from less severe initiating events can plausibly be precluded by passive design features. In such a reactor, natural heat-transfer mechanisms suffice to keep temperatures below those needed, given the radioactivity inventory and material properties, to produce a violation of release limits unless the large-scale geometry is badly distorted.

Level 3 – "Small-scale passive-safety assurance." Safety is assured by passive mechanisms of release limitation as long as severe violations of small-scale geometry, such as a large break in a major coolant pipe, are avoided, and escalation to fatality-capable

violations from less severe initiating events can plausibly be precluded by passive design features. In such a reactor, sufficiency of natural heat-transfer mechanisms to keep temperatures low enough, given its radioactivity inventories and materials properties, to avoid a violation of release limits can only be assured while the coolant boundary is substantially intact.

Level 4 – "Active safety assurance." There are credible initiating events that can only be prevented from escalating to site-boundary-release limit violations or reconfigurations by means of active safety systems. This is the conventional approach of add-on safety.

The public is adequately protected by all four levels of safety assurance. To understand the meaning of adequate protection of the public, the concept of safety assurance can be further strengthened in the context of probabilistic risk assessment. The risk-based safety goal for TITAN is that fusion accidents would not increase the individual cancer risk of the public by more than 0.1% of the prevailing risk. As a consequence of this goal, a site-boundary whole-body dose limit of 25 rem for accidental release for fission reactors (10CFR100 [3]) has been adopted.

19.3. SAFETY-DESIGN FEATURES

The TITAN-II FPC is cooled by an aqueous lithium-salt solution and therefore the cooling circuit is a pressurized-water system. Furthermore, the primary coolant contains tritium at a high concentration of 50 Ci/kg. A passive safety system is thus required to handle different accident scenarios, to control the potential release of high-pressure primary coolant which contains tritium, and to prevent the release of induced radioactivities in the reactor structural materials even under the conditions of a loss-of-coolant-accident.

Different approaches for passively safe design of fission pressurized-water reactors (PWRs) were reviewed. It was concluded that the most passive approach is the Secure-P (PIUS) design [6] developed in Sweden. The PIUS design approach is to enclose the fission reactor vessel and the primary-loop system into a prestressed concrete vessel filled with cold pressurized water. The hot coolant loop and the cold pool can communicate through upper and lower density locks. One of the key safety features of the PIUS design is the termination of the fission reaction by passively introducing the cold pool of borated water into the fission core through the density locks, when necessary.

Two points of contention for the PIUS design are the stability and reliability of the density locks and the cost of the massive prestressed concrete vessel. These two

requirements are unnecessary for a fusion reactor such as TITAN-II, however the safety advantages of a pool design can be fully utilized. Therefore, to achieve a high level of safety assurance, the complete TITAN-II FPC, the pressurized primary-coolant system, and the steam generators are submerged in a pool of low-temperature, low-pressure water as shown in Figure 19.3-1. The cold pool of water acts as a heat sink to dilute the reactor thermal and decay afterheat energy and also eliminates the possibility of releasing tritiated water vapor or other radioactive material to the environment.

The basic sources of thermal energy at reactor shutdown are from the plasma thermal and magnetic energy, the thermal energy of the hot loop, and the induced afterheat power in the FPC structure. In the TITAN-II design, the FPC and the primary-loop circuit are arranged such that during a loss-of-flow accident (LOFA), natural circulation will be developed to remove the blanket afterheat to the secondary loop. In the case of a major coolant-pipe break, the coolant in the hot loop will mix with the pool of water since the complete primary loop is in the pool. With this mixing, the temperature of the pool will only rise slightly because of the much larger volume of the water pool. The pool also acts as a heat sink for the decay afterheat in the structural material of the FPC. In fact, even if the heat transfer from the pool to the surrounding earth is ignored, it would take more than seven weeks for the temperature of the water pool to reach 100 °C. Therefore,

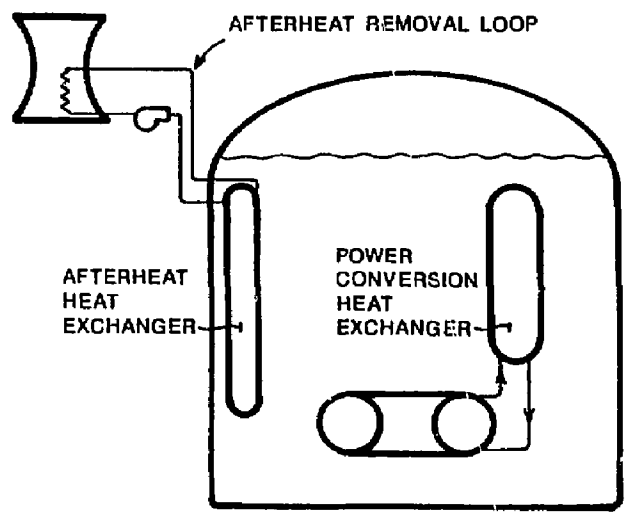

Figure 19.3-1. The TITAN-II "loop-in-pool" configuration.

the potential release of tritium or other radionuclides in the primary-coolant loop to the public is significantly reduced.

19.3.1. Safety Scenarios

Based on the "loop-in-pool" concept of the TITAN-II design, different scenarios for handling normal and off-normal situations were evaluated and are discussed in the following section. The size and operating conditions of the TITAN-II water pool are determined by these analyses.

19.3.1.1. Normal operation

Under normal operation, the FPC is actively cooled by the primary-coolant loop system. In the TITAN-II design, the primary-cooling circuit is not completely insulated from the pool so that the pool can absorb the decay afterheat power in case of LOFA in either the primary circuit or the steam generators. The level of decay afterheat in the TITAN-II FPC is estimated at 34 MW after one full-power year (FPY) of operation at 18 MW/m^2 of neutron wall loading. Therefore, during the normal operation, 34 MW of thermal power is conducted through the steam generator vessel and primary-coolant piping walls to the pool. This power is then removed by separate heat exchangers in the pool.

The pool temperature should be kept as low as possible to maintain an adequate heat-sink capability in the pool in case of an accident. On the other hand, the pool temperature should be reasonably high such that the size of the afterheat-removal heat exchangers in the pool, which are capable of removing the steady power of 34 MW, can be minimized. The exact pool temperature should be determined by detailed design. For the TITAN-II reactor, a pool temperature range of 60 to 70 °C is found to be reasonable based on detailed evaluation of the accident scenarios.

19.3.1.2. Loss of primary-coolant flow

In the accidental condition of the loss of flow in the primary-coolant circuit, plasma operation should be terminated. The steam generators are located above the TITAN-II FPC and the available static head in the primary-coolant loop is more than adequate to establish natural circulation in the primary loop (a static head of one meter is needed

for the removal of the afterheat). This afterheat power can then be removed from the primary loop through the steam generators or will be absorbed by the water pool.

19.3.1.3. Loss of primary-coolant pressure

Any sizable leakage in the primary-coolant circuit will result in loss of pressure in the primary-coolant circuit. In this case, the plasma operation should be terminated. The primary coolant will be mixed with the coolant of the cold pool and the pool water temperature will rise. The pool must also absorb the afterheat power from the FPC. The thermal energy in the pool is then removed by the afterheat removal system in the pool. Detailed analysis was performed to estimate the initial temperature rise in the pool after mixing and to find out how fast the pool water temperature would rise should the afterheat-removal system in the pool also fail.

This thermal analysis was performed by using the code TOPAZ [7]. The decay afterheat power as a function of time was provided from neutronics calculations considering key contributing isotopes: ^{56}Mn, ^{55}Fe, ^{54}Mn, ^{60}Co, ^{14}C, ^{32}Si, and ^{185}W. Spatial distributions of the afterheat power from these isotopes were integrated through the entire FPC. This integrated afterheat power as a function of time after shutdown is shown in Figure 19.3-2. The afterheat-power-density distribution in the TITAN-II pool volume itself was also included in the calculation. To simplify the thermal analysis, a cylindrical geometry was used instead of the complicated geometry of the TITAN-II reactor. The water pool has a diameter of 36 m and a height of 31 m. The pool boundary consists of a 0.25-cm-thick steel liner and a 50-cm-thick concrete wall. Thermal conduction to the surrounding earth was considered. The surrounding earth was assumed to extend 100 m both in the radial direction and underneath the pool. Also, to simulate the effect of natural circulation in the pool, a high value for the thermal conductivity of the water in the pool was used.

Several calculations have been performed with different initial and boundary conditions. Figure 19.3-3 shows the estimated temperature rise of the cold pool as a function of time after the accident. These results indicate that the instantaneous mixing of the hot primary loop with the cold pool will cause the pool temperature to rise only 2 °C. This small increase is mainly due to the much larger volume of water in the pool than the volume in the primary loop, and the smaller specific heat capacity of the primary loop containing 6.4 at. % of lithium. Cases 1 and 2 in Figure 19.3-3 correspond to two different initial pool temperatures at 62 and 72 °C. It is estimated that it would take, respectively, more than 116 and 92 days for the water in the pool to reach 100 °C. As

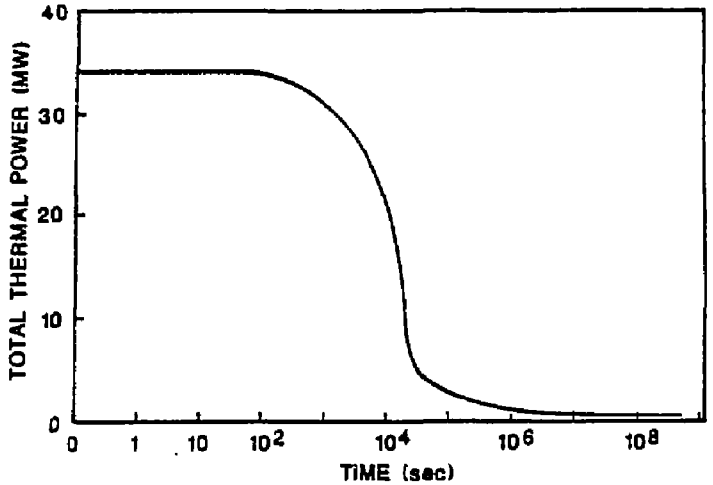

Figure 19.3-2. The integrated afterheat power in TITAN-II FPC as a function of time after shutdown.

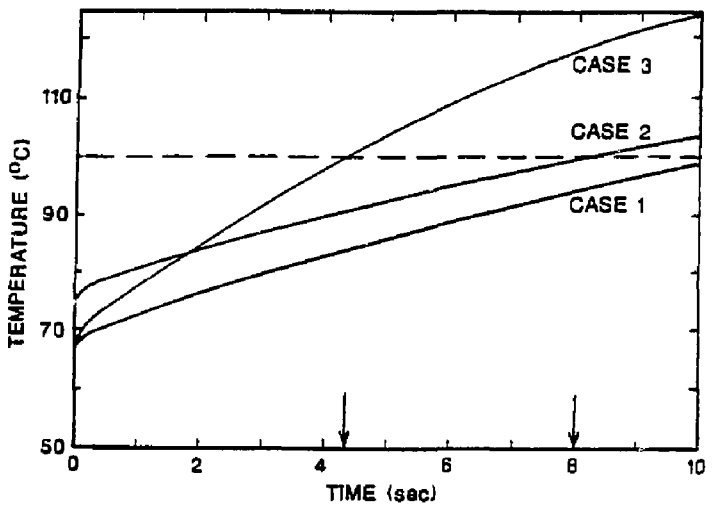

Figure 19.3-3. Estimated temperature of the TITAN-II water pool temperature as a function of time after shutdown.

a comparison, case 3 in Figure 19.3-3 shows that if the pool boundary is thermally insulated, and with an initial pool temperature of 62 °C, it would still take 49 days for the pool water to reach 100 °C. These analyses show that the TITAN-II pool is fully adequate to handle the decay afterheat produced in the FPC even if the pool active afterheat-removal system is not operational, allowing enough time for the recovery or replacement of the afterheat-removal system.

19.3.1.4. Catastrophic failure of primary loop and pool containment

In the catastrophic situation of the failure of the primary loop and the pool containment, the worst accident would be the release of the tritium inventory of the primary loop. At a tritium concentration of 50 Ci/kg in the primary-coolant loop, the complete release of the primary-loop water would amount to 1.37 kg of tritium, which would be higher than the allowable release of ~ 200 g [8] during severe hypothetical accidents (10CFR100) [3]. The complete release of the tritium inventory, however, is a very unlikely event because of the presence of the large pool of water. Also, it is assumed that the induced radioactivities in the structure of the FPC would not be released. This latter assumption is again based on the presence of the large pool of water which would absorb the decay afterheat power.

19.3.1.5. Routine releases

For the TITAN-II design, routine tritium releases and handling of ^{14}C waste are more of a concern than the releases under severe accidents. The potential tritium-leakage rate from the TITAN-II reactor depends on a trade-off between the acceptable level of tritium release and the costs of leakage control and the tritium-recovery system (Section 18). The issues of routine handling of ^{14}C waste are discussed in Section 19.5.

19.3.2. Pipe Break in the Pool

A potential accident for pressurized-water systems is a double-ended rupture of a main coolant line. The escaping jet of the primary coolant (as steam), which may contain radioactive material, will raise the pressure inside the primary containment building and may result in the release of radioactivity to the environment. Another advantage of the TITAN-II water pool surrounding the FPC is the potential to suppress the consequences

of a double-ended rupture of the primary-coolant circuit by containing the escaping jet of the primary coolant inside the water pool.

The question arises: If a design-basis accident (DBA) occurs, can the TITAN-II pool prevent a "blow through" of the escaping jet of tritiated water to the surface of the pool? Under a blow-through condition, the pressurized primary coolant can escape directly through the pool of water into the containment building, leading to a high pressure rise and escape of tritium. For our evaluation, the TITAN-II DBA is postulated to occur in the hot leg at a location closest to the water surface in the pool. To prevent the escape of the primary coolant, the minimum pool height above the location of the postulated accident is then identified (Section 19.3.2.2).

19.3.2.1. Fission reactor experience

Energy suppression and fission-product transport in pressure-suppression pools of boiling-water reactors were studied in the early 1970s [9]. A facility was constructed in which steam could be discharged through single or multiple down-comers under the surface of a water pool. In these experiments, the ratio of the maximum visible length of the steam jet to the inside diameter of the steam tube (L/D) was measured as a function of steam flow rate and water temperature. To examine the fission-product transport, iodine was dissolved in the steam.

Pressure-suppression experiments were performed using steam mass-flow rates up to 2.25×10^6 kg/h-m^2 into a degassed or air-saturated pool of water at temperatures up to 60 °C. The maximum inner diameter of the steam tube was about 2 inches. The use of ordinary process water (non-degassed) in the pool resulted in the production of numerous gas (air) bubbles of small diameter (< 1 mm) at a rate which appeared to depend on the steam injection rate. These bubbles are highly undesirable since they trap volatile fission gases (iodine) and transport them to the surface of the pool. Using a degassed pool of water eliminated the production of air bubbles and the character and size of the steam jet could be observed readily. Furthermore, for subsonic steam-flow conditions the L/D ratio is larger in non-degassed than in degassed water (a longer jet of steam). On semilog plots, the observed values of L/D showed a linear relationship with the steam mass-flow rate ($\dot{G}$), with a sharp increase in the value of L/D above sonic flow conditions. The empirical equations for L/D values [9], after conversion to SI units, are

$$\frac{L}{D} = 0.492 \ln \dot{G} - 4.45 \qquad (19.3\text{-}1)$$

for steam mass-flow rates below 8.3510^5 kg/h-m^2, and

$$\frac{L}{D} = 3.18 \ln \dot{G} - 32.57 \qquad (19.3\text{-}2)$$

for steam mass-flow rates above 8.3510^5 kg/h-m^2. Note that the maximum measured value of the L/D ratio was about 2 in the experiments which were carried out up to a flow rate of 2.2510^6 kg/h-m^2 in degassed water at 60 °C. At that maximum flow rate, Equation 19.3-2 predicts a L/D ratio of 3.85, higher than the observed value of 2 in the experiments.

19.3.2.2. Minimum pool height

The TITAN-II pool is designed to prevent blow throughs. To estimate the flow rate of steam from a coolant-pipe break in TITAN-II, simple empirical correlations for the critical flow rate are used. The critical flow rate of a two-phase mixture is defined as the flow rate at which a drop in the pressure of the discharge plenum for the pipe no longer results in an increase in the flow rate through the pipe. The critical flow depends on the flow regime, *i.e.*, it is a function of the ratio of the length of the discharge pipe to the diameter of the discharge. According to the DBA, the pipe break is to occur as close to the pool surface as possible. This means that the length of the discharge pipe would be much larger than the break diameter. Therefore, the Fauske correlation [10] for large ratios of discharge length to diameter (> 12) is used which results in a maximum steam flow rate of 3.2×10^7 kg/h-m^2 from the 7-MPa TITAN-II coolant loop. Using the sonic-flow steam-jet correlation (Equation 19.3-2), the maximum jet L/D ratio is found to be about 12.3. Thus, for a double-ended rupture of a 0.5-m-diameter hot leg, at least 6 to 7 m of cold (60 °C), fully degassed water is needed above the break to prevent a direct discharge of steam into the containment building.

It should be noted that in the experiments conducted by Stanford and Webster [9], the jet was directed downward, *i.e.*, towards the bottom of the tank. Therefore, applicability of these correlations to a jet pointing towards the top of the tank (as in TITAN-II) may be questioned. But the escaping steam, flowing at supersonic velocities, *does not* form bubbles that are collapsed under the hydrostatic pressure of the pool. Instead, steam is absorbed at an almost perfect sink: the water-jet interface. Because of the nature of the dissipation of the steam jet, it can be argued that the direction of the jet will not drastically affect the L/D ratio of the jet. Upward-pointed steam jets will probably be clipped at the tip and steam bubbles can separate from the top of the jet cone and rise before collapsing.

Experiments are needed to clarify these issues, but preliminary investigations indicate that a pool height of about 10 m above the primary-coolant pipes is sufficient to prevent blow throughs.

19.4. LOSS-OF-FLOW & LOSS-OF-COOLANT ACCIDENTS

Two of the major accidents postulated for the FPC are the loss-of-flow accident (LOFA) and the loss-of-coolant accident (LOCA). Demonstration of the level of safety attainable by the power plant requires in-depth analyses of the response of the FPC to these accidents. Thermal response of the first wall, blanket, and shield of the TITAN-II design to LOFA and LOCA are modeled using a finite-element heat-conduction code. The results of these analyses helped guide the engineering design of the reactor so that the maximum level of safety can be achieved. The principal concern of these analyses is to predict the temperature history and peak temperature of the torus assembly during the accident. Several heat conduction codes are available to model the thermal response of the system during LOCA and LOFA scenarios. Finite-element codes such as ANSYS [11], TACO2D [12], and TOPAZ [7] have sufficient flexibility to handle the time-dependant, nonlinear problem. For the safety analysis of the TITAN-II design, TACO2D is used and analytical checks have been performed, when possible, to verify the results.

19.4.1. Accident Models

An elevation view of TITAN-II is shown in Figure 19.4-1. A cutaway view of the first wall, blanket, and shield is illustrated in Figure 19.4-2 which shows the repetitive nature of the toroidal and radial cross sections. Therefore, a simple geometric model can be used to represent the radial build of the blanket. The use of symmetry conditions reduces the blanket to the configuration shown in Figure 19.4-3. The coarseness of this finite-element mesh appears, at first, to be inconsistent with transient-problem analysis. The problem under study, however, is primarily one of heat capacity and heat flow between components which is mainly governed by the radiation between surfaces and, therefore, is insensitive to the size of the elements within the materials.

The spatial variation of the afterheat at shutdown and the time-dependance of the decay heat in the first wall are shown in Figure 19.4-4. The initial value of the decay heat at shutdown is 12.7 W/cm^3 and the heating rate in the beryllium is zero.

Three accident scenarios have been studied for TITAN-II. The first case is a LOCA without the pool to verify the necessity and/or impact of the low-pressure pool. The

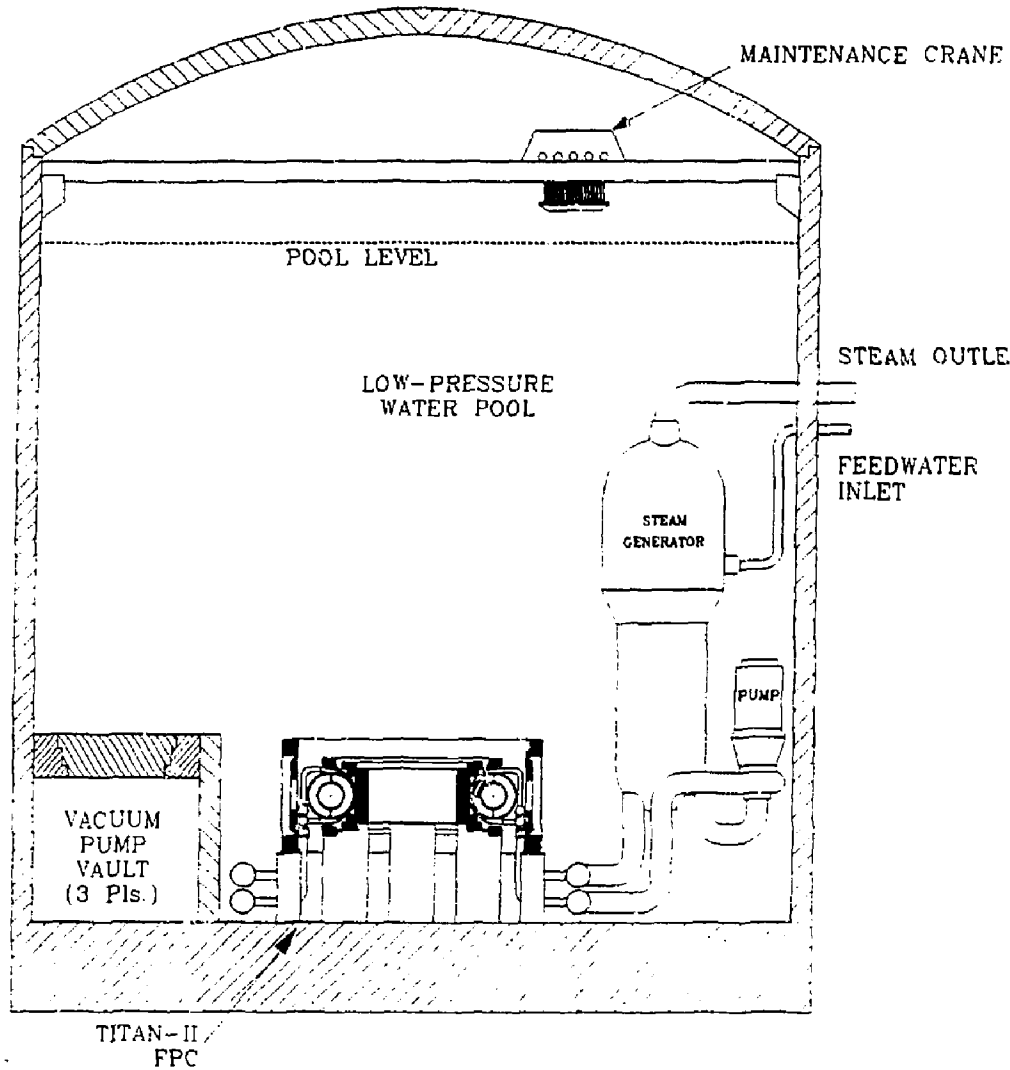

Figure 19.4-1. The elevation view of the TITAN-II fusion power core.

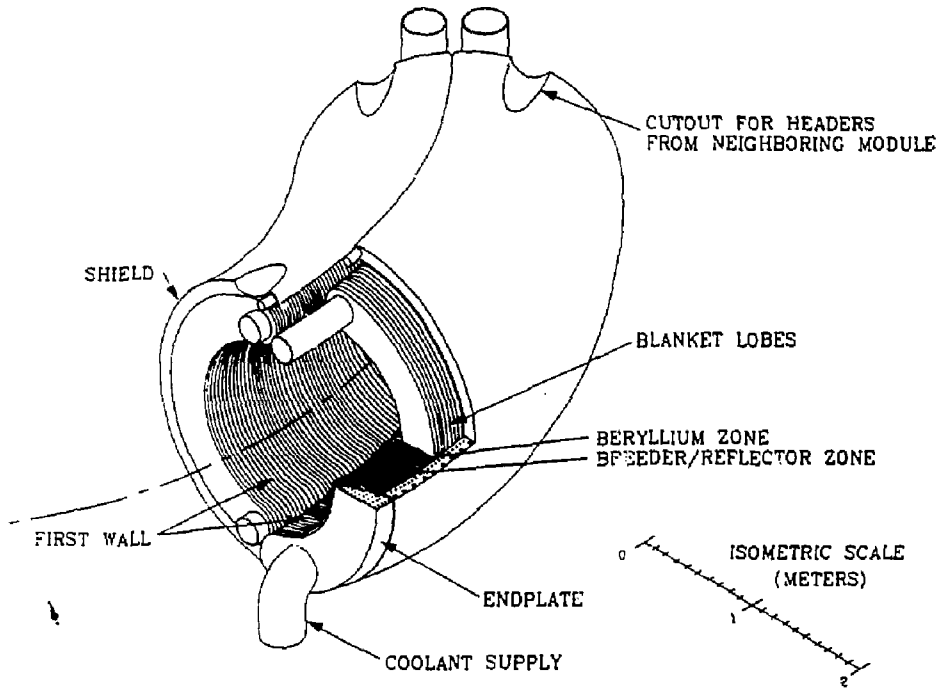

Figure 19.4-2. Cut-away view of the TITAN-II fusion power core.

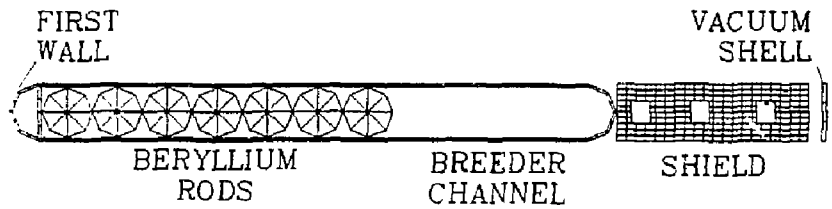

Figure 19.4-3. Finite-element model of the TITAN-II fusion power core used in LOFA and LOCA analysis.

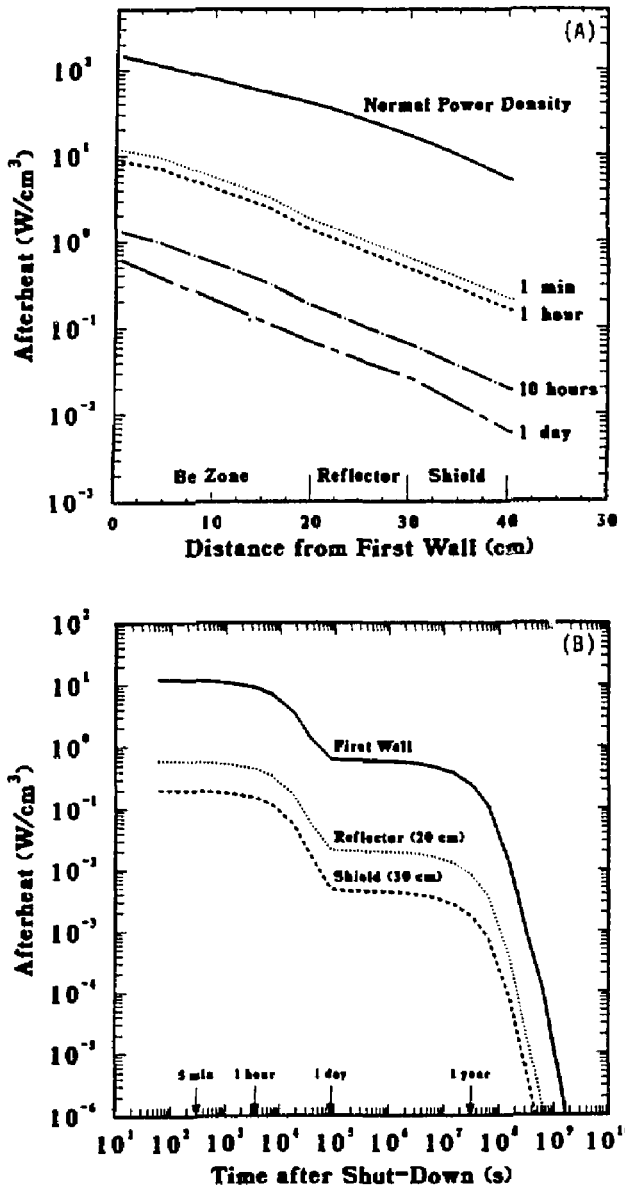

Figure 19.4-4. The level of decay afterheat in the TITAN-II fusion power core at shutdown (A) and as a function of time after shutdown (B).

second case is a LOFA with the pool. The final case is a LOCA with the pool in which the primary-coolant piping is assumed to have ruptured into the low-pressure pool. For all three accident scenarios, the plasma is assumed to have shut down at the instant of the accident initiation. Pump coast down and the time required for primary-loop evacuation will likely negate the effect of a short plasma shutdown period. The effect of a finite plasma shutdown time was not included.

The initial temperature fields are quite different for the above three accident scenarios. Detailed analytical solution of the fluid flow during the transients was beyond the scope of this analysis; however, a qualitative description of the fluid transients is presented and appropriate boundary and initial conditions are used in the numerical analysis. In general, all of the initial temperature fields are based on the maximum coolant temperature (*i.e.*, the coolant exit temperature, 330 °C).

19.4.2. LOCA without the Pool

This is the classic light-water-reactor LOCA, without any means of re-flood. One of the cold legs in the primary loop suffers a guillotine break and the primary loop is emptied after a short drain period. The break is below the level of the torus, therefore no coolant can be trapped inside the FPC. The effect of finite drain time and finite plasma shutdown time are assumed to cancel out. Thus, the initial temperature for the numerical analysis is set at 330 °C. The only heat-removal mechanism is radiation at the back of the vacuum boundary, which is behind the shield. The heat is radiated to the surrounding structure (ohmic-heating coils, coil supports, *etc.*) which are at ambient temperature.

Figure 19.4-5 shows the temperature histories of the first wall and front of the shield as functions of time after shutdown. The peak temperatures are reached after 3.3 hours, quicker than for TITAN-I. The peak temperatures in the first wall and beryllium are 1780 and 1755 °C, respectively, 360 and 471 °C above the melting points for the ferritic steel and beryllium. The necessity of the low-pressure pool is clearly evident from these results.

19.4.3. LOFA with the Pool

This accident can occur, for example, during a loss of off-site power without diesel-generator backup. As before, it is assumed that the heat removal provided by the finite pump coast-down time is sufficient to remove any heat generated by a finite plasma

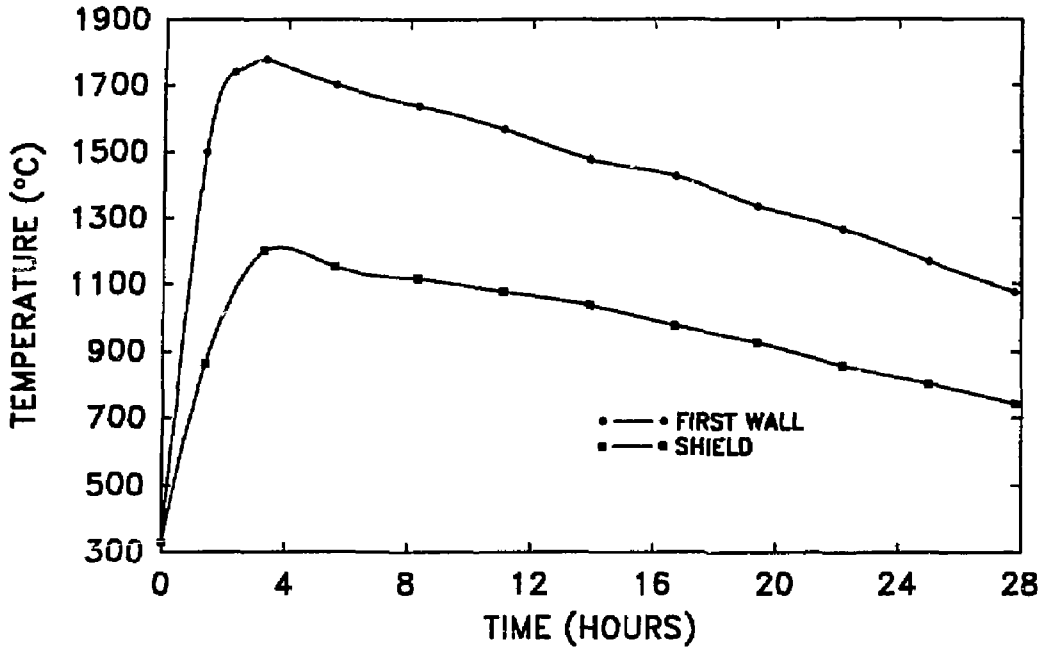

Figure 19.4-5. Thermal response of the TITAN-II FPC to a complete LOCA without the pool as a function of time after the initiation of the accident.

shutdown time. Pump coast-down time is expected to be in excess of one minute. If the plasma shutdown time approaches the pump coast-down time, then this assumption is not valid. In order to model the worst-case accident, it is assumed that no heat removal is provided by the steam generator, and that the pool heat-removal system has also failed. Therefore, the initial temperature is conservatively set to the coolant outlet temperature, 330 °C.

In this scenario, the decay afterheat in the FPC is removed by natural convection of the pool water in contact with the vacuum shell, behind the shield. An average, initial heat-transfer coefficient between the vacuum shell and the pool is estimated to be 0.001 W/cm^2-°C for a horizontal cylinder with a radius of 120 cm. Although the temperature of the water pool rises with time after this accident (Section 19.3.1.3), this increase in pool temperature occurs over a time scale much longer than the torus heat-up period. Thus, the natural circulation in the pool would not be affected during the torus heat-up period.

Natural convection of the primary coolant inside the blanket also removes the decay afterheat which is then lost through the walls of the primary-coolant piping and steam generators to the pool (Section 19.3.1.2). In fact, the normal inlet and outlet temperature conditions of the TITAN-II blanket are sufficient to remove the decay afterheat. The average heat-transfer coefficient for heat removal inside the blanket is estimated at $0.037\,W/cm^2\text{-}°C$. The initial bulk temperature of the pressurized, primary coolant is 330 °C and the pool temperature is 60 °C.

Figure 19.4-6 shows the temperature of the TITAN-II FPC as a function of time after the initiation of the accident. For this accident scenario, very little temperature excursion is observed, primarily because of the presence of natural convection within the pool and the primary loop. The first-wall peak temperature of 348 °C is reached after 355 seconds. The TITAN-II reactor appears to be capable of withstanding the loading conditions of this accident scenario.

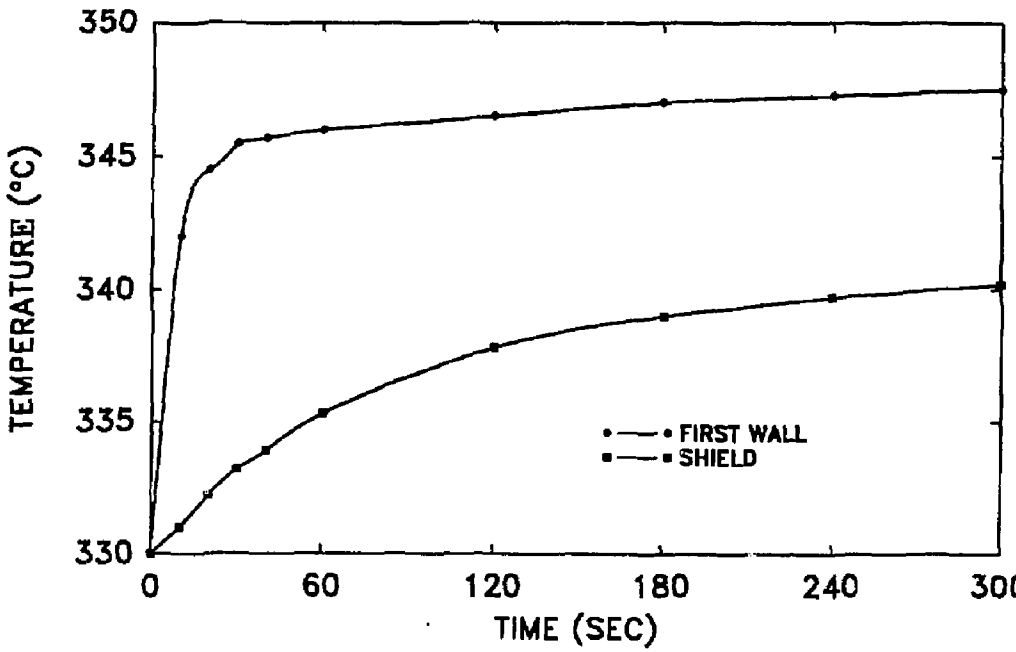

Figure 19.4-6. Thermal response of the TITAN-II FPC to a LOFA with the pool as a function of time after the initiation of the accident.

19.4.4. LOCA with the Pool

This accident scenario is the most complex. The accident is initiated with a guillotine break in the primary cold leg, below the level of the torus. The consequences of this accident have been broken into the following four basic phases.

Phase I: Initial primary-loop de-pressurization. At the onset of the accident, a very rapid ($\sim$ 1 s) de-pressurization of the primary loop occurs until the primary-loop pressure reaches the saturation pressure of the primary coolant. For the salt concentration levels used in TITAN-II, the saturation pressure is 5.6 MPa at 330 °C. The time required for this initial de-pressurization from 7 MPa normal operating pressure to 5.6 MPa is very short, on the order of one second, and many factors influence this initial de-pressurization time. For modeling the thermal response of the TITAN-II FPC, the de-pressurization is assumed to be instantaneous. On the other hand, if force calculations were needed, such as required for analyzing a pipe-whip, then a more precise time constant would be necessary.

Phase II: Primary-loop blow down. Following the initial de-pressurization to saturation conditions, a slower de-pressurization takes place until the primary loop and the pool are at equal pressure. Choked flow at the pipe break determines the rate of de-pressurization. As the pressure in the primary loop drops below the saturation pressure of the primary coolant, flashing of the primary coolant occurs and the sudden volume change forces the coolant out of the pipe break (blow-down phase). As with the initial de-pressurization, there are many factors which limit the rate of blow down. Typical design-basis accidents for PWRs will fully de-pressurize in 10 to 20 seconds, provided that no emergency core-cooling system is engaged.

For accident analysis of the TITAN-II FPC, the pipe break is assumed to be at the lowest point of the primary loop (*i.e.*, the worst case accident) since any steam that forms inside the primary piping is trapped because of the buoyancy force. At a pressure of 5.6 MPa, the change in specific volume of the primary coolant from liquid to steam is 27 times. Thus, only about 4% of the primary fluid needs to be vaporized to fill the entire primary loop with a steam bubble. At lower pressures the relative change in specific volume would be even greater. Therefore, it is conservatively assumed that at the end of the blow-down phase, the entire primary loop will be filled with 330 °C steam (operating conditions).

The blow-down phase is assumed to last 20 seconds. It is assumed that during this phase, the heat transfer in the primary loop is linearly decreasing to zero to reflect that the trapped steam does not have any heat capacity or natural circulation. The steam does provide a weak conduction path for heat flow from the steel to the beryllium rods. At the end of the 20 seconds blow-down phase, thermal radiation between internal structures takes place. Initially this radiation is quite small because the temperatures are low. But, as the temperature of the FPC structure increases, the radiation path plays an important role in the removal of the decay afterheat.

Phase III: Primary-loop re-flood. During the re-flood phase, heat is lost from the primary loop (steam) to the surrounding pool and the steam trapped in the primary loop begins to condense. This occurs at the break interface and through the pipe walls. As the steam condenses, its specific volume decreases and the primary-loop pressure decreases. As the pressure drops, the pool water is forced into the primary loop until all of the steam has condensed. The condensation rate depends on a great number of variables; for this analysis, it is assumed that this phase would last 5 minutes. Virtually any condensation rate can be designed into the system simply by adding insulation to the piping (decreased rate of condensation), or by exposing more primary piping to the pool water (increased rate of condensation).

During the re-flood phase, the TITAN-II reactor torus is conservatively assumed to be filled with steam until all of the primary loop is filled with pool water. However, it is assumed that the steam temperature decreases linearly with time from 330 to 150 °C, which is the saturation temperature of pure water at 0.5 MPa. Since the TITAN-II reactor torus is located at very nearly the lowest point in the primary loop, it will experience re-flood conditions sooner than the remainder of the primary loop, an effect not accounted for here.

Phase IV: Natural circulation. The final phase of the design-basis accident is the onset of natural circulation. The TITAN-II reactor is configured so that natural circulation of liquid water is effective in removing the initial decay afterheat with minimal elevation of the steam generator above the reactor torus (Section 19.3.1.3). For this analysis, natural circulation is assumed to be fully developed upon the completion of the primary-loop re-flood phase.

Many assumptions, mostly conservative, have been made for the above four-phase accident scenario. One major assumption is that the steam generator has no influence

on the accident scenario. In reality, the steam generator would cool to the temperature of the condenser coolant (nominally 20 °C) and would increase the rate of condensation inside the primary loop. The location of the torus relative to the pipe break is also important. In a realistic design, the torus should be at the lowest point in the primary system. This reduces the amount of piping below the torus and also decreases the volume of piping that needs to be re-flooded before pool water reaches the torus. Any pipe that breaks above the torus will not trap steam inside the FPC, and the reactor torus will, therefore, refill immediately following the blow down.

Thermal response of the TITAN-II fusion power core to this accident scenario is shown in Figure 19.4-7. The peak temperature of the FPC is 732 °C which is 688 °C below the melting point of the ferritic steel. The peak beryllium temperature is 481 °C which is 802 °C below its melting point. Figure 19.4-7 shows that the initial temperature rise in the first wall is linear in time at a rate of about 2.4 °C/s. At the end of the re-flood period (after 300 s), the rate of temperature increase in the first wall is reduced to about 0.62 °C/s. In this analysis, the blanket re-flood is modeled as a step change in the heat-transfer coefficient to account for the natural convection in the primary loop. This step change occurs 300 seconds after the initiation of the accident and accounts for the sudden drop in the first-wall temperature.

The selection of a 300-s re-flood time is somewhat arbitrary since, by design, a wide range of re-flood times can be chosen. Therefore, thermal response of the TITAN-II FPC is also examined for a case that does not include re-flood, *i.e.*, the steam bubble remains in the primary loop and only the radiation inside the blanket to the back of the vacuum boundary governs the heat transport. The result of this analysis is shown in Figure 19.4-7. For this scenario, the first-wall temperature peaks at 1721 °C after 10,500 s (2.9 hours) which is 500 °C *above* the melting point of the ferritic steel. The result of the accident with no re-flood can be used as a design curve to predict the maximum allowable re-flood time. For example, if the design goal is to limit the peak temperature to two-thirds of the melting point ($2/3\,T_m = 1129\,\mathrm{K} = 856\,^\circ\mathrm{C}$), then re-flood must begin no later than seven minutes after the accident initiation. If, on the other hand, the design limit is the melting point of the steel, then the maximum time to re-flood is about 47 minutes.

19.4.5. Discussion

The necessity of the low-pressure pool is clearly evident from the results of the LOCA-without-pool scenario. Peak temperatures well in excess of the melting point of the

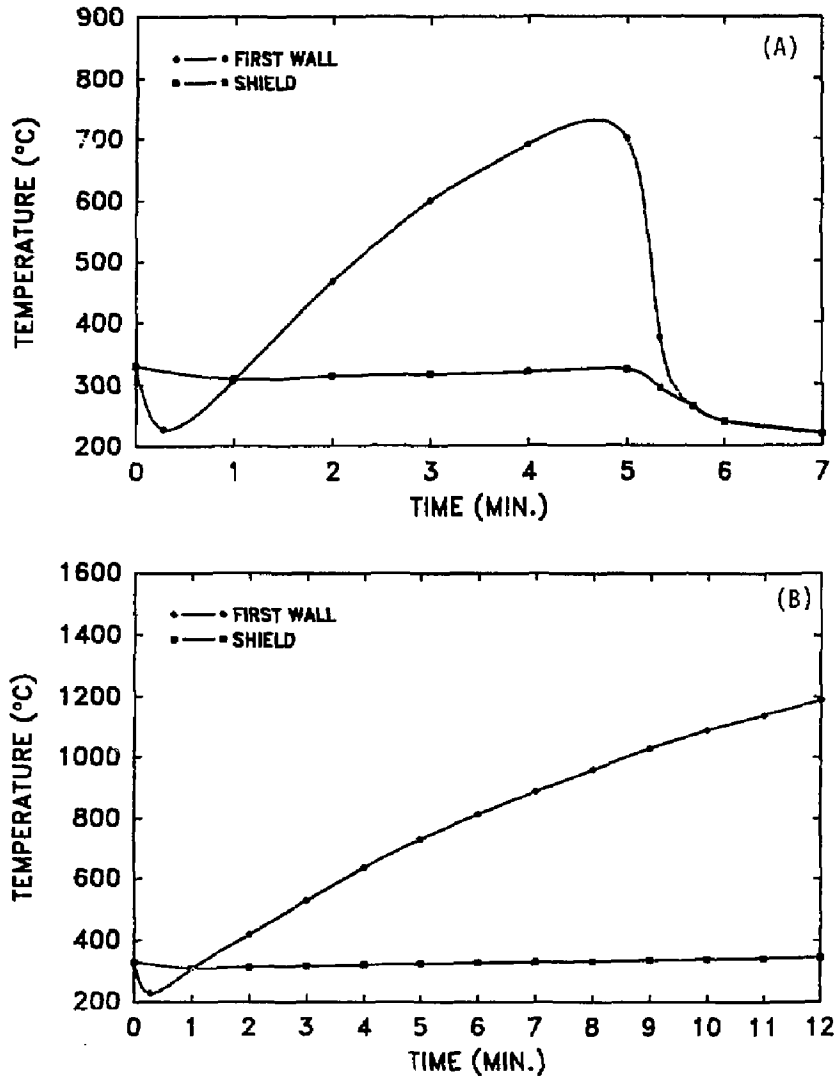

Figure 19.4-7. The thermal response of the TITAN-II FPC to a LOCA with the low-pressure pool as a function of time after the initiation of the accident with a re-flood time of 300 s (A) and with no re-flood (B).

structure are predicted, thus leading to damage to the FPC and potential release of radioactivity. The consequences of a LOFA with pool are minimal, primarily because of the natural circulation in the primary loop and the large heat capacity of the pool. By design, the primary loop will have a heat loss rate to the pool equal to the initial decay afterheat, thereby ensuring adequate heat removal.

A LOCA with pool can have severe temperature excursions if the design of the primary loop does not account for this type of accident. Specifically, the primary-coolant piping must allow for fast condensation of the trapped steam so that re-flood will occur within the desired time period. A re-flood time of approximately 10 minutes will prevent the temperature of FPC structural material from exceeding two-thirds of its melting point, most likely preventing any structural damage. The internal pressure of the blanket during this accident is low ($\sim$ 0.35 MPa) and thermal-creep rupture should not pose a problem if peak temperatures are below the two-thirds limit.

The LOCA-with-pool scenario is the worst credible accident envisioned. If the torus is at the lowest point in the system, then a trapped steam bubble is impossible and the LOCA cannot occur. This design criteria is chosen for TITAN-II; however, a small length of primary pipe is necessary below the torus to help the development of natural convection.

19.5. RADIOACTIVE-WASTE DISPOSAL

19.5.1. Radioactive-Waste-Disposal Issues

The classification of nuclear waste for disposal is given under the Code of Federal Regulations, specifically 10CFR61 [1]. Four waste classes have been defined: Class A (segregated waste), Class B (stable waste), Class C (intruder waste), and geologic waste. The first three classes of waste are eligible for near-surface burial, while the last class needs deep geologic burial. Radionuclides with half-lives of less than five years will decay by at least six orders of magnitude in 100 years after disposal. These radionuclides can be reasonably managed to meet either Class-A or Class-B disposal requirements. For long-lived radionuclides with half-lives greater than 100 years, however, it will be difficult to meet either Class-A or Class-B disposal requirements solely by radioactive decay to reduce the activity level. To qualify as Class-C or better nuclear waste, the nuclear components in a fusion reactor should minimize the quantity of their alloying and/or impurity elements that would produce long-lived radionuclides.

The limiting-specific activities for near-surface (Class A, B, and C) disposal of nuclear waste were also specified in 10CFR61 regulations for the following radionuclides: ^{59}Ni, ^{94}Nb, ^{99}Tc, ^{129}I, ^{90}Sr, ^{137}Cs, and alpha-emitting transuranic nuclides with half-lives greater than five years. These limiting-specific activities were given primarily for radionuclides relevant to present-day applications such as fission-based nuclear reactors. Many radionuclides with half-lives greater than five years, such as ^{42}Ar (half-life 33 y), ^{108m}Ag (127 y), and ^{186m}Re (2×10^5 y), may be produced by fusion reactors in the elements constituting the structural alloy, the divertor collecting plates, and impurities in the structural alloys. However, the limiting-specific activities for near-surface disposal of nuclear waste containing these nuclides are not available in 10CFR61.

Evaluations of limiting-specific activities for fusion-relevant nuclides were made based on 10CFR61 values. A complete work was recently performed by Fetter [14] providing limiting-specific activities for near-surface disposal of all radionuclides with atomic numbers less than 84. These evaluations, consistent in methodology with the 10CFR61 regulations, were used in the waste-disposal analysis of the TITAN reactors.

19.5.2. Radioactive-Waste-Disposal Ratings of TITAN-II Reactor

The neutron spectra at the first wall, blanket breeder zone, shield, and toroidal-field (TF) coil components of the TITAN-II design are given in Table 19.5-I. In general, a factor of 30 reduction in both total- and fast-neutron fluxes is provided by the TITAN-II blanket and shield.

The neutron fluxes calculated for the reference TITAN-II reactor were used as the input to the activation calculation code, REAC [15]. Table 19.5-II summarizes the maximum allowable concentration levels of niobium, molybdenum, silver, terbium, iridium, and tungsten in various TITAN-II reactor components to qualify for Class-C near-surface-burial waste. Note that the elements given here are primarily those elements identified in Section 13.7 as the most undesirable, appearing as either alloying elements or impurities in the structural alloys. As shown in Table 19.5-II, the allowable concentration levels for Nb, Mo, Ag, Tb, and Ir impurities are, respectively, 0.6, 2.6, 0.33, 0.2, and 0.05 appm in the reduced-activation ferritic-steel structural alloy of the TITAN-II FPC. These levels are, in general, factors of 2 to 10 lower than the allowable concentration of the same elements in the TITAN-I FPC components. This is mainly caused by the softer neutron spectrum in TITAN-II (because of the presence of better neutron-moderation materials, beryllium and water) which results in a higher neutron-capture reaction rate in the TITAN-II FPC components.

Table 19.5-I.

NEUTRON SPECTRUM IN THE TITAN-II FPC

Component[a]	Neutron Flux (n/cm^2)	Flux-Reduction Factor[b]	Fast-Neutron Fraction[c]
First wall & Be zone	5.3×10^{15}	–	59%
Breeder zone	8.0×10^{14}	7.9	54%
Hot shield	3.8×10^{14}	1.9	61%
TF coils	1.8×10^{14}	2.3	57%

(*a*) Flux values at the side of component facing the plasma.

(*b*) Defined as the ratio of flux in the front of the component to that in the back.

(*c*) For $E_n \geq 0.1$ MeV.

The first-wall, blanket, and shield components of the TITAN-II reactor are all integrated in a one-piece lobe design and are all replaced every year. Therefore, one may estimate the allowable concentration levels of the impurity elements by averaging over all components in the lobe. The maximum allowable impurity concentration in the "averaged" TITAN-II FPC are shown in Table 19.5-II and are more easily met than the more restricted levels in the first wall and the blanket Be zone. Comparing the maximum allowable concentration to the expected nominal impurity level (Table 19.5-II), it appears that the concentration limits for all these impurity elements, except niobium and terbium, are readily achievable when the average-limiting concentration levels are imposed. Careful impurity control processes are necessary for Nb and Tb when the structural alloy is fabricated.

The reduced-activation, ferritic steel 9-C used as structural material for the TITAN-II reactor contains tungsten as one of the important alloying elements replacing molybdenum which is an undesirable element for Class-C waste disposal. However, the tungsten content should also be controlled because of the production of a second-step reaction-daughter radionuclide, ^{186m}Re (with a half-life of 200,000 years). The allowable concentration levels of tungsten in the TITAN-II FPC components are also shown in Table 19.5-II.

The "averaged" allowable concentration level of tungsten is 11.0%, more than two orders of magnitude larger than the present tungsten level in the reduced-activation ferritic steels (0.89%).

The waste-disposal ratings of the TITAN-II FPC with nominal level of impurities and 0.89% of tungsten in the presently available reduced-activation ferritic steels (present case), and for controlled impurity levels (controlled case) are presented in Table 19.5-III. These waste-disposal ratings were estimated for the irradiated blanket-lobe assembly averaged after 1 FPY at 18 MW/m^2 of neutron wall loading. It can be seen that with

Table 19.5-II.

MAXIMUM CONCENTRATION LEVELS OF KEY IMPURITIES IN TITAN-II REACTOR COMPONENTS TO QUALIFY AS CLASS-C WASTE[a]

Element	Major Nuclide (Activity Limit)	Maximum Concentration in Component[b]				Nominal Level[c]
		FW & Be Zone	Breeder Zone	Shield	Average	
Nb	^{94}Nb (0.2 Ci/m^3)	0.6	1.7	7.7	2.4	0.1%
Mo	^{99}Tc (0.2 Ci/m^3)	2.6	53	588	22	1.0%
	^{94}Nb (0.2 Ci/m^3)					
Ag	^{108m}Ag (3 Ci/m^3)	0.33	0.83	4.2	1.3	1
Tb	^{158}Tb (4 Ci/m^3)	0.2	1.0	2.4	0.85	5
Ir	^{192m}Ir (2 Ci/m^3)	0.05	0.09	0.2	0.13	5
W	^{186m}Re (9 Ci/m^3)	1.9%	9.1%	116.0%	11.0%	0.9%

(*a*) Based on operation at 18 MW/m^2 of neutron wall loading for 1 FPY.
Note that a conservative lifetime fluence value of 15 MW y/m^2 is used for the TITAN-II reference design (0.8 FPY at 18 MW/m^2).

(*b*) All concentrations in appm expect those noted in atomic percentage.

(*c*) From Reference [16].

Table 19.5-III.

WASTE-DISPOSAL RATINGS FOR THE "AVERAGED" TITAN-II BLANKET[a]

	Present Case		Controlled Case	
Element	Nominal Level[c] (appm)[b]	Class-C Rating	Controlled Level (appm)[b]	Class-C Rating
Nb	0.1%	8.33	1[d]	0.42
Mo	1.0%	0.27	6[d]	0.30
Ag	1	0.054	0.07	0.054
Tb	5	1.06	0.1[d]	0.10
Ir	5	0.0077	0.001	0.0077
W	0.9%[e]	0.081	0.9%	0.081
TOTAL		9.78		0.96

(a) Based on operation at 18 MW/m^2 of neutron wall loading for 1 FPY. Note that a conservative lifetime fluence value of 15 MW y/m^2 is used for the TITAN-II reference design (0.8 FPY at 18 MW/m^2).

(b) All concentrations in appm expect those noted in atomic percentage.

(c) From Reference [16].

(d) Controlled levels lower than impurity levels in ferritic steel.

(e) Present tungsten content in the reduced-activation ferritic steel.

nominal impurity levels (present case), a Class-C waste-disposal rating of 9.78 is estimated for the TITAN-II FPC, with main contributing elements Nb (85%), Tb (11.0%), and Mo (2.8%). These elements should be controlled to levels below those presently available in the structural alloy. In the controlled case of Table 19.5-III, we have presented a possible case for the impurity control: Nb (from 20 to 1 appm), and Tb (from 0.9 to 0.1 appm). The resulting waste-disposal rating is about 1.0 for this controlled case.

Assuming that the structural alloy meets all required levels of impurity and alloying elements as shown in the controlled case in Table 19.5-III, estimates are made the TITAN-II reactor materials and related waste quantities for Class-C disposal. The divertor-shield coverage is taken as 13% in the TITAN-II design, identical to the TITAN-I design. The results are presented in Table 19.5-IV. The annual replacement mass of TITAN-II FPC is estimated at about 71 tonne/FPY (9.1 m^3), assuming that the entire blanket lobe and the divertor shield are replaced every FPY. Note that a conservative lifetime fluence of 15MW y/m^2 is used for the TITAN-II reference design (0.8 FPY at 18 MW/m^2). In addition, Table 19.5-IV is for a modified design with a 0.03-m shield and a 0.17-m blanket breeder zone, rather than the 0.1-m shield and 0.1-m blanket breeder zone of the reference design. The reduced shield thickness in this design decreases the annual replacement mass by about 50 tonne/FPY and also satisfies the structural-design aspects of the blanket lobe. The penalty for this modified design is a 1.5% reduction in the blanket energy multiplication.

The lifetime (30 FPY) components in the TITAN-II design are the TF, ohmic-heating (OH), and equilibrium-field (EF) coils, and the shield for the EF coils. The averaged annual replacement mass from the disposal of these lifetime components is also given in Table 19.5-IV and is estimated to be about 25 tonne/FPY (3.1 m^3). Thus, the averaged annual replacement mass of the entire TITAN-II reactor, both 1-FPY and lifetime components, is about 96 tonne/FPY, or about 12% of the total mass of the TITAN-II FPC and is similar to that of the TITAN-I design.

In addition to the Class-C waste disposal materials and quantities discussed above, the TITAN-II divertor plates are fabricated with W-26Re alloy as in the TITAN-I design (Section 13.7). The annual replacement mass of this non-Class-C waste is about 0.35 tonne/FPY, about 0.4% of the total annual replacement mass. Because of the nitrate salt dissolved in the aqueous-solution coolant, the TITAN-II reactor is also producing ^{14}C from ^{14}N (n,p) reactions. The annual production rate of ^{14}C is about 5.2×10^4 Ci. Using the present 10CFR61 regulations, where the allowable concentration of ^{14}C for Class-C disposal is 8 Ci/m^3 and if ^{14}C remains in the aqueous-solution coolant, the coolant should be replaced at a rate of 7×10^3 tonne/FPY (6.5×10^3 m^3). The replacement mass of the

Table 19.5-IV.

SUMMARY OF TITAN-II REACTOR MATERIALS AND RELATED WASTE QUANTITIES FOR CLASS-C WASTE DISPOSAL[a]

Component	Material	Lifetime (FPY)[a]	Volume (m^3)	Weight (tonne)	Annual Replacement Mass (tonne/FPY)
First wall	Ferritic steel (9-C)	1	0.26	2.0	2.0
Be zone	Ferritic steel (9-C)	1	2.5	19.7	19.7
Breeder zone	Ferritic steel (9-C)	1	2.0	15.3	15.3
Shield	Ferritic steel (9-C)	1	3.9	30.5	30.5
TF coils	Modified steel		0.54	4.8	0.08
	Copper		3.8	34.0	1.13
	Spinel		0.54	2.2	0.08
	TOTAL	30	4.9	41.0	1.39
OH coils	Modified steel		5.4	49.	1.63
	Copper		38.2	342.	11.4
	Spinel		5.4	23.	0.77
	TOTAL	30	49.0	414.	13.8
EF-coils shield	Modified steel	30	5.6	50.	1.7
Divertor shield	Ferritic steel	1	0.48	3.78	3.78
TOTAL CLASS-C WASTE (lifetime)			334.	2643.	88.1

(a) Based on operation at 18 MW/m^2 of neutron wall loading for 1 FPY. Note that a conservative lifetime fluence value of 15 $MW\,y/m^2$ is used for the TITAN-II reference design (0.8 FPY at 18 MW/m^2).

coolant can be reduced to about 80 tonne/FPY, if Fetter's evaluation [14] is used as the limiting value (700 Ci/m^3). Because of the large quantities of aqueous solution to be disposed of annually and uncertainties in the transport of the ^{14}C isotope in the primary loop, extraction of the ^{14}C activity from the coolant and disposal of the concentrated quantity as non-Class-C waste should be considered.

19.6. SUMMARY AND CONCLUSIONS

Strong emphasis has been given to safety engineering in the TITAN study. Instead of an add-on safety design and analysis task, the safety activity was incorporated into the process of design selection and integration at the beginning of the study. This approach was projected to enhance the potential of attaining the design goals of design simplicity, passive safety, high availability, and low cost of electricity.

The safety-design objectives of the TITAN-I design are: (1) to satisfy all safety-design criteria as specified by the U. S. Nuclear Regulatory Commission on accidental releases, occupational doses, and routine effluents; and (2) to aim for the best possible level of safety assurance.

The key safety feature of the TITAN-II design is the low-pressure, low-temperature water pool that surrounds the FPC and the entire primary-coolant system. Detailed safety analyses have been performed which show that the TITAN-II pool can contain the thermal and afterheat energy of the FPC and will remain at a low enough temperature so that tritium or other radioactive material in the primary-coolant system will not be released. Therefore, the public safety is assured by maintaining the integrity of the water pool. Since the water-pool structure can be considered a large-scale geometry, the TITAN-II design can be rated as a level-2 of safety assurance design [5,4]. The potential safety concerns are the control of routine tritium releases and the handling of ^{14}C waste.

Plasma-accident scenarios need to be further evaluated as the physics behavior of RFPs becomes better understood. Preliminary results indicate that passive safety features can be incorporated into the design so that the accidental release of plasma and magnetic energies can be distributed without leading to major releases of radioactivity. Activities in this area need to be continued, especially for high-power-density devices. It should be pointed out that for the TITAN-II design, plasma-related accidents are of concern from the consideration of investment protection and would have minimum impact on public safety. This characteristic is again, a result of the presence of the large pool of water that allows the passive protection of the public.

REFERENCES

[1] "Standards for Protection Against Radiation," U. S. Nuclear Regulatory Commission, Code of Federal Regulations, Title 10, Part 0 to 199 (1986).

[2] "Domestic Licensing of Production and Utilization Facilities," U. S. Nuclear Regulatory Commission, Code of Federal Regulations, Title 10, Chapter 1, Part 50 (1984).

[3] "Reactor Site Criteria," U. S. Nuclear Regulatory Commission, Code of Federal Regulations, Title 10, Chapter 1, Part 100 (1975).

[4] S. J. Piet, "Approaches to Achieving Inherently Safe Fusion Power Plants," *Fusion Technol.* **10** (1986); also "Inherent/Passive Safety For Fusion," in *Proc. 7th ANS Topical Meeting on Tech. of Fusion Energy*, Reno, NV (1986).

[5] J. P. Holdren *et al.*, "Summary of the Report of the Senior Committee on Environmental, Safety and Economic Aspects of Magnetic Fusion Energy," Lawrence Livermore National Laboratory report UCRL-53766-Summary (1987); also J. P. Holdren *et al.*, "Exploring the Competitive Potential of Magnetic Fusion Energy: The Interaction of Economics with Safety and Environmental Characteristics," *Fusion Technol.* **13** (1988) 7.

[6] "Adapting the LWR to Future Needs: SECURE-P (PIUS)," Power Engineering (September 1985).

[7] A. B. Shapiro, "TOPAZ – A Finite Element Heat Conduction Code for Analyzing 2-D Solids," Lawrence Livermore National Laboratory report UCID-20045 (1984).

[8] I. Maya and K. R. Schultz, "Final Report, Inertial Confinement Fusion Reaction Chamber and Power Conversion System Study," General Atomics report GA-A17842 (1985).

[9] L. E. Stanford and C. C. Webster, "Energy Suppression and Fission Product Transport in Pressure-Suppression Pools," Oak Ridge National Laboratory report ORNL-TM-3448 (1972).

[10] H. K. Fauske, "The Discharge of Saturated Water through Tubes," *Chem. Eng. Prog. Symp. Series* **59** (1965) 210.

[11] G. J. Desalvo and J. A. Swanson, "ANSYS User's Manual," Swanson Analysis Systems, Inc. (1979).

[12] P. J. Burns, "TACO2D – A Finite Element Heat Transfer Code," Lawrence Livermore National Laboratory report UCID-17980, Rev. 2 (1982).

[13] "Licensing Requirements for Land Disposal of Radioactive Waste," U. S. Nuclear Regulatory Commission, Code of Federal Regulations, Title 10, Part 61 (1982).

[14] S. Fetter, E. T. Cheng, and F. M. Mann, "Long-Term Radioactivity in Fusion Reactors," *Fusion Eng./Des.* **6** (1988) 123.

[15] F. M. Mann, "Transmutation of Alloys in MFE Facilities as Calculated by REAC (A Computer Code for Activation and Transmutation Calculations)," Hanford Engineering and Development Laboratory report HEDL-TME 81-37 (1982).

[16] D. L. Smith *et al.*, "Blanket Comparison and Selection Study, Final Report," Argonne National Laboratory report ANL/FPP-84-1 (1984).

20. TITAN-II MAINTENANCE PROCEDURES

Steven P. Grotz Richard L. Creedon Patrick I. H. Cooke
Robert A. Krakowski Farrokh Najmabadi Clement P. C. Wong

Contents

20. TITAN-II MAINTENANCE PROCEDURES

20.1. INTRODUCTION

The TITAN reactors are compact, high-power-density designs. The small physical size of these reactors permits each design to be made of only a few pieces, allowing a single-piece maintenance approach [1,2]. Single-piece maintenance refers to a procedure in which all of components that must be changed during the scheduled maintenance are replaced as a single unit, although the actual maintenance procedure may involve the movement, storage, and reinstallation of some other reactor components. In TITAN designs, the entire reactor torus is replaced as a single unit during scheduled maintenance. Furthermore, because of the small physical size and mass of the TITAN-II FPC, the maintenance procedures can be carried out through vertical lifts, allowing a much smaller reactor vault. The advantage of using fully toroidal units with vertical lifts for maintenance has been verified in some fusion experiments [3].

The single-piece maintenance procedure is expected to result in the shortest period of downtime during the scheduled maintenance period because: (1) the number of connects and disconnects needed to replace the components will be minimized and (2) the installation time is much shorter because the replaced components are pretested and aligned as a single unit before committment to service. Furthermore, recovery from unscheduled events will be more standard and rapid because complete components are replaced and the reactor is brought back on line. The repair work will then be performed outside the reactor vault.

A single-piece maintenance of the entire reactor torus (including the first wall, blanket, and divertor modules) will have the additional benefits of: (1) no adverse effects resulting from the interaction of new materials operating in parallel to radiation-damaged material; (2) complete and extensive testing of the entire torus assembly can be performed before commitment to service, which is expected to result in increased reliability; and (3) it will be possible to continually modify the torus assembly as may be indicated by the reactor performance and technological developments and to fully exploit the learning curves.

In this section, the layout of the main power-plant buildings (Section 20.2) and the proposed maintenance procedures for the TITAN-II reactor (Section 20.3) are presented. A comparison of the TITAN-II single-piece maintenance procedure with a modular approach is difficult because: (1) the TITAN-II fusion power core (FPC) is designed so that

the advantages of a single-piece approach are fully utilized and a different design should have been produced to compare and quantify the benefits of single-piece maintenance procedures, (2) little data is available on times that would be required for each step during the maintenance procedure, and (3) data are needed on "mean time-to-failure" and "mean time-to-repair" of various components in order to quantify the impact of the maintenance procedure on the overall plant availability. Therefore, only those steps that are likely to be different between single-piece and modular approaches have been identified. Pretesting of the reactor torus to full operating condition is one of the potential advantages of the TITAN-I and TITAN-II single-piece approach. Pretesting of TITAN reactors is discussed in Section 14.4 and, thus, is not reported here.

20.2. TITAN-II PLANT LAYOUT

The elevation view of the TITAN-II design is shown in Figures 20.2-1 and 20.2-2. All of the TITAN-II maintenance procedures are performed with vertical lifts. As a result, the reactor vault and reactor building are smaller. The vertical lift of various components is performed by a moveable bridge crane. The heaviest components are the reactor torus weighing about 180 tonnes and the moveable upper OH-coil set (120 tonnes). Vertical lift of these components is easily manageable by existing cranes (conventional bridge cranes have a lift limit of about 500 tonnes and special-order cranes are available with lift limits exceeding 1600 tonnes).

The lifetime of the TITAN-II reactor torus (including the first wall, blanket, shield, and divertor modules) is estimated to be in the range of 15 to 18 MW y/m^2, and the more conservative value of 15 MW y/m^2 will require the change-out of the reactor torus (including the toroidal-field coils) on a yearly basis for operation at 18 MW/m^2 of neutron wall loading with 76% availability. The toroidal-field coils would be reused at a later date.

The TITAN-II reactor is a "loop-in-pool" design which is cooled with an aqueous solution of a dissolved lithium salt, $LiNO_3$. The major feature of the TITAN-II reactor is that the entire primary loop is located the bottom of a low-temperature, atmospheric-pressure, pure-water pool (Figure 20.2-1). Detailed safety analyses have been performed (Section 19) which show that the TITAN-II pool can contain the afterheat energy of the FPC and will remain at a low enough temperature such that tritium or other radioactive material in the primary-coolant system will not be released.

The first wall and blanket of the TITAN-II design consist of stamped side plates made of the low-activation, high-strength ferritic steel alloy, 9-C [4]. These plates, called

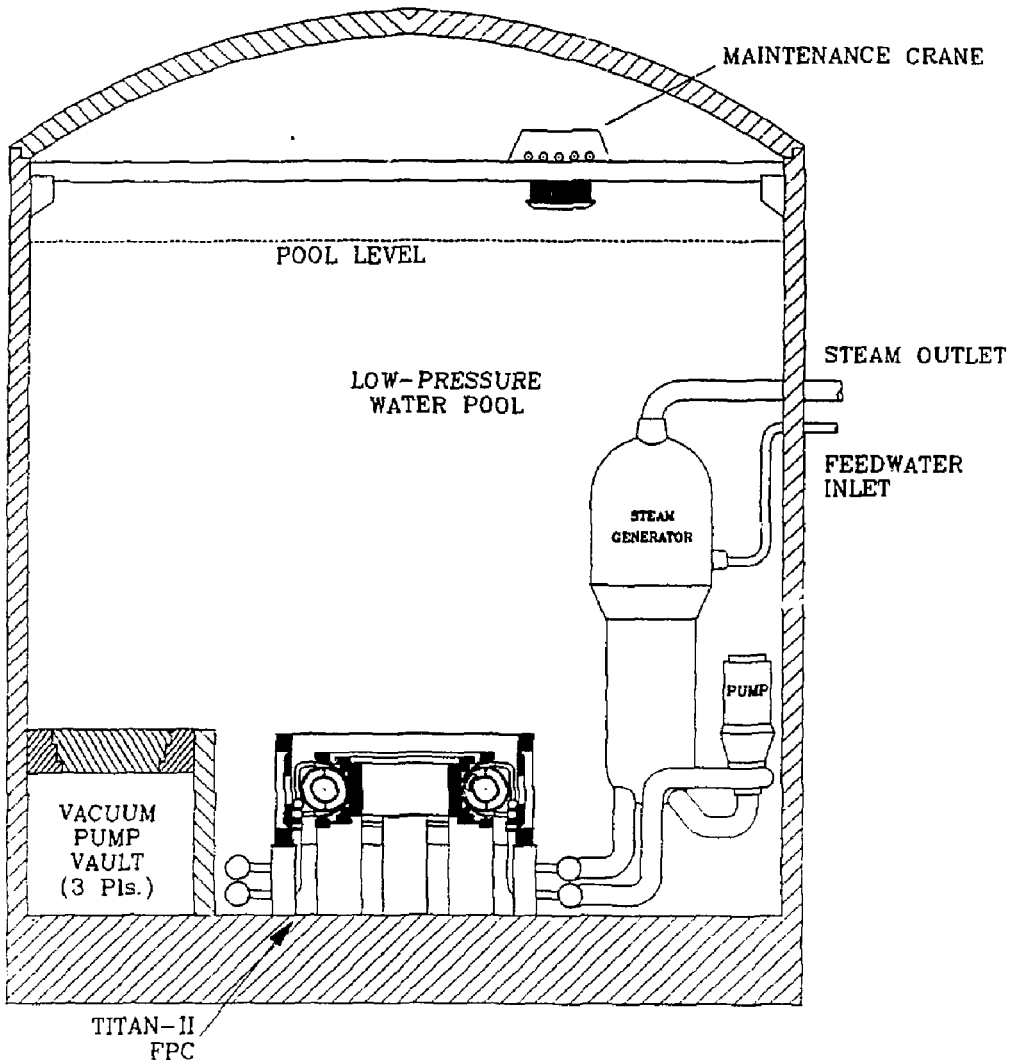

Figure 20.2-1. Elevation view of the TITAN-II reactor building through the reactor centerline showing the FPC, water pool, and maintenance crane.

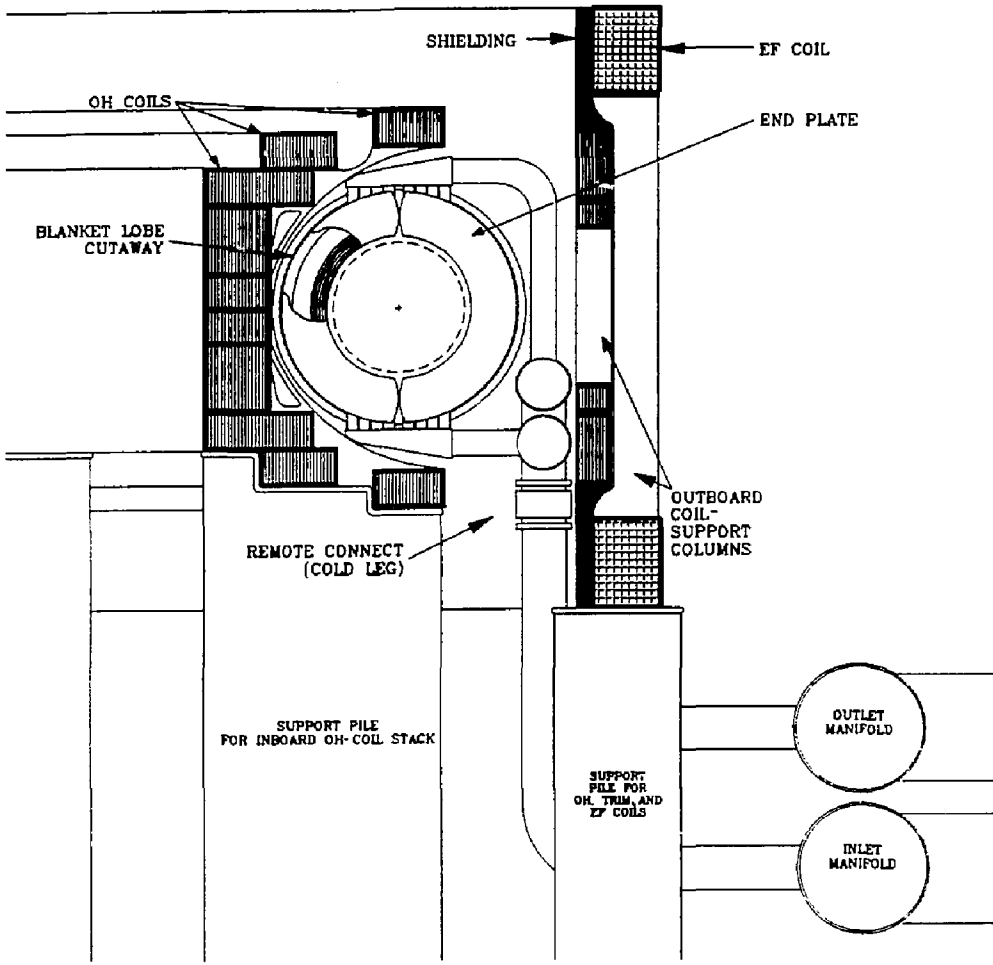

Figure 20.2-2. Poloidal cross section of the TITAN-II fusion power core illustrating the major components and coolant flow paths.

"J-plates" because of their cross section, are assembled into blanket lobes as shown in Figure 20.2-3. Inside each of the lobes are 9-C-clad beryllium rods which occupy the first 20 cm behind the first wall. The blanket lobes are stacked side-by-side to form a blanket module. The shield is used as a clamp to restrain the lobes from any movement. A cross section and an isometric view of a blanket module are shown, respectively, in Figures 20.2-4 and 20.2-5. Twelve blanket modules and three divertor sections are assembled into a single reactor torus in preparation for installation into the reactor chamber.

The vacuum boundary for the FPC, located outside the toroidal-field (TF) coils, acts as a boundary between the pool and the hot torus. The TF coils occupy the space between the back of the shield and the vacuum shell (Figure 20.2-4). Vacuum-duct penetrations through the vacuum shell are located in the regions near the divertors. Isolation valves, as illustrated in Figure 20.2-6, are required at all of the underwater connections (hydraulic, electrical, and vacuum). The vacuum-tank concept of TITAN-I was not used here because it would provide excessive thermal insulation between the pool and the FPC and the pool could not act as a heat sink for the decay heat during off-normal events.

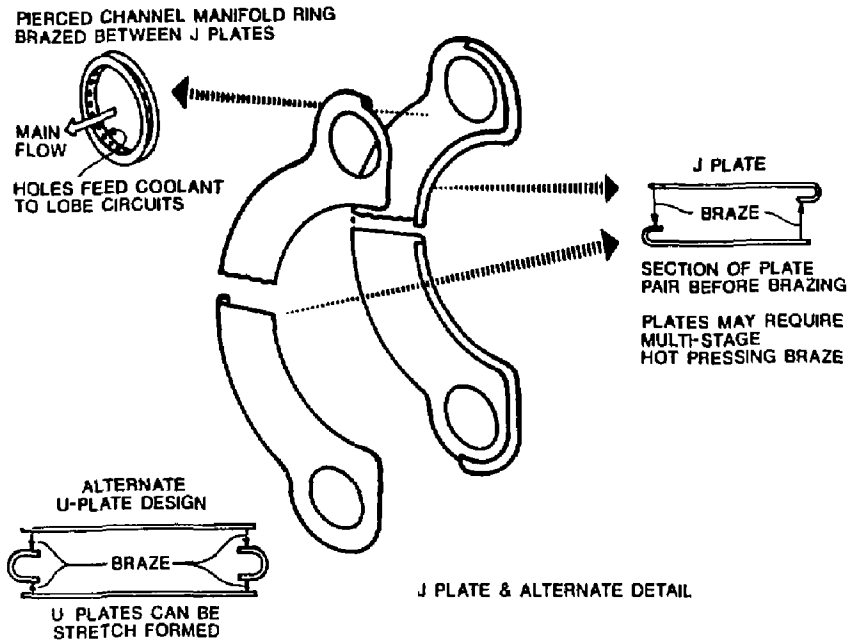

Figure 20.2-3. The TITAN-II blanket lobe, J-plate design.

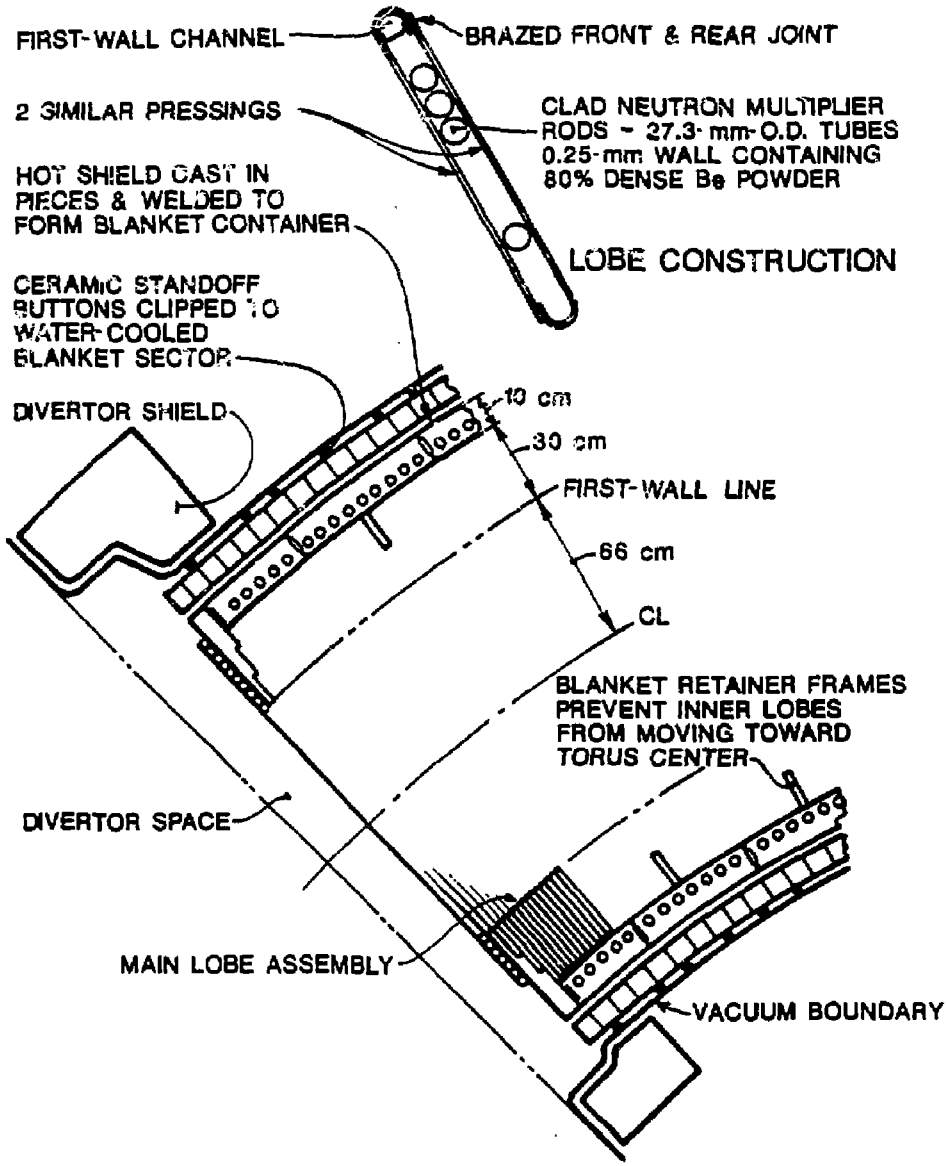

Figure 20.2-4. Cross section of a TITAN-II blanket module.

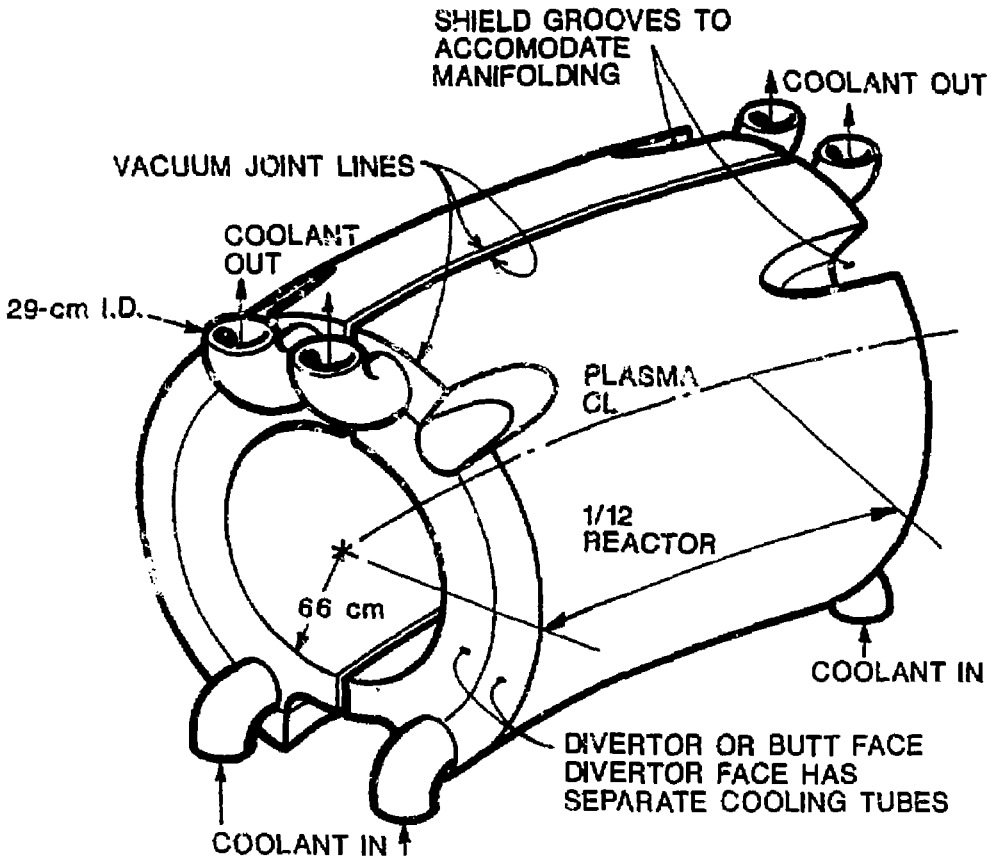

Figure 20.2-5. Isometric view of a TITAN-II blanket module.

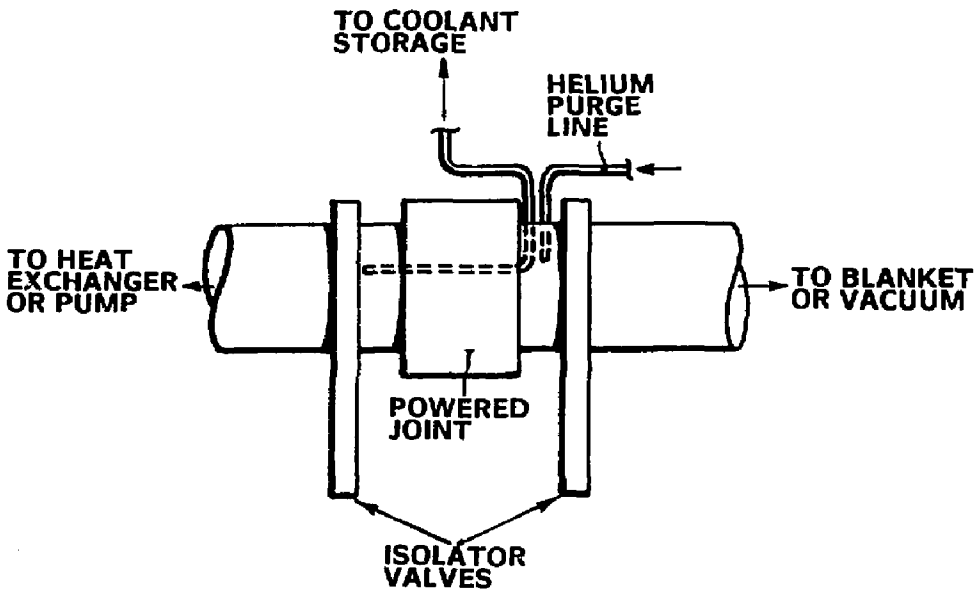

Figure 20.2-6. Illustration of a proposed isolation valve for the TITAN-II vacuum ducts.

20.3. MAINTENANCE PROCEDURES

A key assumption for the TITAN maintenance program, as in other fusion reactor studies, is that a high degree of automation is available. In the TITAN-II design, powered joints are used extensively for hydraulic and electrical connect/disconnects. The use of powered joints allows many tasks to be done quickly and in parallel. Together with the single-piece maintenance scheme, which reduces the number of joints to a minimum, this approach is expected to result in a dramatic reduction in the required time to perform the maintenance operations and to increase the overall reliability. The powered joints for the coolant circuits are located on the hot and cold legs of the aqueous-solution supplies as is shown in Figure 20.2-2. Additional connect and disconnect powered joints are also provided for the upper OH-coil-set electrical and cooling circuits. Examples of powered joints [2] are shown in Section 14.3.

One of the unique aspects of the TITAN-II maintenance procedures is the presence of the large water pool surrounding the FPC. Three maintenance options are available:

1. Perform all required maintenance under water without draining the pool. This option maintains the pool as a safety barrier until the torus assembly is removed from the pool. Also, the pool drain time does not affect the scheduling of the maintenance.

2. Drain the entire pool prior to maintenance operations. A benefit is that double valves to prevent water infiltration into the vacuum and electrical systems are not required. Pool drain time and cost for pool-water storage need to be considered.

3. The third approach, a hybrid of the above two approaches, provides an intermediate cylinder around the FPC. In this case, only the central portion of the pool would be pumped out prior to maintenance. This approach also does not require double valves to prevent water infiltration into the vacuum and electrical systems. Compared to second approach, the pumping time is reduced and water storage requirements are smaller. However, this approach requires additional structure.

Because of the perceived safety advantages and simplicity, the TITAN study adopted maintenance method number one: to perform the maintenance procedures under water. Fourteen principal tasks must be accomplished for the annual, scheduled maintenance of the TITAN-II fusion power core. These steps are listed in Table 20.3-I. Tasks that will require a longer time to complete in a modular design are also identified in Table 20.3-I (assuming the same configuration for the modular design as that of TITAN-II). Another potential benefit of the single-piece maintenance approach is that the recovery from any unscheduled event will be standard and similar to the procedures of Table 20.3-I for the scheduled maintenance. It should be noted that the economic impact of a disabled FPC is dominated by the downtime of the plant and not by the capital cost of a new FPC.

Vertical lifts have been chosen for the component movements during maintenance. Vertical lifts allow a more compact reactor building, consistent with the TITAN-II design goal. In addition, if one to provide horizontal access near the bottom of the pool, the design of the pool surrounding the FPC would be very complicated and the integrity of the pool would be questionable. Vertical lifts of the components are performed by a moveable bridge crane as shown in Figure 20.2-1. Lift limits for conventional bridge cranes is around 500 tonnes, with special-order crane capacities in excess of 1000 tonnes. The most massive components lifted during TITAN-II maintenance are the reactor torus

Table 20.3-I.

PRINCIPAL TASKS DURING THE TITAN-II MAINTENANCE PROCEDURE

1. Orderly shutdown of the plasma and discharge of the magnets;
2. Continue cooling the FPC at a reduced level until the decay heat is sufficiently low to allow natural convection cooling in the atmosphere;
3. During the cool-down period:
   a. Continue vacuum pumping until sufficient tritium is removed from the FPC,
   b. Valve-off all systems which will be disconnected during maintenance (*i.e.*, vacuum and electrical systems) and, depending on the maintenance method, drain the water pool above the FPC,
   c. Disconnect electrical and coolant supplies from the upper OH-coil set,
   d. Break vacuum;
4. Drain primary coolant from FPC;
5. Lift OH-coil set and store in the lay-down area;
6. Disconnect primary-coolant supplies at ring headers;[a]
7. Lift the reactor torus and move to the hot cell;[a]
8. Inspect FPC area;
9. Install the new, pretested torus assembly;[a]
10. Connect primary-coolant supplies, TF-coil electrical supplies, and re-weld all vacuum ducts;[a]
11. Replace the upper OH-coil set and connect electrical and coolant supplies;
12. Hot test the FPC;[b]
13. Pump-down the system;
14. Initiate plasma operations.

(*a*) The time required to complete these tasks is likely to be longer for a modular system than for a single-piece system, assuming similar configuration.

(*b*) The new torus assembly is pretested and aligned before committment to service. Only minimum hot testing would be required.

(180 tonnes) and the upper OH-coil set (OH coils 2 through 4) and its support structure (120 tonnes), which are easily manageable by the conventional cranes. The OH coils are reinstalled following the installation of the new torus assembly. Once the new torus is lowered into position, vertically oriented remote connects attach the torus to the stationary primary-coolant supplies.

A simple comparison of modular and single-piece maintenance approaches can be made using Table 20.3-I by assuming a modular design for TITAN-II with the same dimensions and wall loading but with toroidal segmentation which separates the reactor torus into three or more units for maintenance purposes. Examination of the maintenance steps listed in Table 20.3-I indicates that 5 of the 14 tasks (6, 7, 9, 10, and 12) would likely be more time consuming for a modular reactor. Some of the differences are associated with those steps that involve interfaces between modules and lifting of individual modules. Since the lifting of individual modules is done in series rather than in parallel, the total number of module transfers requires more time even though the lighter, modular unit may be transported somewhat faster than the complete reactor torus.

One of the crucial steps in Table 20.3-I is the installation of the new reactor torus at the bottom of the TITAN-II pool (step 9). A modular design will require additional time in order to align the modules into a full torus (depending on the required degree of precision). Another important difference between the modular and single-piece approaches is the degree of pretesting that can be performed outside of the reactor vault. A comprehensive set of pretests are envisioned for the TITAN reactors (Section 14.4). For a modular design, those pretests that require a fully assembled torus should be performed after the installation of the modules into the reactor vault as a complete torus, which will increase the maintenance period and the downtime.

Similar to the maintenance procedures for the TITAN-I design, a self-consistent comparison of the TITAN-II single-piece maintenance procedure with a modular approach is difficult because very little information is available on the time needed to perform each of the maintenance tasks listed in Table 20.3-I. Furthermore, the TITAN-II FPC is designed such that the advantages of a single-piece approach are fully exploited and a different modular-type design should have been produced for a self-consistent comparison.

The comparison between the single-piece and modular maintenance procedures is even more difficult for unscheduled events because such a comparison would require an extensive data base on the mean time-to-failure and the mean time-to-repair of various components of the reactor. Recovery from a major event will be shorter with the single-piece maintenance approach. It is possible that for minor events, the mean time-to-repair for a modular approach will be shorter. However, for a modular approach, recovery from

unscheduled events requires additional equipment, each designed to handle and repair certain failure modes. In a single-piece approach, recovery from unscheduled events will be, in principle, standard and similar to a scheduled maintenance procedure. One should also note that the sector-to-sector interfaces in a modular design add to the number of possible fault areas, hence, possibly reducing overall reliability.

20.4. SUMMARY

The TITAN reactors are compact, high-power-density designs. The small physical size of these reactors permits each design to be made of only a few pieces, allowing a single-piece maintenance approach. Also, because of the small physical size and mass of the TITAN-II FPC, the maintenance procedures can be carried out through vertical lifts, allowing a much smaller reactor vault.

The major tasks required for annual maintenance of the TITAN-II FPC have been identified. Single-piece maintenance of the reactor torus (including the first wall, blanket, shield, TF coils, and divertor modules) appears feasible and must be performed yearly. Following the removal of the old torus, a new, fully pretested assembly is installed.

Potential advantages of single-piece maintenance procedures are identified:

1. Shortest period of downtime resulting from scheduled and unscheduled FPC repairs;
2. Improved reliability resulting from integrated FPC pretesting in an on-site, non-nuclear test facility where coolant leaks, coil alignment, thermal-expansion effects, *etc.* would be corrected by using rapid and inexpensive hands-on repair procedures prior to committing the FPC nuclear service;
3. No adverse effects resulting from the interaction of new materials operating in parallel to radiation-exposed materials;
4. Ability to modify continually the FPC as may be indicated or desired by reactor performance and technological developments; and
5. Recovery from unscheduled events would be more standard and rapid. The entire reactor torus is replaced and the reactor is brought back on line with the repair work being performed, afterwards, outside the reactor vault.

A high level of pretesting ensures that the new torus will behave as designed, and will have a higher reliability than individual modules that have not been tested together as a single operating unit under reactor-like conditions. It appears that the single-piece maintenance approach, together with a detailed pretesting program, can substantially improve the availability of the TITAN-II reactor.

REFERENCES

[1] R. L. Hagenson, R. A. Krakowski, C. G. Bathke, R. L. Miller, M. J. Embrechts, *et al.*, "Compact Reversed-Field Pinch Reactors (CRFPR): Preliminary Engineering Considerations," Los Alamos National Laboratory report LA-10200-MS (1984).

[2] C. Copenhaver, R. A. Krakowski, N. M. Schnurr, R. L. Miller, C. G. Bathke, *et al.*, "Compact Reversed-Field Pinch Reactors (CRFPR)," Los Alamos National Laboratory report LA-10500-MS (1985).

[3] D. W. Graumann, "Experience with the Modular Concept of the OHTE Experimental Device During Initial Assembly, Operations, and the Mid-Experiment Upgrade," GA Technologies report GA-A17077 (1983).

[4] D. S. Gelles, N. M. Ghoniem, and R. W. Powell, "Low Activation Ferritic Alloys Patent Description," University of California Los Angeles report UCLA-PPG-1049 (1987).

APPENDIX B

Contents

APPENDIX B

B.1. TABLE OF TITAN-II REACTOR PARAMETERS

1. CHARACTERISTIC MACHINE DIMENSIONS

1.1. Reactor Envelope [1-1]		
1.1.1.	Height	5.52 m
1.1.2.	Outside diameter	12.47 m
1.1.3.	Circumference	39.18 m
1.1.4.	Volume	674.16 m^3
1.2. Plasma Chamber		
1.2.1.	Major toroidal radius, R_T	3.90 m
1.2.2.	Plasma minor radius, r_p	0.60 m
1.2.3.	First wall minor radius, r_{FW}	0.66 m
1.2.4.	Plasma volume, V_p	27.71 m^3
1.2.5.	Plasma chamber volume	33.53 m^3
1.2.6.	First wall surface area [1-2]	163.25 m^2
1.2.7.	Number of sectors [1-3]	3
1.3. Reactor Pool [1-4]		
1.3.1.	Average height	33 m
1.3.2.	Outside diameter	38 m
1.3.3.	Wall thickness	1 m
1.3.4.	Circumference	119 m
1.3.5.	Volume	29,600 m^3

2. PLASMA PARAMETERS

2.1. Fuel Cycle		DT/Li
2.2. Plasma Dimensions		
2.2.1.	Major radius, R_T	3.90 m
2.2.2.	Minor radius, r_p	0.60 m
2.2.3.	Plasma cross section	circular

2.3. Electron Density, n_e [2-1]	
2.3.1. Average electron density	9.3×10^{20} m^{-3}
2.3.2. Central electron density	1.4×10^{21} m^{-3}
2.4. Ion Density, n_i [2-1]	
2.4.1. Average ion density	8.9×10^{20} m^{-3}
2.4.2. Central ion density	1.3×10^{21} m^{-3}
2.5. Average Alpha-Particle Density, n_α [2-2]	4.5×10^{19} m^{-3}
2.6. Ion Temperature, T_i [2-1]	
2.6.1. Average ion temperature	10 keV
2.6.2. Central ion temperature	15 keV
2.7. Electron Temperature, T_e [2-1]	
2.7.1. Average electron temperature	10 keV
2.7.2. Central electron temperature	15 keV
2.8. Average Alpha-Particle Energy, E_α [2-2]	68 keV
2.9. Effective Plasma Ion Charge, Z_{eff} [2-3]	1.690
2.10. Global Energy-Confinement Time, τ_E [2-4]	0.22 s
2.11. Effective Global Thermal Diffusivity, $\chi_E = (3/16)r_p^2/\tau_E$ [2-4]	0.31 m^2/s
2.12. Electron Energy-Confinement Time, τ_{E_e} [2-4]	0.28 s
2.13. Particle Confinement Time at Burn, τ_p	
2.13.1. Without recycling [2-5]	1.10 s
2.13.2. With recycling [2-6]	
2.13.2.1. Fuel ions (average)	3.68 s
2.13.2.2. Helium	1.52 s
2.14. Lawson Parameter, $n_i\tau_E$ [2-4]	1.92×10^{19} s/m^3
2.15. Plasma Toroidal Current, I_ϕ [2-7]	17.8 MA
2.16. Average Toroidal Current Density, j_ϕ [2-7]	15.7 MA/m^2

2.17. Toroidal Field, B_ϕ [2-1]	
2.17.1. Average	3.90 T
2.17.2. At plasma edge	0.38 T
2.17.3. At plasma axis	11.85 T
2.17.4. Peak field on the coil [2-8]	5.1 T
2.18. Poloidal Field, B_θ [2-1]	
2.18.1. Average	6.21 T
2.18.2. At plasma edge	5.93 T
2.19. Vertical Field,	
2.19.1. At plasma axis	1.56 T
2.19.2. Decay index, n	0.40
2.19.3. Stray field at startup	2.30 T
2.20. Poloidal Beta, $\beta_\theta = 2\mu_0 p/B_\theta^2(r_p)$	0.22
2.21. Toroidal Beta $\beta = 2\mu_0 p/ < B_\phi >^2$	0.52
2.22. Engineering Beta [2-9]	7.75
2.23. Reversal Parameter, F [2-7],[2-10]	
2.23.1. Mean value at burn	−0.1
2.23.2. During OFCD oscillation	−0.03 to −0.17
2.24. Pinch Parameter, Θ [2-7],[2-10]	
2.24.1. Mean value at burn	1.56
2.24.2. During OFCD oscillation	1.50 to 1.62
2.25. Safety Factor, $q = rB_\phi/RB_\theta$	
2.25.1. On axis	0.11
2.25.2. At plasma edge	-0.01
2.25.3. Radius of reversal surface ($q = 0$)	0.55 m
2.26. Streaming Parameter, j_ϕ/n	
2.26.1. During startup (maximum value)	6.5×10^{-14} A-m
2.26.2. At burn	1.8×10^{-14} A-m
2.27. Electron Streaming Parameter, $\xi = v_D/v_{th}$	
2.27.1. During startup (maximum value)	2.0×10^{-2}
2.27.2. At burn	1.9×10^{-3}

D

2.28. Radiation Fraction [2-8]		
2.28.1. Core plasma	0.70	
2.28.2. Scrape-off layer	0.23	
2.28.3. Divertor plasma	0.04	
2.28.4. Total radiation fraction	0.97	
2.28.5. Radiation fraction to first wall, f_{RAD}	0.95	
2.28.6. Radiation fraction to divertor plate	0.02	
2.29. Current Drive [2-11]		
2.29.1. Method	OFCD	
2.29.2. Frequency, f	25	Hz
2.29.3. Toroidal-flux swing, $\delta\phi/\phi_o$	0.035	
2.29.4. Θ variation	1.50 to 1.62	
2.29.5. F variation	−0.03 to −0.17	
2.29.6. Input power (toroidal/poloidal circuits)		
2.29.6.1. Real (supplied) power [2-11]	38.23/4.61	MW
2.29.6.2. Reactive power	1285.71/249.15	MVA
2.29.7. Power-supply dissipation [2-12]	15.34	MW
2.29.8. Current-drive power [2-11]	54.64	MW
2.29.9. Efficiency, I_ϕ/P_{CD} [2-13]	0.33	A/W
2.30. Plasma Heating Method	Ohmic	
2.31. Plasma Ohmic Dissipation	28.5	MW
2.32. Plasma Energy Gain, $Q_p = P_f/P_\Omega$ [2-14]	80.2	

3. POWER OUTPUT

3.1. Plasma Fusion Power, P_f	2289.8	MW
3.1.1. Neutron power, P_n	1831.3	MW
3.1.2. Alpha-particle power, P_α	458.5	MW
3.2. Blanket Energy Multiplication, M	1.36	
3.3. Nuclear Power ($MP_n + P_\alpha$)	2949.1	MW
3.4. Ohmic Heating Power, P_Ω [8-1]	28.5	MW

3.5. Power to First Wall	
3.5.1. Surface heating, $f_{RAD}(P_\alpha + P_\Omega)$	462.7 MW
3.5.2. Nuclear heating	
3.5.2.1. Structure	36.6 MW
3.5.2.2. Coolant	258.4 MW
3.5.3. OFCD heating (eddy currents) [3-2]	*nil*
3.5.4. Coolant-pumping power [3-2]	12.5 MW
3.5.5. Total thermal power, P_{FW}	770.2 MW
3.6. Power to Multiplier Zone	
3.6.1. Nuclear heating	
3.6.1.1. Structure	214.5 MW
3.6.1.2. Coolant	690.9 MW
3.6.1.2. Beryllium	819.9 MW
3.6.2. OFCD heating (eddy currents) [3-2]	0.1
3.6.3. Coolant-pumping power [3-3]	28.2 MW
3.6.6. Total thermal power, P_{MZ}	1753.6 MW
3.7. Power to Breeder/Reflector Zone	
3.7.1. Nuclear heating	
3.7.1.1. Structure	27.9 MW
3.7.1.2. Coolant	281.2 MW
3.7.2. OFCD heating (eddy currents) [3-2]	0.1
3.7.3. Coolant-pumping power [3-3]	5.1 MW
3.7.6. Total thermal power, P_{BZ}	314.3 MW
3.8. Power to Hot Shield	
3.8.1. Nuclear heating	
3.8.1.1. Structure	148.9 MW
3.8.1.2. Coolant	8.3 MW
3.8.2. OFCD heating (eddy currents) [3-2]	*nil*
3.8.3. Coolant-pumping power [3-3]	2.6 MW
3.8.4. Total thermal power, P_{HS}	159.8 MW
3.9. Power to Divertor Plate	
3.9.1. Surface heating, $(1 - f_{RAD})(P_\alpha + P_\Omega)$	24.3 MW
3.9.2. Nuclear heating	
3.9.2.1. Structure	2.8 MW
3.9.2.2. Coolant	1.2 MW
3.9.3. Coolant-pumping power [3-3]	0.5 MW
3.9.4. Total thermal power, P_{DP}	28.8 MW

3.10. Total Reactor Thermal Power, P_{th}		
3.10.1. First wall thermal power	770.2	MW
3.10.2. Multiplier-zone thermal power	1753.6	MW
3.10.3. Breeding-zone thermal power	314.3	MW
3.10.4. Hot shield thermal power	159.8	MW
3.10.5. Divertor plate thermal power	28.8	MW
3.10.6. Total	3026.7	MW
3.11. Thermal-Cycle Efficiencies, η_{th}	0.350	
3.12. Gross Electric Power, P_{ET}	1059.3	MWe
3.13. Recirculating Power		
3.13.1. TF joule losses	16.0	MWe
3.13.2. Divertor joule losses	9.8	MWe
3.13.3. OFCD system [8–4]	54.6	MWe
3.13.4. Coolant-pumping power	48.9	MWe
3.13.5. Auxiliary power [8–5]	30.0	MWe
3.13.6. Total	*159.3*	*MWe*
3.14. Recirculating-Power Fraction, ϵ	0.150	
3.15. Engineering Q $(= 1/\epsilon)$	6.650	
3.16. Net Electric Power	900.0	MWe
3.17. Net Plant Efficiency, $\eta_p = \eta_{th}(1-\epsilon)$	0.30	
3.18. Mass Power Density, MPD [8–6]	806	kWe/tonne
3.19. Plasma Power Density, P_f/V_p	83	MW/m^3

4. REACTOR COOLANT SYSTEM

4.1. First Wall System [4-1]	Semi-circular channels separated from blanket lobes single-pass, poloidal coolant flow	
4.1.1. Coolant	Aqueous $LiNO_3$ Solution ($A_{Li} = 6.4\%$)	
4.1.2. Structural material	Ferritic Steel (9-C)	
4.1.3. Channel outer diameter [4-1]	30.0	mm
4.1.4. Channel inner diameter [4-1]	27.0	mm
4.1.5. Erosion allowance	0.25	mm
4.1.6. Number of channels	840	
4.1.7. Structure volume fraction	0.17	
4.1.8. Coolant volume fraction	0.62	
4.1.9. Void volume fraction	0.21	
4.1.10. Structure volumetric heating	202	MW/m^3
4.1.11. Coolant volumetric heating	270	MW/m^3
4.1.12. Outlet temperature	603	K
4.1.13. Inlet temperature	571	K
4.1.14. Outlet pressure	7	MPa
4.1.15. Inlet pressure [4-2]	8	MPa
4.1.16. Pressure drop	0.5	MPa
4.1.17. Maximum primary stress	98	MPa
4.1.18. Maximum secondary stress	363	MPa
4.1.19. Maximum wall temperature	776	K
4.1.20. Coolant flow rate (total)	1150	kg/s
4.1.21. Coolant flow velocity	22.6	m/s
4.1.22. Reynolds number, Re	1.49×10^6	
4.1.23. Nusselt number, Nu	2360	
4.1.24. Prandtl number, Pr	16.5	
4.1.25. Critical heat flux	8.3	MW/m^2
4.1.26. Subcooling at exit	16.5	°C
4.2. Multiplier-Zone System [4-1]	First zone of the blanket lobes single-pass, poloidal coolant flow	
4.2.1. Coolant	Aqueous $LiNO_3$ Solution ($A_{Li} = 6.4\%$)	
4.2.2. Structural material	Ferritic Steel (9-C)	
4.2.3. Multiplier Material	Beryllium	
4.2.4. Lobe width	30.0	mm
4.2.5. Zone radial dimension	200.0	mm
4.2.6. Lobe wall thickness	1.4	mm
4.2.7. Number of Lobes	840	
4.2.8. Structure volume fraction [4-3]	0.12	
4.2.9. Coolant volume fraction [4-3]	0.29	
4.2.10. Multiplier volume fraction [4-3]	0.59	

4.2.11. Structure volumetric heating [4-4]	180	MW/m^3
4.2.12. Coolant volumetric heating [4-4]	140	MW/m^3
4.2.13. Beryllium volumetric heating [4-4]	240	MW/m^3
4.2.14. Outlet temperature	603	K
4.2.15. Inlet temperature	571	K
4.2.16. Outlet pressure	7	MPa
4.2.17. Inlet pressure [4-2]	8	MPa
4.2.18. Pressure drop [4-4]	1	MPa
4.2.19. Maximum beryllium temperature	846	K
4.2.20. Coolant flow rate (total)	2.6×10^4	kg/s
4.2.21. Coolant flow velocity [4-4]	14	m/s
4.2.22. Reynolds number, Re [4-4]	2.7×10^5	
4.2.23. Nusselt number, Nu [4-4]	601	

4.3. Breeder/Refelector-Zone System [4-1]	Second zone of the blanket lobes single-pass, poloidal coolant flow	
4.3.1. Coolant	Aqueous $LiNO_3$ Solution ($A_{Li} = 6.4\%$)	
4.3.2. Structural material	Ferritic Steel (9-C)	
4.3.3. Lobe width	30.0	mm
4.3.4. Zone radial dimension	100.0	mm
4.3.5. Lobe wall thickness	1.4	mm
4.3.6. Number of Lobes	840	
4.3.7. Structure volume fraction	0.09	
4.3.8. Coolant volume fraction	0.91	
4.3.9. Structure volumetric heating	40	MW/m^3
4.3.10. Coolant volumetric heating	40	MW/m^3
4.3.11. Outlet temperature	603	K
4.3.12. Inlet temperature	571	K
4.3.13. Outlet pressure	7	MPa
4.3.14. Inlet pressure [4-2]	8	MPa
4.3.15. Coolant flow rate (total)	4660	kg/s
4.3.15. Pressure drop	5.0×10^{-4}	MPa
4.3.16. Maximum wall temperature	621	K
4.3.18. Coolant flow velocity	1.0	m/s
4.3.19. Reynolds number, Re	1.5×10^5	
4.3.20. Nusselt number, Nu	376	

4.4. Hot Shield System [4-1]	Two-piece shield, welded to from blanket container with two rows of coolant channels single-pass, poloidal coolant flow	
4.4.1. Coolant	Aqueous $LiNO_3$ Solution ($A_{Li} = 6.4\%$)	
4.4.2. Structural material	Ferritic Steel (9-C)	
4.4.3. Radial thickness	100	mm
4.4.4. Channel inner diameter		
4.4.4.1. 1st row	12.7	mm
4.4.4.2. 2nd row	19.0	mm
4.4.5. Structure volume fraction	0.90	
4.4.6. Coolant volume fraction	0.10	
4.4.7. Structure volumetric heating		
4.4.7.1. 1st row	22	MW/m^3
4.4.7.2. 2nd row	9	MW/m^3
4.4.8. Coolant volumetric heating		
4.4.8.1. 1st row	10	MW/m^3
4.4.8.2. 2nd row	5	MW/m^3
4.4.9. Outlet temperature	603	K
4.4.10. Inlet temperature	571	K
4.4.11. Outlet pressure	7	MPa
4.4.12. Inlet pressure [4-2]	8	MPa
4.4.13. Pressure drop		
4.4.13.1. 1st row	2.2×10^{-2}	MPa
4.4.13.2. 2nd row	4.7×10^{-3}	MPa
4.4.14. Maximum wall temperature		
4.4.14.1. 1st row	682	K
4.4.14.2. 2nd row	700	K
4.4.15. Coolant flow rate (total)	2440	kg/s
4.4.16. Coolant flow velocity		
4.4.16.1. 1st row	6.5	m/s
4.4.16.2. 2nd row	3.7	m/s
4.4.17. Reynolds number, Re		
4.4.17.1. 1st row	3.3×10^5	
4.4.17.2. 2nd row	2.8×10^5	
4.4.18. Nusselt number, Nu		
4.4.18.1. 1st row	706	
4.4.18.2. 2nd row	619	

4.5. Divertor Plate System [4–5]	The armor is brazed to a bank of circular tubes with multiple-pass, radial/toroidal coolant flow	
4.5.1. Coolant	Aqueous $LiNO_3$ Solution ($A_{Li} = 6.4\%$)	
4.5.2. Structural material		
4.5.2.1. Armor	W-26Re	
4.5.2.2. Coolant tube	W-26Re	
4.5.3. Coolant-tube outer diameter	10.0	mm
4.5.4. Coolant-tube inner diameter	8.0	mm
4.5.5. Armor thickness	1.0	mm
4.5.6. Outlet temperature	618	K
4.5.7. Inlet temperature	591	K
4.5.8. Outlet pressure	14	MPa
4.5.9. Inlet pressure [4–6]	15	MPa
4.5.10. Maximum primary stress	83	MPa
4.5.11. Maximum secondary stress	505	MPa
4.5.12. Maximum wall temperature	1052	K
4.5.13. Coolant flow rate (total)	433	kg/s
4.5.14. Maximum coolant flow velocity [4–7]	20	m/s
4.6. Coolant-Circulator Type		
4.6.1. First wall, blanket, hot shield	Single-stage centrifugal pump	
4.6.2. Divertor Plate	Double-stages centrifugal pump	
4.7. Power Input to Each Circulator [4–8]		
4.7.1. First wall, blanket, hot shield	48.4	MWe
4.7.2. Divertor Plate	0.5	MWe
4.8. Thermal-Energy Storage	not required	
4.9. Peak Temperature During a Loss-of-Flow Accident (LOFA) [4–9]		
4.9.1. First wall	621	K
4.9.2. Beryllium zone	617	K
4.9.3. Hot shield	613	K
4.10. Peak Temperature During a Loss-of-Coolant Accident (LOCA) [4–10]		
4.10.1. First wall	1005	K
4.10.2. Beryllium zone	754	K
4.10.3. Hot shield	603	K

5. INTERMEDIATE COOLANT SYSTEM [5-1]

5.1. Secondary Coolant	none

6. STEAM GENERATION SYSTEM

6.1. Steam Outlet Temperature	581 K
6.2. Steam Outlet Pressure	7.2 MPa
6.3. Total Steam Flow Rate	1466 kg/s
6.4. Feedwater Inlet Temperature	514 K
6.5. Number of Steam Generators per sector	1
6.6. Gross Thermal-Power Efficiency	0.350
6.7. Gross Electric Output	1059.3 MWe

7. SHIELD COOLANT SYSTEM [7-1]

7.1. EFC-Shield [7-2]	None

8. REACTOR AUXILIARY SYSTEM

8.1. Vacuum Pumping System	
8.1.1. Vacuum and plasma chamber pressure	
8.1.1.1. Base plasma chamber pressure	10^{-5} mtorr
8.1.1.2. Divertor duct pressure [8-1]	20 – 100 mtorr
8.1.2. Temperature of neutral gas	700 K
8.1.3. Plasma chamber volume	33.6 m^3
8.1.4. Vacuum chamber volume [8-2]	110. m^3
8.1.5. Particle throughput [8-3]	
8.1.5.1. DT	6.7×10^{21} s^{-1}
8.1.5.2. Helium	8.2×10^{20} s^{-1}
8.1.6. Conductance of the divertor duct	
8.1.6.1. For DT	215 m^3/s
8.1.6.2. For He	224 m^3/s
8.1.7. Type of pumps [8-4]	Turbo-molecular
8.1.8. Number of vacuum pumps [8-4],[8-5]	16
8.1.9. Helium pumping speed (per pump) [8-6]	20 m^3/s

8.2. Magnet Cooling System		
8.2.1. Toroidal-field coils [8-7]		
8.2.1.1. Coolant	Water	
8.2.1.2. Cooling load	19.6	MW
8.2.2. Divertor-field coils [8-7]		
8.2.2.1. Coolant	Water	
8.2.2.2. Cooling load	14.1	MW
8.2.3. Ohmic-heating coils [8-7]		
8.2.3.1. Coolant	Water	
8.2.3.2. Peak Cooling load during startup	200 to	MW
8.2.3.3. Cooling load during normal operation	2.7	MW
8.2.4. Equilibrium-field coils [8-8]		
8.2.4.1. Coolant	Liquid helium	
8.2.4.2. Cooling load [8-9]		
8.3. Plasma-Fueling System [8-10]		
8.3.1. Type	DT pellet	
8.3.2. Fuel composition	50% D, 50% T	
8.3.3. Fueling rates	0.035	g/s
8.3.4. Pellet diameter	3.4	mm
8.3.5. Pellet speed	2.1	km/s
8.3.6. Pellet injection frequency	6.25	s^{-1}
8.4. Tritium-Processing and Recovery System		
8.4.1. Type	Vapor-phase catalytic exchange	
8.4.2. Total tritium inventory [8-11]	4.00	kg
8.4.3. Tritium handling rate	0.46	kg/d
8.4.4. Water processing rate	9.64×10^4	kg/d
8.4.5. Primary-coolant tritium concentration	50	Ci/kg
8.4.6. Blanket detritiation factor	0.93	per pass

9. REACTOR COMPONENTS

9.1. First wall, Blanket, and Shield [9-1]		
9.1.1. Structural material	Ferritic Steel	(9-C)
9.1.2. Breeding material [9-2]	Aqueous $LiNO_3$ Solution	(A_{Li} = 6.4%)
9.1.3. Neutron multiplier material	Beryllium	
9.1.4. Tritium breeding ratio (TBR) [9-3]	1.22	
9.1.5. Number of modules [9-4]	1	
9.1.6. Weight of modules	180	tonnes
9.1.7. Largest single component [9-4]		
9.1.7.1. Weight	180	tonnes
9.1.7.2. Dimensions (diameter×height)	10.0 × 2.3	m
9.1.9. Lifetime [9-5]	1	y

9.2. Divertor		
9.2.1. Type	Toroidal-field divertors	
9.2.2. Number of divertors	3	
9.2.3. Neutralizer plate		
9.2.3.1 Armor	W-26Re	
9.2.3.2 Coolant tube	W-26Re	
9.2.3.3 Coolant	Aqueous $LiNO_3$ Solution	($A_{Li} = 6.4\%$)
9.2.4. Weight of each divertor	10	tonnes
9.2.5. Dimensions (diameter×height)	3 × 3	m
9.2.6. Lifetime [9-5]	1	y
9.3. Magnets		
9.3.1. Ohmic-heating coils [9-6],[9-7]		
9.3.1.1. Type	Normal	
9.3.1.2. Number	13	
9.3.1.3. Conductor	Copper	
9.3.1.4. Structure	Steel	
9.3.1.5. Insulator	Spinel ($MgAl_2O_4$)	
9.3.1.6. Coolant	Water	
9.3.1.7. Operating temperature	20 – 80	°C
9.3.1.8. Maximum stress in coil	33	MPa
9.3.1.9. Mean coil radius	2.42 – 5.66	m
9.3.2. Equilibrium-field coils [9-8]		
9.3.2.1. Type	Superconducting	
9.3.2.2. Number	2	
9.3.2.3. Conductor	Nb-Ti	
9.3.2.4. Structure	Steel	
9.3.2.5. Stabilizer	Copper	
9.3.2.6. Coolant	Liquid helium	
9.3.2.7. Operating temperature	4	K
9.3.2.8. Mean stress in coil [9-8]		
9.3.2.9. Mean coil radius	5.94	m
9.3.3. Toroidal-field coils [9-5]		
9.3.3.1. Type	Normal	
9.3.3.2. Number	30	
9.3.3.3. Conductor	Copper	
9.3.3.4. Structure	Steel	
9.3.3.5. Insulator	Spinel ($MgAl_2O_4$)	
9.3.3.6. Coolant	Water	
9.3.3.7. Operating temperature	20 – 80	°C
9.3.3.8. Mean stress in coil [9-9]		
9.3.3.9. Mean coil radius	1.12	m

9.3.4. Divertor-field coils		
9.3.4.1. Type	Normal	
9.3.4.2. Number	9	
9.3.4.3. Conductor	Copper	
9.3.4.4. Structure	Steel	
9.3.4.5. Insulator	Spinel ($MgAl_2O_4$)	
9.3.4.6. Coolant	Water	
9.3.4.7. Operating temperature	20 – 80	°C
9.3.4.8. Mean stress in coil [9–9]		
9.3.4.9. Mean coil radius	0.8	m
9.3.5. Maximum force transmitted to building [9–10]		
9.3.6. Maximum toroidal field		
9.3.6.1. At plasma axis	11.85	T
9.3.6.2. At plasma edge	0.38	T
9.3.6.3. At TF coil	0.38	T
9.3.7. Total stored energy [9–11]		
9.3.7.1. Poloidal field	3.6	GJ
9.3.7.2. Toroidal field	0.7	GJ
9.3.8. Largest single component [9–12]		
9.3.8.1. Weight	250	tonnes
9.3.8.2. Dimensions (diameter×height)	5.9 × 0.80	m
9.4. Energy Transfer and Storage	None	
9.5. Plasma Heating		
9.5.1. Type	Ohmic	
9.5.2. Frequency	–	
9.5.3. Power to plasma [9–13]	35	MW
9.5.4. Transmission method		
9.5.5. Power reflected from plasma	–	
9.5.6. Power loss in transmission	–	
9.5.7. Power loss in amplifiers	–	
9.5.8. Power loss in power supplies [9–14]	5	MW
9.5.9. System input power [9–15]	500	MW
9.5.10. Heating time [9–15]	11	s

10. ELECTRICAL-POWER REQUIREMENTS

10.1. Cold-Plasma Startup Power from Grid [10-1]	500 MW
10.2. Auxiliary Power Requirements (Normal Operation)	
10.2.1. Electrical energy storage	None
10.2.2. Toroidal-field coils	16.0 MW
10.2.3. Divertor-field coils	9.8 MW
10.2.4. OFCD [10-2]	54.6 MW
10.2.5. First wall, blanket, and shield coolant circulators	48.4 MW
10.2.6. Divertor plate coolant circulators	0.5 MW
10.2.7. Other auxiliary systems [10-3]	30.0 MW
10.2.8. Total	159.3 MW

11. BUILDINGS

11.1. Reactor Pool [11-1]	
11.1.1. Characteristic dimensions	
11.1.1.1. Outside diameter	38 m
11.1.1.2. Height	33 m
11.1.2. Enclosed volume	29600 m^3
11.1.3. Minimum wall thickness	1 m
11.1.4. Internal pressure	1 atm
11.1.5. Containment atmosphere	Air
11.2. Turbine Building [11-2]	
11.2.1. Characteristic dimensions	
11.2.1.1. Length	86 m
11.2.1.2. Width	40 m
11.2.1.3. Height	32 m
11.2.2. Total enclosed volume	2.64×10^5 m^3
11.3. Reactor Service Building	
11.3.1. Characteristic dimensions [11-3]	

12. REACTOR MAINTENANCE

12.1. First Wall, Blanket, Shield, and Divertor	
12.1.1. Lifetime	1 y
12.1.2. Weight	180 tonnes
12.2. OH and EF Magnet	
12.2.1. Lifetime [12-1]	40 y
12.2.2. Weight	332 tonnes
12.3. Radicactive Material Storage for Life of Plant [12-1]	
12.3.1. Total Class C [12-2]	
12.3.1.1. Weight	2642 tonnes
12.3.1.2. Volume	328 m^3
12.3.2. Total non-Class C [12-3]	
12.3.2.1. Weight	11 tonnes
12.3.2.2. Volume	1 m^3
12.4. Overall Plant Availability	0.76

FOOTNOTES TO TABLE B.1

1–1) The reactor envelope is defined by the cylinder enclosed by the upper and lower EF coils.

1–2) The first wall is corrugated, therefore, the total plasma-facing area is $\frac{\pi}{2}(2\pi R_T)\,2\pi(r_{FW}+d/2)$, where d is the outer diameter of the first-wall channels.

1–3) Sectors are used only for factory manufacturing and shipment to the site. Each sector consists of four blanket modules. These sectors, together with divertor modules, are assembled on-site into a single torus and tested to full operational condition prior to installation into the reactor vault.

1–4) The TITAN-II fusion power core is submerged in a pool of water (1 atm) to achieve a high level of safety assurance.

2–1) During the startup, plasma profiles are assumed to be

$$\begin{aligned} n(r)/n_o &= (1-r/r_p)^{2.8} \\ T(r)/T_o &= (1-r/r_p)^{4} \\ \mu(r)/\mu_o &= (1-r/r_p)^{8}\ . \end{aligned}$$

During the steady-state burn, TITAN-II operates with a highly radiative plasma (through injection of xenon impurities). The plasma profiles at burn are computed in Section 5.3. and are:

$$\begin{aligned} n(r)/n_o &= 1.00-0.86(r/r_p)^{3.44} \\ T(r)/T_o &= \begin{cases} 1.00-3.26(r/r_p)^{2.85} & \text{for } 0.00<r/r_p<0.25 \\ 1.12-0.71(r/r_p) & \text{for } 0.25<r/r_p<0.83 \\ 0.56-0.55(r/r_p)^{14.02} & \text{for } 0.83<r/r_p<1 \end{cases} \\ \mu(r)/\mu_o &= 1.00-0.44(r/r_p)^{6}-0.56(r/r_p)^{8}\ . \end{aligned}$$

2–2) Averaged value over both fast and thermal components.

2–3) The TITAN-II design operates with a highly radiative plasma by deliberately doping the plasma with xenon impurities.

2–4) Assuming a beta-limited confinement time of the form $\tau_E = c_\nu I_\phi^\nu r_p^2 f(\beta_\theta)$.

2–5) Assumed to be $\tau_p \simeq 4\tau_{E\alpha}$.

2–6) Based on self-consistent core-plasma, edge-plasma, and neutral-particle transport calculations.

2–7) Represents the mean value during the OFCD cycle (see item 2.29).

2–8) Including the poloidal field. The field produced by the coil is 0.4 T.

2–9) The engineering beta is defined as the ratio of the average plasma pressure to the maximum field strength on the toroidal-field coils.

2–10) The reversal parameter is held constant during the startup (by adjusting the toroidal-field strength), and the values of the pinch parameter are from equilibrium calculations.

2–11) Results of detailed calculations assuming full-coverage TF coils (Section 7). The results of Section 7 are scaled to include the effects of discreteness of the TF coils and the currents in the divertor coils which should be also oscillated to keep the separatrix in its position. For this case, the total supplied real power is 54.6 MW, including 28.55 MW delivered to the plasma (26.8 MW by the toroidal-field circuit and 1.76 MW by the poloidal-field circuit), 4.3 MW to oscillate the divertor coils, 15.34 MW dissipation in the power supplies and bussing, and 3.60, 2.66, and 0.19 MW joule heating in TF coils, in poloidal-field coils, and in the first wall and blanket by eddy currents. The power to TF and divertor coils represent the AC component of the currents in these coils.

2–12) Assuming a power supply efficiency, $Q = 100$.

2–13) A "wall-plug" efficiency including power-supply losses and the power to the divertor coils (see footnote 2–10)

2–14) All of the current-drive power deposited in the plasma appears as ohmic heating power.

3–1) All of the current-drive power deposited in the plasma appears as ohmic heating power.

3–2) Heating by eddy currents induced in the first wall and blanket by OFCD cycles.

3–3) Assuming an efficiency of 90% for coolant-circulation pumps.

3–4) Including the losses in the divertor coils (see footnote 2–10).

3–5) Allocated for housekeeping and auxiliary functions.

3–6) Mass power density is defined as the ratio of the net electric output to the mass of the FPC which includes the first wall, blanket, shield, divertor modules, coils, and related structure.

4–1) The first wall and blanket of the TITAN-II are integrated in the form of blanket lobes. The first 20 cm of the blanket lobe behind the first wall region (the multiplier zone) include 7 beryllium rods (diameter of 26 mm) clad in ferritic steel 9-C (cladding thickness of 0.25 mm). The last 10 cm of the blanket lobe is the breeder/reflector zone. 70 blanket lobes are staggered side by side to form a blanket module. Four blanket modules are assembled together into a sector. Each sector is supported by a two-piece shield that form a blanket container. TITAN-II reactor torus has three sectors, separated by three divertor modules. The ^{6}Li enrichment level in the coolant is 12%.

4–2) Inlet pressure of the first-wall, blanket, and shield coolant circuit. The pressure at the inlet of each component is reduced to the design level by orifices in order to use one pump system for all components.

4–3) Averaged over the entire system.

4–4) Values for the first multiplier cell.

4–5) The TITAN-II divertor plate is made of an armor which is brazed to a bank of circular, constant-cross-section tubes. Manifolds and headers are not included.

4–6) Inlet pressure of the divertor-plate coolant circuit is set by the maximum pressure drops in divertor-coolant tubes. The pressure at the inlet of some of the divertor-coolant tubes are lower than 15 MPa and orifices are used to reduce the pressure to the desired value at the inlet of these tubes.

4–7) The maximum coolant flow velocity, imposed as a constraint on the thermal-hydraulic design of the divertor plate. The coolant-flow velocity in most of tubes are lower than this value.

4–8) The efficiency of circulating pumps is assumed to be 90%.

4–9) In the presence of the low-pressure pool. Peak temperatures are reached 355 seconds after the initiation of the accident.

4–10) In the presence of the low-pressure pool. Peak temperatures are reached 300 seconds after the initiation of the accident (a re-flood time of 300 s is assumed).

5–1) Because the pressure in the steam generator (7.2 MPa) is larger than the primary coolant pressure (7.0 MPa), an intermediate heat exchanger deemed unnecessary. The divertor plate power, however, are deposited in the primary coolant circuit through a heat exchanger.

7–1) Power is recovered from the hot shield (see item 4.3.)

7–2) The EF shield is cooled by the pool water.

8–1) The pressure in the vacuum duct varies in the poloidal direction.

8–2) Not including the vacuum ducts.

8–3) Based on neutral transport calculations (Section 5.5). Particle throughput is enriched by about a factor 3 in He (with respect to DT throughput) and also by a factor of about 3 in D (with respect to T).

8–4) The turbo-molecular pumps are backed by 12 scroll pumps with pumping speed of 600 m^3/hr, operating between 50 mtorr and atmospheric pressure.

8–5) Based on the required total pumping speed of 260 m^3/s, only 13 pumps are needed. The additional 3 pumps are in reserve.

8–6) Assuming out-gassing rate of 10^{-11} to 10^{-12} torr-l/s, the required pumping speed to maintain the base pressure in the plasma chamber is in the range 3 to 35 m^3/s, much lower than the required pumping speed of 260 m^3/s for removal of the He ash.

8–7) Includes both steady state and OFCD contributions.

8–8) A pair of normal-conducting, EF trim coils are used during startup and OFCD cycles. Cooling loads for these coils are included in item 8.2.3.

8–9) The EF coils are based on present day technology with Nb-Ti conductor. Detailed design for these coils, therefore, was not performed.

8–10) The neutral-transport calculation of plasma exhaust shows some enrichment in D in the exhaust (Section 5). The effect of this enrichment is not included in this item. Also, plasma-driven permeation of D and T ions through the first wall is ignored.

8–11) Including tritium in storage (1 kg) and in the low-pressure pool (0.94 kg).

9–1) The first-wall and blanket of the TITAN-II are integrated in the form of blanket lobes. The first 20 cm of the blanket lobe behind the first wall region (the multiplier zone) include 7 beryllium rods (diameter of 26 mm) clad in ferritic steel 9-C (cladding thickness of 0.25 mm). The last 10 cm of the blanket lobe is the breeder/reflector zone. 70 blanket lobes are staggered side by side to form a blanket module. Four blanket modules are assembled together into a sector. Each sector is supported by a two-piece shield that form a blanket container. TITAN-II reactor torus has three sectors, separated by three divertor modules. The ^{6}Li enrichment level in the coolant is 12%.

9–2) With a ^{6}Li enrichment level of 12% in the coolant.

9–3) Based on 1-D neutronics calculations of the final design.

9–4) The reactor torus is assembled on-site from 3 pre-fabricated sectors interlinked by the 3 divertor. The reactor torus is installed and removed as one single piece.

9–5) Based on a lifetime of 15 MW-y/m^2.

9–6) Also act as the driver coils for the OFCD system.

9–7) Includes a pair of normal-conducting, EF trim coils which are used during startup and OFCD cycles.

9–8) The EF coils are based on present day technology with Nb-Ti conductor. Detailed design for these coils, therefore, was not performed.

9–9) The TF and divertor coils are based on present day technology with water-cooled copper conductor. Detailed design for these coils, therefore, was not performed.

9–10) Primarily caused by the weight of the FPC.

9–11) Including the plasma stored energy. The poloidal magnetic energies stored in the system are 0.3 GJ internal to the plasma and 3.2 GJ external in the plasma, noting that the plasma current and the EFC current are flowing in opposite directions. The toroidal magnetic stored energy internal to the plasma is 0.4 GJ and external to the plasma is 0.02 GJ.

9–12) The largest component is the EF coil, including the EFC shield.

9–13) Maximum value during startup.

9–14) Assuming an efficiency of 99% for power supplies.

9–15) Time from cold startup to ignition.

10–1) Maximum value during startup.

10–2) Including the losses in the divertor coils (see footnote 2–10).

10–3) Includes the refrigeration systems, vacuum systems, tritium-extraction systems, feed-water pumps, heat-rejection systems, and other miscellaneous reactor auxiliary systems.

11–1) The TITAN-II fusion power core is submerged in a pool of water (1 atm) to achieve a high level of safety assurance.

11–2) Turbine-building dimensions were scaled from those of the MARS reactor design (B. G. Logan *et al.*, Lawrence Livermore National Laboratory report, UCRL-53480, 1984).

11–3) Not calculated.

12–1) Assuming 30 full-power-year operation with 76% availability.

12–2) Including first wall, blanket, shield, and magnets.

12–3) The divertor target plates, if they have to be disposed of separately.

B.2. SYSTEMS CODE PARAMETERS OF TITAN-II

```
1     TITAN Reversed-Field Pinch Reactor calculations  .  (ver. 9.q)
 1 1 0 0 0 0 1 1 0                                        01/12/88

                    plasma parameters

plasma aspect ratio, A                                          6.500
plasma minor radius (m)                                         0.600
plasma toroidal major radius (m)                                3.900
plasma volume (m^3)                                            27.714
plasma/first-wall radius ratio, x                               0.909
plasma current (MA)                                            17.797
toroidal current density (MA/m^2)                              15.736
plasma ion temperature (keV)                                   10.000
plasma electron temperature (keV)                               9.500
plasma fus. prod. temperature (keV)                            65.000
plasma impurity temperature (keV)                              10.000
Lawson parameter * t2 (1.0e22 s keV^2/m^3)                      1.917
Lawson parameter (1.0e20 s/m^3)                                 1.917
plasma (total) ion density (1.0e20/m^3)                         8.912
plasma electron density (1.0e20/m^3)                            9.309
ion (D,T,He3,He4,Xe) density fractions:
                  0.48484   0.48484   0.00000   0.03000   0.00033
effective plasma charge, Zeff                                   1.690
energy confinement time (s)                                     0.215
alpha ion particle confinement time (steady state) (s)          0.857
thermal diffusivity (m^2/s)                                     0.314
dt fusion power density (MW/m^3)                               82.623
fusion power, Pf (MW)                                        2289.807
alpha power (MW)                                              458.482
bremsstrahlung power (MW)                                     131.824
poloidal beta (incl. fus. prods. and imps., Zeff>1.0)           0.220
poloidal beta (only fuel ions and electrons, Zeff=1.0)          0.200
pinch parameter, theta                                          1.556
reversal parameter, |F|                                         0.100
streaming parameter (1.0e-14 A m)                               1.766
streaming function (1.0e-3)                                     1.858
plasma ohmic dissipation during burn (MW)                      28.462
plasma loop voltage (V)                                         1.599
gdt, gohm, gbr =    1.403   2.924   1.172
OFCD   plasma Poynting   power (tor/pol) (MW)   3947.656     246.545
OFCD       FW dissipated power (tor/pol) (MW)      0.000       0.011
OFCD  blanket dissipated power (tor/pol) (MW)      0.011       0.191
OFCD     coil dissipated power (OHC/TFC/PEFC/SEFC) (MW)
                    0.171    18.804     0.000     2.482
OFCD    total dissipated power (tor/pol) (MW)     18.815       2.855
OFCD terminal real(lcst) power (OHC/TFC/PEFC/SEFC) (MW)
                    1.147    32.930     0.000     3.450
OFCD power-supply dissipated power, pcdps (MW)                  9.929
OFCD total dissipated power, pcdd (MW)                         46.436
OFCD terminal reactive   power (OHC/TFC/PEFC/SEFC) (MW)
                  101.674   744.569     0.000   146.706
OFCD total reactive   power, pcdr (MW)                        992.949
OFCD power-supply q-value, Q(PS)                              100.000
OFCD circuit q-value, Q(C)                                     21.383
OFCD q-value, Q(CD)                                             1.632
OFCD efficiency figure of merit (A/W)                           0.383
```

1 poloidal field quantities

OH-coil thickness (m)		0.373
average minor radius of coil (m)		1.365
OH coil center offset		0.439
vertical field (T)		1.560
magnetic field level at the coil (T)		2.608
magnetic field level at the plasma surface (T)		5.932
OH coil back-bias power ratio, fgridp=(IOH+/IOH-)^2		1.000
OH coil factor for resistive flux dissipated in startup		0.109
OH coil factor		0.391
OH-coil current swing (MA)		42.685
OH- coil current (MA)		21.342
OH- coil current density (MA/m^2)		9.233
coil stress (MPa)		73.850
OH+ coil current (MA)		21.342
OH+ coil current density (MA/m^2)		9.233
OH coil power supply requirement (MVA)		387.482
mass of OH coil set (tonne)		413.473
ohmic dissipation during back-bias (MW)		107.153
volumetric heating during back-bias (MW/m^3)		1.892
EF coil current (MA)		18.621
EF coil current density (MA/m^2)		20.554
EF coil power supply requirement (MVA)		312.278
mass of EF coil set (tonne)		246.668
magnetic energy stored in coil (MJ)		4138.053
ohmic dissipation during burn (MW)		0.000
volumetric heating during burn (MW/m^3)		0.000
plasma startup risetime (s)		8.000

Ref,zef,delef (m) = 5.9363e+00 2.3622e+00 6.7303e-01

0 toroidal field quantities

TF-coil thickness (m)		0.046
average minor radius of coil (m)		1.105
mass of coil (tonne)		40.832
initial toroidal bias field (T)		3.406
reversed-toroidal field during the burn (T)		0.381
magnetic energy stored in the coil (MJ)		434.327
TF-coil current (MA)		7.436
TF coil current density (MA/m^2)		9.233
ohmic dissipation during burn (MW)		13.625
volumetric heating during burn (MW/m^3)		2.436

0 impurity control

first-wall surface area (m^3)		101.617
total divertor plate surface area (m^2)	N= 3	6.965
first-wall/divertor surface heat flux (MW/m^2)	4.552	3.495
radiation fraction, frad		0.950
scrape-off thickness (m)		0.060
DF-coil current (MA)		0.596
DF coil current density (MA/m^2)		35.700
mass of coil (tonne)		1.960
ohmic dissipation during burn (MW)		11.979

1 engineering summary

thermal conversion efficiency	0.350
auxiliary site power fraction of Pg, faux	0.060
primary loop pumping power fraction of Pg, fpmp	0.010
engineering q-value, QE	7.198
recirculating power fraction, eps=1/QE	0.139
net plant efficiency	0.301
ohmic q-value, Qt	41.453
plasma q-value, Qp	80.452
total thermal power, Pth (MW)	2986.301
fusion power, Pf (MW)	2289.807
tritium burnup (kg/day)	0.352
fractional burnup	0.057
tritium thru-put (no recycle) (kg/day)	6.192
blanket LM 6Li enrichment	0.300
14.06-MeV neutron load, Iw (MW/m^2)	18.022
14.06-MeV neutron energy multiplication in blanket, M	1.360
2.45-MeV neutron load (MW/m^2)	0.000
2.45-MeV neutron energy multiplication in blanket, M	0.000
first-wall radius (m)	0.660
FW/SW/blanket/gap/reflector/gap/shield thickness (m)	0.412
shield/coil gap thickness (m)	0.010
TF-coil thickness (m)	0.046
TF-coil/OH-coil gap thickness (m)	0.050
OH-coil thickness (m)	0.373
minor radius of system (m)	1.552
blanket volume (m^3)	19.744
reflector volume (m^3)	14.203
shield volume (m^3)	13.067
EF-coil shield volume (m^3)	47.726
TF-coil volume (m^3)	5.593
OH-coil volume (m^3)	56.640
EF-coil volume (m^3)	33.790
DF-coil volume (m^3)	0.269
mass of FW/SW/blanket (tonne)	21.265
mass of reflector (tonne)	14.750
mass of OHC shield (tonne)	91.140
mass of EFC shield (tonne)	286.356
mass of TF coil set (tonne)	40.832
mass of OH coil set (tonne)	413.473
mass of EF coil set (tonne)	246.668
mass of DF coil set (tonne)	1.960
total coil-set mass (tonne)	702.934
FPC (FW/SW/B/R/S/C) mass (tonne)	1116.855
mass power density, MPD (kWe/tonne)	805.835
system power density (MWt/m^3)	16.114
mass utilization (tonne/MWt)	0.374
mass of FPC structure (tonne)	466.208
blanket power density (MW/m^3)	54.280
magnetic energy recovery time (s)	1.531

B.3. COST SUMMARY OF TITAN-II REACTOR

Fusion reactor economic evaluation (ver. 4.3)

* 01/11/88

acc. no.	account title	million dollars (1986)	
20. 1.	land & privilege acquisition	4.500	
20. 2.	relocation of buildings, utilities, highways, etc.	0.500	
20.	land & land rights		5.000
21. 1. 1.	general yard improvements		
21. 1. 2.	waterfront improvements		
21. 1. 3.	transportation access (off site)		
21. 1.	site improvements & facilities	15.200	
21. 2. 1.	basic building structures	69.881	
21. 2. 2.	building services	2.696	
21. 2. 3.	containment structures	40.446	
21. 2. 4.	architectural	10.111	
21. 2.	reactor building	122.255	
21. 3. 1.	basic building structures	40.446	
21. 3. 2.	building services	2.696	
21. 3. 3.	architectural	2.022	
21. 3.	turbine building	45.165	
21. 4. 1.	intake structures		
21. 4. 2.	discharge structures		
21. 4. 3.	unpressurized intake & discharge conduits		
21. 4. 4.	recirculating structures		
21. 4. 5.	cooling tower systems		
21. 4.	cooling system structures	9.747	
21. 5. 1.	basic building structures	10.826	
21. 5. 2.	building services	0.715	
21. 5. 3.	architectural	0.809	
21. 5.	power supply & energy storage building	12.350	
21. 6. 1.	reactor auxiliaries building(incl. switchgear bay)	4.399	
21. 6. 2.	hot cell building	72.749	
21. 6. 3.	fuel storage building	11.535	
21. 6. 4.	control room building	6.179	
21. 6. 5.	diesel generator building	2.764	
21. 6. 6.	administration building	1.173	
21. 6. 7.	service building	2.535	
21. 6. 8.	cryogenics building	1.227	
21. 6. 9.	miscellaneous structures & building work	2.481	
21. 6.	miscellaneous buildings	103.137	
21. 7.	ventilation stack	2.440	
21.88.	spare parts allowance		
21.99.	contingency allowance		
21.	structures & site facilities		310.301

22. 1. 1. 1.	breeding material(incl. tritium breeding)	0.895	
22. 1. 1. 2.	first wall & structural material	1.063	
22. 1. 1. 3.	attenuators, reflectors, & multipliers	8.684	
22. 1. 1. 4.	wall modifiers(coatings, liners, limiters, etc.)		
22. 1. 1. 5.	reflector	3.689	
22. 1. 1. 6.	other		
22. 1. 1.	FW/BW/blanket/reflector		14.332
22. 1. 2. 1.	primary	22.793	
22. 1. 2. 2.	secondary	6.051	
22. 1. 2.	shield		28.844
22. 1. 3. 1.	toroidal field coils	3.578	
22. 1. 3. 2.	ohmic-heating coils	36.236	
22. 1. 3. 3.	equilibrium field coils	43.238	
22. 1. 3. 4.	diverter field coils	0.172	
22. 1. 3. 5.	other coils		
22. 1. 3.	magnets		83.224
22. 1. 4. 1.	beam heating(neutral, ion or electron)		
22. 1. 4. 2.	rf heating	0.000	
22. 1. 4. 3.	laser heating		
22. 1. 4. 4.	other heating systems		
22. 1. 4.	supplemental heating system		
22. 1. 5. 1.	reactor structure		
22. 1. 5. 2.	equipment support structure		
22. 1. 5.	primary structure & support		11.785
22. 1. 6. 1.	plasma chamber vacuum(incl. pumps/comp./pipe)		
22. 1. 6. 2.	magnet dewar vacuum(incl. pumps/comp./pipe)		
22. 1. 6. 3.	suppl. heating vacuum(incl. pumps/comp./pipe)		
22. 1. 6. 4.	direct converter vacuum(incl. pumps/comp./pipe)		
22. 1. 6. 5.	reactor vacuum system(low grade)		
22. 1. 6. 6.	reactor vacuum wall	10.189	
22. 1. 6.	reactor vacuum systems(unless integral elsewhere)		10.189
22. 1. 7. 1.	EF-coil power supplies	9.958	
22. 1. 7. 2.	OH-coil power supplies	9.691	
22. 1. 7. 3.	TF-coil power supplies	0.682	
22. 1. 7. 4.	DF-coil power supplies	0.599	
22. 1. 7. 5.	other power supplies	1.348	
22. 1. 7. 6.	current drive power supplies	49.650	
22. 1. 7. 7.	control system		
22. 1. 7. 8.	central energy storage		
22. 1. 7. 9.	other incl. busbars		
22. 1. 7.	power supply, switching & energy storage		71.927
22. 1. 8.	impurity control		6.198
22. 1. 9. 1.	vacuum tank		
22. 1. 9. 2.	direct converter modules		
22. 1. 9. 3.	thermal panels		
22. 1. 9. 4.	power conditioning equipment		
22. 1. 9.	direct energy conversion system		
22. 1.10.	ccrh breakdown system		2.142
22. 1.	reactor equipment		228.641

22. 2. 1. 1.	pumps & motor drives(modular & nonmodular)	
22. 2. 1. 2.	piping	
22. 2. 1. 3.	heat exchangers	
22. 2. 1. 4.	tanks(dump,make-up,clean-up,trit.,hot storage)	
22. 2. 1. 5.	clean-up system	
22. 2. 1. 6.	thermal insulation, piping & equipment	
22. 2. 1. 7.	tritium extraction	
22. 2. 1. 8.	pressurizer	
22. 2. 1. 9.	other	
22. 2. 1.	primary coolant system	83.655
22. 2. 2. 1.	pumps & motor drives(modular & nonmodular)	
22. 2. 2. 2.	piping	
22. 2. 2. 3.	heat exchangers	
22. 2. 2. 4.	tanks(dump,make-up,clean-up,trit.,hot storage)	
22. 2. 2. 5.	clean-up system	
22. 2. 2. 6.	thermal insulation, piping & equipment	
22. 2. 2. 7.	tritium extraction	
22. 2. 2. 8.	pressurizer	
22. 2. 2. 9.	other	
22. 2. 2.	intermediate coolant system	
22. 2. 3. 1.	pumps & motor drives(modular & nonmodular)	
22. 2. 3. 2.	piping	
22. 2. 3. 3.	heat exchangers	
22. 2. 3. 4.	tanks(dump,make-up,clean-up,trit.,hot storage)	
22. 2. 3. 5.	clean-up system	
22. 2. 3. 6.	thermal insulation, piping & equipment	
22. 2. 3. 7.	tritium extraction	
22. 2. 3. 8.	pressurizer	
22. 2. 3. 9.	other	
22. 2. 3.	secondary coolant system	0.000
22. 2.	main heat transfer & transport systems	83.655
22. 3. 1. 1.	refrigeration	
22. 3. 1. 2.	piping	
22. 3. 1. 3.	fluid circulation driving system	
22. 3. 1. 4.	tanks	
22. 3. 1. 5.	purification	
22. 3. 1.	magnet cooling system	
22. 3. 2. 1.	refrigeration	
22. 3. 2. 2.	piping	
22. 3. 2. 3.	fluid circulation driving system	
22. 3. 1. 4.	tanks	
22. 3. 2. 5.	purification	
22. 3. 2.	shield & structure cooling system	2.697
22. 3. 3. 1.	refrigeration	
22. 3. 3. 2.	piping	
22. 3. 3. 3.	fluid circulation driving system	
22. 3. 3. 4.	tanks	
22. 3. 3. 5.	purification	
22. 3. 3.	supplemental heating system cooling system	
22. 3. 4. 1.	refrigeration	
22. 3. 4. 2.	piping	
22. 3. 4. 3.	fluid circulation driving system	
22. 3. 4. 4.	tanks	
22. 3. 4. 5.	purification	
22. 3. 4.	power supply cooling system	
22. 3. 5.	other cooling systems (ECCS)	100.009
22. 3.	auxiliary cooling systems	102.707

22. 4. 1.	liquid waste processing & equipment		
22. 4. 2.	gaseous wastes & off-gas processing system		
22. 4. 3.	solid waste processing equipment		
22. 4.	radioactive waste treatment & disposal		4.831
22. 5. 1.	fuel injection systems	10.001	
22. 5. 2.	fuel processing systems	13.656	
22. 5. 3.	fuel storage	5.808	
22. 5. 4.	atmospheric tritium recovery	2.119	
22. 5. 5.	water tritium recovery systems	139.549	
22. 5. 6.	blanket tritium recovery systems		
22. 5. 7.	other		
22. 5.	fuel handling & storage systems		170.326
22. 6. 1. 1.	blanket & coil maintenance equipment		
22. 6. 1. 2.	components rotated into service to allow maint.		
22. 6. 1. 3.	other maintenance equipment		
22. 6. 1.	maintenance equipment		
22. 6. 2.	special heating systems(start-up,trace, etc.)		
22. 6. 3.	coolant receiving, storage & make-up systems		
22. 6. 4.	gas systems		
22. 6. 5.	building vacuum systems		
22. 6.	other reactor plant equipment		44.041
22. 7. 1.	reactor isc equip.(burn control, diagnostics, etc.		
22. 7. 2.	radiation monitoring systems		
22. 7. 3.	isolated indicating & recording gauges, etc.		
22. 7.	instrumentation & control(isc)		31.561
22.98.	spare parts allowance		
22.99.	contingency allowance		
22.	reactor plant equipment		461.762

23. 1. 1.	turbine-generators & accessories		
23. 1. 2.	foundations		
23. 1. 3.	standby exciters		
23. 1. 4.	lubricating system		
23. 1. 5.	gas systems		
23. 1. 6.	rehosters		
23. 1. 7.	shielding		
23. 1. 8.	weather-proof housing		
23. 1.	turbine-generators	83.263	
23. 2.	main steam (or other fluid) system	6.755	
23. 3. 1.	water intake common facilities		
23. 3. 2.	circulating water systems		
23. 3. 3.	cooling towers		
23. 3. 4.	other systems which reject heat to the atmosphere		
23. 3.	heat rejection systems	36.377	
23. 4. 1.	condensers		
23. 4. 2.	condensate system		
23. 4. 3.	gas removal system		
23. 4. 4.	turbine by-pass systems(excl. piping)		
23. 4.	condensing systems	19.356	
23. 5. 1.	regenerators & recuperators		
23. 5. 2.	pumps		
23. 5. 3.	tanks		
23. 5.	feed heating system	10.628	
23. 6. 1.	turbine auxiliaries		
23. 6. 2.	auxiliaries cooling system(excl. piping)		
23. 6. 3.	make-up treat. system(excl. piping)		
23. 6. 4.	chemical treat. & condensate purification systems		
23. 6. 5.	central lubrication service system(excl. piping)		
23. 6.	other turbine plant equipment	56.630	
23. 7.	instrumentation & control(i&c) equipment	10.656	
23.98.	spare parts allowance		
23.99.	contingency allowance		
23.	turbine plant equipment		223.656

24. 1. 1.	generator circuits		
24. 1. 2.	station service		
24. 1.	switchgear	12.116	
24. 2. 1.	station service & startup transformers		
24. 2. 2.	low voltage unit substation & lighting transformer		
24. 2. 3.	battery system		
24. 2. 4.	diesel engine generators		
24. 2. 5.	gas turbine generators		
24. 2. 6.	motor generator sets		
24. 2.	station service equipment	20.006	
24. 3. 1.	main control board for electric system		
24. 3. 2.	auxiliary power & signal boards		
24. 3.	switchboards (incl. heat tracing)	7.608	
24. 4. 1.	gen. station grounding sys. & cathodic protection		
24. 4.	protective equipment	1.845	
24. 5. 1.	concrete cable tunnels, trenches & envelopes		
24. 5. 2.	cable trays & support		
24. 5. 3.	conduit		
24. 5. 4.	other structures		
24. 5.	electrical structures & wiring containers	21.160	
24. 6. 1.	generator circuits wiring		
24. 6. 2.	station service power wiring		
24. 6. 3.	control wiring		
24. 6. 4.	instrument wiring		
24. 6. 5.	containment penetrations		
24. 6.	power & control wiring	43.736	
24. 7. 1.	reactor building lighting		
24. 7. 2.	turbine building lighting		
24. 7. 3.	reactor auxiliaries building lighting		
24. 7. 4.	radioactive waste building lighting		
24. 7. 5.	fuel storage building lighting		
24. 7. 6.	miscellaneous buildings lighting		
24. 7. 7.	yard lighting		
24. 7.	electrical lighting	11.055	
24.98.	spare parts allowance		
24.99.	contingency allowance		
24.	electric plant equipment		118.505

25. 1. 1.	cranes, hoists, monorails, & conveyors		
25. 1. 2.	railway		
25. 1. 3.	roadway equipment		
25. 1. 4.	watercraft		
25. 1. 5.	vehicle maintenance equipment		
25. 1.	transportation & lifting equipment	21.140	
25. 2. 1.	air systems(excl. piping)		
25. 2. 2.	water systems(excl. piping)		
25. 2. 3.	auxiliary heating boilers(excl. piping)		
25. 2.	air & water service systems	16.650	
25. 3. 1.	local communications systems		
25. 3. 2.	signal systems		
25. 3.	communications equipment	8.386	
25. 4. 1.	safety equipment		
25. 4. 2.	shop, laboratory, & test equipment		
25. 4. 3.	office equipment & furnishings		
25. 4. 4.	change room equipment		
25. 4. 5.	environmental monitoring equipment		
25. 4. 6.	dining facilities		
25. 4.	furnishings & fixtures	1.618	
25.98.	spare parts allowance		
25.99.	contingency allowance		
25.	miscellaneous plant equipment		47.794
26. 1.	reactor coolant	16.901	
26. 2.	intermediate coolant		
26. 3.	turbine cycle working fluids		
26. 4.	other materials	0.337	
26. 5.	Ar reactor-building cover gas		
26.98.	spare parts allowance		
26.99.	contingency allowance		
26.	special materials		17.239

Los Alamos fusion reactor economic evaluation (ver. 4.5)

• 01/12/88

acc. no.	account title	million dollars (1986)	
20.	land & land rights	5.000	
21.	structures & site facilities	318.301	
22.	reactor plant equipment	665.762	
22. 1. 1.	FW/BW/blanket/reflector	14.332	
22. 1. 2.	shield	28.644	
22. 1. 3.	magnets	83.224	
22. 1. 4.	supplemental heating systems	0.000	
22. 1. 5.	primary structure & support	11.785	
22. 1. 6.	reactor vacuum systems(unless integral elsewhere)	10.189	
22. 1. 7.	power supply, switching & energy storage	71.927	
22. 1. 8.	impurity control	6.198	
22. 1. 9.	direct energy conversion system	0.000	
22. 1.10.	scrh breakdown system	2.142	
22. 1.	reactor equipment	228.641	
23.	turbine plant equipment	223.656	
24.	electric plant equipment	118.505	
25.	miscellaneous plant equipment	47.794	
26.	special materials	17.239	
90.	direct cost (not incl. spares and contingency)		1388.250
91.	construction services & equipment		138.826
92.	home office engineering & services		138.826
93.	field office engineering & services		138.826
94.	owner's cost		69.413
96.	project contingency		138.826
97.	interest during construction (IDC)		226.250
99.	total cost		2239.232

					constant	then-current
thermal power (MWth)	= 2986.30	unit direct cost ($/kWe)	[90]=	1542.51	1542.51
gross electric power (MWe)	= 1045.21	unit base cost ($/kWe)	[94]=	2236.64	2236.64
net electric power (MWe)	= 900.00	unit total cost ($/kWe)	[99]=	2488.11	3409.59
1/recirculating power fraction QE=	7.198	capital return (mill/kWeh)	=	29.94	69.75
plant availability factor	= 0.759	O&M(2.00%) (mill/kWeh) [40-47,51]=		6.73	9.54
construction= 6 yr: constant then-current		M/R/R replace. (mill/kWeh)	[50]=	1.25	1.78
FCR= 0.0800 0.1360		decomissioning allowance	=	0.00	0.00
fIDC= 0.1124 0.2444		deuterium fuel (mill/kWeh)	[02]=	0.05	0.05
fIDC= 0.0000 0.2000		COE (mill/kWeh)	=	37.96	81.12

B.4. COST DATA BASE FOR TITAN-II REACTOR

cost data base (ver. 4.3)

date:01/12/88

acc. no.	account title UC(1986) = 1.348 x UC(1980)	unit cost(1980)	no. of units	refs.
20. 1. 0. 0	land & privilege acquisition	3.338e+03 $/acre	1.000e+01	18
20. 2. 0. 0	relocation of buildings, utilities, highways, etc.	3.710e+02 $/acre	1.000e+01	18
20. 0. 0. 0	land & land rights	0.	1.000e+00	
21. 1. 1. 0	general yard improvements	0.	1.000e+00	
21. 1. 2. 0	waterfront improvements	0.	1.000e+00	
21. 1. 3. 0	transportation access (off site)	0.	1.000e+00	
21. 1. 0. 0	site improvements & facilities	1.128e+07 $	1.000e+00	18
21. 2. 1. 0	basic building structures	3.000e+02 $/m^3	1.766e+05	13,18
21. 2. 2. 0	building services	2.000e+06 $	1.000e+00	13,14,+
21. 2. 3. 0	containment structures	3.000e+07 $	1.000e+00	13,14,+
21. 2. 4. 0	architectural	7.500e+06 $	1.000e+00	13,14,+
21. 2. 0. 0	reactor building	0.	1.000e+00	
21. 3. 1. 0	basic building structures	3.000e+07 $	1.000e+00	13,14,16
21. 3. 2. 0	building services	2.000e+06 $	1.000e+00	13,14,+
21. 3. 3. 0	architectural	1.500e+06 $	1.000e+00	13
21. 3. 0. 0	turbine building	0.	1.000e+00	
21. 4. 1. 0	intake structures	0.	1.000e+00	
21. 4. 2. 0	discharge structures	0.	1.000e+00	
21. 4. 3. 0	unpressurized intake & discharge conduits	0.	1.000e+00	
21. 4. 4. 0	recirculating structures	0.	1.000e+00	
21. 4. 5. 0	cooling tower systems	0.	1.000e+00	
21. 4. 0. 0	cooling system structures	6.981e+05 $/unit	8.849e+00	2,13,14
21. 5. 1. 0	basic building structures	8.038e+06 $	1.000e+00	13,14
21. 5. 2. 0	building services	5.368e+05 $	1.000e+00	13,14
21. 5. 3. 0	architectural	6.000e+05 $	1.000e+00	13
21. 5. 0. 0	power supply & energy storage building	0.	1.000e+00	
21. 6. 1. 0	reactor auxiliaries building(incl. switchgear bay)	3.260e+06 $	1.000e+00	13,14
21. 6. 2. 0	hot cell building	5.396e+07 $	1.000e+00	13,14
21. 6. 3. 0	fuel storage building	8.638e+06 $	1.000e+00	13,14
21. 6. 4. 0	control room building	1.100e+06 $	1.000e+00	13,14
21. 6. 5. 0	diesel generator building	2.050e+06 $	1.000e+00	13,14
21. 6. 6. 0	administration building	8.700e+05 $	1.000e+00	13,14
21. 6. 7. 0	service building	1.880e+06 $	1.000e+00	13,14
21. 6. 8. 0	cryogenics building	9.100e+05 $	1.000e+00	13,14
21. 6. 9. 0	miscellaneous structures & building work	1.810e+06 $	1.000e+00	13,14
21. 6. 0. 0	miscellaneous buildings	0.	1.000e+00	
21. 7. 9. 0	ventilation stack	1.815e+06 $	1.000e+00	13,14
21.98. 0. 0	spare parts allowance	0. fraction	-1.000e+00	2,13,14
21.99. 0. 0	contingency allowance	0. fraction	-1.000e+00	2,13,14
21. 0. 0. 0	structures & site facilities	0.	1.000e+00	

22. 1. 1. 1	breeding material(incl. tritium breeding)	2.927e+02	$/kg	2.267e+01	15,18
22. 1. 1. 2	first wall & structural material	1.709e+01	$/kg	2.126e+04	18
22. 1. 1. 3	attenuators, reflectors, & multipliers	3.338e+02	$/kg	1.93[illegible]e+04	18
22. 1. 1. 4	wall modifiers(coatings, liners, limiters, etc.)	0.		1.000e+00	
22. 1. 1. 5	reflector	1.855e+02	$/kg	1.475e+04	6
22. 1. 1. 6	other	0.		1.000e+00	
22. 1. 1. 0	FW/SW/blanket/reflector	0.		1.000e+00	
22. 1. 2. 1	primary	1.855e+02	$/kg	9.114e+04	18
22. 1. 2. 2	secondary	1.567e+01	$/kg	2.864e+05	18
22. 1. 2. 0	shield	0.		1.000e+00	
22. 1. 3. 1	toroidal field coils	6.507e+01	$/kg	4.083e+04	18
22. 1. 3. 2	ohmic-heating coils	6.500e+01	$/kg	4.135e+03	18
22. 1. 3. 3	equilibrium field coils	1.300e+02	$/kg	2.467e+05	18
22. 1. 3. 4	divertor field coils	6.500e+01	$/kg	1.968e+03	18
22. 1. 3. 5	other coils	0.		1.000e+00	
22. 1. 3. 0	magnets	0.		1.000e+00	
22. 1. 4. 1	beam heating(neutral, ion or electron)	0.		1.000e+00	
22. 1. 4. 2	rf heating	1.654e+09	$/W	0.	16,17
22. 1. 4. 3	laser heatin	0.		1.000e+00	
22. 1. 4. 4	other heating systems	0.		1.000e+00	
22. 1. 4. 0	supplemental heating systems	0.		1.000e+00	
22. 1. 5. 1	reactor structure	0.		1.000e+00	
22. 1. 5. 2	equipment support structure	0.		1.000e+00	
22. 1. 5. 0	primary structure & support	1.125e+05	$/m^3	7.770e+01	13,14
22. 1. 6. 1	plasma chamber vacuum(incl. pumps/comp./pipe)	0.		1.000e+00	
22. 1. 6. 2	magnet dewar vacuum(incl. pumps/comp./pipe)	0.		1.000e+00	
22. 1. 6. 3	suppl. heating vacuum(incl. pumps/comp./pipe)	0.		1.000e+00	
22. 1. 6. 4	direct converter vacuum(incl. pumps/comp./pipe)	0.		1.000e+00	
22. 1. 6. 5	reactor vacuum system(low grade)	0.		1.000e+00	
22. 1. 6. 6	reactor vacuum wall	2.500e+06	$/unit	1.823e+00	9
22. 1. 6. 0	reactor vacuum systems(unless integral elsewhere)	0.		1.000e+00	
22. 1. 7. 1	EF-coil power supplies	2.365e+01	$/kVA	3.123e+05	18
22. 1. 7. 2	OH-coil power supplies	1.855e+01	$/kVA	3.675e+05	18
22. 1. 7. 3	TF-coil power supplies	3.709e+01	$/kVA	1.361e+04	18
22. 1. 7. 4	DF-coil power supplies	3.709e+01	$/kVA	1.191e+04	18
22. 1. 7. 5	other power supplies	1.000e+06		1.000e+00	
22. 1. 7. 6	current drive power supplies	3.709e+01	$/kVAr	9.929e+05	18
22. 1. 7. 7	control system	0.		1.000e+00	
22. 1. 7. 8	control energy storage	0.		1.000e+00	
22. 1. 7. 9	other incl. busbars	0.	$	1.000e+00	
22. 1. 7. 0	power supply, switching & energy storage	0.		1.000e+00	
22. 1. 8. 0	impurity control	6.680e+05	$/m^2	6.965e+00	18
22. 1. 9. 1	vacuum tank	0.		1.000e+00	
22. 1. 9. 2	direct converter modules	0.		1.000e+00	
22. 1. 9. 3	thermal panels	0.		1.000e+00	
22. 1. 9. 4	power conditioning equipment	0.		1.000e+00	
22. 1. 9. 0	direct energy conversion system	0.		1.000e+00	
22. 1.10. 0	ecrh breakdown system	1.589e+06	$	1.000e+00	13
22. 1. 0. 0	reactor equipment	0.		1.000e+00	

22. 2. 1. 1	pumps & motor drives(modular & nonmodular)	0.		1.000e+00		
22. 2. 1. 2	piping	0.		1.000e+00		
22. 2. 1. 3	heat exchangers	0.		1.000e+00		
22. 2. 1. 4	tanks(dump,make-up,clean-up,trit.,hot storage)	0.		1.000e+00		
22. 2. 1. 5	clean-up system	0.		1.000e+00		
22. 2. 1. 6	thermal insulation, piping & equipment	0.		1.000e+00		
22. 2. 1. 7	tritium extraction	0.		1.000e+00		
22. 2. 1. 8	pressurizer	0.		1.000e+00		
22. 2. 1. 9	other	0.		1.000e+00		
22. 2. 1. 0	primary coolant system	2.078e+04	$/MWth	2.886e+01	10	
22. 2. 2. 1	pumps & motor drives(modular & nonmodular)	0.		1.000e+00		
22. 2. 2. 2	piping	0.		1.000e+00		
22. 2. 2. 3	heat exchangers	0.		1.000e+00		
22. 2. 2. 4	tanks(dump,make-up,clean-up,trit.,hot storage)	0.		1.000e+00		
22. 2. 2. 5	clean-up system	0.		1.000e+00		
22. 2. 2. 6	thermal insulation, piping & equipment	0.		1.000e+00		
22. 2. 2. 7	tritium extraction	0.		1.000e+00		
22. 2. 2. 8	pressurizer	0.		1.000e+00		
22. 2. 2. 9	other	0.		1.000e+00		
22. 2. 2. 0	intermediate coolant system	0.		1.000e+00		
22. 2. 3. 1	pumps & motor drives(modular & nonmodular)	0.		1.000e+00		
22. 2. 3. 2	piping	0.		1.000e+00		
22. 2. 3. 3	heat exchangers	0.		1.000e+00		
22. 2. 3. 4	tanks(dump,make-up,clean-up,trit.,hot storage)	0.		1.000e+00		
22. 2. 3. 5	clean-up system	0.		1.000e+00		
22. 2. 3. 6	thermal insulation, piping & equipment	0.		1.000e+00		
22. 2. 3. 7	tritium extraction	0.		1.000e+00		
22. 2. 3. 8	pressurizer	0.		1.000e+00		
22. 2. 3. 9	other	0.		1.000e+00		
22. 2. 3. 0	secondary coolant system	5.220e+05	$/MWth	2.905e-04	10	
22. 2. 0. 0	main heat transfer & transport systems	0.		1.000e+00		
22. 3. 1. 1	refrigeration	7.566e+01	$/unit	3.303e-03	23	
22. 3. 1. 2	piping	0.		1.000e+00		
22. 3. 1. 3	fluid circulation driving system	0.		1.000e+00		
22. 3. 1. 4	tanks	0.		1.000e+00		
22. 3. 1. 5	purification	0.		1.000e+00		
22. 3. 1. 0	magnet cooling system	0.		1.000e+00		
22. 3. 2. 1	refrigeration	0.		1.000e+00		
22. 3. 2. 2	piping	0.		1.000e+00		
22. 3. 2. 3	fluid circulation driving system	0.		1.000e+00		
22. 3. 2. 4	tanks	0.		1.000e+00		
22. 3. 2. 5	purification	0.		1.000e+00		
22. 3. 2. 0	shield & structure cooling system	6.700e+02	$/MWth	2.926e+03	13	
22. 3. 3. 1	refrigeration	0.		1.000e+00		
22. 3. 3. 2	piping	0.		1.000e+00		
22. 3. 3. 3	fluid circulation driving system	0.		1.000e+00		
22. 3. 3. 4	tanks	0.		1.000e+00		
22. 3. 3. 5	purification	0.		1.000e+00		
22. 3. 3. 0	supplemental heating system cooling system	0.		1.000e+00		
22. 3. 4. 1	refrigeration	0.		1.000e+00		
22. 3. 4. 2	piping	0.		1.000e+00		
22. 3. 4. 3	fluid circulation driving system	0.		1.000e+00		
22. 3. 4. 4	tanks	0.		1.000e+00		
22. 3. 4. 5	purification	0.		1.000e+00		
22. 3. 4. 0	power supply cooling system	0.		1.000e+00		
22. 3. 5. 0	other cooling systems (ECCS)	7.418e+07	$	1.000e+00		
22. 3. 0. 0	auxiliary cooling systems	0.		1.000e+00		

22. 4. 1. 0	liquid waste processing & equipment	0.		1.000e+00	
22. 4. 2. 0	gaseous wastes & off-gas processing system	0.		1.000e+00	
22. 4. 3. 0	solid waste processing equipment	0.		1.000e+00	
22. 4. 0. 0	radioactive waste treatment & disposal	1.200e+03	$/MWth	2.986e+03	13,14
22. 5. 1. 0	fuel injection systems	3.709e+06	$	2.000e+00	10
22. 5. 2. 0	fuel processing systems	3.709e+04	$/unit	2.731e+02	10
22. 5. 3. 0	fuel storage	3.709e+06	$	1.000e+00	10
22. 5. 4. 0	atmospheric tritium recovery	1.486e+04	$/m^3/hr	1.059e+02	10
22. 5. 5. 0	water tritium recovery systems	4.570e-02	$/W	2.200e+09	
22. 5. 6. 0	blanket tritium recovery systems	0.		1.000e+00	
22. 5. 7. 0	other	0.		1.000e+00	
22. 5. 0. 0	fuel handling & storage systems	0.		1.000e+00	
22. 6. 1. 1	blanket & coil maintenance equipment	0.		1.000e+00	
22. 6. 1. 2	components rotated into service to allow maint.	0.		1.000e+00	
22. 6. 1. 3	other maintenance equipment	0.		1.000e+00	
22. 6. 1. 0	maintenance equipment	0.		1.000e+00	
22. 6. 2. 0	special heating systems(start-up,trace, etc.)	0.		1.000e+00	
22. 6. 3. 0	coolant receiving, storage & make-up systems	0.		1.000e+00	
22. 6. 4. 0	gas systems	0.		1.000e+00	
22. 6. 5. 0	building vacuum systems	0.		1.000e+00	
22. 6. 0. 0	other reactor plant equipment	1.094e+04	$/MWth	2.986e+03	13,14
22. 7. 1. 0	reactor i&c equip.(burn control, diagnostics, etc.	0.		1.000e+00	
22. 7. 2. 0	radiation monitoring systems	0.		1.000e+00	
22. 7. 3. 0	isolated indicating & recording gauges, etc.	0.		1.000e+00	
22. 7. 0. 0	instrumentation & control(i&c)	2.341e+07	$	1.000e+00	13,14
22.98. 0. 0	spare parts allowance	0.	fraction	-1.000e+00	2,13,14
22.99. 0. 0	contingency allowance	0.	fraction	-1.000e+00	2,13,14
22. 0. 0. 0	reactor plant equipment	0.		1.000e+00	

23. 1. 1. 0		turbine-generators & accessories	0.			1.000e+00	
23. 1. 2. 0		foundations	0.			1.000e+00	
23. 1. 3. 0		standby exciters	0.			1.000e+00	
23. 1. 4. 0		lubricating system	0.			1.000e+00	
23. 1. 5. 0		gas systems	0.			1.000e+00	
23. 1. 6. 0		reheaters	0.			1.000e+00	
23. 1. 7. 0		shielding	0.			1.000e+00	
23. 1. 8. 0		weather-proof housing	0.			1.000e+00	
23. 1. 0. 0	turbine-generators		4.758e+05	$/unit		1.200e+02	2,13,14
23. 2. 0. 0	main steam (or other fluid) system		1.678e+03	$/MWth		2.966e+03	12
23. 3. 1. 0		water intake common facilities	0.			1.000e+00	
23. 3. 2. 0		circulating water systems	0.			1.000e+00	
23. 3. 3. 0		cooling towers	0.			1.000e+00	
23. 3. 4. 0		other systems which reject heat to the atmosphere	0.			1.000e+00	
23. 3. 0. 0	heat rejection systems		4.319e+04	$/unit		4.270e+02	10
23. 4. 1. 0		condensate	0.			1.000e+00	
23. 4. 2. 0		condensate system	0.			1.000e+00	
23. 4. 3. 0		gas removal system	0.			1.000e+00	
23. 4. 4. 0		turbine by-pass systems(excl. piping)	0.			1.000e+00	
23. 4. 0. 0	condensing systems		2.753e+04	$/unit		5.215e+02	2,13,14
23. 5. 1. 0		regenerators & recuperators	0.			1.000e+00	
23. 5. 2. 0		pumps	0.			1.000e+00	
23. 5. 3. 0		tanks	0.			1.000e+00	
23. 5. 0. 0	feed heating system		2.648e+01	$/unit		1.586e+03	2,13,14
23. 6. 1. 0		turbine auxiliaries	0.			1.000e+00	
23. 6. 2. 0		auxiliarios cooling system(excl. piping)	0.			1.000e+00	
23. 6. 3. 0		make-up treat. system(excl. piping)	0.			1.000e+00	
23. 6. 4. 0		chemical treat. & condensate purification systems	0.			1.000e+00	
23. 6. 5. 0		central lubrication service system(excl. piping)	0.			1.000e+00	
23. 6. 0. 0	other turbine plant equipment		4.462e+05	$/unit		6.479e+01	2,13,14
23. 7. 0. 0	instrumentation & control(incl equipment		2.820e+05	$/unit		9.049e+00	2,13,14
23.98. 0. 0	spare parts allowance		0.		fraction	-1.000e+00	2,13,14
23.99. 0. 0	contingency allowance		0.		fraction	-1.000e+00	2,13,14
23. 0. 0. 0	turbine plant equipment		0.			1.000e+00	

24. 1. 1. 0	generator circuits	0.		1.000e+00		
24. 1. 2. 0	station service	0.		1.000e+00		
24. 1. 0. 0	switchgear	6.600e+01	$/unit	1.045e+03	2,13,14	
24. 2. 1. 0	station service & startup transformers	0.		1.000e+00		
24. 2. 2. 0	low voltage unit substation & lighting transformer	0.		1.000e+00		
24. 2. 3. 0	battery system	0.		1.000e+00		
24. 2. 4. 0	diesel engine generators	0.		1.000e+00		
24. 2. 5. 0	gas turbine generators	0.		1.000e+00		
24. 2. 6. 0	motor generator sets	0.		1.000e+00		
24. 2. 0. 0	station service equipment	1.420e+04	$/unit	1.045e+01	13,16	
24. 3. 1. 0	main control board for electric system	0.		1.000e+00		
24. 3. 2. 0	auxiliary power & signal boards	0.		1.000e+00		
24. 3. 0. 0	switchboards (incl. heat tracing)	5.400e+01	$/unit	1.045e+03	2,13,14	
24. 4. 1. 0	gen. station grounding sys. & cathodic protection	0.		1.000e+00		
24. 4. 0. 0	protective equipment	2.110e+06	$	1.000e+00	13,14	
24. 5. 1. 0	concrete cable tunnels, trenches & envelopes	0.		1.000e+00		
24. 5. 2. 0	cable trays & support	0.		1.000e+00		
24. 5. 3. 0	conduit	0.		1.000e+00		
24. 5. 4. 0	other structures	0.		1.000e+00		
24. 5. 0. 0	electrical structures & wiring containers	1.568e+07	$	1.000e+00	13,14,+	
24. 6. 1. 0	generator circuits wiring	0.		1.000e+00		
24. 6. 2. 0	station service power wiring	0.		1.000e+00		
24. 6. 3. 0	control wiring	0.		1.000e+00		
24. 6. 4. 0	instrument wiring	0.		1.000e+00		
24. 6. 5. 0	containment penetrations	0.		1.000e+00		
24. 6. 0. 0	power & control wiring	3.244e+07	$	1.000e+00	13,14,+	
24. 7. 1. 0	reactor building lighting	0.		1.000e+00		
24. 7. 2. 0	turbine building lighting	0.		1.000e+00		
24. 7. 3. 0	reactor auxiliaries building lighting	0.		1.000e+00		
24. 7. 4. 0	radioactive waste building lighting	0.		1.000e+00		
24. 7. 5. 0	fuel storage building lighting	0.		1.000e+00		
24. 7. 6. 0	miscellaneous buildings lighting	0.		1.000e+00		
24. 7. 7. 0	yard lighting	0.		1.000e+00		
24. 7. 0. 0	electrical lighting	8.200e+06	$	1.000e+00	13,14,+	
24.98. 0. 0	spare parts allowance	0.	fraction	-1.000e+00	2,13,14	
24.99. 0. 0	contingency allowance	0.	fraction	-1.000e+00	2,13,14	
24. 0. 0. 0	electric plant equipment	0.		1.000e+00		

25. 1. 1. 0	cranes, hoists, monorails, & conveyors	0.		1.000e+00		
25. 1. 2. 0	railway	0.		1.000e+00		
25. 1. 3. 0	roadway equipment	0.		1.000e+00		
25. 1. 4. 0	watercraft	0.		1.000e+00		
25. 1. 5. 0	vehicle maintenance equipment	0.		1.000e+00		
25. 1. 0. 0	transportation & lifting equipment	1.568e+07	$	1.000e+00	13,14	
25. 2. 1. 0	air systems(excl. piping)	0.		1.000e+00		
25. 2. 2. 0	water systems(excl. piping)	0.		1.000e+00		
25. 2. 3. 0	auxiliary heating boilers(excl. piping)	0.		1.000e+00		
25. 2. 0. 0	air & water service systems	1.235e+07	$	1.000e+00	13,14	
25. 3. 1. 0	local communications systems	0.		1.000e+00		
25. 3. 2. 0	signal systems	0.		1.000e+00		
25. 3. 0. 0	communications equipment	6.220e+06	$	1.000e+00	13,14	
25. 4. 1. 0	safety equipment	0.		1.000e+00		
25. 4. 2. 0	shop, laboratory, & test equipment	0.		1.000e+00		
25. 4. 3. 0	office equipment & furnishings	0.		1.000e+00		
25. 4. 4. 0	change room equipment	0.		1.000e+00		
25. 4. 5. 0	environmental monitoring equipment	0.		1.000e+00		
25. 4. 6. 0	dining facilities	0.		1.000e+00		
25. 4. 0. 0	furnishings & fixtures	1.280e+06	$	1.000e+00	2	
25.98. 0. 0	spare parts allowance	0.	fraction	-1.000e+00	2,13,14	
25.99. 0. 0	contingency allowance	0.	fraction	-1.000e+00	2,13,14	
25. 0. 0. 0	miscellaneous plant equipment	0.		1.000e+00		
26. 1. 0. 0	reactor coolant	2.927e+02	$/kg	4.203e+04	13,14	
26. 2. 0. 0	intermediate coolant	0.		1.000e+00		
26. 3. 0. 0	turbine cycle working fluids	0.		1.000e+00		
26. 4. 0. 0	other materials	1.500e+05	$	1.000e+00	13,14	
26. 5. 0. 0	Ar reactor-building cover gas	0.		1.000e+00		
26.98. 0. 0	spare parts allowance	0.	fraction	-1.000e+00		
26.99. 0. 0	contingency allowance	0.	fraction	-1.000e+00		
26. 0. 0. 0	special materials	0.		1.000e+00		

90.	0.	0.	0	direct cost (mat incl. spares and contingency)	0.		1.000e+00	
91.	0.	0.	0	construction services & equipment	1.000e-01	fraction	-1.000e+00	4,10
92.	1.	0.	0	systems engineering	0.		-1.000e+00	
92.	2.	0.	0	management	0.		-1.000e+00	
92.	3.	0.	0	quality assurance	0.		-1.000e+00	
92.	4.	0.	0	safety & environmental engineering	0.		-1.000e+00	
92.	0.	0.	0	home office engineering & services	1.000e-01	fraction	-1.000e+00	4,10
93.	1.	0.	0	construction management	0.		-1.000e+00	
93.	2.	0.	0	inspection	0.		-1.000e+00	
93.	3.	0.	0	preoperational testing	0.		-1.000e+00	
93.	0.	0.	0	field office engineering & services	1.000e-01	fraction	-1.000e+00	4,10
94.	1.	0.	0	project administration	0.		-1.000e+00	
94.	2.	0.	0	staff training & plant startup	0.		-1.000e+00	
94.	3.	0.	0	inventories & spares	0.		-1.000e+00	
94.	0.	0.	0	owner's cost	5.000e-02	fraction	-1.000e+00	4,10
95.	0.	0.	0	process contingency	0.	fraction	-1.000e+00	4,10
96.	0.	0.	0	project contingency	1.000e-01	fraction	-1.000e+00	4,10
97.	0.	0.	0	interest during construction (IDC)	1.124e-01	fraction	-1.000e+00	4,10
98.	0.	0.	0	escalation during construction (EDC)	0.	fraction	-1.000e+00	4,10
99.	0.	0.	0	total cost	0.		9.887e+02	

REFERENCES

[1] S. C. Schulte, T. L. Wilke, and J. R. Young, "Fusion Reactor Design Studies–Standard Accounts for Cost Estimates," Battelle (Pacific Northwest Laboratory) report PNL-2648 (1978).

[2] S. C. Schulte, W. E. Bickford, C. E. Willingham, S. K. Ghose, and M. G. Walker, "Fusion Reactor Design Studies - Standard Unit Costs and Cost Scaling Rules," Pacific Northwest Laboratory report PNL-2987 (1979).

[3] D. L. Phung, "A Method for Estimating Escalation and Interest During Construction (EDC and IDC)," in *Proc. 2nd Miami Conf. on Alternative Energy Sources* (December 10-13, 1979).

[4] W. R. Hamilton, D. C. Keeton, and S. L. Thomson, "Cost Accounting System for Fusion Studies," Oak Ridge National Laboratory report ORNL/FEDC-85/7 (1985).

[5] J. G. Delene, H. I. Bowers, and M. L. Meyers, "Nuclear Energy Cost Data Base," U. S. DOE report DOE/NE-0044/3 (1985).

[6] "Pressurized Water Reactor Plant," United Engineers and Constructors, Inc. report Wash-1230m 1 (1972).

[7] A. A. Hollis, "An Analysis of the Estimated Capital Cost of a Fusion Reactor," AERE Harwell Laboratory report AERE-R.9933 (1981).

[8] B. Badger, G. L. Kulcinski, R. W. Conn, C. W. Maynard, K. Audenaerde, *et al.*, "Tokamak Engineering Test Reactor," University of Wisconsin report UWFDM-191 (1977).

[9] TFCX Design Team, "Cost Summary Addendum to the Preconceptual Design Report," Princeton Plasma Physics Laboratory report A-Axxx-8407-010 (1984).

[10] S. L. Thomson, "Reference Cost Data for Fusion," Oak Ridge National Laboratory report ORNL/FEDC-86-8 (1986).

[11] W. R. Spears, "The SCAN-2 Cost Model," NET Project report Nr. 62 (1986).

[12] R. L. Hagenson and R. A. Krakowski, "Compact Reversed-Field Pinch Reactors (CRFPR): Sensitivity Study and Design-Point Determination," Los Alamos National Laboratory report LA-9389-MS (1982).

[13] C. C. Baker, M. A. Abdou, R. M. Arons, A. E. Bolon, C. D. Boley, *et al.*, "STARFIRE – A Commercial Tokamak Fusion Power Plant Study," Argonne National Laboratory report ANL/FPP-80-1 (1980).

[14] C. G. Bathke, D. J. Dudziak, R. A. Krakowski, W. B. Ard, D. A. Bowers, *et al.*, "The Elmo Bumpy Torus Reactor and Power Plant Conceptual Design," Los Alamos National Laboratory report LA-8882-MS (1981).

[15] B. Badger, I. N. Sviatoslavsky, S. W. Van Sciver, G. L. Kulcinski, G. A. Emmert, D. T. Anderson, *et al.*, "UWTOR-M: A Conceptual Modular Stellarator Power Reactor," University of Wisconsin report UWFDM-550 (1982).

[16] K. Evans Jr., "A Tokamak Reactor Cost Model Based on STARFIRE/WILDCAT Costing," Argonne National Laboratory report ANL/FPP/TM-168 (1983).

[17] J. Sheffield, R. A. Dory, S. M. Cohn, J. G. Delene, L. Parsly, D. E. T. F. Ashby, and W. T. Reiersen, "Cost Assessment of a Generic Magnetic Fusion Reactor," *Fusion Technol.* **9** (1986) 199.

[18] B. G. Logan, C. D. Henning, G. A. Carlson, R. W. Werner, D. E. Baldwin, *et al.*, "MARS Mirror Advanced Reactor Study Final Report," Lawrence Livermore National Laboratory report UCRL-53480 (1984).

[19] R. L. Hagenson, R. A. Krakowski, C. G. Bathke, R. L. Miller, M. J. Embrechts, *et al.*, "Compact Reversed-Field Pinch Reactors (CRFPR): Preliminary Engineering Considerations," Los Alamos National Laboratory report LA-10200-MS (1984).

[20] R. L. Reid, R. J. Barrett, T. G. Brown, G. E. Gorker, R. J. Hooper, *et al.*, "The Tokamak Systems Code," Oak Ridge National Laboratory report ORNL/FEDC-84/9 (1985).

[21] C. Copenhaver, R. A. Krakowski, N. M. Schnurr, R. L. Miller, C. G. Bathke, *et al.*, "Compact Reversed-Field Pinch Reactors (CRFPR): Fusion-Power-Core Integration Study," Los Alamos National Laboratory report LA-10500-MS (1985).

[22] G. E. Gorker, "Electrical Systems for RFP Lithium Blanket Magnets," Oak Ridge National Laboratory report ORNL/FEDC-M-E/M-068 (1986).

[23] T. R. Strobridge, "Cryogenic Refrigerators – An Updated Survey," National Bureau of Standards Technical note 655 (1974).

[24] "MINIMARS Conceptual Design: Final Report," J. D. Lee, Ed., Lawrence Livermore National Laboratory report UCID-20773 (1986).

[25] D. Ehst, C. C. Baker, J. Brooks, R. Buxbaum, and Y. Cha, "Tokamak Power Systems Studies–FY1986: A Second Stability Power Reactor," Argonne National Laboratory report ANL/FPP/86-1 (1987).